Study Report on the Earthquake-induced Natural Terrain Landslide Hazard Assessment

GEO Report No. 343

Arup

Geotechnical Engineering Office
Civil Engineering and Development Department
The Government of the Hong Kong
Special Administrative Region

Study Report on the Earthquake-induced Natural Terrain Landslide Hazard Assessment

GEO Report No. 343

Arup

First published, December 2018

Prepared by:

Geotechnical Engineering Office,
Civil Engineering and Development Department,
Civil Engineering and Development Building,
101 Princess Margaret Road,
Homantin, Kowloon,
Hong Kong.

Preface

In keeping with our policy of releasing information which may be of general interest to the geotechnical profession and the public, we make available selected internal reports in a series of publications termed the GEO Report series. The GEO Reports can be downloaded from the website of the Civil Engineering and Development Department (http://www.cedd.gov.hk) on the Internet.
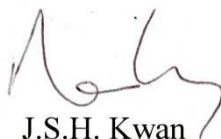
W.K. Pun
Head, Geotechnical Engineering Office
December 2018

Foreword

This GEO Report presents a study of the earthquake-induced natural terrain landslide hazard of a Study Area in the North-west New Territories of Hong Kong. The study was conducted by Arup, in collaboration with the GEO and the Guangdong Engineering Earthquake Resistance Research Institute (GEERRI) of the Earthquake Administration of Guangdong Province (EAGP). It serves as a regional assessment to estimate the order of magnitude of the likelihood of earthquake-induced natural terrain landslides.

The study approach has been derived based on consolidating the findings of a comprehensive literature review on local and overseas state-of-the-art papers. The work involves an assessment of the earthquake-induced slope displacements using both numerical analyses and empirical correlations and a detailed landslide susceptibility assessment. The effects of topographic amplification on the seismic ground motions as well as the effects of rainfall on slopes have been duly considered. This study also covers the seismic stability of boulder fall. Microzonation maps for the Study Area have been produced.

This Report was prepared by a team led by Dr J.W. Pappin of Arup, in collaboration with the GEO and the GEERRI. The team members are Dr H. Jiang, Mr R.C.H. Koo, Mr Y.B. Yu, Dr P.L. Chen and Ms M.M.L. So. This work was coordinated by Dr J.S.H. Kwan and overseen by Mr Y.K. Shiu and Mr K.K.S. Ho. Draft versions of the Report were circulated to relevant Government departments and local academics for comment. The contributions of all parties are gratefully acknowledged.

J.S.H. Kwan
Chief Geotechnical Engineer/Standards and Testing

Executive Summary

An assessment of the earthquake-induced natural terrain landslide hazard for a Study Area in the North-west New Territories of Hong Kong has been carried out in this study.

This study is a regional assessment to estimate the order of magnitude of the likelihood of earthquake-induced natural terrain landslides in Hong Kong. The earthquake-induced landslide susceptibility has been examined relative to the rainfall-induced landslide susceptibility. The adopted regional assessment approach is consistent with the regional perspective considered by a study undertaken previously by the Geotechnical Engineering Office on the global quantitative risk assessment of earthquake-induced landslides of man-made slopes in Hong Kong. Such regional perspective provides insights on the overall scale of the problem. This study is a hazard assessment and the direct consequences of earthquake-induced natural terrain landslides are not considered.

Based on a literature review of some local and overseas state-of-the-art papers, the methodology for landslide and boulder fall hazard assessments has been formed. For earthquake-induced landslides, the slope displacements have been assessed using both numerical modelling (by *Oasys* SIREN and Dynamic FLAC) and empirical correlations (Jibson et al, 1998; Hsieh & Lee, 2011) for the seismic ground motions with 2% and 10% probabilities of being exceeded in the next 50 years. Based on the literature review, it is found that the vertical seismic ground acceleration would not have any significant effect on the slope displacements. On the other hand, the topographic effects of 30 m, 100 m and 300 m ridge heights have been considered in this study. It is found that the topographic effects of higher ridges could significantly increase the induced slope displacements. The results have been interpreted in terms of a static factor of safety corresponding to a threshold displacement value of 100 mm, above which earthquake-induced landslides are likely to be triggered according to the literature review. It is concluded that the slopes need to be close to failure at the time of earthquake should there be any significant earthquake-induced landslide hazards.

For the seismic stability of boulders, a series of simplified one-dimensional dynamic time stepping analyses have been carried out to determine the likelihood of boulder instability under 2%, 10% and 63% in 50 years ground motions. The topographic effects of 30 m, 100 m and 300 m ridge heights have also been considered for the 2% and 10% in 50 years ground motions. In addition, the analyses have been performed to assess the combined effect of horizontal and vertical accelerations (without topographic effect) for the 2% in 50 years ground motions. The results indicate that seismic loadings are critical on the boulder stability only if the boulders are close to failure at the time of earthquake.

A seismic microzonation map has been produced for natural terrain landslide susceptibility taking into account the combined effects of seismic ground motions and rainstorms. This is done by considering how much time the natural terrain is close to failure as a result of rainstorms when an earthquake event takes place. The microzonation map is formed based on a landslide susceptibility map derived from past landslides (up to 2009) recorded in the Enhanced Natural Terrain Landslide Inventory. Overall, the effect of earthquakes on triggering natural terrain landslides is small. There could be an increase of the failure probability of being less than one tenth of that expected from rainstorms alone. To cater

for those uncertainties resulting from different assumptions made, a sensitivity study has been carried out to illustrate the maximum credible effect of seismic ground motions on the natural terrain landslide hazards.

A rock fall and boulder fall susceptibility map has also been produced in qualitative terms based on the boulder density and the overall slope angle.   This map has not been changed by considering the effects of seismic ground motions.

The implication of distress of natural hillsides, which may be caused by earthquakes and would increase the rainfall-induced landslide susceptibility, has not been considered in this study.   Furthermore, debris resulting from earthquake-induced landslides may be deposited on natural hillsides and it is liable to be re-mobilised under subsequent rainstorms.   Thus, the potential increase of natural terrain landslide hazards after a large earthquake event should not be neglected.   It is believed that a 'reactive approach', including inspection and mapping of potential slope distress as well as major debris deposits close to facilities, could be a pragmatic approach to deal with post-earthquake landslide hazards.   If a major earthquake occurs in Hong Kong, slope inspections and mapping of vulnerable areas on the natural hillsides should be carried out in the same way as the inspections that would be performed for buildings and infrastructure.

Contents

List of Tables

List of Figures

1   Introduction

1.1   Background

The Geotechnical Engineering Office (GEO) of the Civil Engineering and Development Department (CEDD) has previously assessed the potential effects of earthquakes on the stability of man-made slopes and retaining walls in Hong Kong (e.g. Wong & Ho, 2000; Au-Yeung & Ho, 1995).   As the management of natural terrain landslide hazards is a focus of the post-2010 Landslip Prevention and Mitigation Programme, there is a need to examine the responses and stability of natural terrain in Hong Kong under an earthquake event.

On 1st April 2009, GEO commissioned Ove Arup & Partners Hong Kong Limited (Arup) to undertake the Investigation Assignment of "Pilot Seismic Microzonation Study in North-west New Territories for the Study of Potential Effect of Earthquake on Natural Terrain" under Agreement No. CE 49/2008 (GE).   The Guangdong Engineering Earthquake Resistance Research Institute (GEERRI) is a sub-consultant to Arup on this Assignment.

The above study involves (a) an overall seismic hazard assessment of Hong Kong; (b) an area-specific seismic microzonation assessment for a Study Area in the North-west New Territories; and (c) an evaluation of the potential effects of earthquakes on the natural terrain, with an account taken of local geology, topography and envisaged ground responses.   The study evaluates the overall seismic hazard assessment of Hong Kong and produces maps delineating zones with similar predicted seismic intensity and motion at the ground surface in the Study Area.   The potential natural terrain landslide hazards associated with the seismic ground motions are also evaluated.   Findings of parts (a) and (b) of the study have been documented in Arup (2015) and Arup (2018) respectively.

This report documents part (c) of the study i.e. an evaluation of the potential effects of earthquakes on the natural terrain.   The results from parts (a) and (b) of the study such as the response spectra for Hong Kong, bedrock seismic ground motion time histories, topographic effects, etc. would be used to evaluate the potential effects of earthquake on the stability of natural terrain and assess the earthquake-induced natural terrain landslide hazards in the Study Area.

1.2   Scope of this Report

The earthquake-induced natural terrain landslide hazard assessment for a Study Area in the North-west New Territories of Hong Kong has been carried out in this study.   Figure 1.2 of Arup (2018) shows the location of the Study Area.   Key items of the work completed under this study are listed as follows.

1.2.1   Literature Review

A review of literature pertaining to the assessment of slope movements under seismic ground motions has been carried out.   Both empirical and analytical methods identified in the literature are discussed.   Some methods have been selected for slope stability analyses in the present study.

1.2.2 Development of Bedrock Seismic Ground Motion Time Histories and Arias Intensity

Horizontal time histories of seismic ground motions have been derived to be compatible with the horizontal uniform hazard response spectra (UHRS) having 10% and 2% probabilities of being exceeded in the next 50 years (or, for simplicity, 10% and 2% in 50 years ground motions) (see Arup (2015) for the UHRS). Analyses of vertical ground motions and the topographic amplification effects have been considered in generating the time histories. The Arias Intensity, which is found to correlate well with the distribution of earthquake-induced landslides (e.g. Jibson, 1993), has been calculated from the time histories.

1.2.3 Methodology for the Analysis of Earthquake-induced Landslide

For the assessment of earthquake-induced landslides, time history-based numerical analyses using *Oasys* SIREN and Dynamic FLAC have been carried out for natural slopes possessing different presumed values of soil strengths and static factor of safety (FoS) to determine the permanent downslope displacements under different levels of seismic ground motions. The displacements have been compared with that calculated using empirical correlations. These empirical correlations are related to the Arias Intensity of the seismic ground motions. The results indicate that for the level of ground motion appropriate to Hong Kong, the slopes need to be close to failure (i.e. possessing a static FoS close to unity) at the time of earthquake should there be any significant likelihood of slope failures.

1.2.4 Methodology for the Analysis of Earthquake-induced Boulder Fall

A one-dimensional dynamic stability analysis program has been developed for this study to assess the boulder fall hazard under seismic loadings. Spherical boulders of 100 kg, 1,000 kg and 10,000 kg have been considered. The results have been presented in terms of the limiting eccentricity necessary for a boulder to fall under a given seismic ground motion. The horizontal ground acceleration time histories derived for site response analyses in Arup (2018) as well as that catered for topographic effects (for 30 m, 100 m and 300 m ridge heights) have been considered for 63%, 10% and 2% in 50 years ground motions. In addition, vertical ground acceleration has been considered for the 2% in 50 years ground motion. The results have been compared with that evaluated using an energy approach, which considers the amount of energy required for a boulder to tip.

1.2.5 Landslide Susceptibility

A landslide susceptibility analysis has been conducted for the Study Area considering the existing geological conditions, topography, drainage, geomorphology and past instability records (up to 2009) obtained from the Enhanced Natural Terrain Landslide Inventory (ENTLI). Various susceptibility factors such as slope angle, geology, slope morphology, drainage have been analysed and compared with the landslide density deduced from the ENTLI data. Susceptibility classes have been defined and the probability of slope failures at any location has been determined for each class. The increase in the probability of slope failures due to earthquake ground motions has been determined together with the topographic amplification

effects. These combined failure probabilities have been used to generate landslide susceptibility maps, which delineate and rank areas of potential landslide hazards within the Study Area.

This study is a regional assessment to provide an order of magnitude of how likely natural terrain landslides would be triggered under an earthquake event in Hong Kong. The earthquake-induced landslide susceptibility has been examined relative to the rainfall-induced landslide susceptibility. The adopted regional assessment approach is consistent with the regional perspective considered by a study undertaken previously by the GEO on global quantitative risk assessment of earthquake-induced landslides of man-made slopes in Hong Kong. Such regional perspective provides insights on the overall scale of the problem. This study is a hazard assessment and the direct consequences of earthquake-induced natural terrain landslides are not considered.

The implication of distress of natural hillsides, which may be caused by earthquakes and would increase the rainfall-induced landslide susceptibility, has not been considered in this study. Furthermore, debris resulted from earthquake-induced landslides may be deposited on natural hillsides and it is liable to be re-mobilised by subsequent rainstorms. Thus, the potential increase of natural terrain landslide hazards after a large earthquake event should not be neglected. It is believed that a 'reactive approach', including inspection and mapping of potential slope distress as well as major debris deposits close to facilities, could be a pragmatic approach to deal with post-earthquake landslide hazards. If a major earthquake occurs in Hong Kong, slope inspections and mapping of vulnerable areas on the natural hillsides should be carried out in the same way as the inspections that would be performed for buildings and infrastructure.

2 Literature Review

2.1 General

The natural terrain landslide susceptibility to seismic ground motions is dependent on the regolith distribution, landslide distribution and levels of ground motions. An assessment can be carried out by empirical relationships based on observed data for earthquake-induced natural terrain landslides in high-seismicity regions. In many seismic codes, the seismic slope stability is assessed by analytical methods using the simplified pseudo-static approach based on the Newmark (1965) method. Theoretical assessments based on non-linear dynamic analyses are also available. In this study, a literature review pertaining to the assessment of earthquake-induced natural terrain landslide susceptibility has been carried out.

The review covers the methodologies for assessing the seismic displacements of slopes in natural terrain, the landslide susceptibility factors and mapping as well as seismic stability of boulders. This section summarises the findings of this literature review, on which the assessment of the earthquake-induced natural terrain landslide susceptibility has been based.

There were some local studies pertaining to natural terrain landslides. For example, Ding (2008) and Halcrow (2009) indicated that if Hong Kong was subjected to a magnitude 7.0 earthquake located within 50 km (e.g. at the Dangan Islands), there would be significant areas of shallow landslides and rock falls. However, such an extreme event may not be considered

as a reasonable design event for Hong Kong. Also, no indication had been given to the probability of such an extreme event in their studies.

Some studies (e.g. Tang et al, 2009 & 2010; Wong & Ding, 2010; Wong et al, 2010) examined the extent of possible neotectonic movements of major faults in Hong Kong as a result of earthquakes and their potential correlations with natural terrain landslides. The studies involved geomorphological assessments, field observations, ground investigation and dating of superficial deposits. It was found that there were two clusters of territory-wide deep-seated landslide aged at around 50,000 and 30,000 years ago that could had been possibly induced by seismic ground motions. Nevertheless, the potential triggering cause due to high intensity rainstorms could not be ruled out. Hence, the studies could not conclude that neotectonic movements had occurred simply by referring to the evidence of historical landslides.

Apart from natural terrain landslide studies, Wong & Ho (2000) presented a quantitative risk assessment of earthquake-induced landslides of man-made slopes in Hong Kong. They provided a very useful methodology for combining the hazards of rainfall-induced landslides with that induced by seismic ground motions. The likelihood of low, moderate and high degrees of soil saturation estimated in that report has been used to estimate the combined effects of rainstorms and earthquakes on the natural terrain landslide hazard in this study (see Section 6).

2.2 Methodology for Seismic Stability Analysis of Slopes in Natural Terrain

The Newmark's method (Newmark, 1965) has been commonly used to assess the slope movements under an earthquake event. Jibson (1993) described a state-of-the-art approach for analysing the seismic slope stability using a simplified method to calculate Newmark displacement. Blake et al (2002) described the ground motion parameters for seismic slope stability analyses. They also recommended the use of pseudo-static seismic loadings in a conventional limit equilibrium analysis as a screening process and a displacement analysis based on an analogy of a rigid block on an inclined plane. The susceptibility of slope failures to the accompanying vertical ground motions as well as the earthquake-induced reactivation of previous landslides were also discussed.

2.2.1 Ground Motion Parameters

Blake et al (2002) concluded that the ground motion parameters from Abrahamson & Silva (1996) and Rathje et al (1998) used in the recommended seismic slope displacement analysis procedures pertaining to the maximum horizontal acceleration, the duration of strong shaking and the mean period of ground motion (T_m). Duration is typically quantified for this purpose as the time span in which 90% of the energy in an earthquake accelerogram is released, or more specifically, as the time between the 5% and 95% normalised Arias Intensity (D_{5-95}). D_{5-95} and T_m are mainly a function of earthquake magnitude (M), site-source distance (r), site conditions (i.e. rock vs. soil), and the type of faulting.

(a) Duration (Abrahamson & Silva, 1996)

Median values of $D_{5\text{-}95}$ of rock can be estimated as follows:

For $r > 10$ km,

$$\ln (D_{5\text{-}95}) \, \text{med} = \ln \left[\frac{\left[\frac{\exp (A_1 + A_2 \, (M - 6))}{10^{1.5M + 16.05}} \right]^{-1/3}}{15.7 \times 10^6} + \frac{(r - 10)}{A_3} \right] + \ln (A_4) \, \text{.....................(2.1)}$$

For $r < 10$ km,

$$\ln \; (D_{5\text{-}95}) \, \text{med} = \ln \left[\frac{\left[\frac{\exp (A_1 + A_2 \, (M - 6))}{10^{1.5M + 16.05}} \right]^{-1/3}}{15.7 \times 10^6} \right] + \ln (A_4) \, \text{..........................(2.2)}$$

where the coefficients A_1, A_2, A_3 and A_4 are listed in Table 2.1.

Table 2.1 Coefficients for Estimating T_m (Blake et al, 2002)

A_1 (s)	A_2 (s)	A_3 (m/s)	A_4 (s)	C_1 (s)	C_2 (s)	C_3 (m/s)	V_1 (m/s)	V_2 (m/s)
5.204	0.851	15.873	2.378	0.411	0.0837	0.00208	1.87	3.477

(b) Mean Period (Rathje et al, 1998)

Rathje et al (1998) defined the mean period (T_m) as the inverse of the weighted average frequency, with weights defined from the Fourier amplitude spectrum over a frequency range from 0.25 to 20 Hz.   For practical application, the authors suggested to estimate the parameter as:

$$\ln (T_m) = \ln (C_1 + C_2 \times (M - 6) + C_3 \times r), \; M \leq 7.25 \; \text{.........................(2.3)}$$

$$\ln (T_m) = \ln (C_1 + 1.25 \times C_2 + C_3 \times r), \; 7.25 \leq M \leq 8.0 \; \text{.....................(2.4)}$$

where parameters C_1, C_2 and C_3 should be selected for a rock site condition using the values presented in Table 2.1.

2.2.2 Pseudo-static Approach

The pseudo-static approach was recommended by Blake et al (2002) as a screening process, which the factor of safety (FoS) would be estimated by entering a horizontal seismic coefficient (k_{eq}) into a conventional slope stability calculation. k_{eq} represents the fraction of the weight of a sliding mass that is applied as an equivalent horizontal force acting through the

centroid of the mass. If FoS > 1, the site passes the screening. If FoS < 1, the site fails and should be subsequently analysed for slope deformation.

The seismic coefficient to be used in the screening analysis is taken as:

$$k_{eq} = f_{eq} \times (MHA_r / g) \dots\dots\dots\dots\dots\dots\dots\dots\dots(2.5)$$

where MHA_r is the maximum horizontal acceleration at a soft rock site, g = acceleration of gravity, and f_{eq} is a factor related to the seismicity of the site, as described below.

Previous pseudo-static procedures for seismic slope stability have specified a single value for f_{eq}, and thus have made implicit and usually very conservative assumptions about the magnitude of earthquakes causing the design-basis MHA_r. The paper suggested a method to reduce any unnecessary conservatism by developing a range of f_{eq} values as a function of magnitude (M) and site-source distance (r). Calculations were performed to evaluate, for various combinations of MHA_r, M and r, the f_{eq} values that lead to a 50% probability of the seismic slope displacement exceeding the chosen threshold Newmark displacements of 5 cm or 15 cm. The results of the calculations are shown in Figure 2.1, and correspond to the following equation:

$$f_{eq} = \left[V_1 - \log_{10}\left(\frac{u}{\left(\frac{MHA_r}{g}\right) \times NRF \times D_{5\text{-}95}} \right) \right] \frac{NRF}{V_2} \dots\dots\dots\dots\dots\dots(2.6)$$

where the coefficients V_1 and V_2 are defined in Table 2.1, u (cm) is the threshold displacement, $D_{5\text{-}95}$ is the median duration from the Abrahamson & Silva (1996) relationship, and NRF is a factor to allow for the non-linear response of the material above the failure surface, which is defined as:

$$NRF \approx 0.6225 + 0.9196 \times Exp\left(\frac{- MHA_r / g}{0.4449} \right)$$

for $0.1 < MHA_r / g < 0.8$.

2.2.3 Newmark's Method

Comparison with other approaches

The Newmark's method was recommended by Jibson (1993) for earthquake-induced landslide stability analysis instead of the pseudo-static analysis or finite-element modelling because:

(i) The pseudo-static analysis, in which an earthquake acceleration acting on a potential landslide mass is treated as a permanent static body force in a limit-equilibrium analysis, has proved to be vastly over-conservative when the peak ground acceleration (PGA) exceeds the yield acceleration of
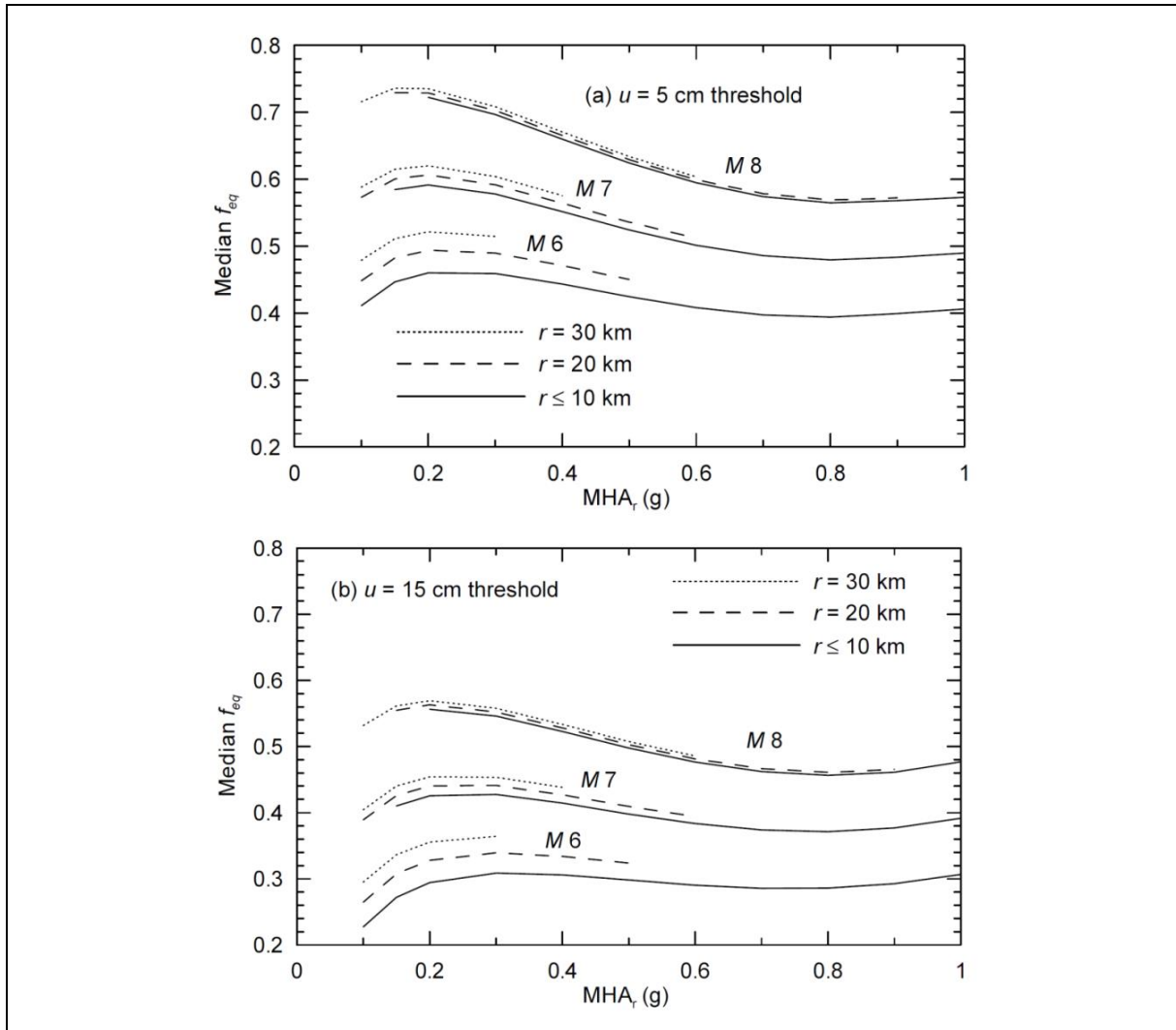
Figure 2.1   Required Values of f_{eq} as Function of MHA_r and Seismological Condition for Threshold Displacements of (a) 5 cm and (b) 15 cm (Blake et al, 2002)

the slope.   According to Wilson & Keefer (1983), many slopes experienced transient earthquake accelerations well above their yield accelerations but induced very little or no permanent displacement.

(ii) The two-dimensional finite-element modelling, which can estimate the strain potentials and slope deformations quite accurately, requires a very broad set of high quality and density data.   This makes it generally impractical and overly expensive.

Applicability of Newmark's method to natural slopes

Originally intended for dams and embankments, the Newmark's method was proved to be applicable to natural slopes by Wilson & Keefer (1983).   This method assumes that the

landslide mass is treated as a rigid-plastic body. As such, the mass is assumed not to deform internally, nor to experience any permanent displacement at a seismic acceleration below the yield level. It deforms plastically along a discrete basal shear surface when the critical acceleration is exceeded.

The author thus highlights that the Newmark's method is the best applied to translational block slides, especially infinite-slope models that are applicable to landslides on natural terrain, and rotational slumps.

It should be noted that the Newmark's method is also not applicable to certain slope materials, which shear strength reduces with increasing strain. In this case, the Newmark's method would underestimate the slope displacements. On the other hand, for visco-elastic materials, it would overestimate the slope displacements due to the viscous damping of the seismic response of the soil.

Steps of Newmark's method of stability analysis

(a) Factor of safety

As noted by Newmark (1965), modelling dynamic slope response requires an input of the undrained or total shear strength parameters. During earthquakes, slope materials would behave in an undrained manner, because excess pore pressures induced by dynamic deformation of the soil column could not dissipate during the brief shaking duration. For a rough estimation of the slope displacements, the authors suggest to use a simple factor-of-safety analysis for infinite slope based on an estimated shear strength.

(b) Thrust angle

The thrust angle (α) is the direction in which the centre of gravity of a sliding mass moves when the displacement first occurs. For an infinite slope, this is the slope angle. For a simple planar block, it is the basal shear surface inclination angle. Newmark (1965) defined the thrust angle for a circular rotational movement as the angle between the vertical and a line segment connecting the centre of gravity of the slide mass and the centre of the slip circle (see Figure 2.2). For irregular shapes, an "equivalent" circular slip surface should be estimated.

(c) Critical acceleration

The critical acceleration (A_c) is the pseudo-static acceleration that leads to a factor of safety (FoS) of unity for a slope or a sliding block. For a rigid block,

$$A_c = (\text{FoS} - 1)\, g \sin \alpha \dots\dots\dots\dots\dots\dots\dots\dots\dots\dots\dots\dots\dots\dots(2.7)$$

The earthquake acceleration time histories are selected using PGA, Arias Intensity and duration as the ground shaking intensity indexes.

Two approaches were suggested by Newmark (1965) for selecting an input ground motion for displacement analyses:
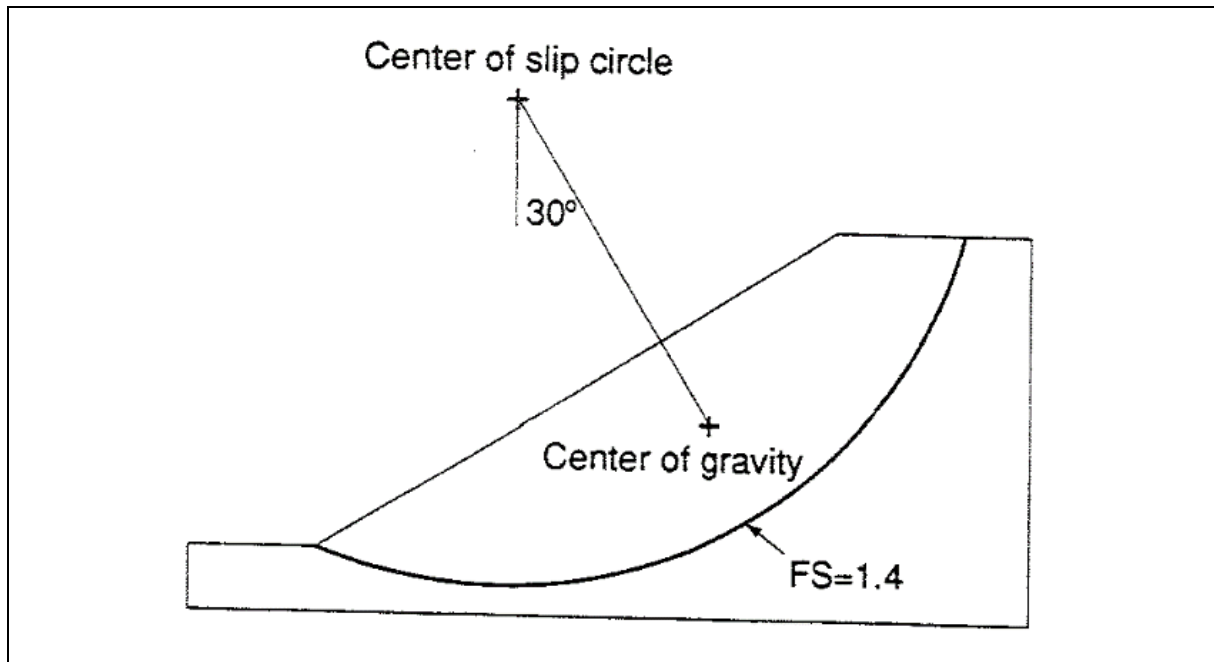
Figure 2.2   Model of Hypothetical Slope (Jibson, 1993)

(i)   Scaling acceleration time histories from actual earthquakes to a desired level of PGA; and

(ii) Using single or multiple cycles of artificial acceleration pulses having simple rectangular, triangular or sinusoidal shapes.

These methods are now considered to be oversimplified to select time histories given the current digitised acceleration time histories possessing a broad range of attributes, including the magnitude and source distance that significantly influence the duration and predominant periods of shaking.   Jibson (1993) suggested the use of Arias Intensity, which was found to correlate well with the distribution of earthquake-induced landslides.

The Arias Intensity (I_a) has an unit of velocity and is defined as:

$$I_a = \pi/2g \int [a(t)]^2 \, dt \quad \text{...(2.8)}$$

where g is gravity, and $a(t)$ is the time history of the ground acceleration. I_a can be estimated based on the following relationships if the time history is not available:

- $\log I_a = M - 2 \log R - 4.1$ (Wilson & Keefer, 1985)

- $I_a = 0.9 \, \text{PGA} \times T$ (reported by R.C. Wilson (U.S. Geological Survey, unpublished data), see Jibson (1993))

  and $\log T = 0.432 \, M - 1.83$ (Dobry et al, 1978)

where *M* and *R* are the moment magnitude of the earthquake and earthquake source distance in kilometres respectively, and *T* is the duration in seconds.

(d) Newmark displacement calculation

The Newmark displacement is calculated by double integrating the parts of ground motions that lie above the yield acceleration, as illustrated in Figure 2.3.   Table 2.2 shows the recommended simple BASIC program that uses the algorithm of Wilson & Keefer (1983) to compute the Newmark displacement from an acceleration time history with a constant time step, with modification to prohibit any upslope displacement.

In addition to the integration of the time history, there are numerous empirical correlations to calculate Newmark displacement based on I_a (Jibson, 1993), horizontal acceleration and the median duration (D_{5-95} (s)) (Blake et al, 2002).
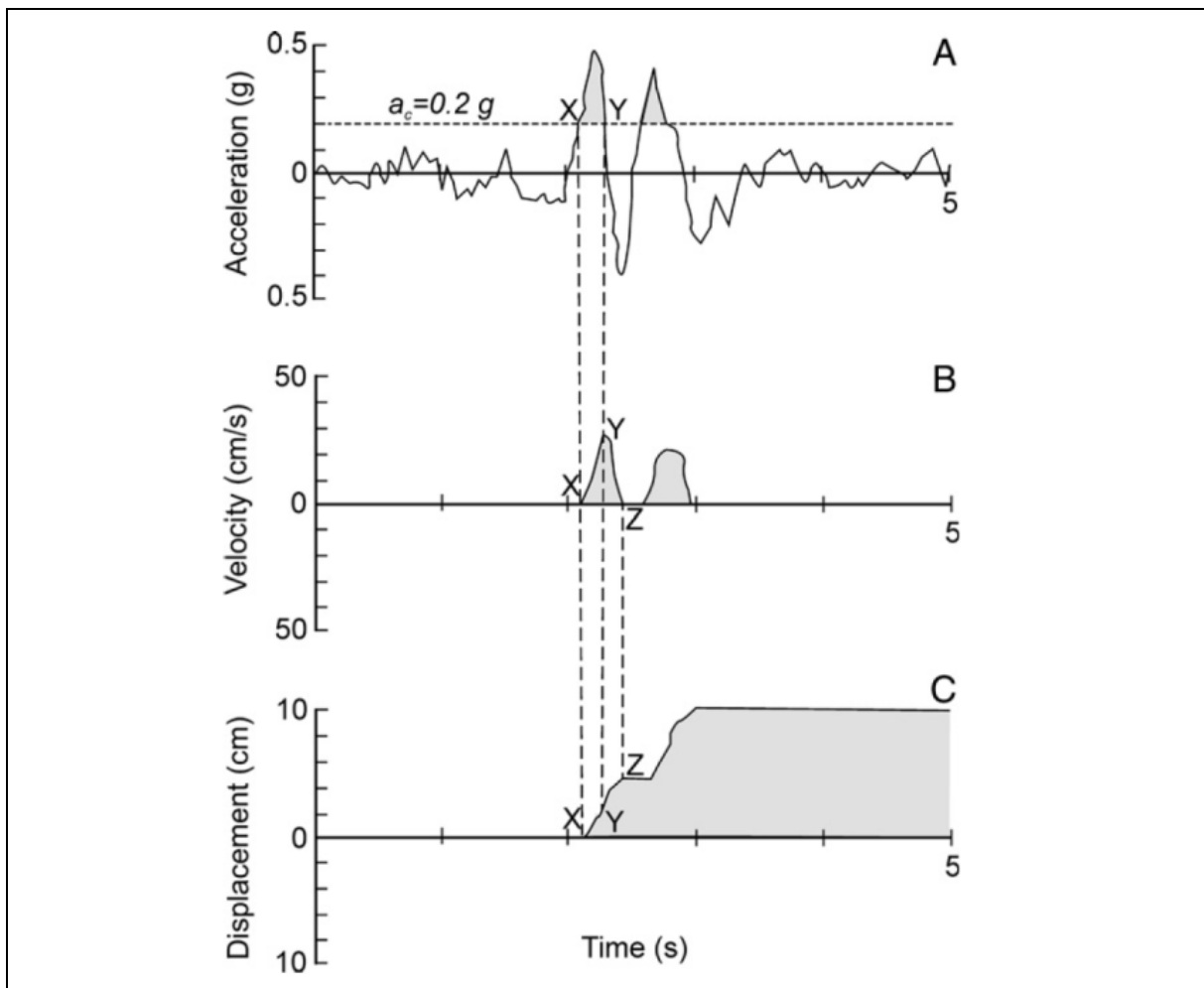
Figure 2.3   Illustration of the Newmark Displacement Calculation Algorithm, Adapted from Wilson & Keefer (1983) (Jibson, 1993)

Table 2.2 BASIC Program for Calculating Newmark Displacement (Jibson, 1993)

Program Step	Instruction
1	REM Program for calculating Newmark displacement
2	REM Input data should be in units of cm/s/s
3	PRINT "Input file should be in cm/s/s"
4	INPUT "What is the name of the input file";A$
5	OPEN "I", #1, A$
6	INPUT "What is the critical acceleration in g's";T:T=980.665*T
7	INPUT "What is the digitization interval in seconds";D
8	INPUT "What is the duration of the record in seconds";Z
9	K=Z/D
10	Q=0
11	R=0
12	S=0
13	Y=0
14	V=0
15	U=0
16	FOR I=1 TO K
17	INPUT #1,A
18	IF V<0.0001 THEN 20
19	GOTO 26
20	IF ABS(A)>T THEN 22
21	GOTO 24
22	N=A/ABS(A)
23	GOTO 27
24	N=A/T
25	GOTO 27
26	N=1
27	Y=A−N*T
28	V=R+D/2*(Y+S)
29	IF V>0 THEN 32
30	V=0
31	Y=0
32	U=Q+D/2*(V+R)
33	Q=U
34	R=V
35	S=Y
36	NEXT I
37	PRINT "Total displacement in centimeters is ";U
38	END

2.2.4 Influence of Vertical Acceleration

2.2.4.1 Yang (2007)

Yang (2007) studied the possible effects of vertical acceleration on the seismic landslide hazard considering the effects of varying the groundwater level. He assumed that the horizontal and vertical seismic coefficients (k_h and k_v respectively) were applied simultaneously and studied the ratios of k_v/k_h = 0.5, 1.0 and 1.5.

Based on an infinite slope model (Figure 2.4), Yang (2007) calculated the vertical acceleration-dependent factor of safety (*FS*) as:

$$FS = \frac{c' + (\sigma - u) \tan \phi'}{[(1 + k_v) \sin \beta + k_h \cos \beta] \gamma z \cos \beta} \quad \text{..(2.9)}$$

where c' is the effective cohesion, ϕ' is the effective friction angle, γ is the unit weight of the soil, σ is the total normal stress, and u is the pore water pressure on the failure plane.

Or further as:

$$FS = \frac{c' + \{[(1 + k_v) \cos \beta - k_h \sin \beta] \gamma - (1 + k_v) \gamma_w m \cos \beta\} z \cos \beta \tan \phi'}{[(1 + k_v) \sin \beta + k_h \cos \beta] \gamma z \cos \beta} \quad \text{.....................(2.10)}$$

where γ_w is the unit weight of water, and m is the ratio of z_w to z (see Figure 2.4) being 0 for a dry slope and 1 for a saturated slope.
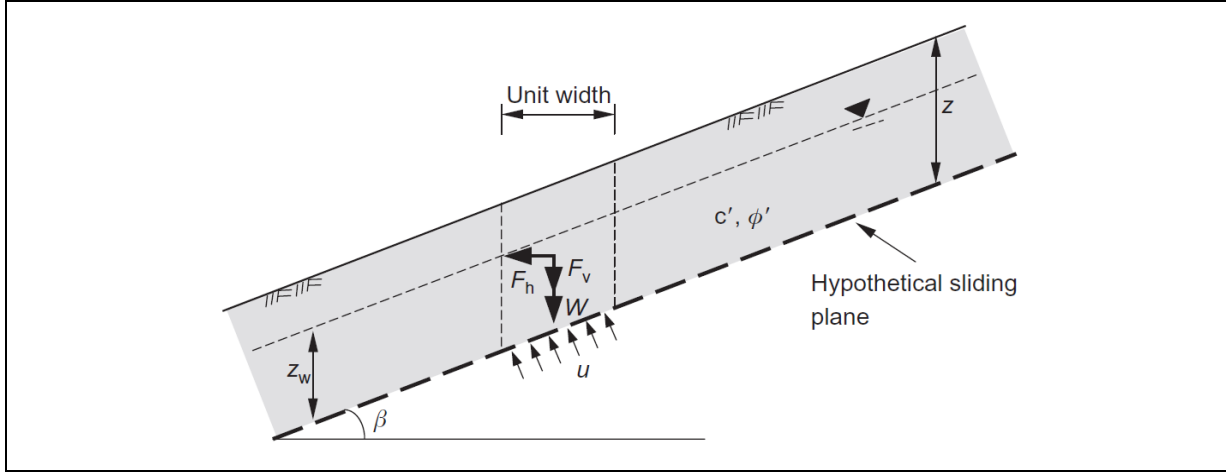
Figure 2.4   Infinite Slope Model (Yang, 2007)

The earthquake-induced excess pore water pressure was not considered. The yield acceleration could then be expressed as:

$$k_{hy} = \left(\frac{a_1 - a_4}{a_5 - a_2}\right) k_v + \left(\frac{a_3 - a_6}{a_5 - a_2}\right) \dots\dots\dots\dots\dots\dots\dots\dots\dots\dots\dots\dots(2.11)$$

where
$a_1 = (\gamma - \gamma_w m) z \cos^2 \beta \tan \phi'$
$a_2 = -\gamma z \sin \beta \cos \beta \tan \phi'$
$a_3 = c' + (\gamma - m\gamma_w) z \cos^2 \beta \tan \phi'$
$a_4 = \gamma z \sin \beta \cos \beta$
$a_5 = \gamma z \cos^2 \beta$
$a_6 = \gamma z \sin \beta \cos \beta.$

Figure 2.5 shows that the effect of vertical acceleration is negligible when $k_h < 0.2$, but tends to become significant at larger k_h values. Regarding the influence of the vertical acceleration on slope displacements, Figure 2.6 illustrates how the vertical acceleration amplifies the slope displacement, which is calculated as:

$$A_d = \frac{d}{d'} = \left(r_y^{-1.09}\right) \left[\frac{1 - r_y \left(a_y'/a_{max}\right)}{1 - \left(a_y'/a_{max}\right)}\right]^{2.53} \dots\dots\dots\dots\dots\dots\dots\dots\dots(2.12)$$

with

$$r_y = \frac{k_{hy}}{k_{hy}'} = \frac{1}{1 - \chi p}$$

where A_d is the displacement amplification factor, $\chi = (a_1 - a_4) / (a_5 - a_2)$, $p = k_v/k_h$ and a'_y is the yield acceleration excluding the effect of vertical acceleration.

However, as mentioned by Yang (2007), the large amplification of displacements is in a relative sense, being only associated with very small displacements.
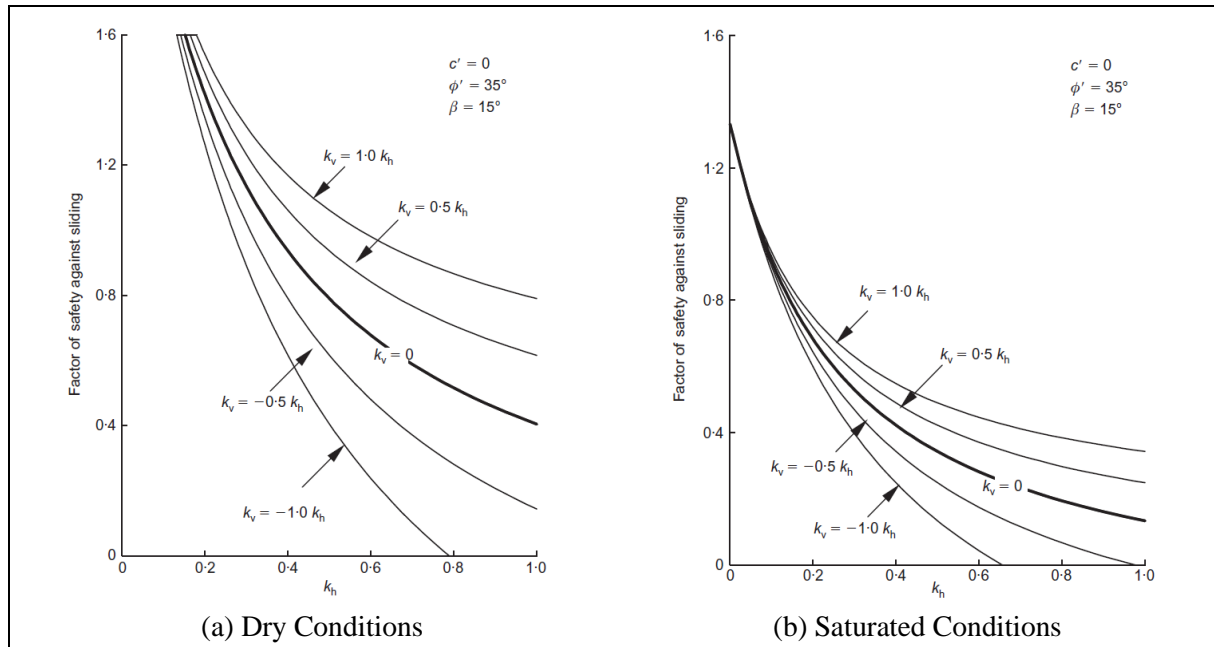
Figure 2.5   Factor of Safety of a Saturated Slope under Various Combinations of k_h and k_v (Yang, 2007)
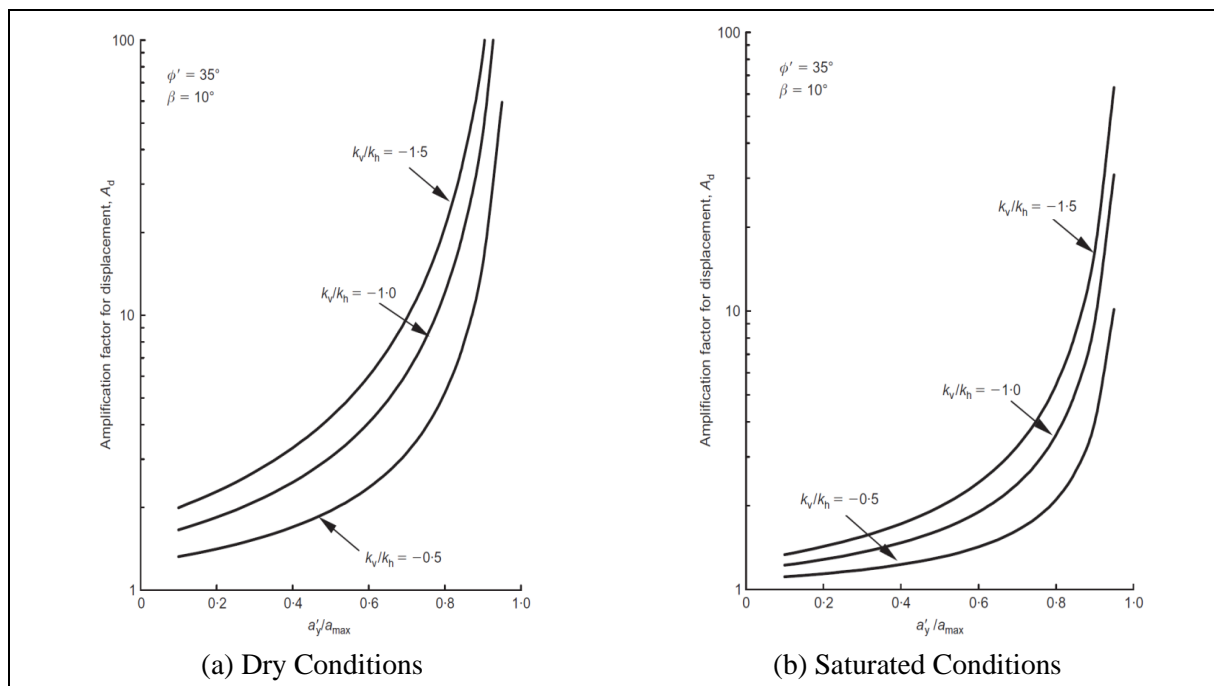
Figure 2.6   Amplification Factor for Permanent Displacement (Yang, 2007)

2.2.4.2 Commentary

This paper sets out to maximise the effects of vertical ground acceleration on slope movements. Figure 2.6 shows amplifications of slope displacement up to 100 times due to vertical acceleration but in reality these large factors only apply to extremely small displacements assessed without considering the vertical seismic ground motion. For a typical case where the peak vertical acceleration is similar to the peak horizontal acceleration, it is most unlikely that the vertical acceleration will be larger than 40% of the horizontal acceleration at the time when the peak horizontal acceleration occurs. It can be concluded from this paper that consideration of vertical acceleration will rarely lead to a significant increase in the estimated downslope displacements.

2.2.5 Reactivated Landslides

Cole et al (1998) studied the earthquake reactivation of pre-existing landslides scars, based on an analysis of two earthquake-reactivated landslides during the 1989 Loma Prieta earthquake in the epicentral region at the central Santa Cruz Mountains.

The two cases studied were characterised through thorough investigation comprising geological mapping, subsurface logging and sampling, and laboratory direct shear testing.   The actual landslide behaviour was then compared with the results of two analytical seismic stability analyses, following the pseudo-static method and cumulative-displacement analysis (i.e. Newmark method).   This study provided a good opportunity to test the dynamic slope stability methods currently used in practice, especially for the case of earthquake-induced reactivation of landslides in natural terrain.

This study concluded that the available methods of cumulative-displacement analysis are applicable to earthquake-reactivated landslides on natural terrain, but investigators should select variables with cautions so as not to underestimate the stability of pre-existing landslides. With a thorough characterisation of landslide geometry, local geological conditions, engineering properties and a selection of conservative strength parameters for the basal rupture surfaces, existing analytical techniques are sufficient for predictions of the order of magnitude when the lowest laboratory shear strengths are used.

2.3 Landslide Displacement Assessment

The Newmark displacement can be estimated by different methods.   Hsieh & Lee (2011) summarised the latest Arias Intensity-based empirical correlations for assessing earthquake-induced slope displacements. Blake et al (2002) also recommended an empirical formula to evaluate the Newmark displacement using the horizontal ground acceleration and the median duration (D_{5-95} (s)), which is also obtained from the build-up of Arias Intensity (I_a) during an earthqauake event.   The most recent empirical correlations proposed by Hsieh & Lee (2011) are discussed below.   In addition, the threshold displacement for landsliding in natural terrain is also discussed.

2.3.1 Arias Intensity Approach (Hsieh & Lee, 2011)

Hsieh & Lee (2011) employed strong-motion data from the 1999 Chi-Chi earthquake, the 1999 Kocaeli earthquake, the 1999 Duzce earthquake, the 1995 Kobe earthquake, the 1994 Northridge earthquake and the 1989 Loma Prieta earthquake to study the worldwide applicability of previous relationships among critical acceleration, Arias Intensity, and Newmark displacement, and refined them according to the new findings.

For example, it was found that the relationships derived by Jibson (1993) and Jibson et al (1998) (see equations below) were not applicable to the 1999 Chi-Chi earthquake dataset.

$$\log D_n = 1.460 \log I_a - 6.642 A_c + 1.546 \pm 0.409, \text{ Jibson (1993)} \dots\dots\dots (2.13)$$

$$\log D_n = 1.521 \log I_a - 1.993 \log A_c - 1.546 \pm 0.375, \text{ Jibson et al (1998)} \dots\dots (2.14)$$

where A_c is critical acceleration (in g), I_a is the Arias Intensity (in m/s), D_n is the downslope displacement (in cm), and the last term is the estimation error of the models.

Different relationships to derive the Newmark displacement were checked against different datasets. The forms of relationships between the Newmark displacement and the Arias Intensity were checked: I_a - D_n, I_a - $\log D_n$ and $\log I_a$ - $\log D_n$ (see Table 2.3). It was found that $\log D_n$ being proportional to $\log I_a$ was a worldwide phenomenon. Therefore, this relationship was regarded as the most accurate. On the other hand, it was demonstrated that there existed a very stable linear relationship between A_c and $\log D_n$ based on the worldwide dataset (see Table 2.4).

Table 2.3   Goodness of Fit to a Line in Different Relationships between D_n and I_a for A_c from 0.01 to 0.4 g (Hsieh & Lee, 2011)

Earthquake	D_n - I_a	$\log D_n$ - I_a	$\log D_n$ - $\log I_a$
Chi-Chi	$R^2 = 0.3 - 0.5$	$R^2 = 0.2 - 0.5$	$R^2 = 0.7 - 0.9$
Duzce & Kocaeli	$R^2 = 0.76 - 0.8$	$R^2 = 0.8 - 0.87$	$R^2 = 0.88 - 0.98$
Kobe	$R^2 = 0.7 - 0.89$	$R^2 = 0.78 - 0.87$	$R^2 = 0.9 - 0.98$
Loma Prieta	$R^2 = 0.6 - 0.8$	$R^2 = 0.32 - 0.5$	$R^2 = 0.77 - 0.85$
Northridge	$R^2 = 0.6 - 0.8$	$R^2 = 0.4 - 0.75$	$R^2 = 0.77 - 0.85$

Table 2.4   Goodness of Fit to a Line in Different Relationships between D_n and A_c (Hsieh & Lee, 2011)

Earthquake	D_n - A_c	$\log D_n$ - A_c	$\log D_n$ - $\log A_c$
Chi-Chi	$R^2 = 0.6 - 0.7$	$R^2 = 0.98 - 0.99$	$R^2 = 0.89 - 0.97$
Duzce & Kocaeli	$R^2 = 0.7 - 0.87$	$R^2 = 0.98 - 0.99$	$R^2 = 0.82 - 0.93$
Kobe	$R^2 = 0.67 - 0.82$	$R^2 = 0.98 - 0.99$	$R^2 = 0.89 - 0.96$
Loma Prieta	$R^2 = 0.64 - 0.88$	$R^2 = 0.98 - 0.99$	$R^2 = 0.88 - 0.96$
Northridge	$R^2 = 0.61 - 0.88$	$R^2 = 0.98 - 0.99$	$R^2 = 0.81 - 0.97$

Based on this study, the authors derived two new forms of relationships (referred as "New Form I" and "New Form II") between log D_n, log I_a and A_c from the 1999 Chi-Chi earthquake dataset, and the worldwide dataset, for both soil and rock site conditions. The generic forms of New Form I and New Form II are shown as follows:

New Form I:

$$\log D_n = C_1 A_c \log I_a + C_2 A_c + C_3 \pm \varepsilon \dots\dots\dots\dots\dots\dots\dots\dots(2.15)$$

New Form II:

$$\log D_n = C_1 \log I_a + C_2 A_c + C_3 A_c \log I_a + C_4 \pm \varepsilon \dots\dots\dots\dots\dots(2.16)$$

Taiwan regional-specific relationships

The dataset that established the following equations are shown in Figure 2.7.

New Form I:

$$\log D_n = 18.388 A_c \log I_a - 21.536 A_c + 2.344 \pm 0.503 \dots\dots\dots\dots(2.17)$$

$R^2 = 0.804$

New Form II:

$$\log D_n = 0.766 \log I_a - 19.945 A_c + 13.744 A_c \log I_a + 2.196 \pm 0.458 \dots\dots\dots(2.18)$$

$R^2 = 0.837$
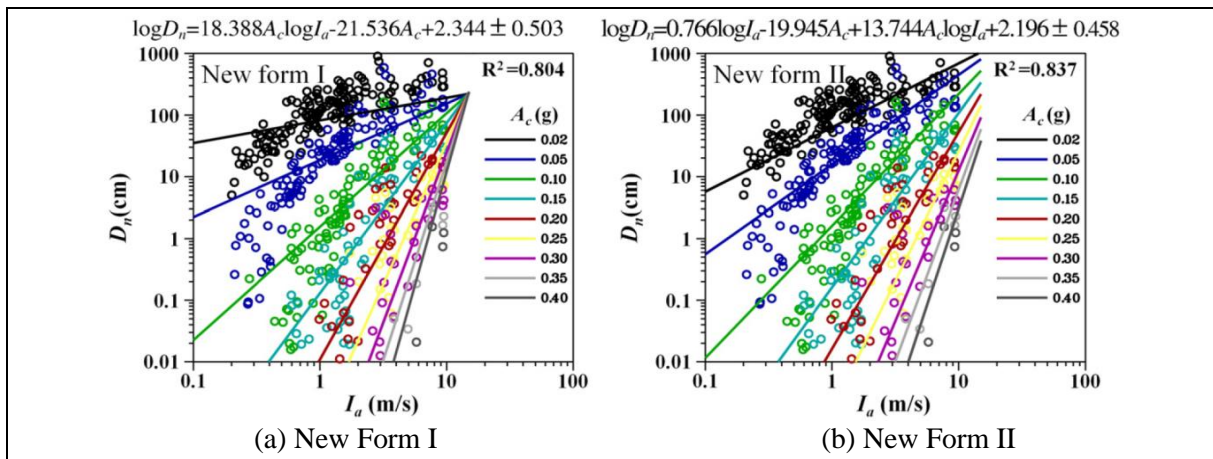
Figure 2.7   Results of the Chi-Chi Dataset Fitting to (a) New Form I, (b) New Form II (Hsieh & Lee, 2011)

Worldwide relationships

The dataset that established the following equations are shown in Figure 2.8.

New Form I:

$$\log D_n = 11.287 A_c \log I_a - 11.485 A_c + 1.948 \pm 0.357 \quad\text{................(2.19)}$$

$R^2 = 0.84$

New Form II:

$$\log D_n = 0.847 \log I_a - 10.62 A_c + 6.587 A_c \log I_a + 1.84 \pm 0.295 \quad\text{............(2.20)}$$

$R^2 = 0.89$
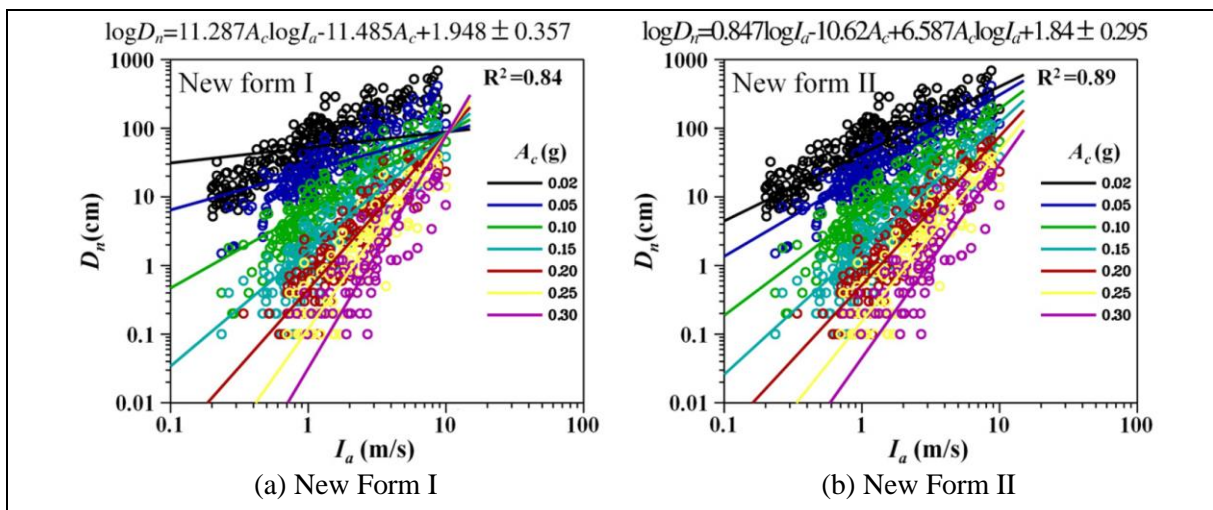
Figure 2.8   Results of Worldwide Dataset Fitting to (a) New Form I, (b) New Form II (Hsieh & Lee, 2011)

Site condition-specific relationships

From 1999 Chi Chi earthquake dataset

The results that led to the following equations are shown in Figure 2.9.

New Form II, rock site:

$$\log D_n = 0.555 \log I_a - 20.488 A_c + 14.555 A_c \log I_a + 2.295 \pm 0.414 \quad\text{..........(2.21)}$$

$R^2 = 0.875$

New Form II, soil site:

$$\log D_n = 0.802 \log I_a - 19.246 A_c + 12.757 A_c \log I_a + 2.153 \pm 0.445 \quad\text{..........(2.22)}$$

$R^2 = 0.843$
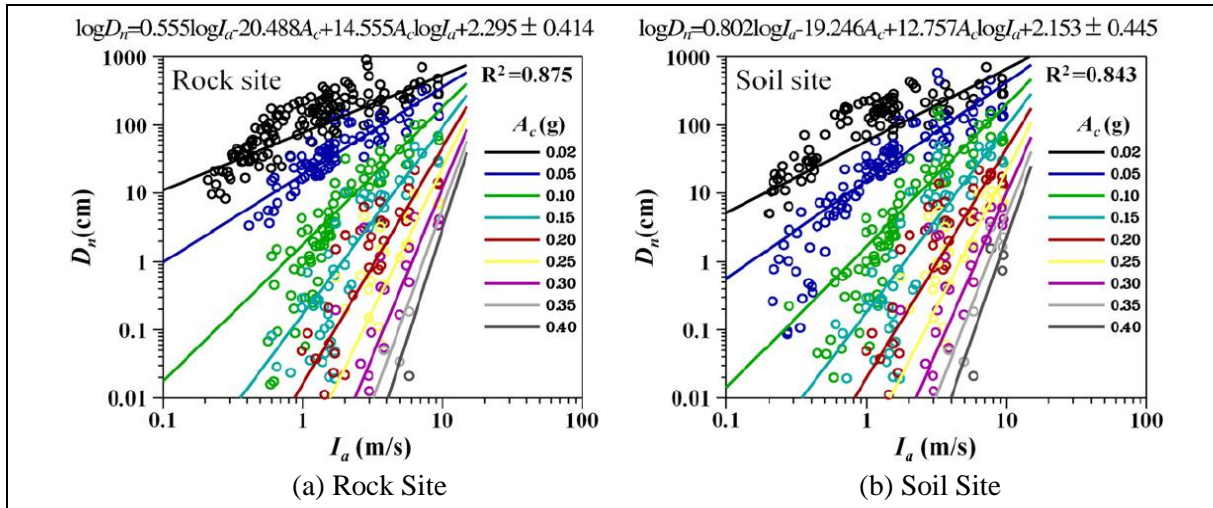
Figure 2.9   Results of the Chi-Chi Dataset Fitting to New Form II (Hsieh & Lee, 2011)

From worldwide dataset

The results that led to the following equations are shown in Figure 2.10.

New Form II, rock site:

$$\log D_n = 0.788\log I_a - 10.166A_c + 5.95A_c\log I_a + 1.779 \pm 0.294 ....(2.23)$$

$R^2 = 0.884$

New Form II, soil site:

$$\log D_n = 0.802\log I_a - 10.981A_c + 7.377A_c\log I_a + 1.914 \pm 0.274 ....(2.24)$$

$R^2 = 0.905$
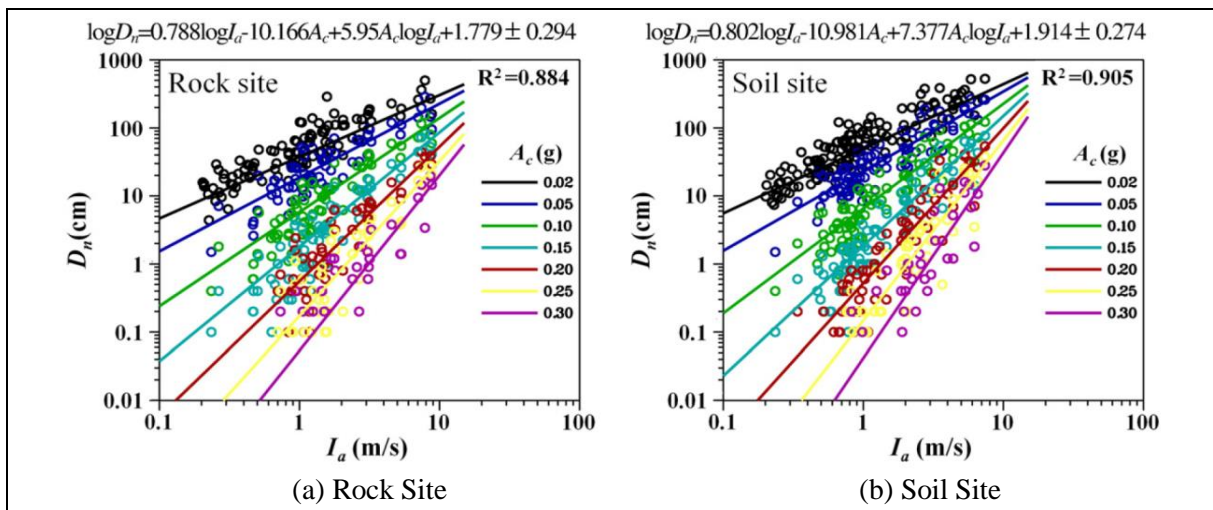
Figure 2.10   Results of Worldwide Dataset Fitting to New Form II (Hsieh & Lee, 2011)

Commentary

This paper recommended new empirical relationships to estimate the Newmark displacement based on the Arias Intensity and the critical acceleration, which are applicable to a region or worldwide. "New Form II" relationships were recommended by the authors. The Taiwan formula should be used in Taiwan and other areas with similar tectonic environments. The global formula could be used elsewhere. They further recommended empirical formulae for soil and rock sites. Because most natural slope failures occur on hillsides, which usually lay on top of bedrock, a rock-site formula may be more applicable for the evaluation of regional earthquake-induced landslide hazard. The soil-site formula, however, should be used for slopes of landfills. For the present study, the worldwide relationships i.e. Equations 2.20 and 2.23 proposed by Hsieh & Lee (2011) would be adopted for further study. Also, the empirical correlation proposed by Jibson et al (1998) i.e. Equation 2.14 is also recommended to comply with the worldwide state-of-practice.

2.3.2 Threshold Displacement

Wieczorek et al (1985) used 50 mm as the critical displacement leading to macroscopic ground cracking and general failures in San Mateo County, California. Keefer & Wilson (1989) used 100 mm as the critical displacement for coherent landslides in the southern California. Jibson & Keefer (1993) used a range of 50 to 100 mm as the threshold displacement for landslides in the Mississippi Valley. Wang & Lin (2010) defined the threshold as 100 to 150 mm for the landslides induced by the 1999 Chi-Chi earthquake in Taiwan. Blake et al (2002) discussed the tolerable Newmark displacement as < 150 mm for slip surface occurring in ductile soils that do not intersect engineered improvement (e.g. landscaped areas and patios). The value was reduced to < 50 mm for slip surfaces intersecting stiff improvements (such as buildings, pools, etc.). All the afore-mentioned threshold displacement values are relevant to this study.

Any level of a threshold displacement can be used based on the ground conditions considered by a specific landslide case study. For example, highly ductile materials may accommodate more displacements without general failure, while brittle materials might accommodate less. What constitutes failure may vary according to the experience of the user (Jibson, 1993). For the present study, the threshold displacement is set as 100 mm, which is an average value suggested in the above literatures.

2.4 Landslide Susceptibility Factors and Map

In addition to the methods introduced above, there are other issues related to the subject of earthquake-induced landslides such as susceptibility factors and others. As such, a review of a Special Issue of Engineering Geology issued in 2011 has been undertaken. This Special Issue was based on the outcomes of an international conference "The Next Generation of Research on Earthquake-Induced Landslides" held in 2009. Its recommendations, particularly for those relevant to Hong Kong, are briefly discussed below.

2.4.1 ISSMFE (1993)

ISSMFE (1993) addressed the zonation of earthquake-induced landslides. Three grades of approach to zonation were determined.

(a) Grade 1 is based on historical earthquake data (earthquake magnitude, distance to fault or epicentre and intensity), as well as geological and geomorphological maps.

(b) Grade 2 requires aerial photos and remote sensing; field studies and vegetation as well as precipitation data.

(c) Grade 3 requires geotechnical investigations and site specific dynamic stability analyses.

For the purpose of the present study, only Grade 1 and Grade 2 zonation approaches have been reviewed.

In general, earthquake-induced slope failures include a variety of phenomena and may be classified into three categories according to Keefer & Wilson (1989):

(a) Category I: falls, disrupted slides and avalanches;

(b) Category II: slumps, block slides and earth flows; and

(c) Category III: lateral spreads and flows.

Among these three classes, the events classified under Category I are associated with shallow-seated landslides and thus are the major concern for the present study.

Grade 1:   Magnitude-distance criteria review

(a) Tamura (1978)

Tamura (1978) conducted case studies on slope failures which occurred during 37 earthquakes in Japan over the past 100 years. Four kinds of distances were adopted in the study as follows:

(i) D_f: distance from a fault to an outer boundary of the zone where many slope failures occurred.

(ii) d_f: distance from a fault to an outer boundary of the zone where a few slope failures occurred.

(iii) D_p: distance from an epicentre to an outer boundary of the zone where many slope failures occurred.

(iv) d_p: distance from an epicentre to an outer boundary of the zone

where a few slope failures occurred.

The magnitude-distance results for this study are shown in Figure 2.11.
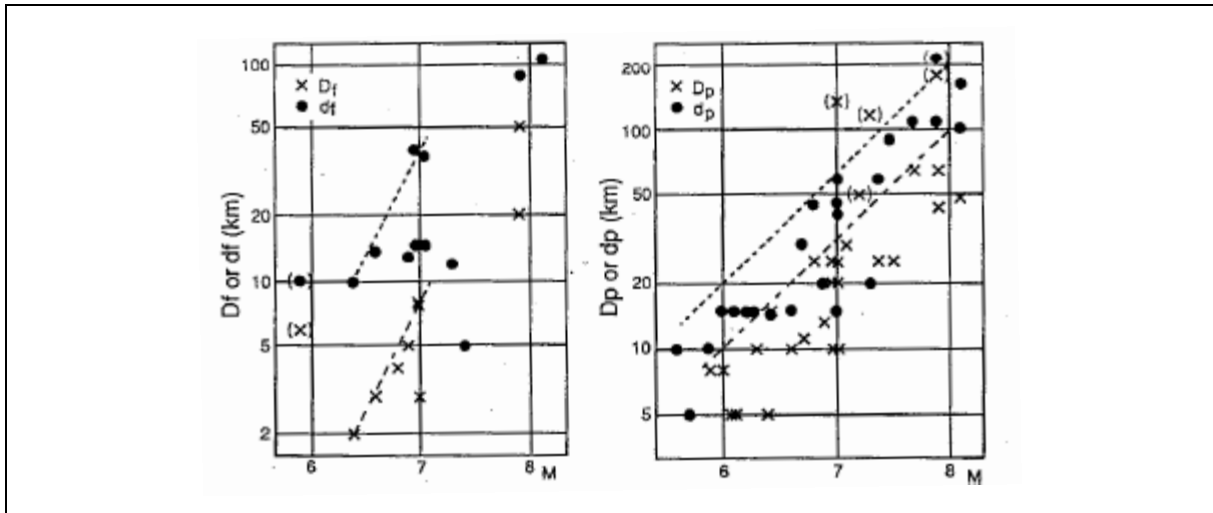
Figure 2.11   Relationships between Magnitude and Distance to Slope Failure in Japan (after Tamura, 1978, from ISSMFE, 1993)

(b) Yasuda & Sugitani (1988)

Yasuda & Sugitani (1988) identified 105 landslide cases that occurred in Japan in the past 100 years and classified them into two groups: surface slides and deep slides.   The magnitude-distance relationships and the lower bound for slope failure for both groups are illustrated in Figure 2.12.
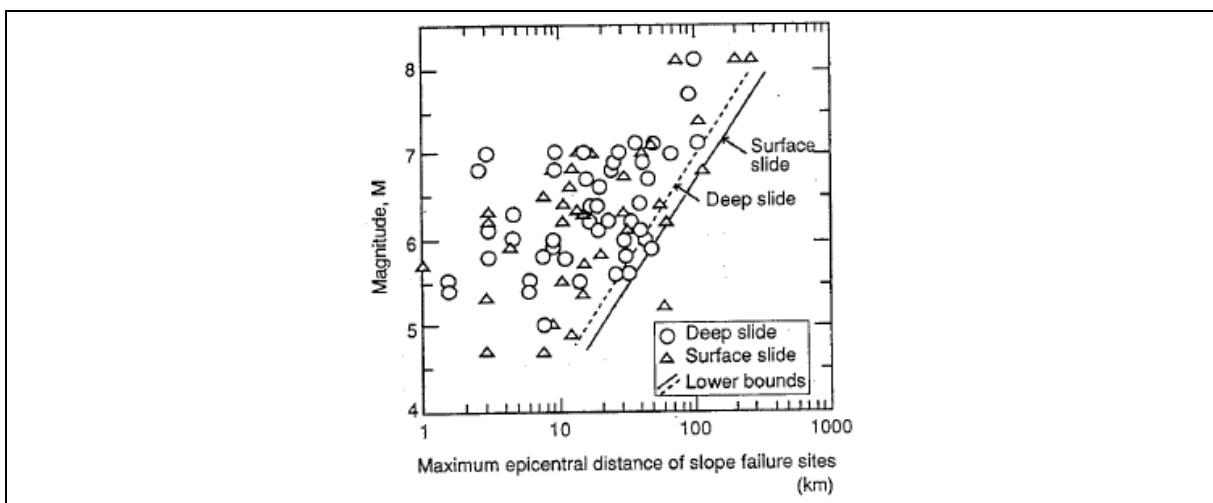
Figure 2.12   Relationships between Magnitude and Maximum Epicentral Distance of Slope Failure in Japan (after Yasuda & Sugitani, 1988, from ISSMFE, 1993)

(c) Keefer & Wilson (1989)

Keefer & Wilson (1989) conducted a statistical analysis for 47 typical events which have occurred since 1811 worldwide.   Those slope failures were classified in Categories I to III as listed above.   Figure 2.13 illustrates the results of this study.
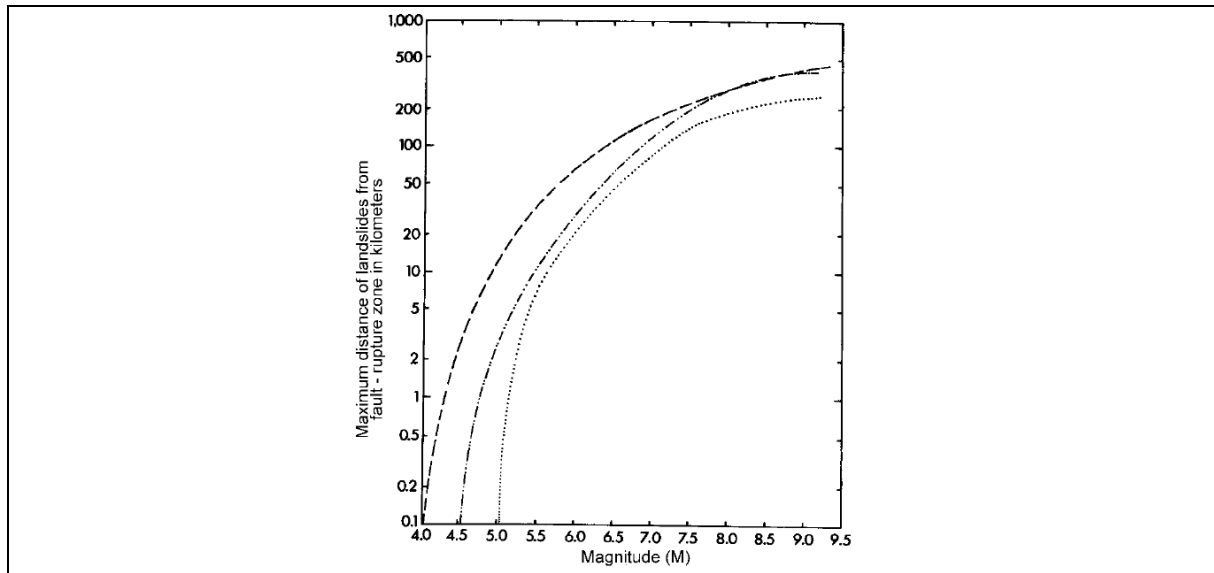
Figure 2.13   Relationships between Magnitude and Maximum Distance of Landslides from Fault-rupture Zone in Kilometres (after Keefer & Wilson, 1989, from ISSMFE, 1993)

(d) ISSMFE (1993) recommended criteria

ISSMFE (1993) presented a summary of the previous magnitude-distance relationship to date as illustrated in Figure 2.14.   However, the authors believed that it was necessary to refine the criteria by catering for the difference of failure criteria between dry-weather countries (like Iran or Armenia) and wet-weather countries (like Japan or the Philippines).   The new recommended relationships are illustrated in Figure 2.15.
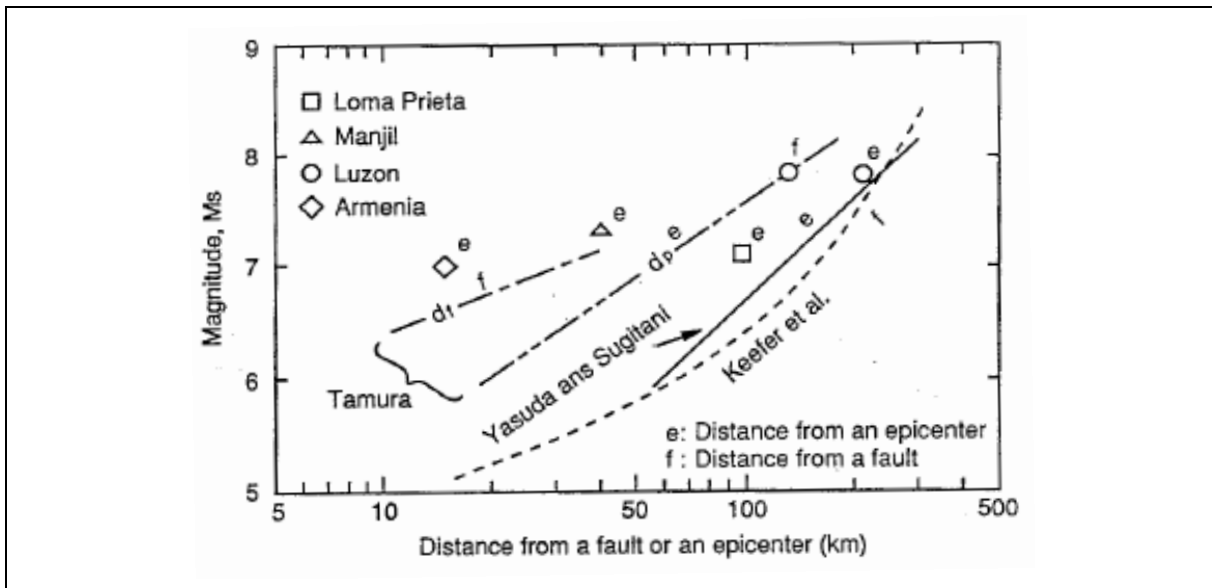
Figure 2.14   Comparison between Magnitude-distance Relationships (ISSMFE, 1993)
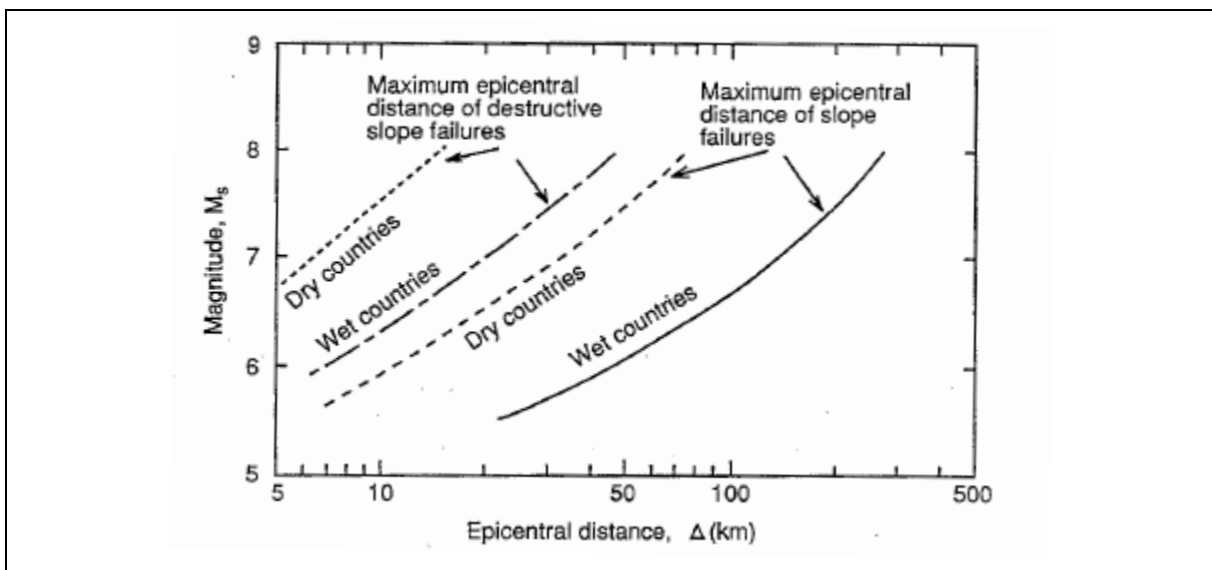
Figure 2.15   Recommended Magnitude-distance Relationships for Dry-weather and Wet-weather Countries (ISSMFE, 1993)

Grade 2:   Susceptibility factors

(a) Kanagawa Prefectural Government (1986), Japan

The findings of this study were based on slope failures that occurred in Japan during three large earthquakes: the 1974 Izuhanto-Oki earthquake; the 1978 Izuoshima-Kinkai earthquake; and the 1984 Naganoken-Seibu earthquake.   The susceptibility to slope failure in each mesh of the map was calculated as the sum of the weighting factors listed in Table 2.5. The classification of the topography of slopes is given in Figure 2.16.

Table 2.5   Weighting Factors Related to Slope Failure (after Kanagawa Prefectural Government, 1986, from ISSMFE, 1993)

Factor	Category	Weight
(a) Maximum surface acceleration (Gal), W_1	0 - 200 200 - 300 300 - 400 400 -	0.0 1.004 2.306 2.754
(b) Length of a contour line (m), W_2	0 - 1,000 1,000 - 1,500 1,500 - 2,000 2,000 -	0.0 0.071 0.320 0.696
(c) Difference between the highest site and the lowest site (m), W_3	0 - 50 50 - 100 100 - 200 200 - 300 300 -	0.0 0.550 0.591 0.814 1.431
(d) Hardness of a rock, W_4	Soil Soft rock Hard rock	0.0 0.169 0.191
(e) Length of faults (m), W_5	No fault 0 - 200 200 -	0.0 0.238 0.710
(f) Length of artificial slopes (m), W_6	0 - 100 100 - 200 200 -	0.0 0.539 0.845
(g) Topography of slope, W_7 (Figure 2.16)	① ② ③ ④	0.0 0.151 0.184 0.207
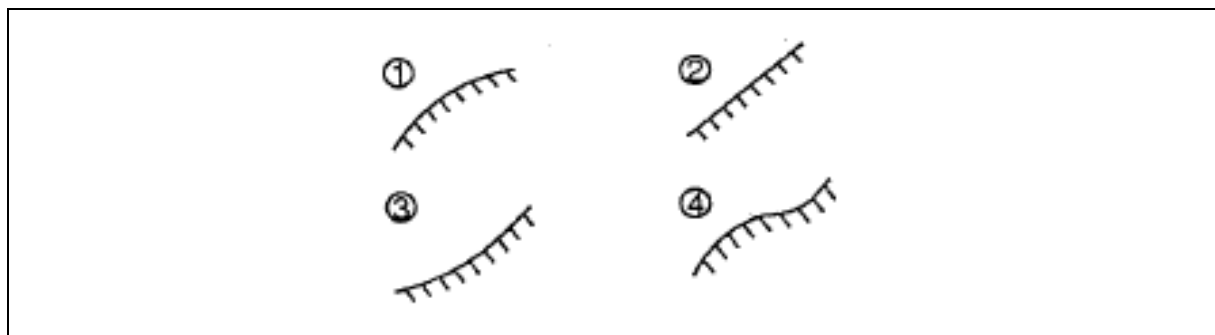
Figure 2.16   Classification of the Topography of Slopes (after Kanagawa Prefecture Government, 1986, from ISSMFE, 1993)

(b) Mora & Vahrson (1994)

Mora & Vahrson (1994) conducted case studies of slope failures in historic earthquakes as well as those induced by heavy rainfall in Central America. Five factors: relative relief, lithology, soil moisture, seismicity and rainfall intensity were considered as triggering factors for slope failure.   The degree of slope failure hazard is defined as follows:

$$H_L = (S_r \times S_l \times S_h) \times (T_s + T_p)$$

where H_L = landslide hazard index (see Table 2.6)
S_r = relative relief index (see Table 2.7)
S_l = lithology susceptibility index (see Table 2.8)
S_h = soil moisture index (see Tables 2.9 and 2.10)
T_s = seismic intensity index (see Table 2.11)
T_p = rainfall intensity index (see Table 2.12).

Table 2.6   Classes of the Potential Landslide Hazards (after Mora & Vahrson, from ISSMFE, 1993)

Class	Susceptibility of Hazard
I	Negligible
II	Low
III	Moderate
IV	Medium
V	High
VI	Very high

Table 2.7   Relative Relief (S_r) Values and their Classes of Influence in Landslide Susceptibility (after Mora & Vahrson, from ISSMFE, 1993)

Relative Relief (m/km^2)	Susceptibility	Parameter, S_r
0 - 75	Very low	0
76 - 175	Low	1
176 - 300	Moderate	2
301 - 500	Medium	3
501 - 800	High	4
> 800	Very high	5

Table 2.8 Classification of Lithologic Influence, According to General Conditions, Representative for Central America (after Mora & Vahrson, from ISSMFE, 1993)

Lithology	Susceptibility	Value, S_l
Permeable limestone, slightly fissured intrusions, basalt, andesites, granites, ignimbrite, gneiss, hornfels; low degree of weathering, low watertable, clean-rugose fractures, high shear strength rocks	Low	1
High degree of weathering of above mentioned lithologies and of hard massive clastic sedimentary rocks; low shear strength; shearable fractures	Moderate	2
Considerable weathered sedimentary, intrusive, metamorphic, volcanic rocks, compacted sandy regolithic soils, considerable fracturing, fluctuating watertables, compacted colluvium and alluvium	Medium	3
Considerable weathered, hydrothermally altered rocks of any kind, strongly fractured and fissured, clay filled; poorly compacted pyroclastic and fluvio-lacustrine soils, shallow watertables	High	4
Extremely altered rocks, low shear resistance alluvial, colluvial and residual soils, shallow watertables	Very high	5

Table 2.9 Classes of Average Monthly Precipitation (after Mora & Vahrson, from ISSMFE, 1993)

Average Monthly Precipitation (mm/month)	Assigned Value
< 125	0
125 - 250	1
> 250	2

Table 2.10   Weighting for Annual Precipitation (after Mora & Vahrson, from ISSMFE, 1993)

Summation of Precipitation Averages*	Susceptibility	Value, S_h
0 - 4	Very low	1
5 - 9	Low	2
10 - 14	Medium	3
15 - 19	High	4
20 - 24	Very high	5

Note :   *Summation of the assigned values in Table 2.8 for 12 months.

Table 2.11   Influence of Seismic Intensity (Modified Mercalli Scale) as Triggering Factor for Landslide Generation (after Mora & Vahrson, from ISSMFE, 1993)

Intensities (MM) $T_r = 100$ Years	Susceptibility	Value, T_s
III	Slight	1
IV	Very low	2
V	Low	3
VI	Moderate	4
VII	Medium	5
VIII	Considerable	6
IX	Important	7
X	Strong	8
XI	Very strong	9
XII	Extremely strong	10

Table 2.12   Influence of Rainfall Precipitation Intensity as Triggering Factor for Landslides (after Mora & Vahrson, from ISSMFE, 1993)

Maximum Rainfall (mm) $n > 10$ Years; $T_r = 100$ Years	Rainfall (mm) $n < 10$ Years; Average	Susceptibility	Value, T_p
< 100	< 50	Very low	1
101 - 200	51 - 90	Low	2
201 - 300	91 - 130	Medium	3
301 - 400	131 - 175	High	4
> 400	> 175	Very High	5

The susceptibility factors proposed in Kanagawa Prefectural Government (1986) and Mora & Vahrson (1994) have been used to generate the susceptibility maps in the present study and some of them have been considered in the susceptibility analysis in Section 5.   To summarise, there is no spatial variation across the Study Area for some proposed susceptibility factors such as maximum surface acceleration, seismic intensity and rainfall intensity and these factors are not taken into account.   The hardness of rock does not lead to any spatial differentiation as the Study Area generally is exposed with "rock and thin soil" (discussed in Section 6.1).   Factors for elevation, topography of slopes and relative relief have been considered in the analyses for the topographic amplification for different ridge height.   As there is no evidence for active fault in Hong Kong, its effect cannot be directly considered.   Lithology and faulting (geological structure) have been considered in the susceptibility analysis and is presented in Sections 5.5.2 and 5.5.3.

2.4.2   Keefer (2002)

Keefer (2002) reviewed the findings of investigations carried out on earthquake-induced landslides worldwide, from 1980 to 2002.

Tables 2.13 and 2.14 summarise the characteristics of the landslides investigated, based on Keefer (1984 & 1999).   The types of slopes and geological environments that resulted in earthquake-induced landslides varied, ranging from overhanging slopes in well-indurated bedrock to unconsolidated sediments with nearly level surfaces.   The minimum slope gradients for various types of landslides were found to range from 0.3° to 40° (Table 2.13).

In general, the materials considered as the most susceptible to earthquake-induced landslides were (1) weakly cemented, weathered, sheared, intensely fractured, or closely jointed rocks, (2) better-indurated rocks having prominent discontinuities, (3) sandy residual or colluvial soils, (4) saturated volcanic soils containing sensitive clay, (5) loess, (6) cemented soils, (7) granular deltaic sediments, (8) granular flood-plain alluvium, and (9) uncompacted, or poorly compacted, granular artificial fill.

Table 2.13   Characteristics of Earthquake-induced Landslides (Keefer, 2002) (Sheet 1 of 2)

Name	Type of movement	Internal disruption	Water content D U PS S	Typical depths	Minimum slope (°)	Typical velocities	Typical volumes	Typical displacements
Disrupted landslides								
Rock falls	Bouncing, rolling, free fall	High or very high	× × × ×	Shallow	40	Extremely rapid	Most less than 1×10^4 m³; maximum reported 2×10^7 m³	May fall to base of steep source slope and move as far as several tens or hundreds of meters farther, on relatively gentle slopes
Disrupted rock slides	Translational sliding	High	× × × ×	Shallow	35	Rapid to very rapid	Most less than 1×10^4 m³; maximum reported 2×10^9 m³	May slide to base of steep source slope and several tens or hundreds of meters farther, on relatively gentle slopes
Rock avalanches	Complex, involving sliding, flow, and occasionally free fall	Very high	× × × ×	Deep	25	Very rapid to extremely rapid	5×10^5–2×10^8 m³ or more	Several kilometers
Soil falls	Bouncing, rolling, free fall	High or very high	× × × ×	Shallow	40	Extremely rapid	Most less than 1,000 m³; maximum volumes not well documented	Most come to rest at or near bases of steep source slopes
Disrupted soil slides	Translational sliding	High	× × PS ×	Shallow	15	Moderate to rapid	Most less than 1×10^4 m³; maximum reported 4.8×10^7 m³	May slide to base of steep source slope and several tens or hundreds of meters farther, on relatively gentle slopes
Soil avalanches	Complex, involving sliding, flow, and occasionally free fall	Very high	× × × ×	Shallow	25	Very rapid to extremely rapid	Volumes not well documented; maximum reported 1.5×10^8 m³	Several tens of meters to several kilometers beyond steep source slopes
Coherent landslides								
Rock slumps	Rotational sliding	Slight or moderate	? × × ×	Deep	15	Slow to rapid	Most between 100 and a few million m³; maximum at least tens of millions of m³	Typically less than 10 m; occasionally 100 m or more
Rock block slides	Translational sliding	Slight or moderate	? × × ×	Deep	15	Slow to rapid	Most between 100 and a few million m³; maximum at least tens of millions of m³	Typically less than 100 m; maximum displacements not well documented
Soil slumps	Rotational sliding	Slight or moderate	? × × ×	Deep	7	Slow to rapid	Most between 100 and 1×10^5 m³; occasionally 1×10^5 to several million m³	Typically less than 10 m; occasionally 100 m or more
Soil block slides	Translational sliding	Slight or moderate	? ? × ×	Deep	5	Slow to very rapid	Most between 100 and 1×10^5 m³; maximum reported 1.12×10^8 m³	Typically less than 100 m; maximum displacements not well documented
Slow earth flows	Translational sliding and internal flow	Slight	× ×	Generally shallow; occasionally deep	10	Very slow to moderate; occasionally, with very rapid surges	Most between 100 and 1×10^6 m³; maximum reported between 3×10^7 and 6×10^7 m³	Typically less than 100 m; maximum displacements not well documented

Table 2.13   Characteristics of Earthquake-induced Landslides (Keefer, 2002) (Sheet 2 of 2)

Name	Type of movement	Internal disruption	Water content D U PS S				Typical depths	Minimum slope (°)	Typical velocities	Typical volumes	Typical displacements
Lateral spreads and flows											
Soil lateral spreads	Translation on fluid basal zone	Generally moderate; occasionally slight or high			×	×	Variable	0.3	Very rapid	Most between 100 and 1×10^5 m^3; largest reported 9.6×10^6 m^3.	Typically less than 10 m; maximum reported 600 m
Rapid soil flows	Flow	Very high	?	?	?	×	Shallow	2.3	Very rapid to extremely rapid	Volumes not well documented; largest are at least several million m^3.	A few m to several km
Subaqueous landslides	Generally lateral spreading or flow; occasionally sliding	Generally high or very high; occasionally moderate or slight			×	×	Variable	0.5	Generally rapid to extremely rapid; occasionally slow to moderate	Volumes not well documented; largest are at least tens of millions of m^3.	Not well documented, but some move more than 1 km

* Notes: Names: "rock" signifies bedrock that is relatively firm and intact prior to landslide initiation, and "soil" signifies loose, unconsolidated or poorly cemented aggregates of particles that may or may not contain organic materials. Internal disruption: "slight" signifies landslide consists of one or a few coherent blocks; "moderate" signifies several coherent blocks; "high" signifies numerous small blocks and individual soil grains and rock fragments; "very high" signifies nearly complete disaggregation into individual soil grains or small rock fragments. Depth: shallow signifies generally < 3 m deep; deep signifies generally > 3 m deep. Water content: D = dry; U = moist but unsaturated; PS = partly saturated; S = saturated. Velocity: very slow = 1×10^{-6}–3×10^{-6} m/min; slow = 3×10^{-6}–3×10^{-5} m/min; moderate = 3×10^{-5}–0.001 m/min; rapid = 0.001–0.3 m/min; very rapid = 0.3–180 m/min; extremely rapid = >180 m/min. (Terminology after Varnes, 1978).

Table 2.14   Relative Abundance of Earthquake-induced Landslides (Keefer, 2002)

Landslide type, listed in order of decreasing total numbers
Very abundant: > 100,000 in the 40 historical earthquakes
Rock falls
Disrupted soil slides
Rock slides
Abundant: 10,000 to 100,000 in the 40 historical earthquakes
Soil lateral spreads
Soil slumps
Soil block slides
Soil avalanches
Moderately common: 1,000 to 10,000 in the 40 historical earthquakes
Soil falls
Rapid soil flows
Rock slumps
Uncommon: 100 to 1,000 in the 40 historical earthquakes
Subaqueous landslides
Slow earth flows
Rock block slides
Rock avalanches

It was found that the approximate magnitudes of the smallest earthquakes that triggered landslides were ~4.0 for rock falls, rock slides, soil falls, and disrupted soil slides; ~4.5 for soil slumps and soil block slides; ~5.0 for soil lateral spreads, rapid soil flows, subaqueous landslides, rock slumps, rock block slides, and slow earth flows; ~6.0 for rock avalanches; and ~6.5 for soil avalanches. As these landslides could also be triggered by other non-seismic agents, Keefer (1984) denoted that the possibility of earthquake-induced landslides could be smaller than those indicated above.

The results from Rodriguez et al (1999) and Hancox et al (1997) were also interpreted in terms of the relationship between the area affected by landslides (km^2) and the moment magnitude, as illustrated in Figure 2.17.

Based on the landslide dataset listed in Table 2.15 (1957-1999), a semi-log relationship for the number of landslides that was expected under a given earthquake magnitude was derived, as illustrated in Figure 2.18.

Note:	Circles are data from earthquakes discussed by Rodriguez et al (1999), plotted using moment magnitude (M); open circle is 1988 Saguenay, Quebec earthquake. Solid line is upper bound of Keefer & Wilson (1989), see Figure 2.12. Dashed line is upper bound of Rodriguez et al (1999). Triangle is datum from 1963 Peria, New Zealand, earthquake, for which area exceeds upper bounds, plotted using Richter local magnitude (M_L), from Hancox et al (1997; 2002).

Figure 2.17   Relations between Area Affected by Landslides and Earthquake Moment Magnitude (Keefer, 2002)
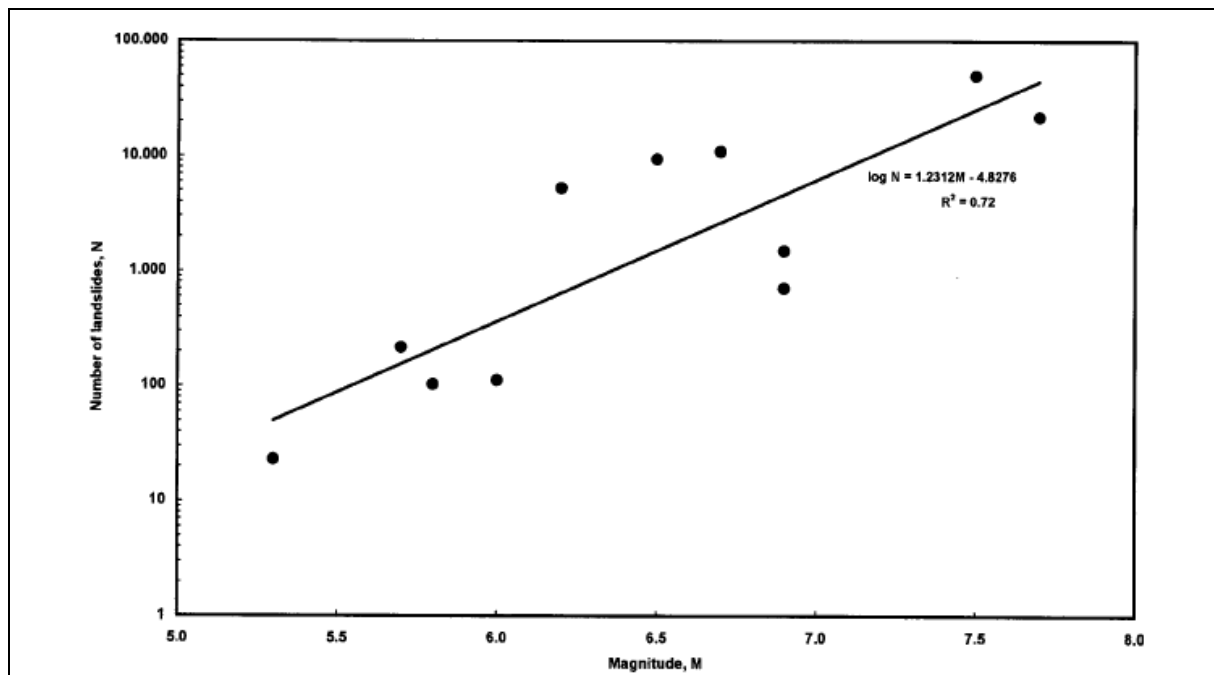
Figure 2.18   Relation between Total Number of Reported Landslides and Earthquake Magnitude for Earthquakes with Comprehensive Inventories of Landslides (Keefer, 2002)

Table 2.15   Number of Documented Landslides Produced by Earthquakes (Keefer, 2002)

Earthquake location	Earthquake date	Earthquake magnitude*	Number of landslides	Approximate percentage by category			Reference
				Disrupted (%)	Coherent (%)	Lateral spreads and flows (%)	
Daly City, Calif. USA	22 May 1957	5.3	23	48	30	22	Bonilla, 1960
Guatemala	4 Feb 1976	7.5	~ 50,000	Most	?	?	Harp et al., 1981; E.L. Harp, unpublished data
Mt. Diablo, Calif. USA	24 Jan 1980	5.8	103	83	17	0	Wilson et al., 1985; Keefer and Wilson, 1989
Mammoth Lakes, Calif. USA	25 May 1980	6.2	5,253	> 98	< 1	< 1	Harp et al., 1984; Keefer and Wilison, 1989; Wieczorek and Jäger, 1996
Coalinga, Calif. USA	2 May 1983	6.5	9,389	> 97	< 2	< 1	Keefer and Wilson (1989); Harp and Keefer (1990)
San Salvador, EI Salvador	10 Oct 1986	5.7	> 216	> 93	< 5	< 2	Rymer, 1987; Rymer and White, 1989
Loma Prieta, Calif. USA	17 Oct 1989	6.9	~ 1,500	74#	26#	0#	Keefer and Manson, 1998
Northridge, Calif. USA	17 Jan 1994	6.7	> 11,000	> 90	< 9	< 1	Harp and Jibson, 1995, 1996
Hygoken-Nanbu, Japan	17 Jan 1995	6.9	674 - 747	81 to 83	13 to 15	3 to 4	Sassa et al., 1995; Fukuoka et al., 1997; Okimura and Torii, 1999
Umbria-Marche, Italy	26 Sep 1997	6.0	100 - 124	61	34	5	Bozzano et al., 1998; Esposito et al., 2000; I. LaRosa, unpublished data
Chi-Chi, Taiwan	21 Sep 1999	7.7	22,000	> 85	11 to 15	< 4	Lin and others, 2001; Sitar and Bardet, 2001

*Magnitudes in bold are moment magnitudes; others are Richer surface-wave (Mt. Diablo) or Richer local (Daly City) magnitude.
#Percentages determined in central area only.

Finally, Keefer (2002) reviewed the threshold values of Arias Intensity for the occurrence of earthquake-induced landslides. Keefer & Wilson (1989) suggested threshold values of 0.11 m/s for disrupted landslides, 0.32 m/s for coherent slides and 0.54 m/s for lateral spreads and flows, whereas Wilson (1993) found the best-fit threshold value for disrupted landslides to be 0.1 m/s (Table 2.16).

Regarding the minimum slope gradients mentioned in Keefer (2002), the area of $< 5°$ was generally considered as the depositional area rather than the erosion area in natural terrain landslides.   Therefore, the probability of landslide occurrence in such a gentle slope was very low.   In Keefer (2002), $0.3°$ was referred as the minimum slope angle for soil lateral spreading, which comprised less than 6% of the total number of landslides reported in the study.

2.4.3   Lee et al (2008)

Lee et al (2008) presented an earthquake-induced landslide susceptibility analysis based on a statistical approach. They adopted the Arias Intensity of an earthquake as a landslide triggering factor. The susceptibility model was proved to be capable of predicting shallow landslides triggered by earthquakes with a similar range of ground shaking without using ground and groundwater data.

Table 2.16   Arias Intensity Thresholds for Landslides (Keefer, 2002)

Landslide category	Arias intensity threshold (m/s)	Reference
Modeling studies		
Disrupted	0.15	Wilson and Keefer, 1985
Disrupted	0.11	Keefer and Wilson, 1989
Disrupted	0.10	Wilson, 1993
Coherent	0.5	Wilson and Keefer, 1985
Coherent	0.32	Keefer and Wilson, 1989
Lateral spreads and flows	0.5	Wilson and Keefer, 1985
Lateral spreads and flows	0.54	Keefer and Wilson, 1989
24 Oct. 1987 Superstition Hills, California earthquake		
Disrupted	0.3 (mean)	Harp and Wilson, 1995
Disrupted	0.1–0.5 (range)	Harp and Wilson, 1995
1 Oct. 1987 Whittier Narrows, California earthquake		
Disrupted	0.06–0.7 (weakly cemented sandstones and conglomerates)	Harp and Wilson, 1995
Disrupted	0.04 (mean, well-cemented rocks)	Harp and Wilson, 1995
Disrupted	0.01–0.07 (range, well-cemented rocks)	Harp and Wilson, 1995

The methodology was applied to a study of earthquake-induced shallow landslides in the Kaohsiung area, central western Taiwan, triggered by the 1999 Chi-Chi earthquake.   The results were then validated against using an example in the neighbouring Tungshih area.

The epicentre of the September 21, 1999 Chi-Chi earthquake (M_w 7.6) was located about 15 km south of the study area (Ma et al, 1999; Kao & Chen, 2000).   Over 9,000 large landslides of various types (with areas greater than 625 m^2), with a total area of 128 km^2 were triggered by the Chi-Chi earthquake (Liao & Lee, 2000).   Of these, 1,316 landslides, with a total area of 22 km^2, were triggered in the Kaohsiung quadrangle, and 1,623 landslides, with a total area of 12 km^2, were triggered in the Tungshih quadrangle.

Methodology and input

The Chi-Chi earthquake event-based landslide inventory for the Kaohsiung quadrangle is shown in Figure 2.19.   Only shallow landslides (including rock falls), which included all of the landslides in the study area, were used in the susceptibility analysis.   Deep-seated landslides, rock avalanches (located outside the study area) and debris flows were studied in a separate project.

The working procedure for the event-based landslide susceptibility analysis, derived from high resolution satellite images taken before and soon after the triggering event, is illustrated in Figure 2.20.   This procedure must be performed separately for each type of terrain because of the differences in their geomorphic and geologic characteristics.   Hilly terrain and mountainous terrain were thus considered separately in the study.   The basic data used included a 40 m × 40 m grid digital elevation model (DEM), SPOT images, 1:5,000 photo-based contour maps, 1:50,000 geologic maps, and earthquake strong-motion records.
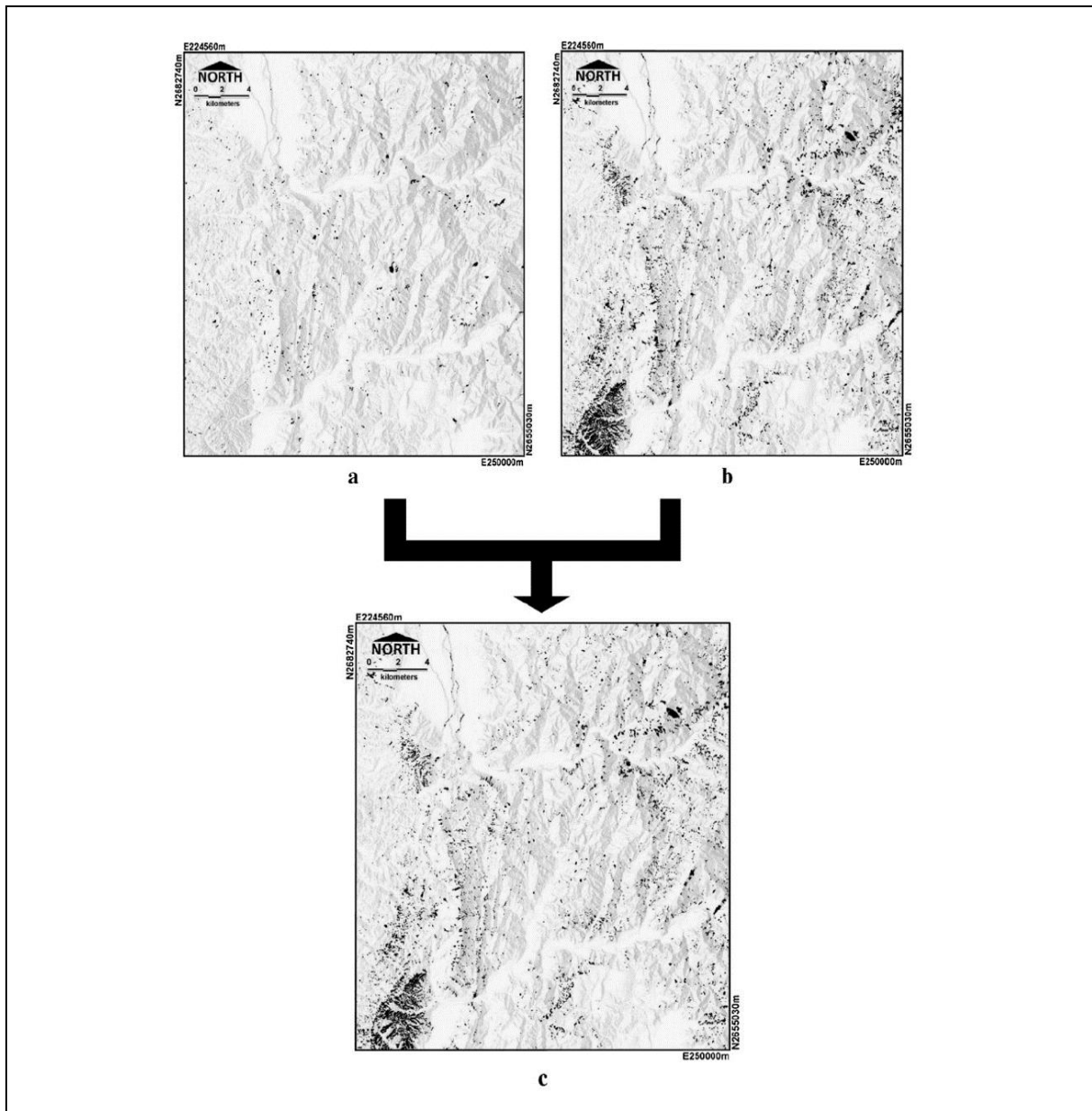
Figure 2.19   Extraction of Landslides Triggered by an Event, Example from the Kaohsiung Quadrangle: (a) Landslides before the Chi-Chi Earthquake; (b) Landslides after the Chi-Chi Earthquake; (c) Landslides Triggered by the Chi-Chi Earthquake (Lee et al, 2008)

Strong-motion seismograms in and around the study area were collected by the Central Weather Bureau, Taiwan.   Base-line correction and filtering of the data were performed according to the standard procedure suggested by the Pacific Earthquake Engineering Research Center (PEER) (Darragh et al, 2004).   The Arias Intensity was then calculated from each corrected seismogram.   The arithmetical means of the Arias Intensities of the NS and EW components were used to represent the earthquake intensity for each of the strong-motion station sites.   These values were interpolated on each grid point in the study area using the Kriging method (Goovaerts, 1997).
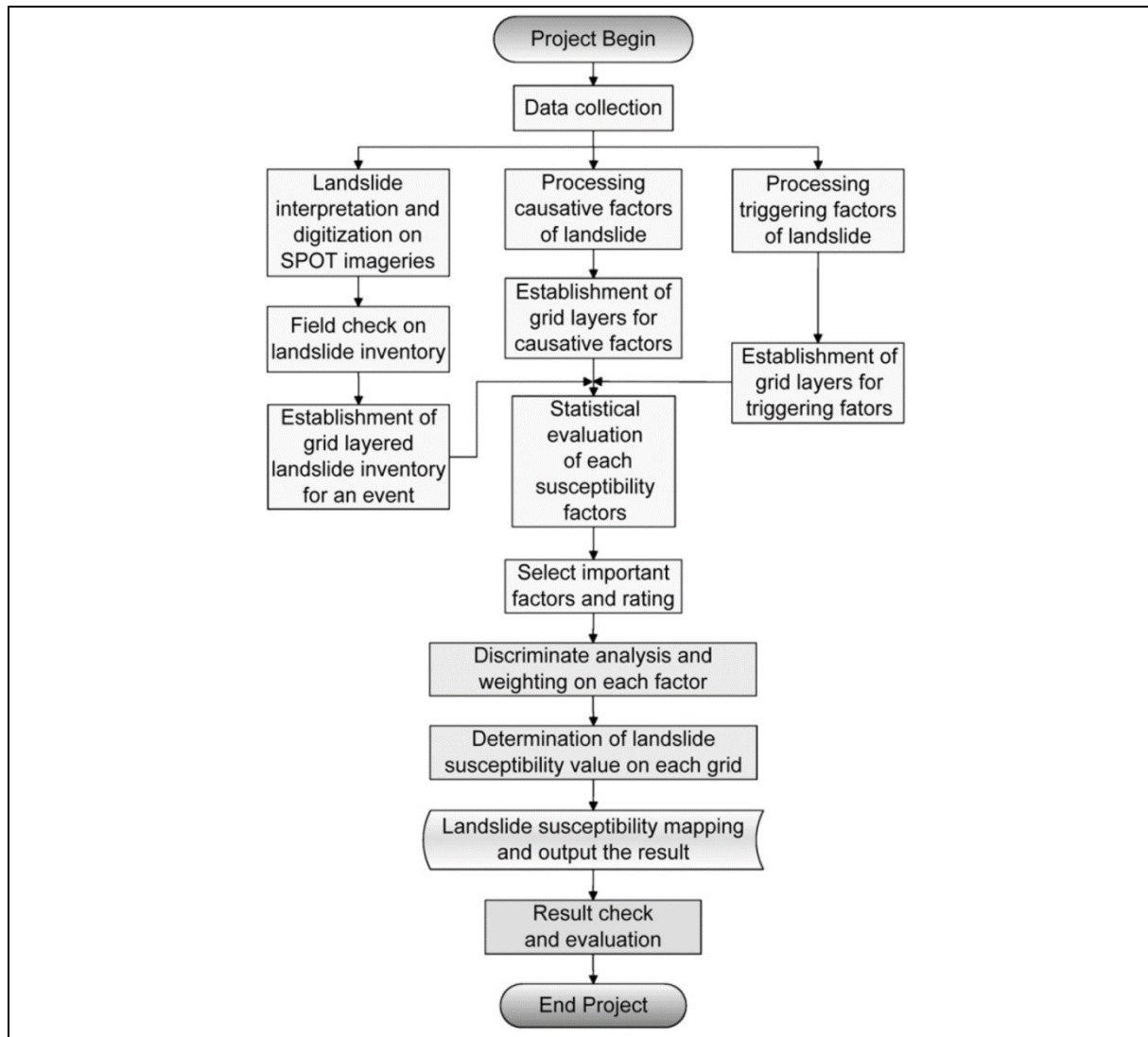
**Figure 2.20   Working Procedure for Event-based Landslide Susceptibility Analysis
(Lee et al, 2008)**

Arias Intensity mapping

The Arias Intensity (I_a) for each station was determined by correcting and processing the strong-motion records of the main shock of the Chi-Chi earthquake and six major aftershocks. Figure 2.21 shows the distribution of I_a for the main shock (stations located on top of ridges, as indicated in the figure, were not included in the interpolation).   Each grid point was checked to find the maximum I_a among the seven earthquake events, and these values were adopted as the intensity that triggered the landslides.

Topographic effect

The authors further considered topographic effects in relation to the earthquake intensity. The height of the grid point above the riverbed was found to be a good factor for making corrections, following the empirical formula proposed by Lin & Lee (2003).
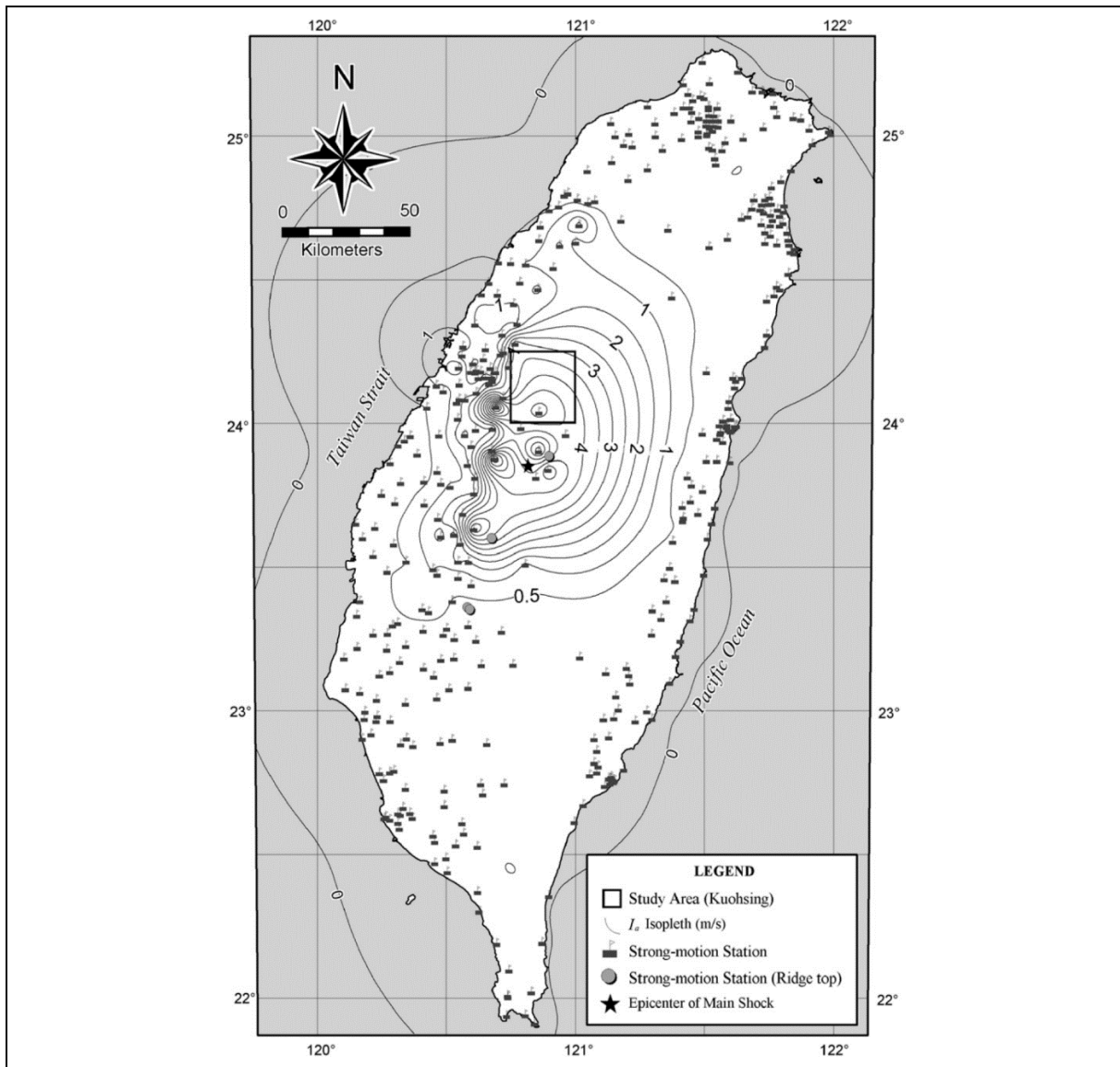
Figure 2.21 Arias Intensity Isopleth of the Main Shock of the Chi-Chi Earthquake. Strong-motion Stations with Indication of Ridge Top Stations, Earthquake Epicentre, and the Study Area are Shown (Lee et al, 2008)

$$I'_a = f I_a \dots\dots\dots\dots\dots\dots\dots\dots\dots\dots\dots\dots\dots\dots\dots(2.25)$$

$$\text{for} \qquad f = \sqrt{\frac{h}{93.8} + 0.287} + 0.464$$

where I_a is the Arias Intensity (m/s), I'_a is the corrected Arias Intensity (m/s), f is the amplification factor, and h is the height relative to the riverbed (m).

The I_a after topographic correction is shown in Figure 2.22(g). Correcting I_a substantially improved the correlation between the landslide ratio and the I_a parameter.

(a) Original arias intensity

(b) Distribution of landslide and non-landslide groups with original arias intensity

(c) Landslide ratio vs. original arias intensity

(d) Height of slope relative to riverbed

(e) Distribution of landslide and non-landslide groups with relative height above riverbed

(f) Landslide ratio vs. height relative to riverbed

(g) Corrected arias intensity

(h) Distribution of landslide and non-landslide groups with corrected arias intensity

(i) Landslide ratio vs. corrected arias intensity

Figure 2.22   Spatial Distribution of the Arias Intensity and Frequency Distribution of the Landslide and Non-landslide Groups and the Landslide Ratio for the Chi-Chi Earthquake Event in the Kaohsiung Quadrangle (Lee et al, 2008)

The amplification factors for heights of 30 m, 100 m and 300 m were calculated using the above empirical formula, as listed in Table 2.17. These are compared with the topographic amplification factors calculated in the present study. Details will be presented later in Section 3.4.2.1.

Table 2.17   Arias Intensity Amplification Factor for Topographic Effect Derived in Lee et al (2008)

Height (m)	30	100	300
Arias Intensity Amplification Factor	1.24	1.63	2.33

Determination of the causative factors

There are more than 50 different landslide-related causative factors commonly used (both in Taiwan and worldwide) for landslide susceptibility analyses (Lin, 2003). The authors selected 14 of the most frequently used, based on both abundance and accessibility. These were the lithology, slope gradient, slope aspect, terrain roughness, slope roughness, total curvature (Wilson & Gallant, 2000), local slope height, total slope height, topographic index (Kirkby, 1975), distance from a road, distance from a fault, distance from a river head, distance from a river bend, and the normalised differential vegetation index (NDVI, Paruelo et al, 2004). All these factors were processed by a raster GIS - ERDAS IMAGINE system. The effectiveness of the factors as discriminators was evaluated by computing the standardised differences for each factor (Davis, 2002) as:

$$D_j = \frac{\overline{A}_j - \overline{B}_j}{S_{pj}} \quad \text{...(2.26)}$$

where A_j is the mean of factor j for group A (landslide), B_j is the mean of factor j for group B (non-landslide), S_{pj} is the pooled standard deviation of factor j and D_j is standardised difference of factor j.

The arger the standardised difference, the more effective the factor is for differentiating between landslide and non-landslide groups. On this basis, of the fourteen causative factors, six of them (lithology, slope gradient, slope aspect, terrain roughness, slope roughness, and total curvature) were finally selected for the event-based landslide susceptibility analysis (EB-LSA) of the earthquake-induced landslides.

The spatial distribution of the values of these six causative factors is shown in Figure 2.23. Terrain roughness at a given point was defined as the standard deviation of elevations within a certain distance (Wilson & Gallant, 2000), i.e. a radius of three pixels in this case. The data were high-pass filtered before calculation of the terrain roughness. Slope roughness was defined as the standard deviation of slope gradients within a radius of three pixels. The definition of total curvature was the same as that used by Wilson & Gallant (2000).

Slope	Slope aspect
Terrain roughness	Slope roughness
Total curvature	Lithology

Note: Lithologic unit: 1. Alluvium; 2. Terrace Deposits; 3. Lateritic Terrace Deposits; 4. Toukoshan Formation (conglomerate dominate); 5. Toukoshan Formation (sandstone and shale dominate); 6. Cholan Formation; 7. Kueichulin Formation; 8. Fulungyuan Formation; 9. Hourdonqkeng Formation; 10. Shihmentsum Formation; 11. Takeng Formation, Tanliaoti Member; 12. Takeng Formation, Shihszeku Member; 13. Shuichangliu Formation; 14. Paileng Formation, Meitzulin Member; 15. Paileng Formation, Tungmou Member.

Figure 2.23   Spatial Distribution of Original Values of Causative Factors in the Kaohsiung Quadrangle (Lee et al, 2008)

Slope gradient, terrain roughness, and Arias Intensity were found to be the predominant factors for the landslide susceptibility assessment of both hilly and mountainous terrains, but lithology was also found to be determinant in hilly terrain.

Landslide susceptibility results and mapping

The spatial probability of landslide occurrence was indicated by the relationhsip between the landslide ratio (probability of failure) and the landslide susceptibility index (LSI) (see Figure 2.24). The spatial probability of a landslide was then used to map the susceptibility classes, as shown in Figures 2.25 and 2.26. The authors then compared actual landslides that occurred during the Chi-Chi earthquake with those on the susceptibility map (Figures 2.25 and 2.26), and observed a general agreement between the landslide pattern and areas of high susceptibility.
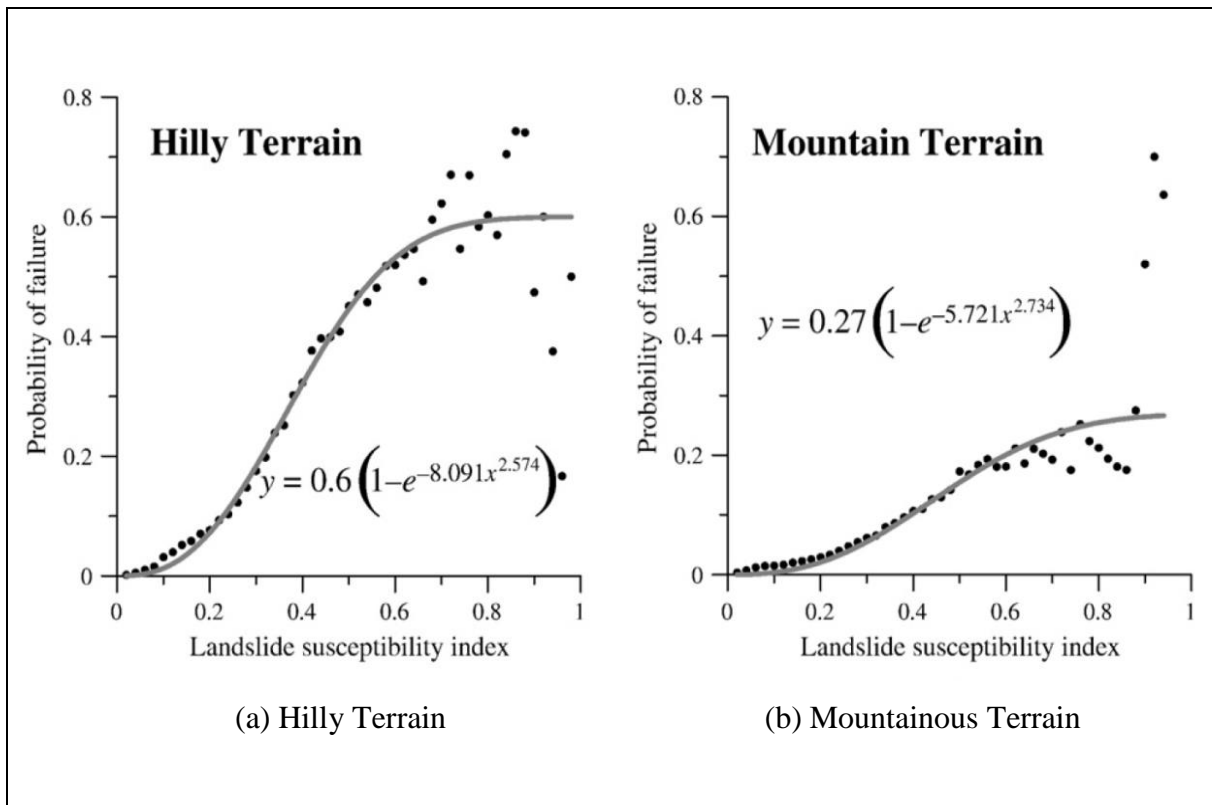
Figure 2.24 **Distribution of Landslide Ratio (Probability of Failure) with Respect to Landslide Susceptibility Index in the Kaohsiung Quadrangle. Weibull Distribution Curves are Shown: (a) Hilly Terrain; (b) Mountainous Terrain (Lee et al, 2008)**
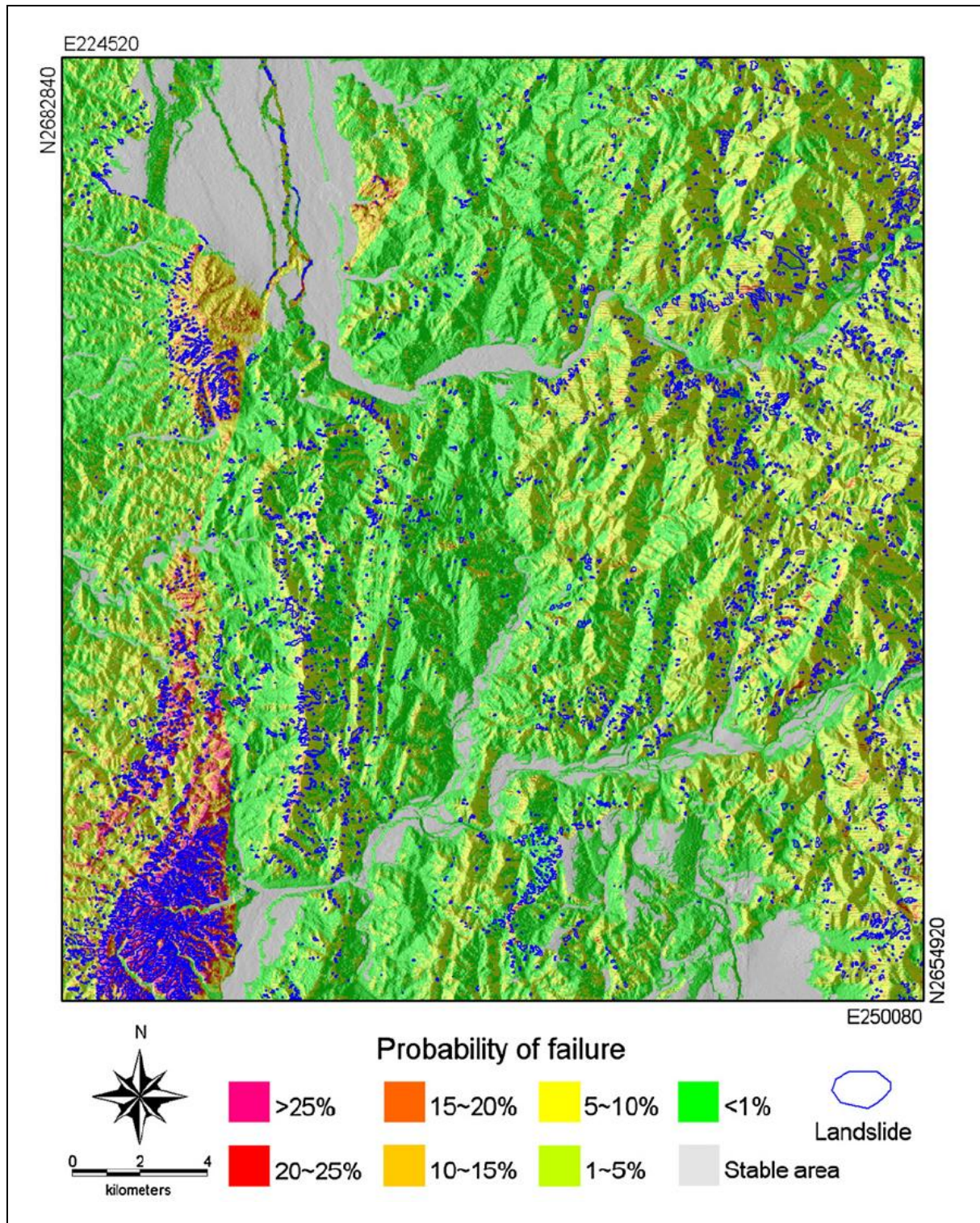
Figure 2.25   Landslide Susceptibility Map of the Kaohsiung Quadrangle Developed Using a Susceptibility Model Trained with the Chi-Chi Landslide Inventory and the Earthquake Shaking Intensity in that Quadrangle.   Landslides Triggered by the Chi-Chi Earthquake are Shown (Lee et al, 2008)
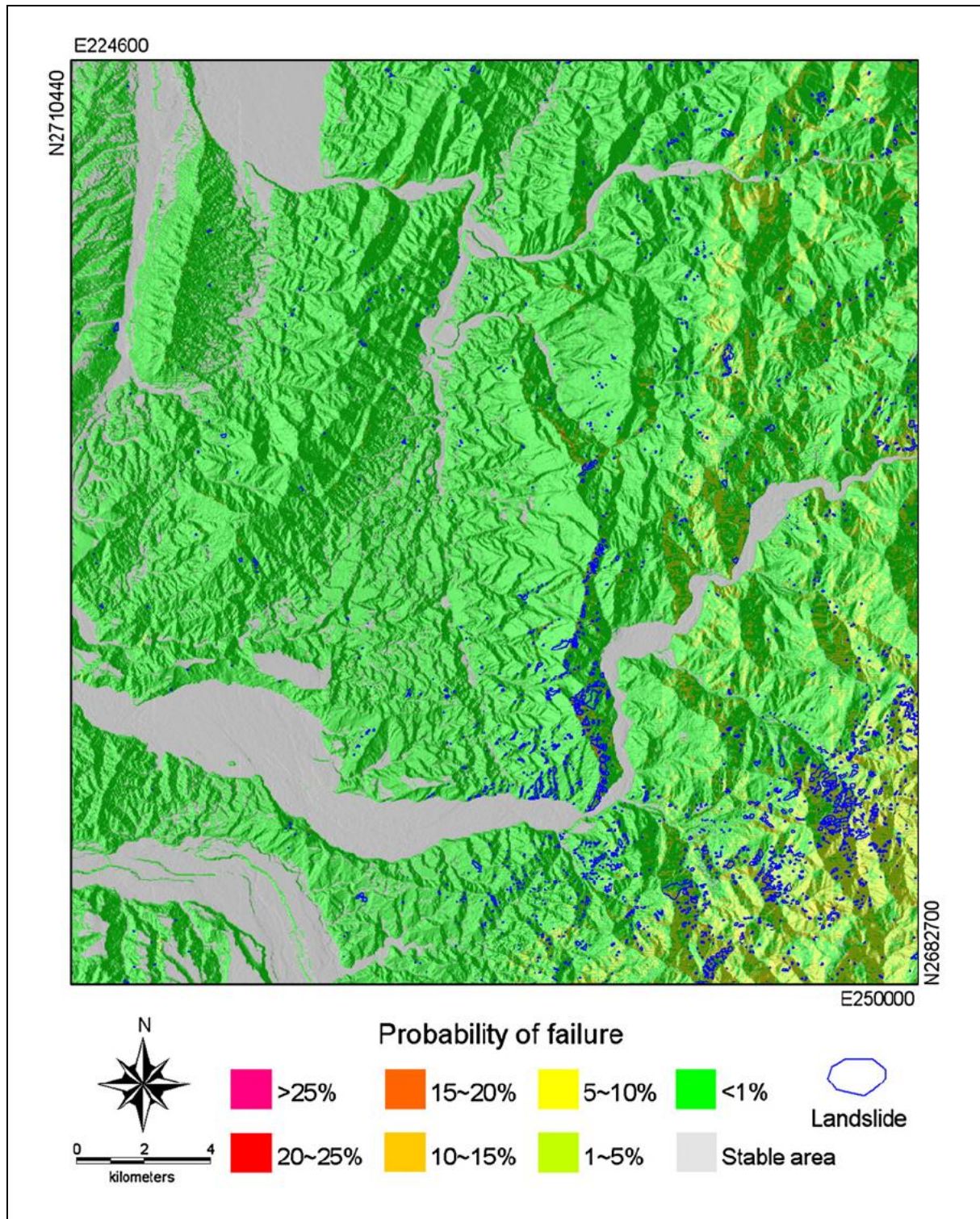
**Figure 2.26   Application of the Kaohsiung Susceptibility Model to the Tungshih
Quadrangle.   Landslides Triggered by the Chi-Chi Earthquake are
Shown (Lee et al, 2008)**

A prediction rate curve method (Chung & Fabbri, 2003) was then used to examine how well the classification results fit the data. The success rate curves for the two terrains are shown in Figures 2.27 and 2.28.   The area under the curve is between 0 and 1; a higher value indicates a higher prediction rate, whereas a value near 0.5 means the prediction is no better than a random guess (Chung & Fabbri, 2003).
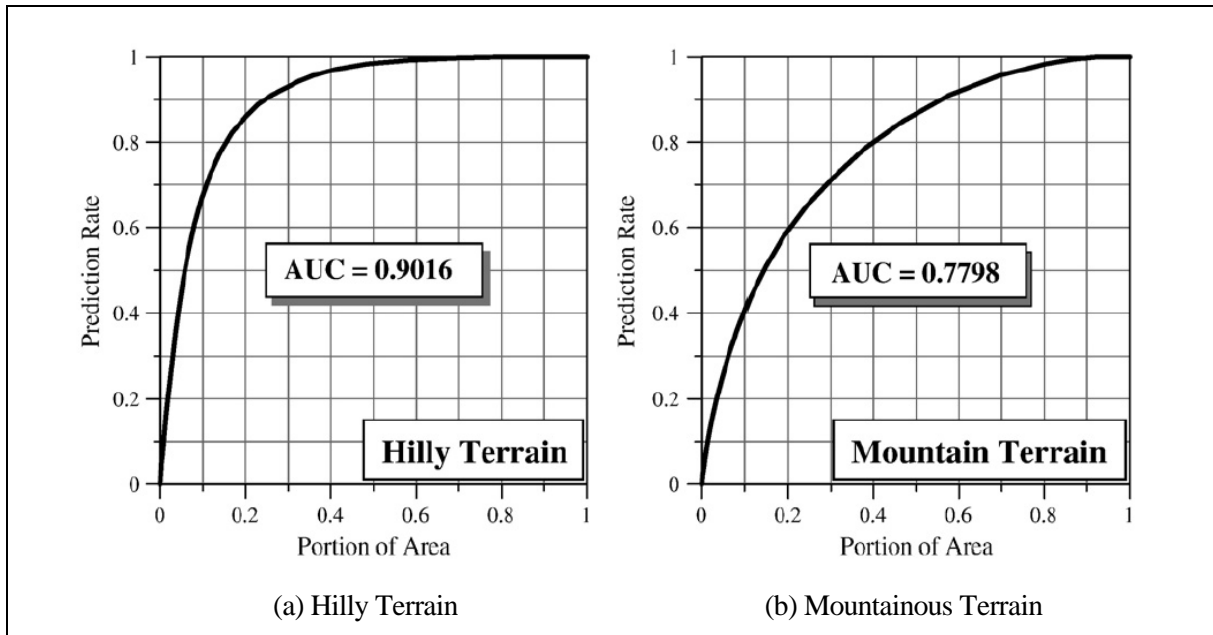
Figure 2.27   Success Rate Curves for the Chi-Chi Earthquake Event in the Kaohsiung Quadrangle: (a) Hilly Terrain; (b) Mountainous Terrain (Lee et al, 2008)
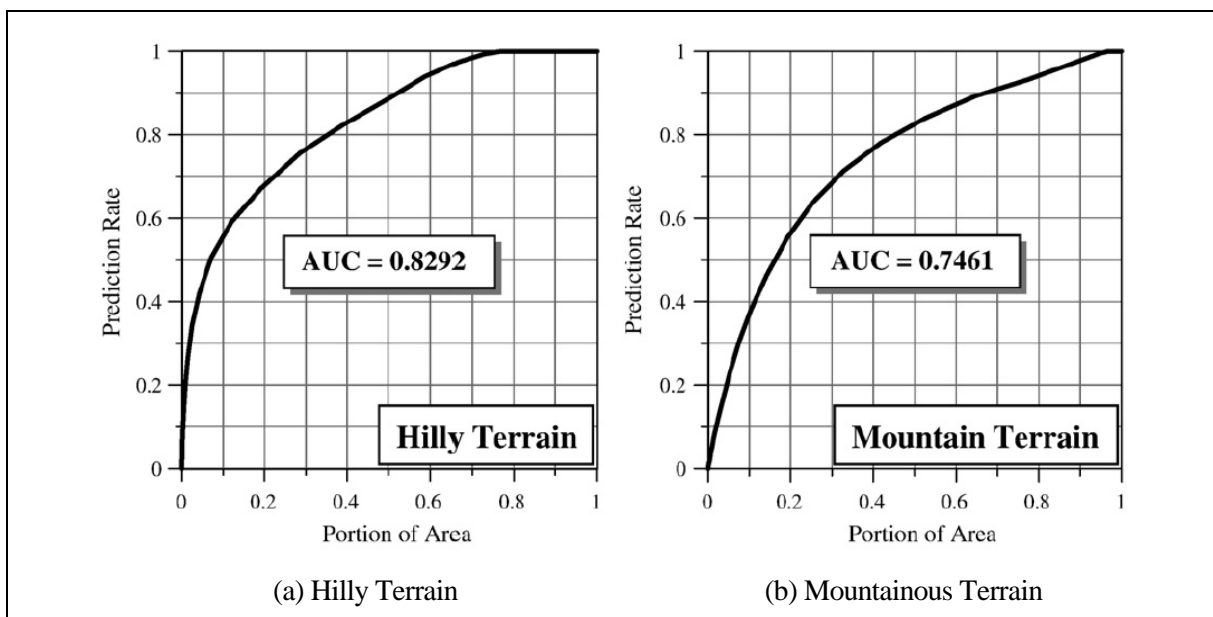
Figure 2.28   Prediction Rate Curves for the Chi-Chi Earthquake Event in the Tungshih Quadrangle: (a) Hilly Terrain; (b) Mountainous Terrain (Lee et al, 2008)

Based on this study, Lee et al (2008) identified the slope gradient, terrain roughness and Arias Intensity as three major factors affecting earthquake-induced landslides. As these factors are site-specific, they may not be applicable to other sites like Hong Kong. However, this study provided an indication to different potential parameters that are worth to be considered.

2.4.4 Sewell & Tang (2012)

Sewell & Tang (2012) integrated the findings of previous studies (Tang et al, 2009 & 2010; Wong & Ding, 2010; Wong et al, 2010) to examine the possible evidence that earthquakes could have triggered landslides in four areas in Hong Kong i.e. Ho Lek Pui Area, Tung Chung East Area, Wong Chuk Yeung Area and Nam Shan/Pui O Area. They also attempted to evaluate possible seismic relationships with sizable natural terrain landslides. In addition, this study reviewed and discussed other possible evidences for recent fault activities in Hong Kong.

According to Sewell & Tang (2012), although a time period of possible fault movement may overlap with a pulse of landslide activity by dating evidence, there was no strong evidence for faults displacing the quaternary deposit in Hong Kong. It was therefore considered that the local neotectonic fault movement had no major influence on relict natural terrain large landslides.

The study also found that the sources of seismic shaking that could trigger landslides in Hong Kong were most likely located outside Hong Kong. This was deduced by the dating results of the faults in Hong Kong that showed little correlation with the pulses of landslide activities.

2.4.5 Parker et al (2011)

Parker et al (2011) examined whether the 2008 Wenchuan earthquake led to a net gain in orogen volume (via rock uplift) or a new loss (via landsliding). It was found that the landslides produced more erodible material than new volume added to the orogen by co-seismic rock uplift. In an accompanying presentation, the factors that potentially contribute to landslides during an earthquake were discussed. It was shown that the fault rupture distance was a dominant factor whilst the hillslope gradient and geology were other potential factors.

2.4.6 Wasowski et al (2011)

Wasowski et al (2011) presented an overview of current issues and future challenges of research on earthquake-induced landslides. They offered some recommendations for future research priorities, as a proposed starting point for the next generation of research on earthquake-induced slope failures, such as the development of seismic inventories, GIS-based regional-scale assessments for seismic landslide susceptibility and long term monitoring on representative test slopes. The authors also indicated that further research work would be needed to improve the understanding regarding measurements and analyses of the seismic site response (including topographic, litho-stratigraphic (soil) factors, ground motion directivity),

and slope dynamic response. Other considerations included the impact of earthquakes on mountain slope evolution and sediment yields, including enhanced landslide generation by precipitation events following earthquakes, and the uncertainty in ground motion inputs and outputs from seismic slope stability analysis. Recent developments in the regional scale analysis and the seismic landslide hazard evaluation, such as Lee et al (2008), Hsieh & Lee (2011), were also reviewed.

2.4.7 Jibson (2011)

Jibson (2011) reviewed the latest methods to assess the stability or performance of slopes during earthquakes. They generally comprise three categories:

(a) pseudo-static analysis,

(b) stress-deformation analysis, and

(c) permanent-displacement analysis.

Despite the pros and cons of each analysis, they are suitable for different situations. The pseudo-static analysis is easy to use, and provides a simple, scalar index of stability. However, this simplicity stems from a rather crude characterisation of the physical processes of dynamic slope behaviour that produces several drawbacks, including the difficulty in rationally selecting a pseudo-static coefficient and assessing the likelihood or results of failure.

The stress-deformation modelling gives more accurate picture of what actually happens in the slope during an earthquake. Although models that account for the complexity of spatial variability of properties and the stress-strain behaviour of slope materials may yield more reliable results, stress-deformation modelling has drawbacks and can be quite challenging because of:

(a) the data acquisition required, commonly including undisturbed soil sampling and extensive laboratory testing of samples;

(b) the need to select a suite of input ground motions;

(c) the need for an accurate, nonlinear, stress-dependent, cyclic model of soil behaviour; and

(d) computational requirements.

The study concluded that the permanent-displacement method such as the Newmark's rigid-block analysis is the best suited to earthquake-induced landslides in natural slopes. More sophisticated coupled analyses were available to account for the fact that a landslide mass is not a rigid body but could deform internally under seismic shaking. In general, simplified decoupled analyses could yield more conservative results, which are within about 20% of the coupled results. Coupled analyses are appropriate for deeper landslides in softer materials, which could include large earth structures and deep landslides. It is, therefore, concluded that

decoupled analyses are sufficient for the present study, which deals with shallow natural terrain failures.

2.4.8 Rathje & Antonakos (2011)

Rathje & Antonakos (2011) evaluated the seismic performance of slopes by predicting the sliding block displacements for critical sliding masses. The current practice adopted a rigid sliding block approach for shallow sliding masses and a decoupled, flexible sliding block approach for deeper/softer sliding masses. This paper presented a unified framework that extended the empirical displacement models for application to flexible sliding masses, where the dynamic response of the sliding mass is important. This framework included predicting the seismic loading for the sliding mass in terms of the maximum seismic coefficient (k_{max}) and the maximum velocity of the seismic coefficient-time history (k-vel$_{max}$). The predictive models were a function of the peak ground acceleration (PGA), peak ground velocity (PGV), the natural period of the sliding mass (T_s), and the mean period of the earthquake motion (T_m). This unified framework provided a consistent approach for predicting the sliding displacement of both rigid and flexible slopes. This modification was a function of T_s and increased the predicted displacement due to the nonlinear response of the soil and the reductions in the amplitude of the seismic loading (i.e. k_{max}). Modification for both the (PGA, M) and (PGA, PGV) models were developed, but the (PGA, PGV) model was recommended because of the significant frequency content information provided by PGV (for rigid sliding) and by k-vel$_{max}$ (for flexible sliding). It was also recommended that when the T_s /T_m ratio was less than or equal to 0.1, the response of slope could be considered as rigid.

2.4.9 Gaudio & Wasowski (2011)

Gaudio & Wasowski (2011) studied the site effects based on the long term accelerometric monitoring conducted on a landslide-prone test area in the Apennine Mountains, Italy, where the presence of site effects enhancing the seismic susceptibility of local slopes had been invoked on the basis of historic accounts of landslides triggered at a large epicentral distance. The recordings relative to low-to-moderate magnitude earthquakes showed significant amplifications affecting hillslope portions covered by a thick layer of colluvium (> 5 m) and pronounced amplification maxima oriented along the local maximum slope direction on a recent deep-seated landslide. The amplifications of the colluvium could be due to the high impedance contrast between surface materials and the underlying substratum.

2.4.10 Keefer (2007)

Keefer (2007) presented some earthquake-induced landslides that showed anomalies compared with the general trend. The key observations are:

(a) While the concentration of landslides typically diminished regularly with distance from the earthquake source, there were some cases of high landslide concentrations that occurred at a relatively great distance (St. George and Tecomán earthquakes). The anomalies of the St. George

event could be attributed to the originally low factor of safety indicated by previous movements in response to rainfall. For the Tecomán case, the terrain (with high landslide occurrence) was found to be underlain by young volcanic rocks, which were typically uncemented or poorly cemented.

(b) In some cases, a high concentration of landslides could occur in slopes having a dry condition at the time of an earthquake. This was observed in steep slopes arising from rapid tectonic uplift, the presence of young and tectonically deformed materials that were uncemented or weakly cemented, and possibly severe shaking in the hanging wall above the blind thrust on which the earthquake occurred.

2.4.11 GEERRI Methodology

The GEERRI methodology is a statistical approach based on data obtained from > 100 historical earthquakes which induced landslides in China. These data were used to generate different factors that possibly contributed to landslides as a result of seismic ground motions. The importance of each factor was assessed by the Certainty-Factor (CF) model proposed by Heckerman (1986). GIS was used to give the ranking spatially by considering the factors at different locations.

The GEERRI concluded that the major factor leading to earthquake-induced landslides was the seismic ground motion. The proximity to a fault on which the earthquake occurred was also a major contributor but this was probably due to the fact that larger ground motions occurred in a closer proximity to the fault.

2.4.12 Commentary

The Arias Intensity has been used as the triggering factor in the susceptibility analysis, and this factor makes the susceptibility model temporally significant.   It is also found to be the most effective factor for interpreting landslide distribution.

The event-based landslide susceptibility analysis (EB-LSA) has an advantage over deterministic methods in that it does not require the inputs of failure depth, material strength, nor groundwater data. It may thus have a better prediction rate. However, a deterministic model can be used anywhere once the required input parameters are available. An EB-LSA model, by contrast, may be applicable only to a small region where the model was trained. Also, another disadvantage of EB-LSA is that the physical meaning of some susceptibility factors may be unclear. More physically-based treatment of the susceptibility factors should be considered in the future to improve the susceptibility model.

Even though the topographic effect has been taken into account in the analyses, it is not very accurately representative of the phenomena as the topographic amplification is not simply proportional to the local height relative to riverbed, but can also be affected by factors such as lithology, geologic structure, and ridge sharpness (Celebi, 1987; Jibson, 1987; Geli et al, 1988;

Ashford et al, 1997; Murphy, 2006). Simulations and the application of multivariate geostatistical methods may be needed to improve the results in the future. Finally, it should be noted that the authors mentioned that extreme condition of earthquake during a storm is not valid for their study model, but the probability for those two events to happen simultaneously is very low.

2.5 Seismic Stability of Boulders

The seismic stability of boulders depends on many parameters, including the geometry, material properties of the boulder and its embedment as well as the geometry of the slope. Two scenarios could be considered for the potential boulder instability i.e. sliding or toppling as a result of an imposed vibration. A review of the literature about seismic stability assessment of boulders has been carried out. The papers studied different simplified approaches for assessing the boulder stability and the pertinent parameters.

2.5.1 Wong & Pang (1991)

The effects of blast-induced ground vibrations were analysed by Wong & Pang (1991). Their findings have been used as the basis for assessing the potential effects of blasting on rock slopes and soil slopes. For the stability of rock blocks on a slope, an energy approach, which took into account the blasting vibration energy transmission to the potential rock block, was recommended. Figure 2.29 illustrates the rock block system subjected to blasting vibration.

Based on the principle of conservation of energy, the following equation was derived:

$$\int_0^{U_\mathrm{f}} \tau A_\mathrm{b}\, \mathrm{d}\delta = \frac{1}{2}\frac{W}{g}\left(V_\mathrm{g}\right)^2 + W\, U_\mathrm{f} \sin\beta \quad\text{.....................................(2.27)}$$

where
A_b = base area of the rock block
τ = shear stress acting along the rock joint
W = weight of the rock block
g = gravity
U_f = downslope displacement of the rock block
β = slope angle.

When considering a multi-directional vibration which propagated in three orthogonal directions x, y and z, Wong & Pang (1991) suggested using the following relationship for evaluating the peak velocity V_p:

$$V_\mathrm{p} = 1.35\ \mathrm{PPV} \quad\text{.....................................(2.28)}$$

where
PPV = max $(\mathrm{PPV}_x, \mathrm{PPV}_y, \mathrm{PPV}_z)$.
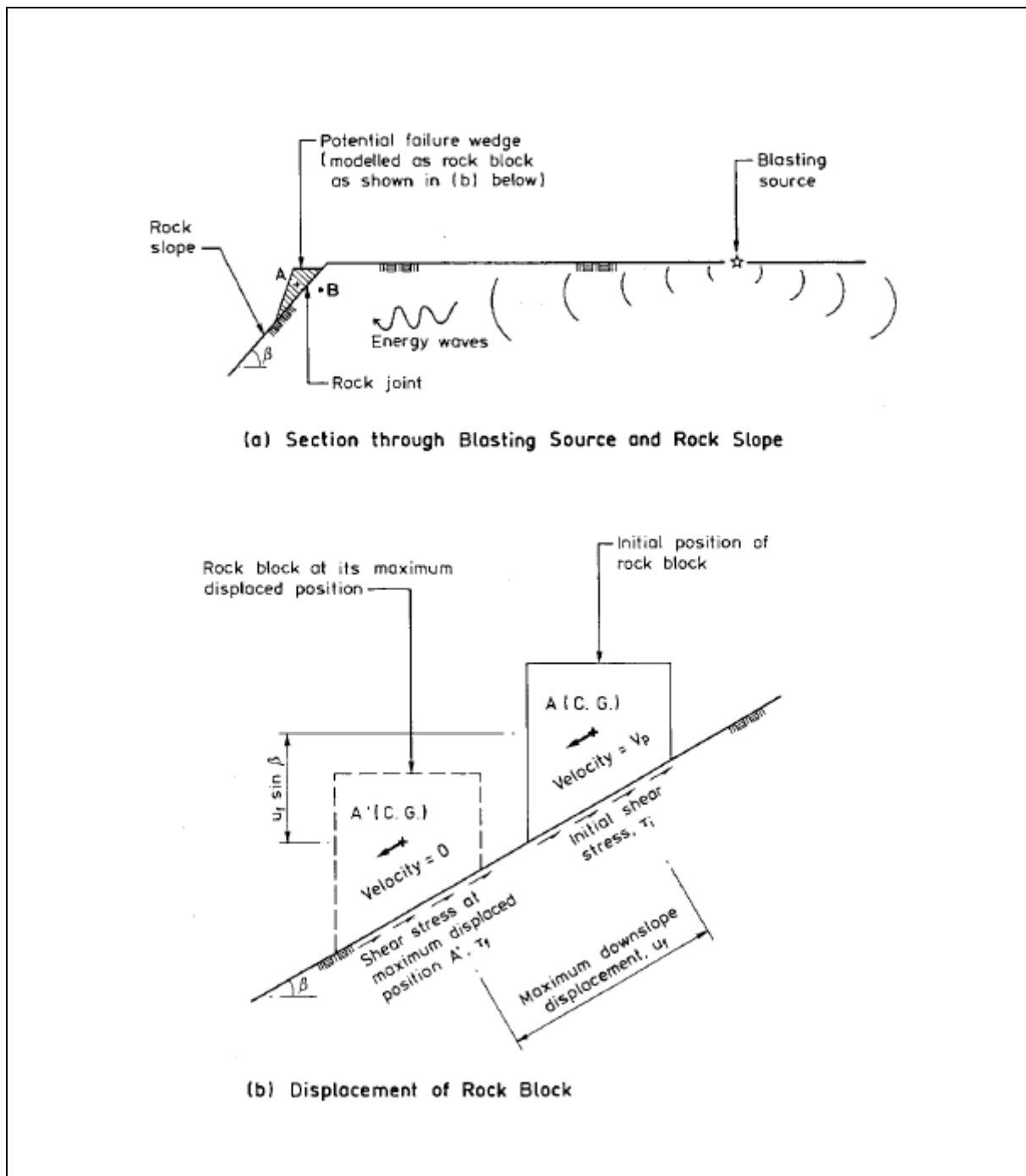
Figure 2.29 Rock Block System Subjected to Blasting Vibration (Wong & Pang, 1991)

This relationship may still be conservative, but was considered to be good enough as it took into account the fact that PPV_x, PPV_y and PPV_z had very remote chance to occur at the same time.   The fundamental energy equation therefore became:

$$\int_0^{U_f} \tau A_b \, d\delta = 0.91 \frac{W}{g} (PPV)^2 + W U_f \sin \beta \quad ....(2.29)$$

Commentary

This energy approach, considering the energy required to move a boulder, can be used for the analysis of the seismic stability of boulders. This approach assumes that the boulder sits on a smooth surface with no embedment in the ground. In the present study, the energy approach will be compared with more complex dynamic stability analysis. Also, the effect of vertical motion will be assessed using the equation suggested by Wong & Pang (1991) for multi-directional vibration. Details are presented in Section 4 of this report.

2.5.2 Haneberg (2009)

Haneberg (2009) described a simplified approach for the preliminary assessment of rock toppling due to earthquakes, blasting, or other vibrations. It was a simplified dynamic method that incorporated information about vibration frequency in addition to acceleration magnitude but had assumed a single-frequency vibration of a rectangular rock. As such, it was not a complete dynamic analysis for an irregular three-dimensional rock with a complicated basal geometry and a full spectrum of frequencies.

Based on the analyses, it was shown that high-frequency vibrations caused by typical blasting operations were unlikely to pose problems even if the peak acceleration values were relatively high. Moderate to large earthquakes generating lower frequency vibrations might, however, topple some rocks at the same or lower accelerations.

Although the method lacked the sophistication of those dynamic or multiple block analyses undertaken by others in site-specific studies, it had an advantage that the input parameters can be easily obtained. For example, the geometric variables can be readily estimated in the field and those vibration information such as the horizontal acceleration and the vibration frequency can be obtained from blasting records or earthquake seismograms. Therefore, this method had the potential of being used for screening or reconnaissance purpose. Haneberg (2009) suggested that the method be used within a geographic information systems (GIS) framework to create rock-toppling potential maps based on the regional seismic hazards and slope-angle maps. This approach has been adopted in the present study.

Haneberg (2009) assessed the risk of toppling of a rectangular block on a slope. Figure 2.30 shows the geometry and the variables of the problem. Both pseudo-static and dynamic stability analyses were carried out.

(a) The pseudo-static analysis led to the following relationship between the horizontal acceleration required for toppling of the rock and the slope angle for a certain block geometry:

$$a_T = g((b/h)\cos\theta - \sin\theta)/(\cos\theta + (b/h)\sin\theta) \dots\dots\dots\dots\dots\dots(2.30)$$

Figure 2.31 illustrates the correlation between the ratio b/h, the peak horizontal acceleration and the slope angle.
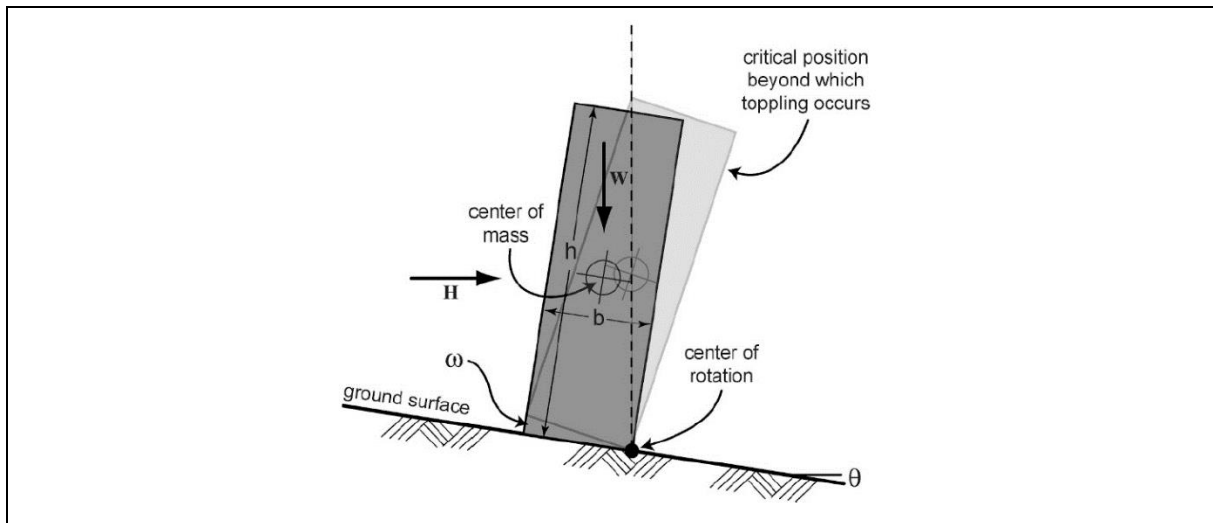
Figure 2.30 Schematic Illustration of the Variables Used to Analyze Vibration-induced Toppling of an Isolated Rock Resting on a Slope and Subject to Horizontal Acceleration (Haneberg, 2009)
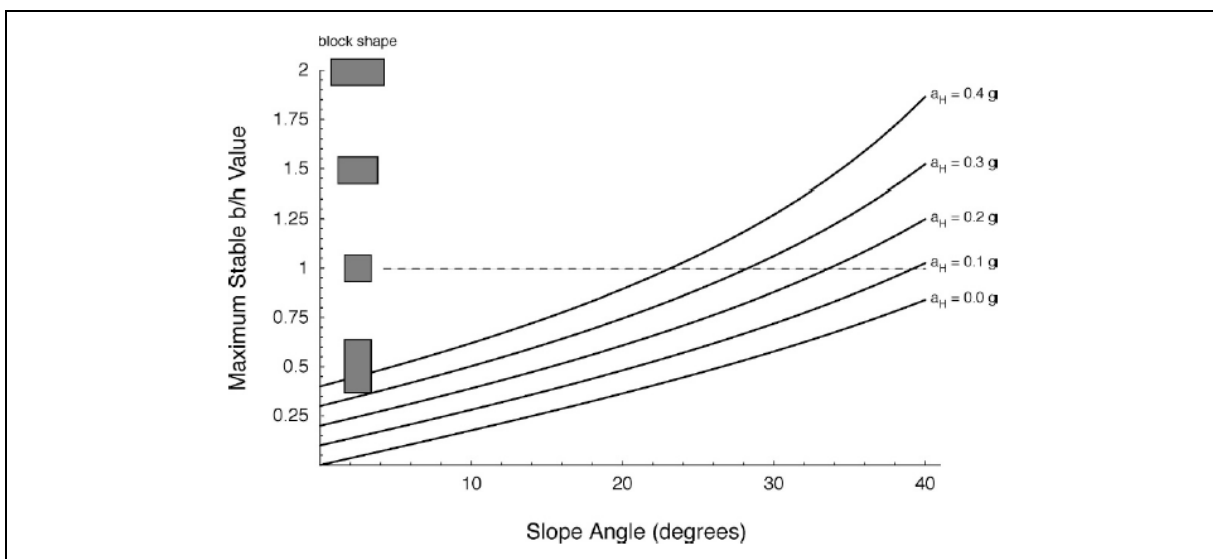
Figure 2.31 Maximum Stable *b*/*h* Ratios as a Function of Slope Angle (*θ*) and Peak Horizontal Acceleration (*a*H) as Given by the Pseudo-static Factor of Safety (Haneberg, 2009)

(b) The dynamic stability analysis assumed a sinusoidal acceleration time history of the form: $a_H = a_p \sin(2f\pi t)$, where f is the frequency in Hz, and a_p is the peak ground horizontal acceleration. This led to the following relationship between the frequency of the time-dependent shaking, the peak ground horizontal acceleration, the slope angle and the geometry of the boulder, as:

$$\int_0^{1/2f} \int_0^{1/2f} a_p \sin(2f\pi t) \, dt \, dt = L_\omega \quad\text{......................................(2.31)}$$

where

$$L_\omega = \frac{\pi\sqrt{h^2 + b^2}}{360} \left[\arctan\left(\frac{b}{h}\right) - \theta\right]$$

Figure 2.32 illustrates the correlation between the slope angle, the frequency of the ground motion that causes toppling, and the peak ground acceleration, for different geometries.
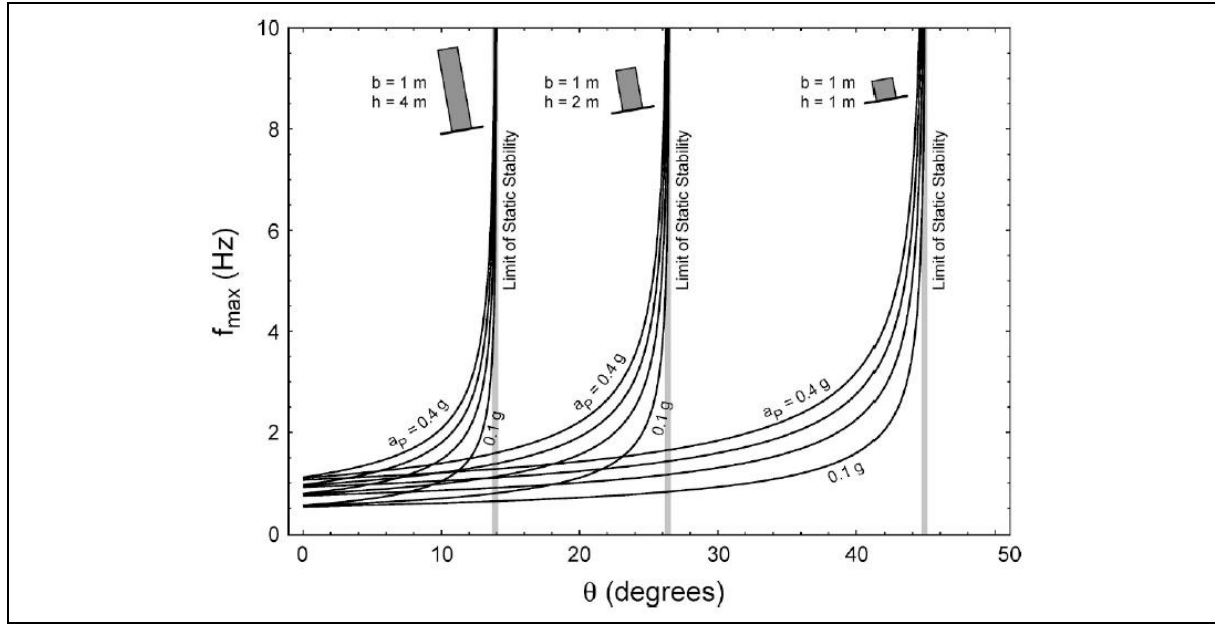
Figure 2.32   Maximum Possible Frequency of Vibrations Capable of Toppling a Rock (f_{max}) for Three Different Sets of b and h Values as a Function of Slope Angle (θ).   For Each Pair of b and h Values, Curves are Plotted for Peak Horizontal Acceleration Values of a_P = 0.1 g, 0.2 g, 0.3 g and 0.4 g (Haneberg, 2009)

The static toppling stability of a rock block was a function of its shape (i.e. its b/h ratio) but not its size (i.e. the individual values of b and h).   Its dynamic toppling stability, however, was shown to be a function of both shape and size.   As the rock size increased, the centre of mass must rotate through a longer linear (but not angular) distance to reach its tipping point, and therefore, lower frequency vibration was required.   Thus, with all other things being equal, short rocks would always be more stable than tall rocks with regard to the vibration-induced toppling.

3 Earthquake-induced Landslide Assessment

3.1 General

The literature review presented in Section 2 covers methodologies for assessing the stability and the displacement of slopes in the event that the ground motion is large enough to result in momentary slope failure.   Based on the literature review, the methodology adopted in the present study for earthquake-induced landslide assessment in natural terrain is introduced in this section.

The assessment adopts numerical models and empirical correlations to evaluate the slope movement (permanent displacement) induced by seismic ground motions.   The methods are essentially an extension of the Newmark's theory, which determines the amount of movement of a rigid block sliding down a frictional surface.   The block only moves when the applied downslope acceleration force exceeds the shear resistance given by the frictional surface.   The acceleration required to match the shear resistance is referred to as the critical acceleration, A_c. The resulted movement is a function of the magnitude and duration over which the applied acceleration exceeds this critical acceleration.   The numerical models require a seismic ground motion in form of a time history.   The empirical models correlate the permanent slope displacement with the Arias Intensity.

Although the seismic ground motion may lead to downslope accelerations greater than the critical acceleration, the downslope movement may still be very small.   It is observed that the downslope movement needs to exceed a threshold limit before the slope fails.   This threshold limit has been set as 100 mm for this study based on the literature review.

It should be noted that the critical acceleration, A_c, of a slope is a direct function of the shear strength of the soil.   Therefore, it will vary with time as the strength varies as a result of seasonal variations of groundwater level.

3.2 Time Histories

The time histories of seismic ground motions with different likelihood of being exceeded in the next 50 years have been developed for input into the numerical analyses.   The derivation of time histories is discussed as follows.   Apart from the horizontal ground motion, the effects of the vertical ground motion and topographic amplification have also been considered for the most critical scenarios.   The Arias Intensity, which is being used to represent the ground motion in the empirical correlations, is derived from the time histories (see Section 3.4).

3.2.1 Horizontal Ground Motion

Time histories of the horizontal ground motion developed in the seismic microzonation study (Arup, 2018) have been used as the basis for the slope stability analyses.   The time histories have been derived to be compatible with the uniform hazard response spectra for bedrock as derived in the seismic hazard assessment (Arup, 2015).   The time histories have been considered for scenarios with different combinations of magnitude and distance, representative of short period (0.2 s) and long period (1 and 5 s) ground motions.   Table 3.1

lists the magnitude-distance combinations that have been considered. Table 3.2 lists the actual earthquake records used as a basis for deriving the time histories in this study. They are the same as those used for the microzonation study (Arup, 2018) except for the 2% in 50 years ground motion (1 s, far-field event), which is based on a record from Alaska.

Table 3.1 Magnitude-distance Combinations from the Seismic Hazard Assessment (Arup, 2015)

Probability of the Ground Motion in the Next 50 Years	Short Period Ground Motion		Long Period Ground Motion					
	0.2 s		0.5 s - 1 s (Near-field Event, $r < 250$ km)		0.5 s - 1 s (for 2%, Far-field Event, $r > 250$ km)		5 s	
	M	R (km)	M	R (km)	M	R (km)	M	R (km)
10%	5.5	30	6.5	60			7	90
2%	5.5	10	7	60	8	250	7.5	90

Table 3.2 List of Selected Rock Time History Records

Source from PEER Strong Motion Database	Event	Date	Magnitude	Distance (km)	Duration (s)		Target Period for M-R Combinations (Refer to Table 3.1)	Target Level Probability of the Ground Motion in 50 years
					Effective (5% of PGA)	Total		
NGA210	Livermore-01	1980-01-24	5.8	30	13.89	24.00	0.2 s	10%
NGA3171	Chi-Chi-Taiwan-05	1999-09-22	6.2	63	20.62	56.99	1 s	
NGA1112	Kobe, Japan	1995-01-16	6.9	100	24.68	77.98	5 s	
NGA133	Friuli-Italy-02	1976-09-15	5.9	14	4.38	16.45	0.2 s	2%
NGA734	Loma Prieta	1989-10-18	6.9	53	10.71	29.69	1 s	
NGA2118	Denali, Alaska	2002-11-03	7.9	274	62.44	86.00	1 s	
NGA1392	Chi-Chi-Taiwan	1999-09-20	7.6	87	30.90	90.00	5 s	

Ground motions having 10% and 2% probabilities of being exceeded in the next 50 years (in short, 10% and 2% in 50 years ground motions) have been used for the slope stability analyses. Figures 3.1 and 3.2 show the spectrally-matched target rock site response spectra (Arup, 2015) for 10% and 2% in 50 years ground motions respectively. It should be noted that for the 2% in 50 years, 1 s, far-field ground motion (resulting from a magnitude 8 event at 250 km), the target response spectrum has been derived for the expected response spectrum for such an event scaled to match the uniform hazard spectrum at 1 s rather than to match the uniform hazard spectrum at all periods as shown in Figure 3.2. It is because the expected spectrum does not match the uniform hazard spectrum at low periods as can be seen from the figure. This poor match had been noted in the microzonation study (Arup, 2018) but for the simplicity of interpretation, it was not specifically considered in the site response analyses at that time. For the present slope displacement studies, this poor match could significantly affect the results as the Arias Intensity would be unrealistically increased by matching the uniform hazard spectrum rather than the expected spectrum from such an event.
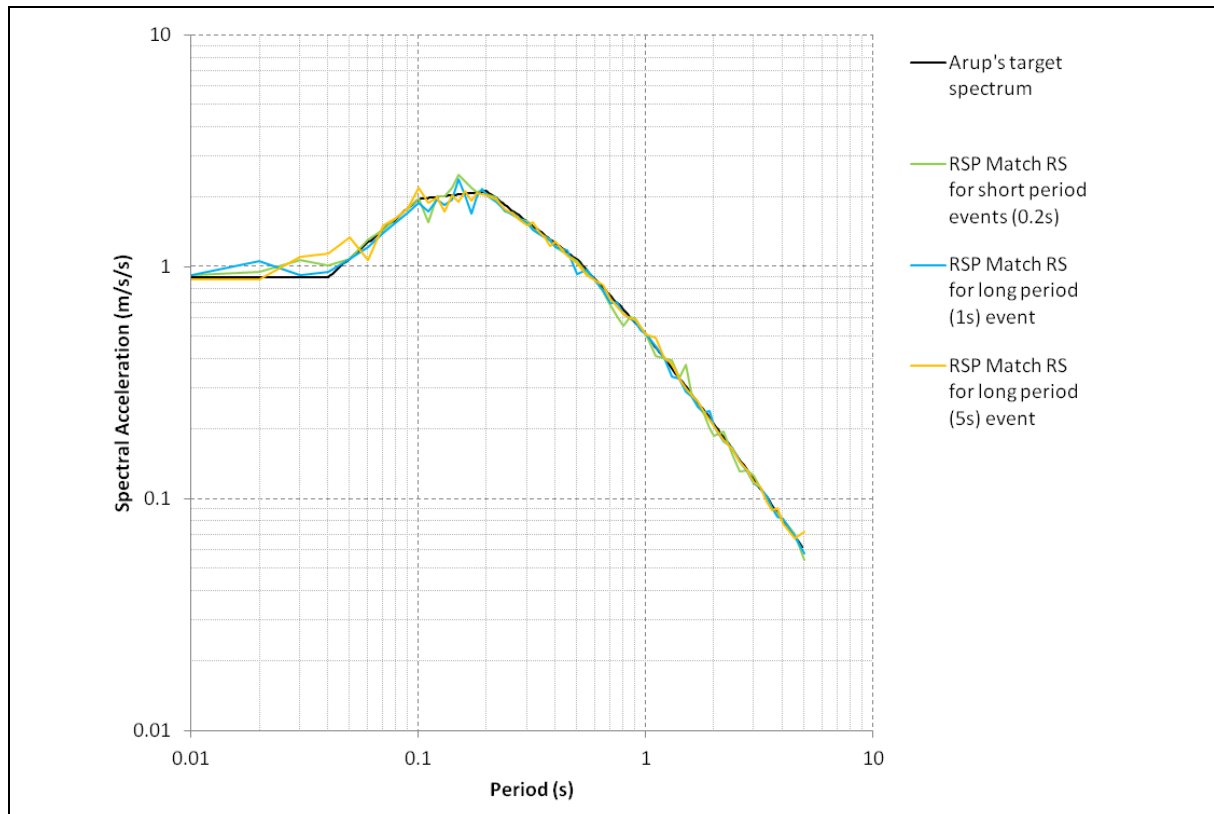
Figure 3.1   Spectra for the 10% in 50 Years Ground Motion
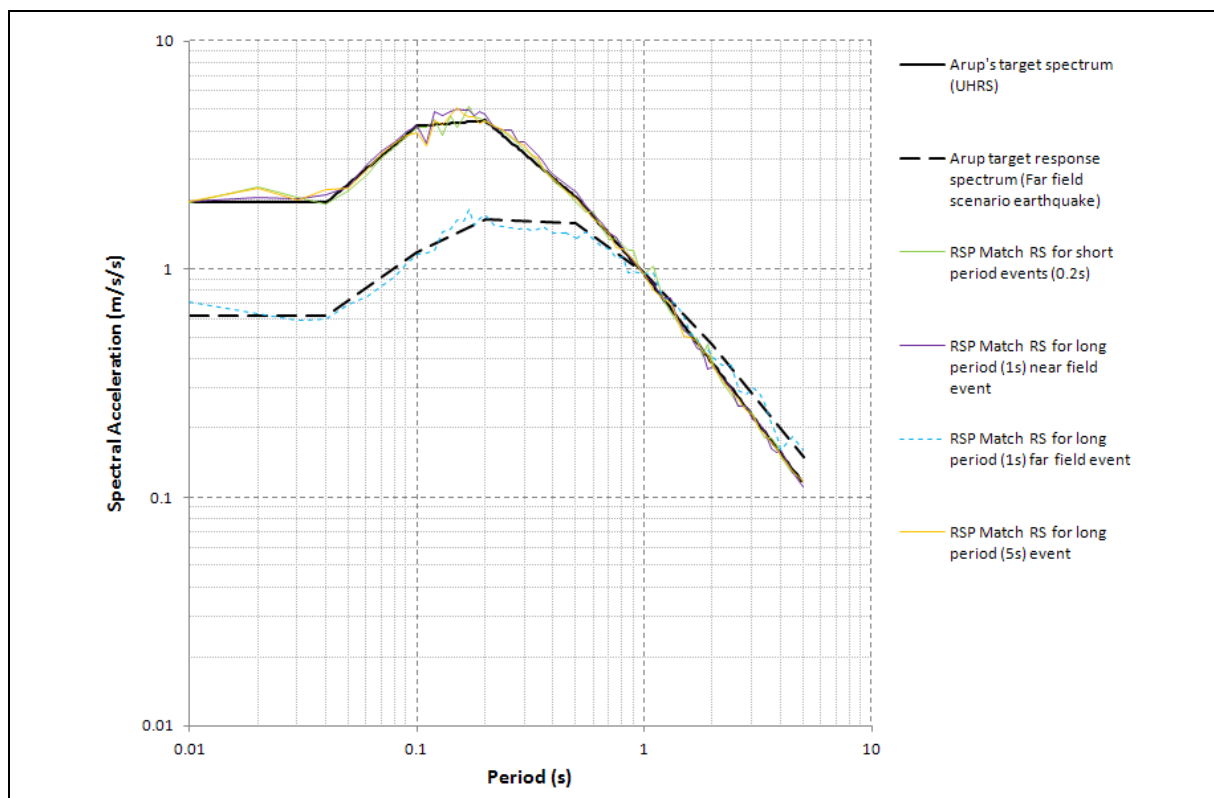
Figure 3.2   Spectra for the 2% in 50 Years Ground Motion

The generated time histories for 10% and 2% in 50 years ground motions are shown in Figures 3.3 and 3.4 respectively.
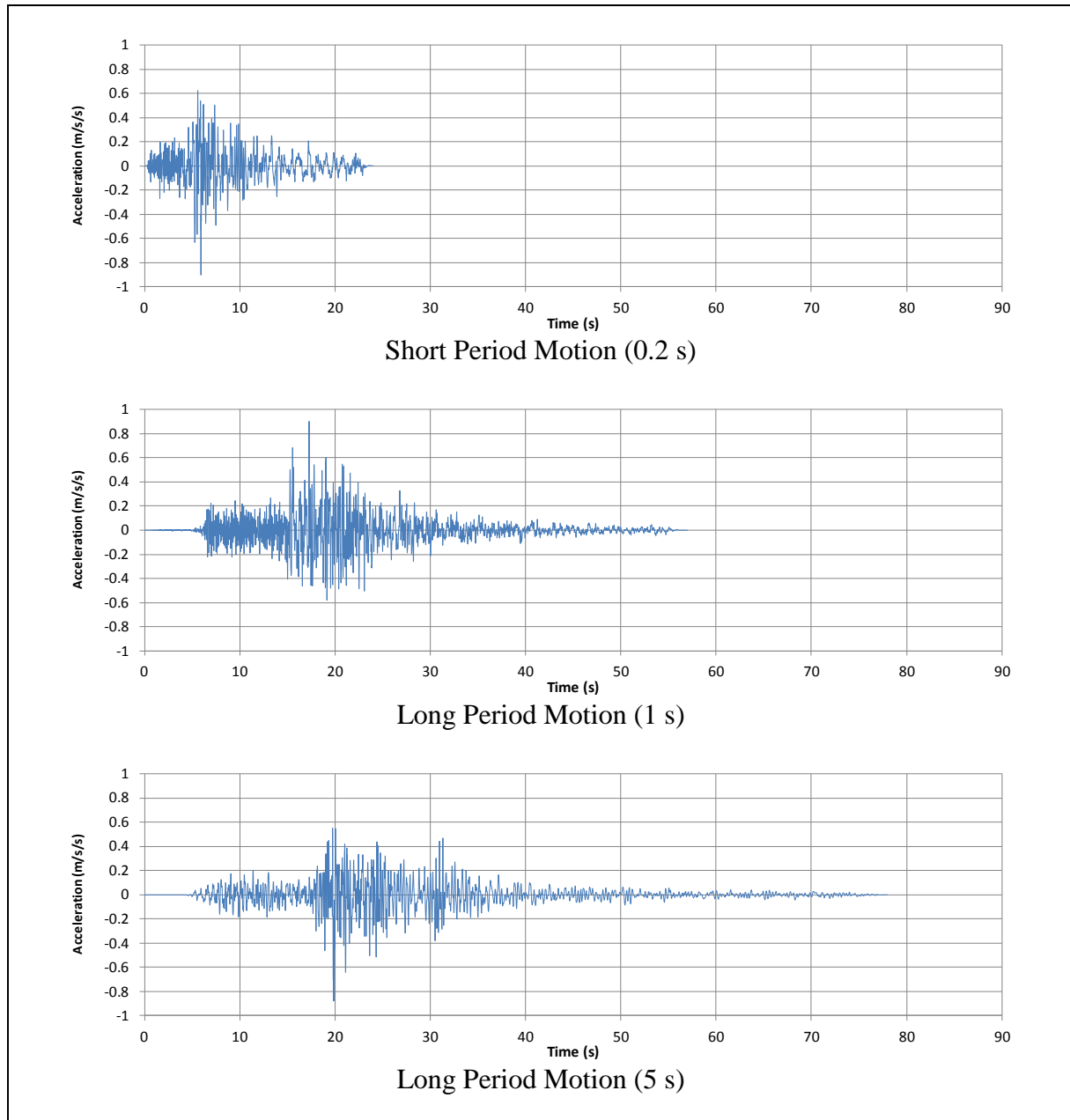
Figure 3.3   Spectrally Matched Rock Input Time Histories for 10% in 50 Years Ground Motion
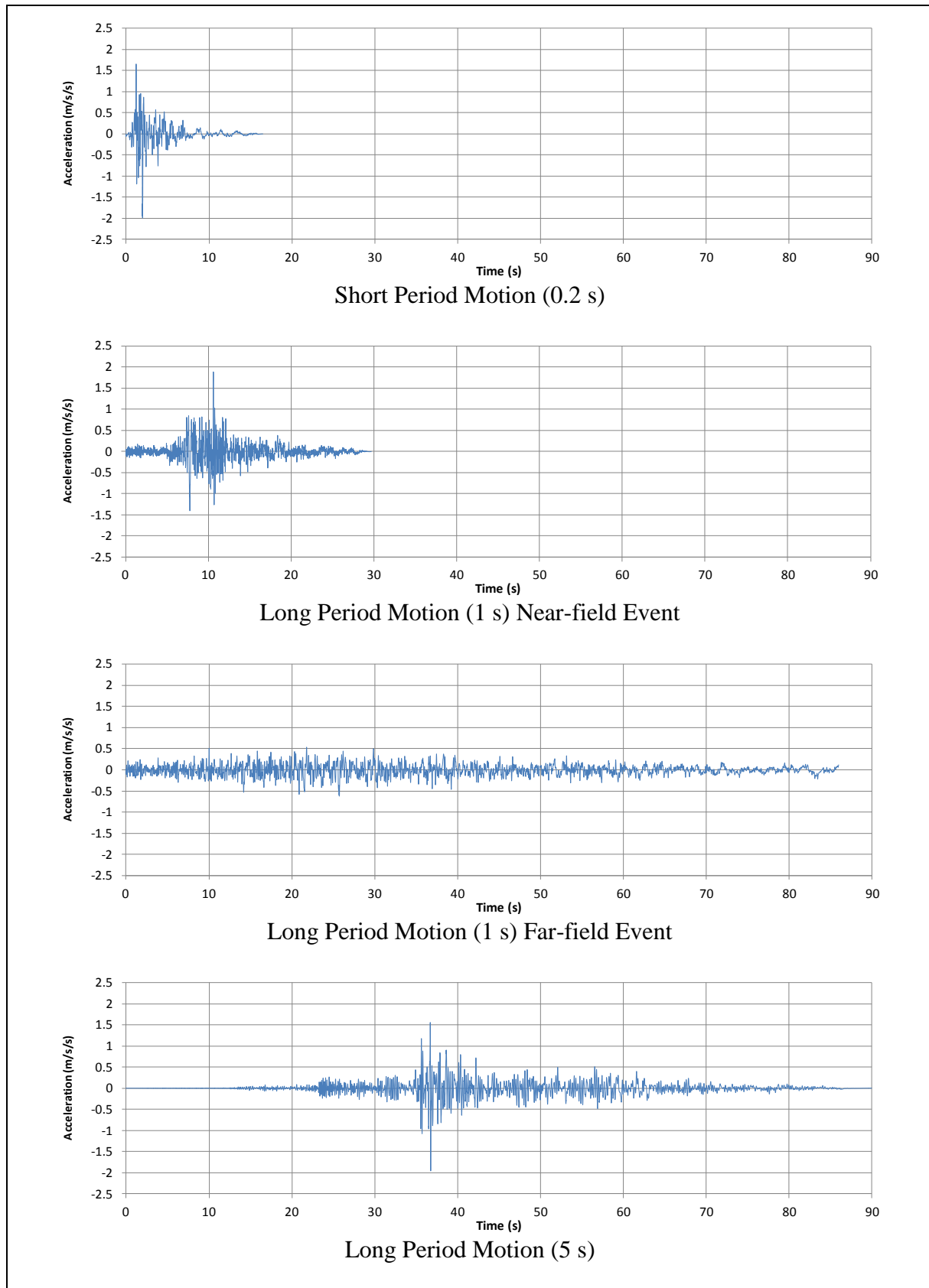
Figure 3.4   Spectrally Matched Rock Input Time Histories for 2% in 50 Years Ground Motion

3.2.2 Ground Motion with Topographic Amplification

To take into account the effect of topographic amplification, the spectral ratios derived in the seismic microzonation study (Arup, 2018) have been adopted to modify the horizontal response spectra.

At low structural periods, the amplification factor generally increases from up to 1.4 at zero period to 2 at the natural period of the crest, which is a function of the crest height. At longer structural periods, the amplification factor reduces back to unity. The spectral ratios for PGA amplification factors of 1.2 and 1.4 are plotted in Figure 3.5. Crest heights of 30 m, 100 m and 300 m have been considered. The target response spectra derived to account for the topographic effect on the horizontal ground motions are plotted in Figures 3.6 to 3.8. As the effect of amplification factor of 1.2 is relatively small, the target response spectra are only plotted for the 2% in 50 years ground motions (see Figure 3.8).
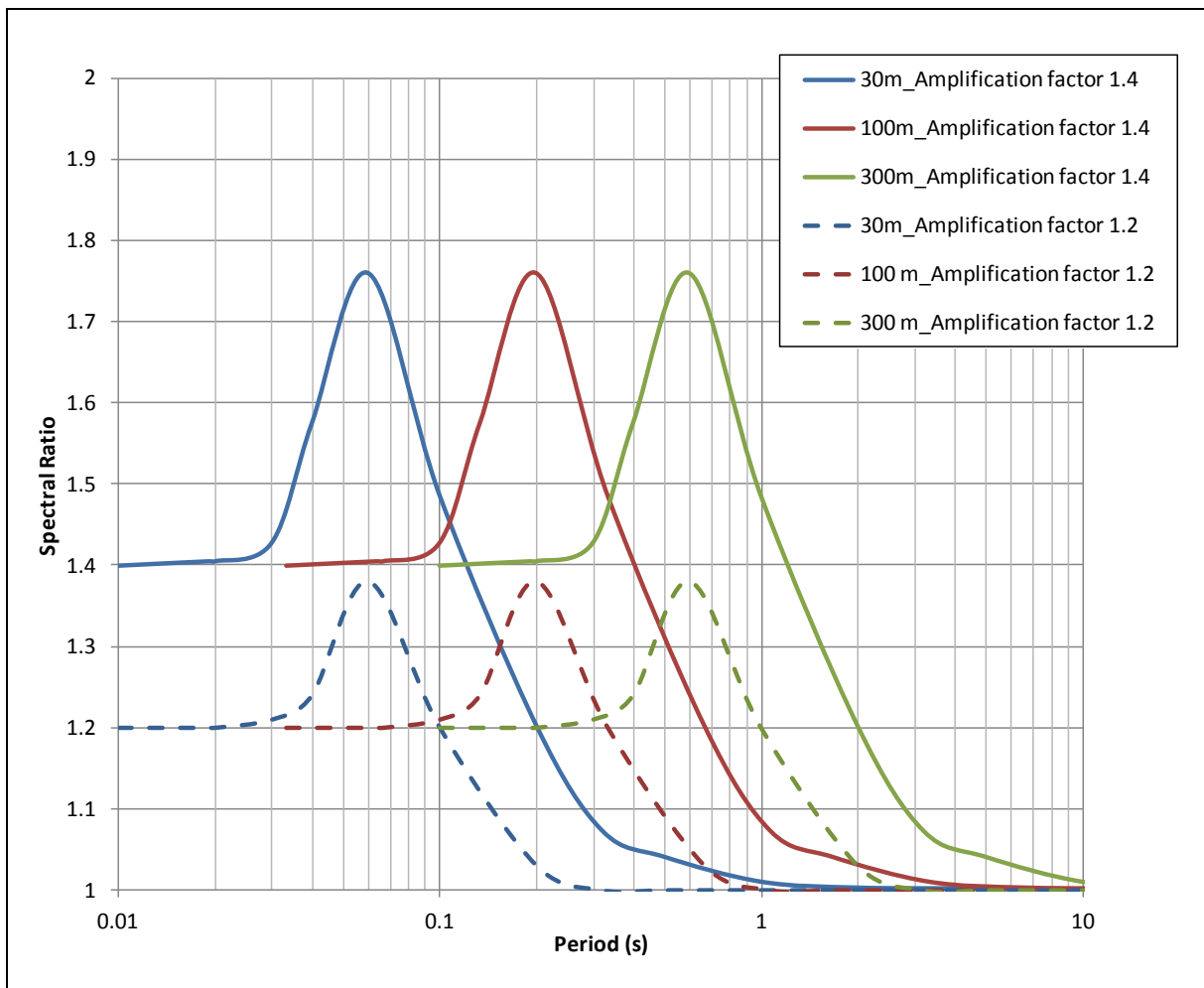
Figure 3.5   Spectral Ratios with Amplification Factors of 1.4 and 1.2 at Zero Period for Ridge 30 m, 100 m and 300 m
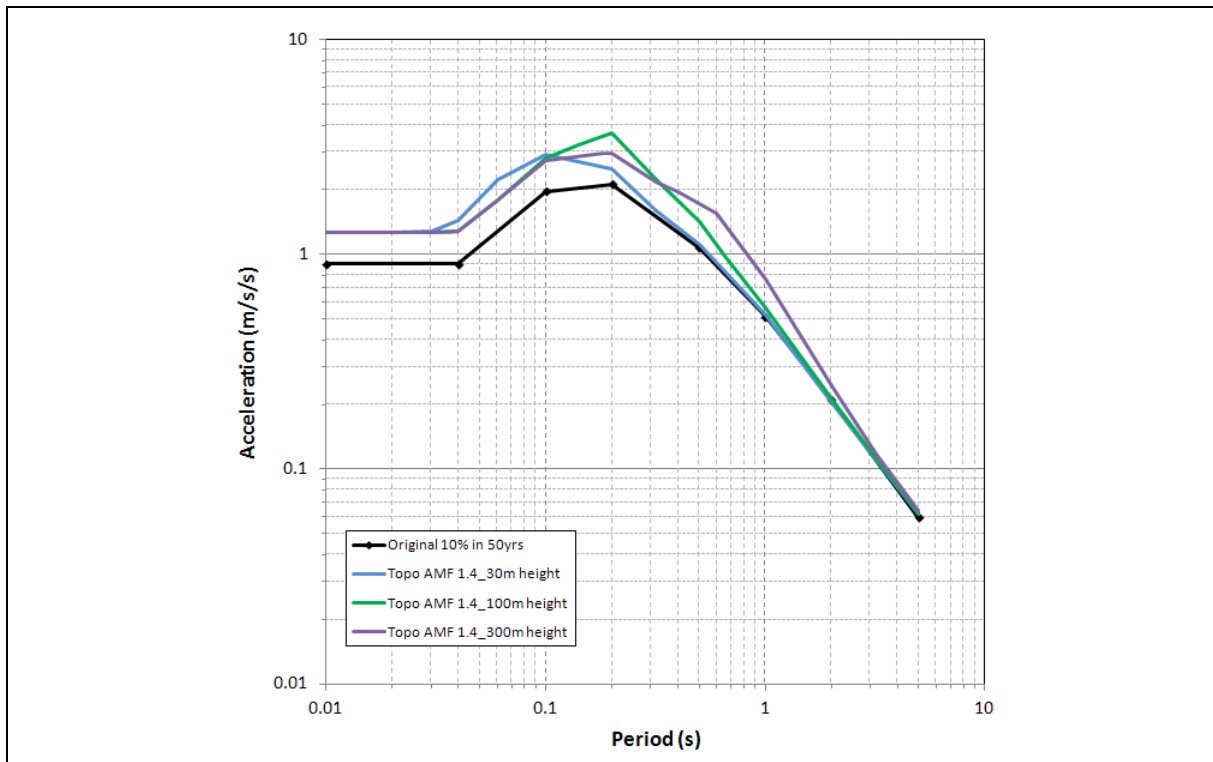
Figure 3.6   Response Spectrum with Amplification Factor of 1.4 at Zero Period for 10% in 50 Years Ground Motion
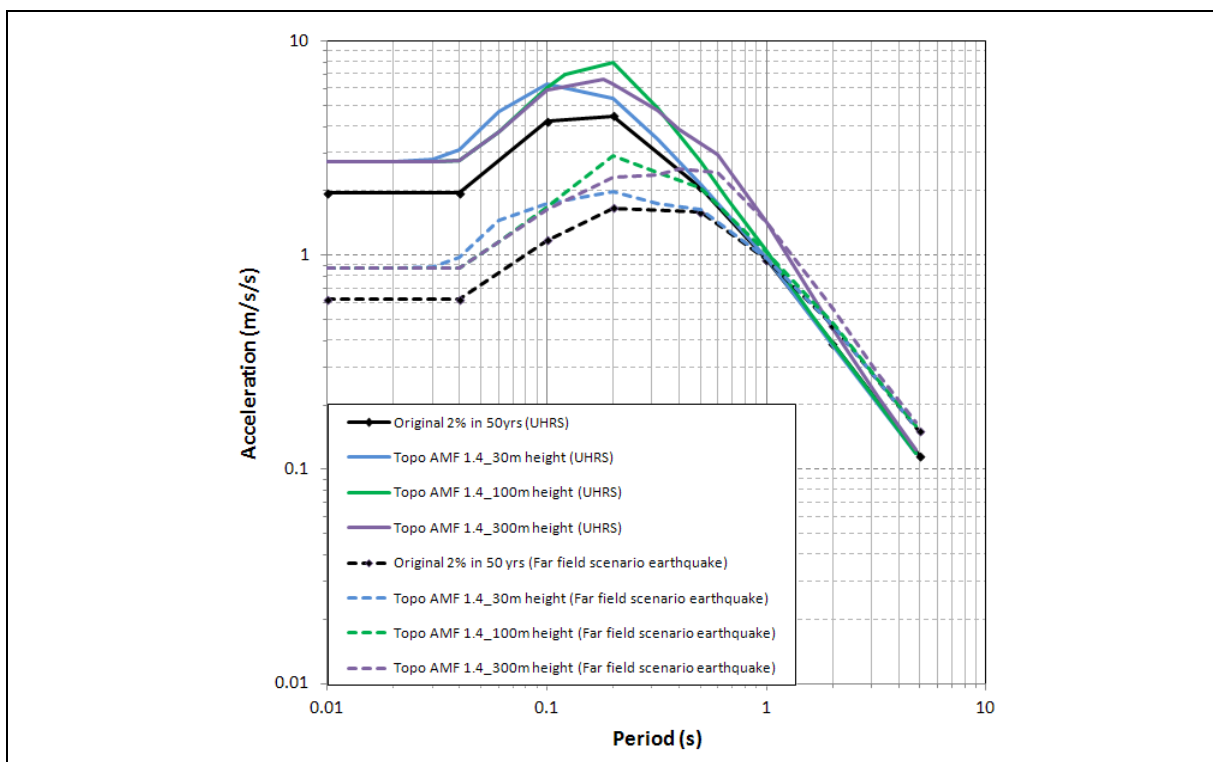
Figure 3.7   Response Spectrum with Amplification Factor of 1.4 at Zero Period for 2% in 50 Years Ground Motion
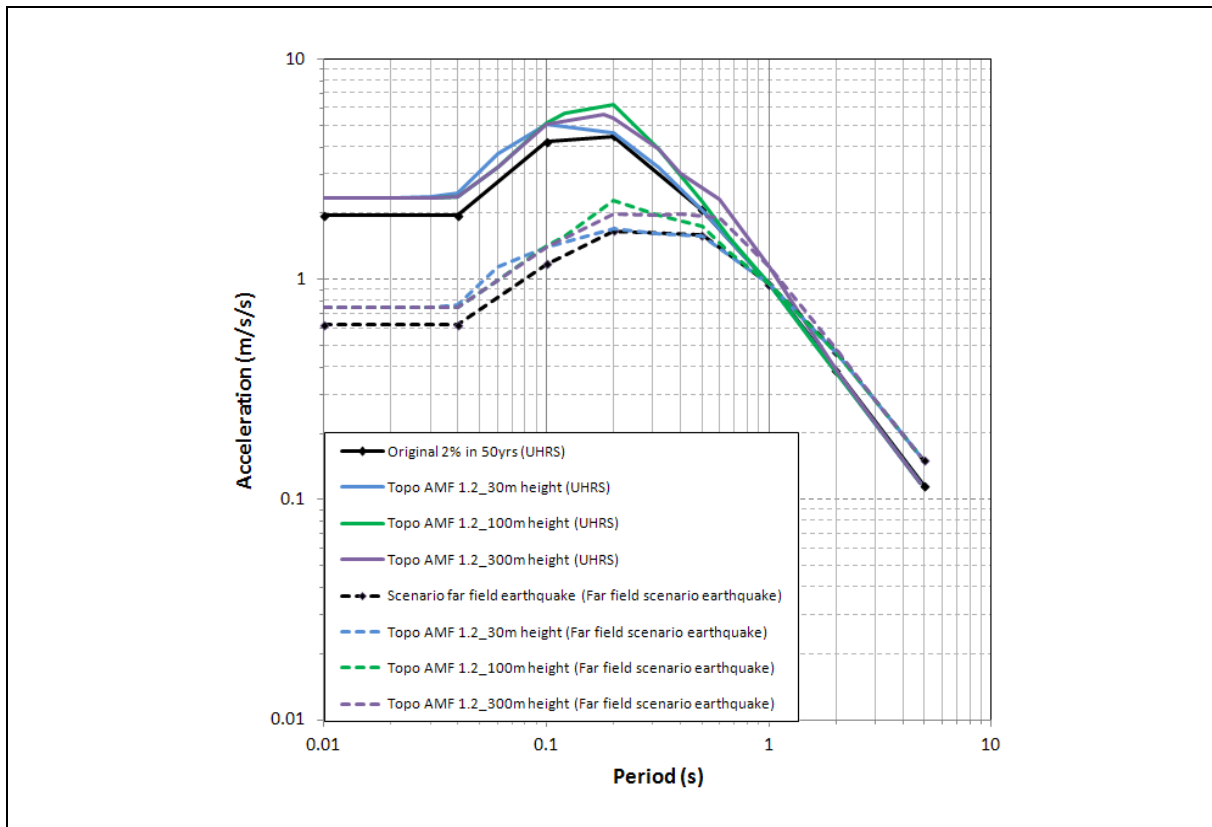
Figure 3.8   Response Spectrum with Amplification Factor of 1.2 at Zero Period for 2% in 50 Years Ground Motion

The time histories have been generated by modifying the same selected time histories as the ones used to derive the horizontal ground motion time histories without topographic effect in the time domain using RSPMATCH (Hancock et al, 2006), so that their response spectra would closely match the targets as shown Figures 3.6 to 3.8. The spectrally matched target response spectra for a PGA amplification factor of 1.4 for 10% and 2% in 50 years ground motions are presented in Figures 3.9 to 3.14.   Figures 3.15 to 3.17 illustrate the target matched response spectra for a PGA amplification factor of 1.2.   Figures 3.18 to 3.20 show the resulted time histories for a PGA amplification factor of 1.4 for the 10% in 50 years ground motions. Figures 3.21 to 3.23 show the corresponding generated time histories for the 2% in 50 years ground motions.   Figures 3.24 to 3.26 show the resulted time histories for a PGA amplification factor of 1.2 for the 2% in 50 years ground motions.
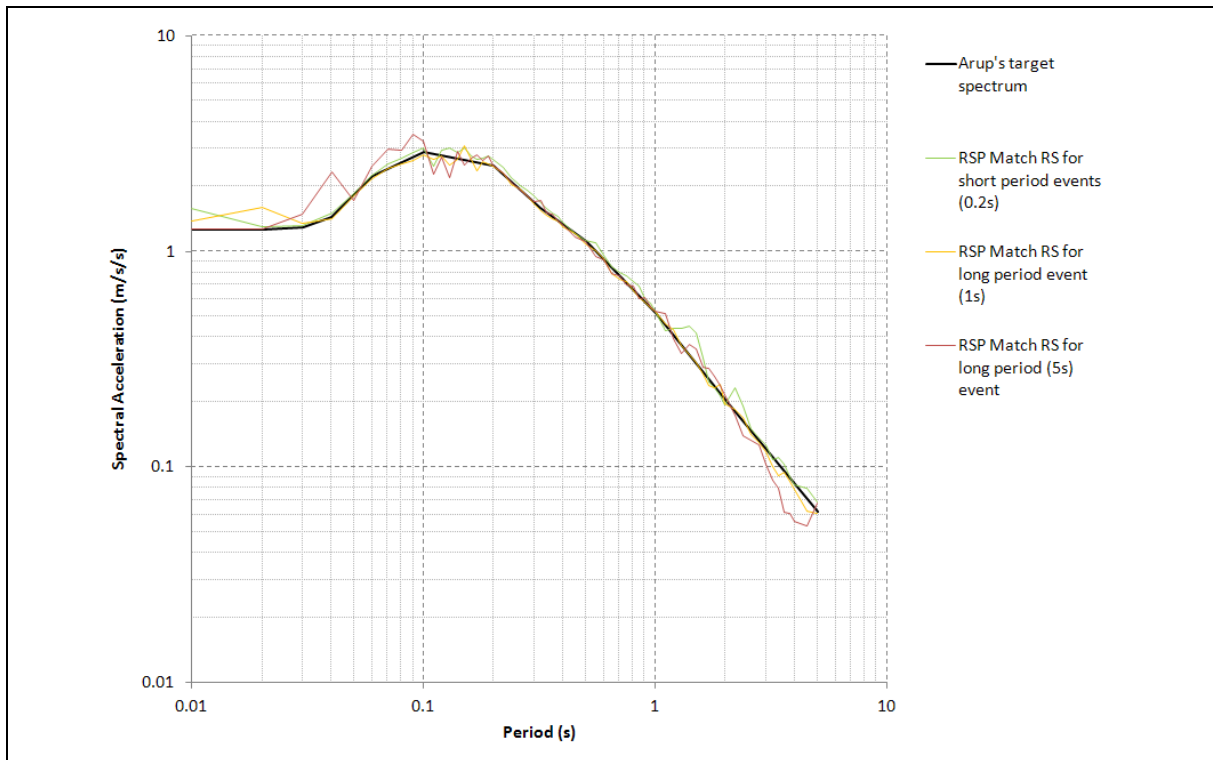
Figure 3.9   30 m Crest Height Target Matched Spectra of 1.4 Amplification Factor for 10% in 50 Years Ground Motion
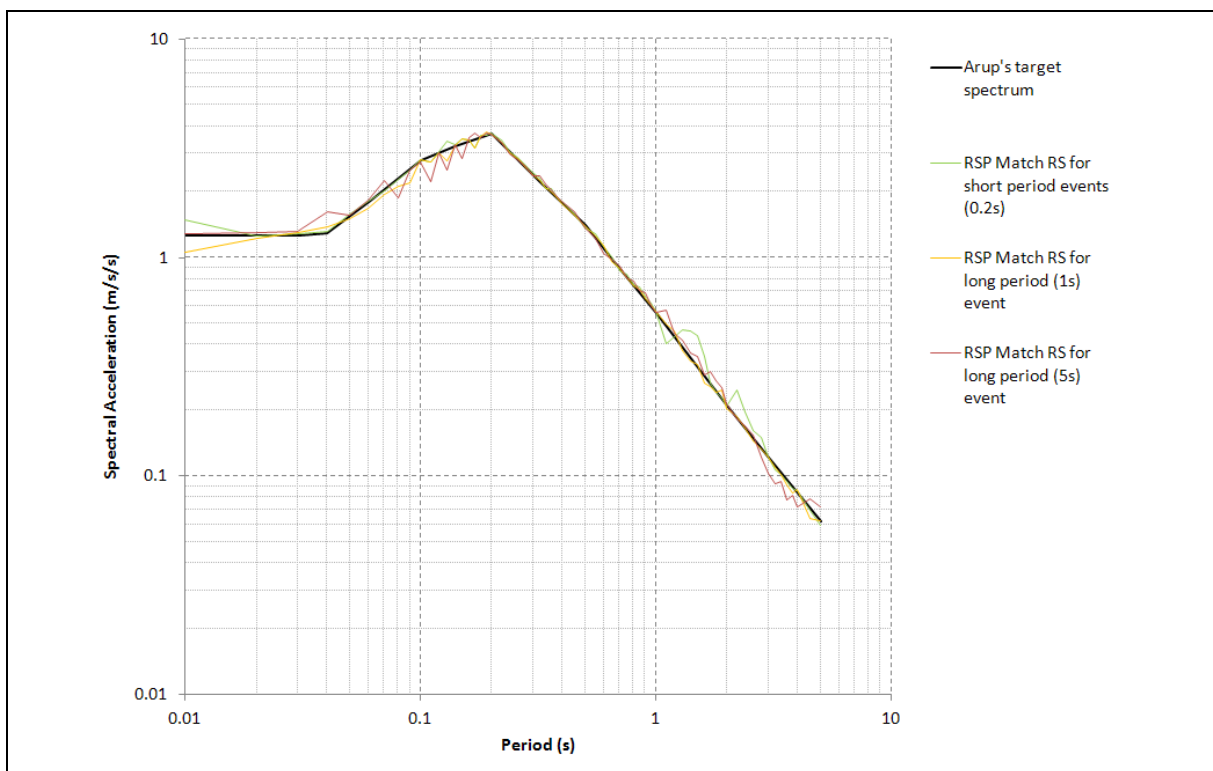
Figure 3.10   100 m Crest Height Target Matched Spectra of 1.4 Amplification Factor for 10% in 50 Years Ground Motion
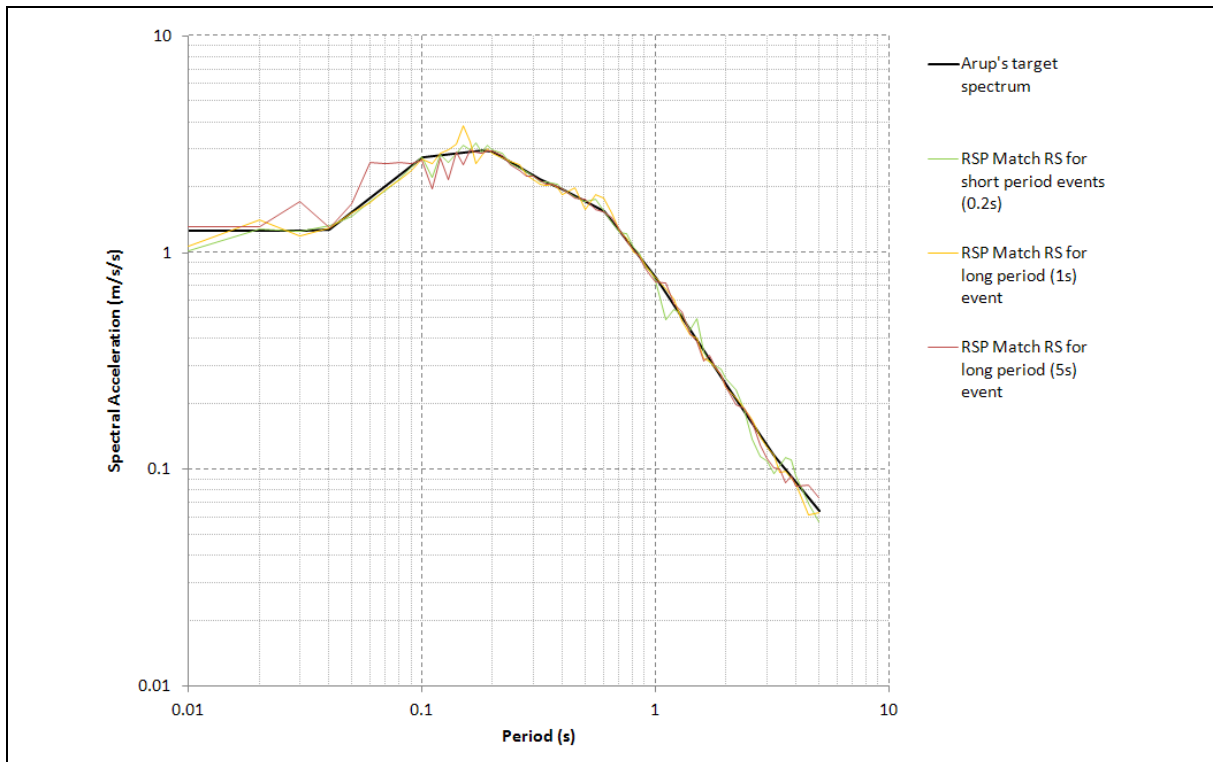
Figure 3.11 300 m Crest Height Target Matched Spectra of 1.4 Amplification Factor for 10% in 50 Years Ground Motion
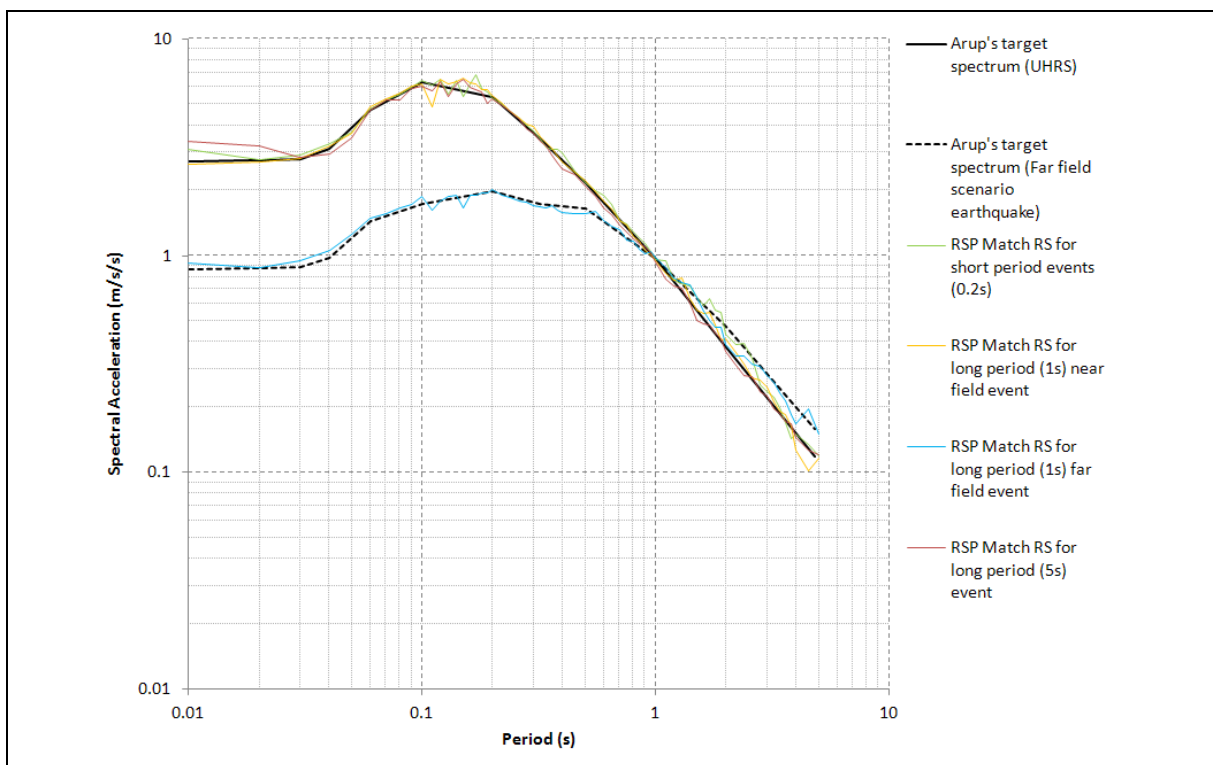
Figure 3.12 30 m Crest Height Target Matched Spectra of 1.4 Amplification Factor for 2% in 50 Years Ground Motion
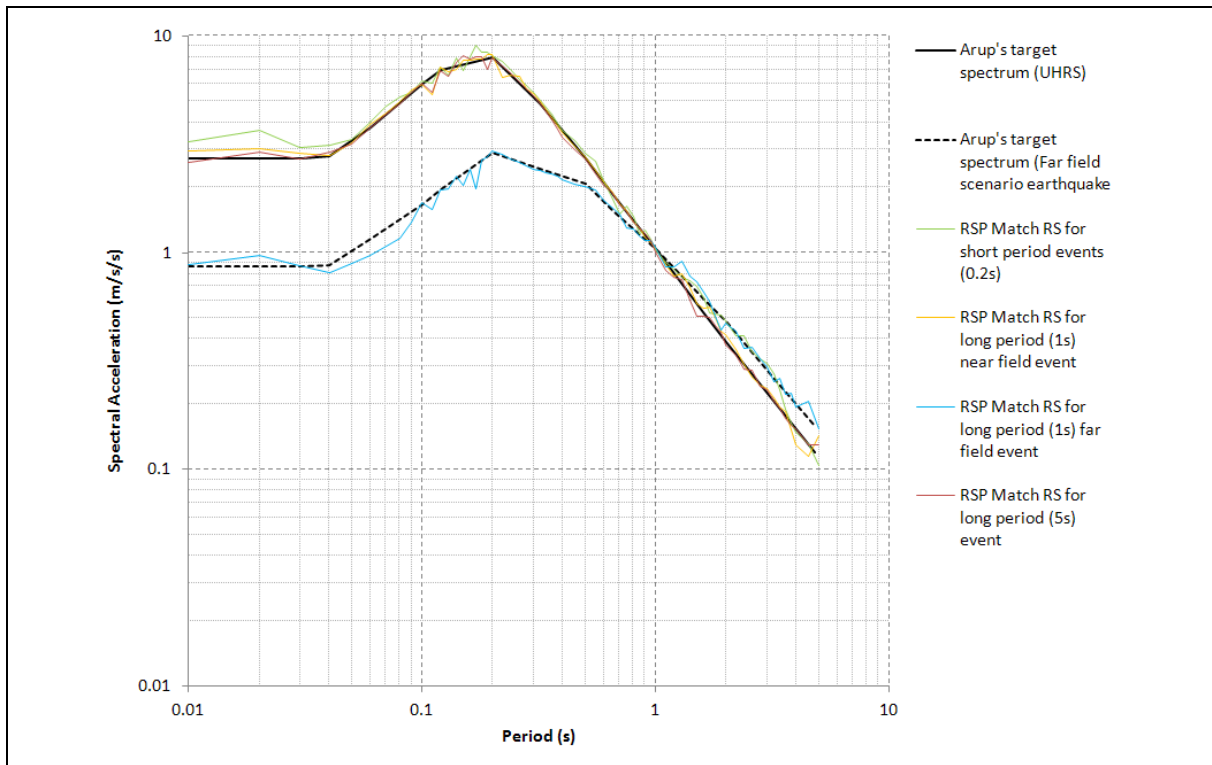
Figure 3.13 **100 m Crest Height Target Matched Spectra of 1.4 Amplification Factor for 2% in 50 Years Ground Motion**
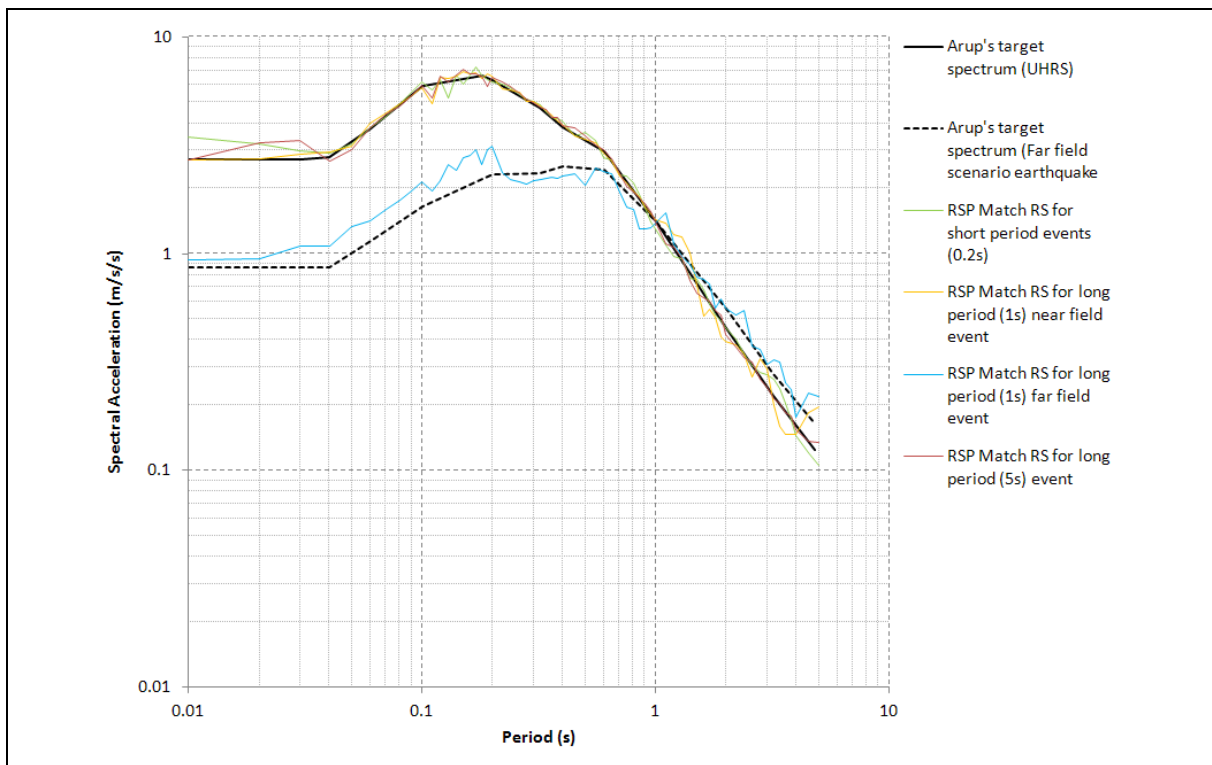
Figure 3.14 **300 m Crest Height Target Matched Spectra of 1.4 Amplification Factor for 2% in 50 Years Ground Motion**
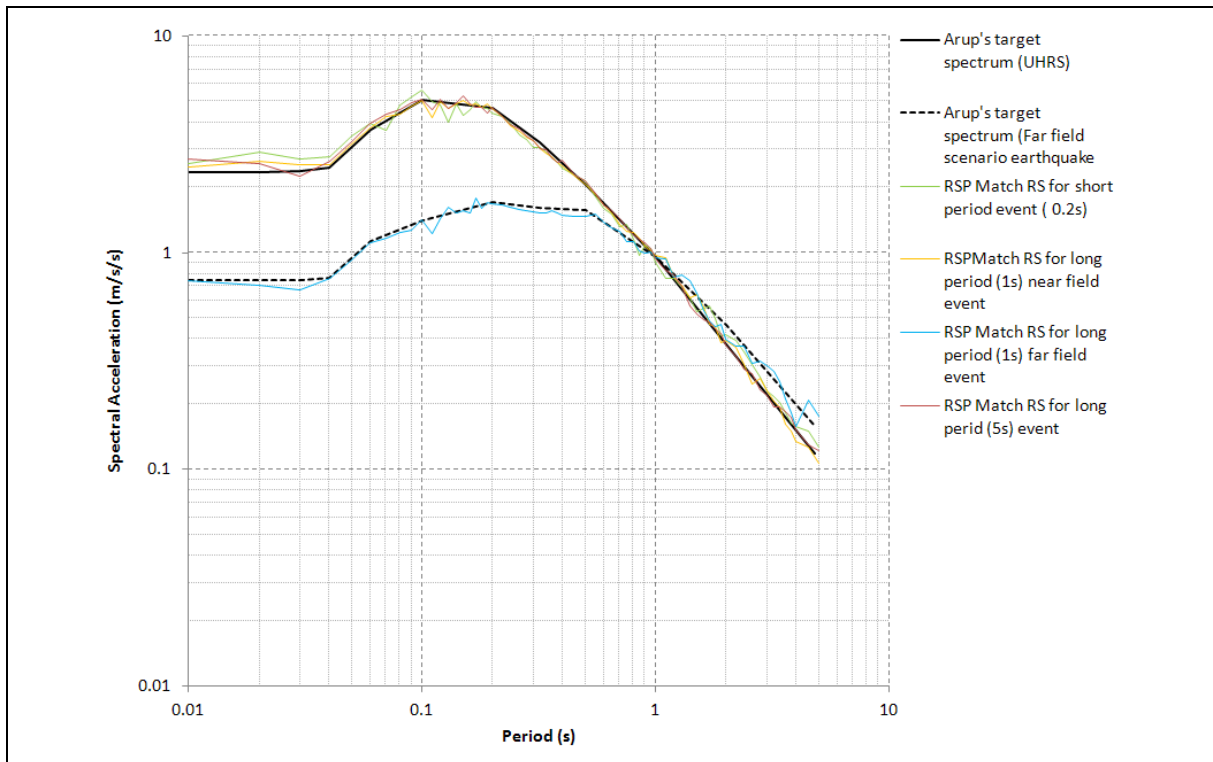
Figure 3.15 30 m Crest Height Target Matched Spectra of 1.2 Amplification Factor for 2% in 50 Years Ground Motion
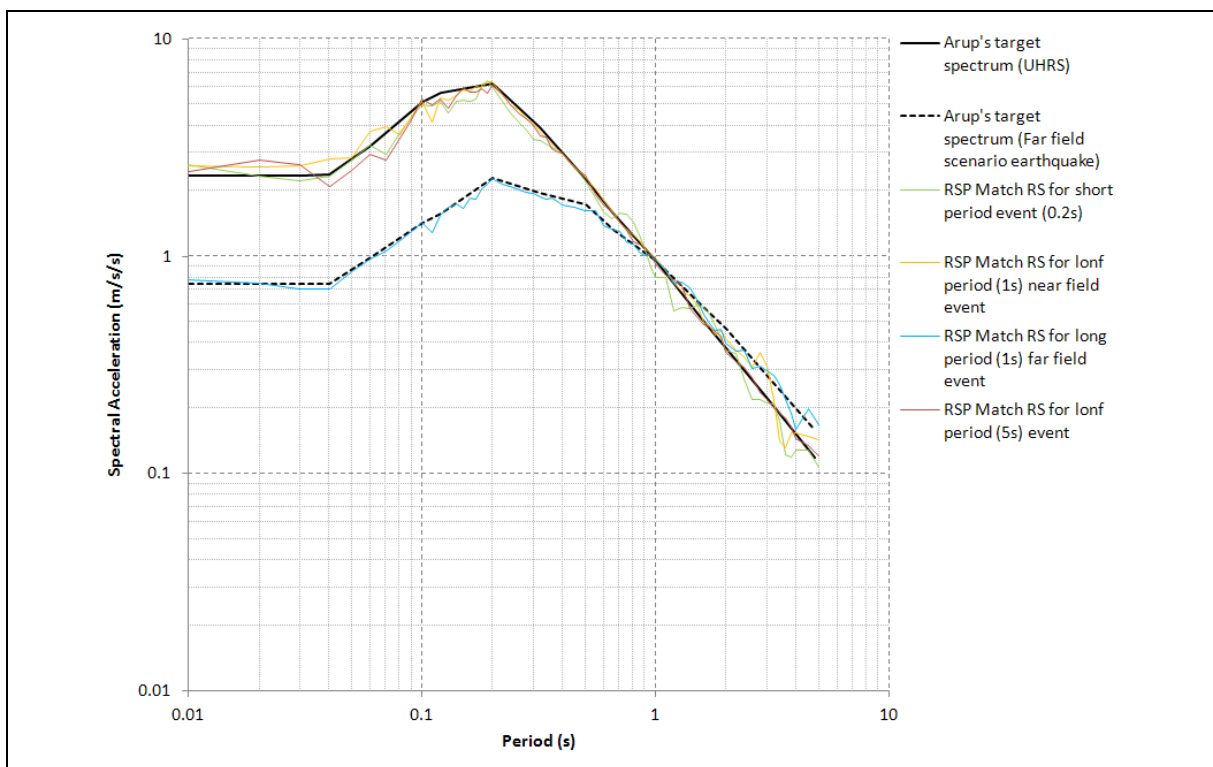
Figure 3.16 100 m Crest Height Target Matched Spectra of 1.2 Amplification Factor for 2% in 50 Years Ground Motion
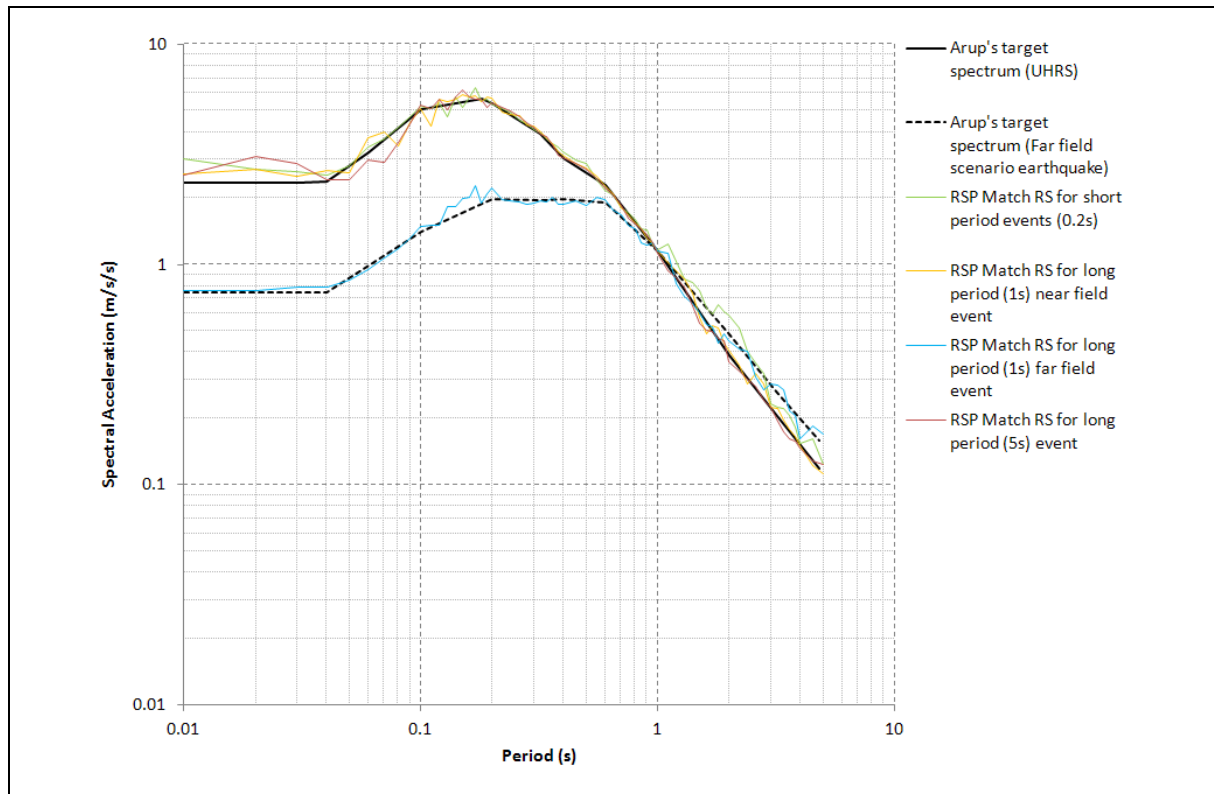
Figure 3.17   300 m Crest Height Target Matched Spectra of 1.2 Amplification Factor for 2% in 50 Years Ground Motion
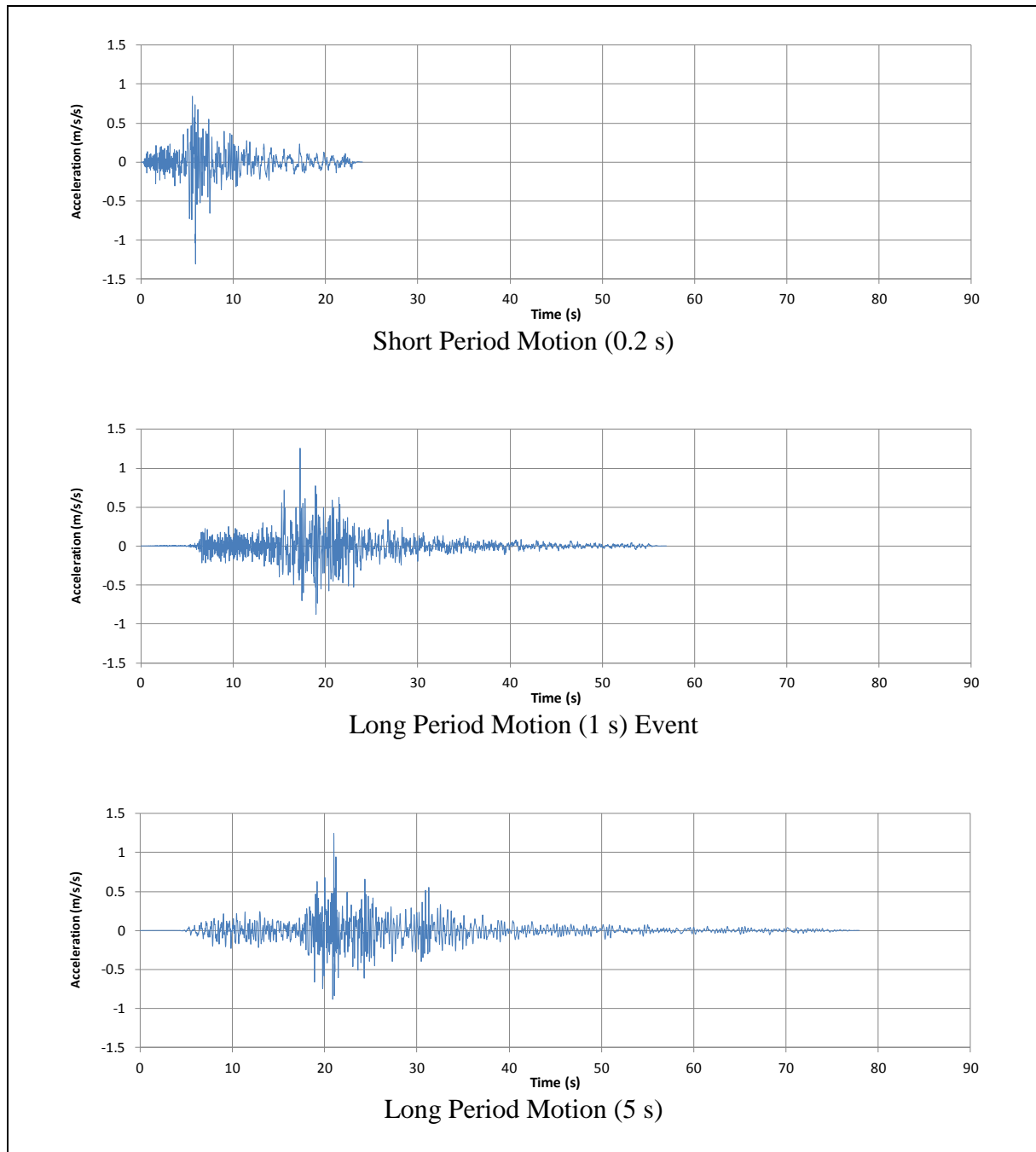
Figure 3.18   30 m Crest Spectrally Matched Time Histories of 1.4 Amplification Factor for 10% in 50 Years Ground Motion

Short Period Motion (0.2 s)

Long Period Motion (1 s) Event

Long Period Motion (5 s)
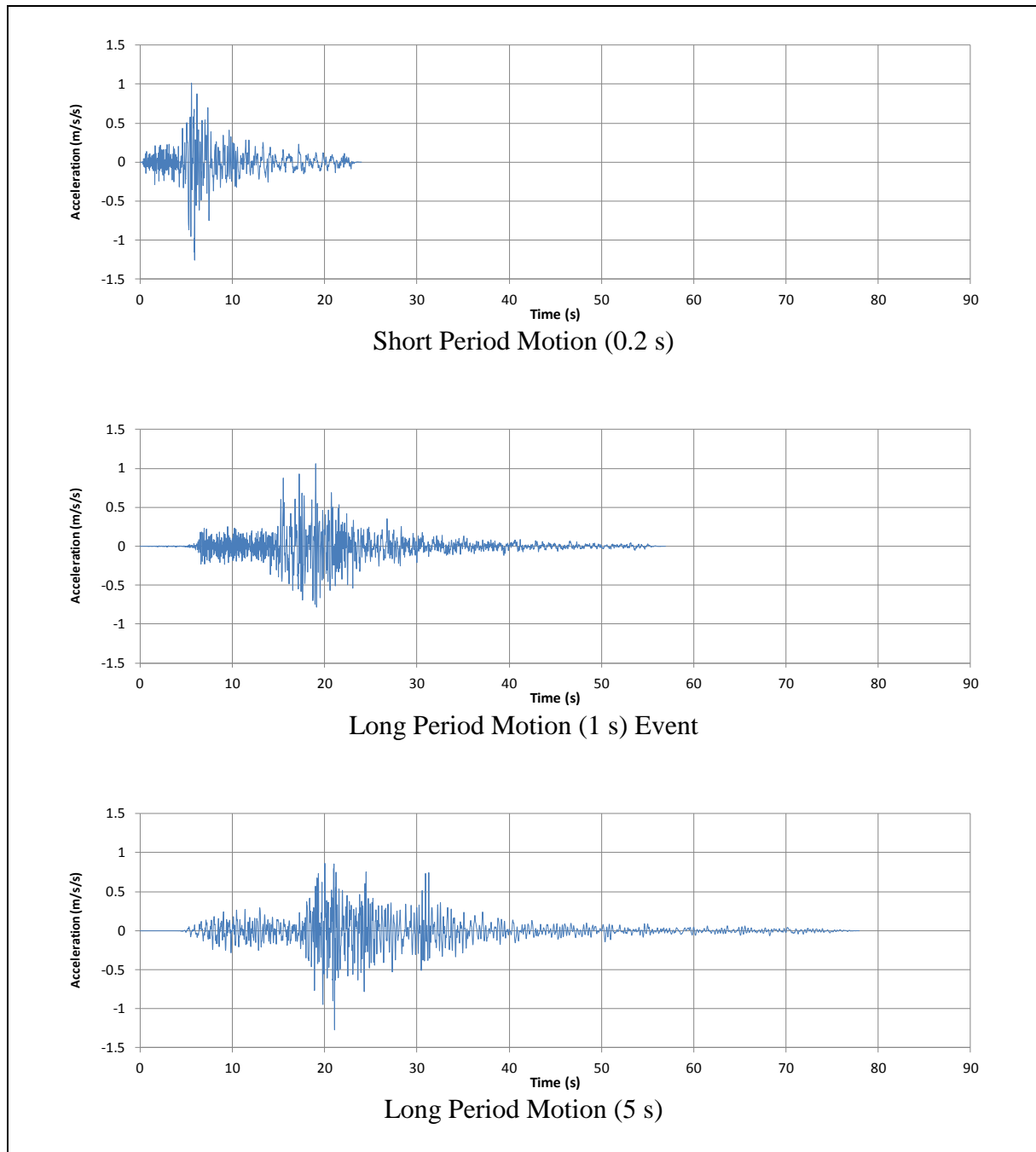
Figure 3.19   100 m Crest Spectrally Matched Time Histories of 1.4 Amplification Factor for 10% in 50 Years Ground Motion
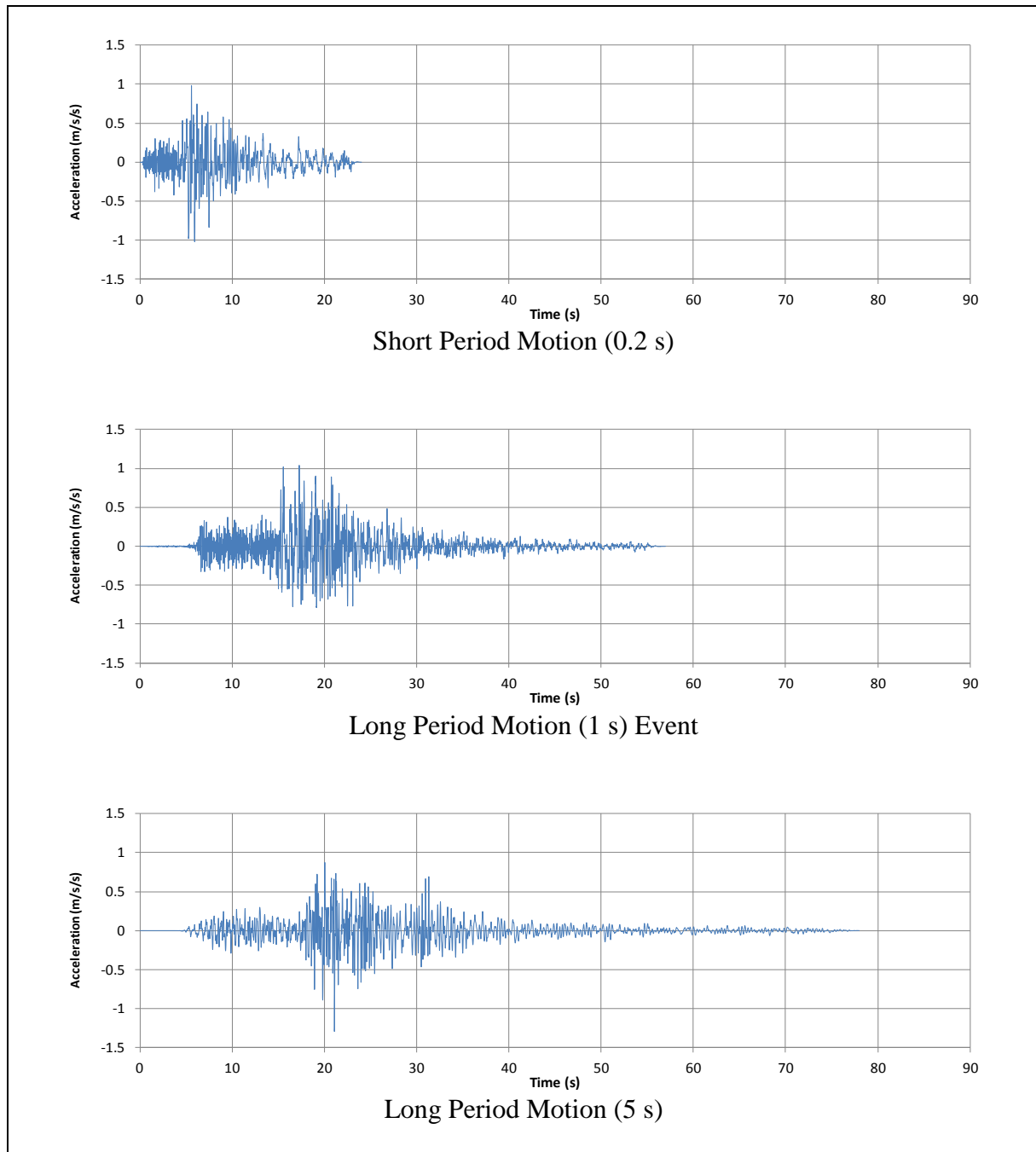
Figure 3.20   300 m Crest Spectrally Matched Time Histories of 1.4 Amplification Factor for 10% in 50 Years Ground Motion
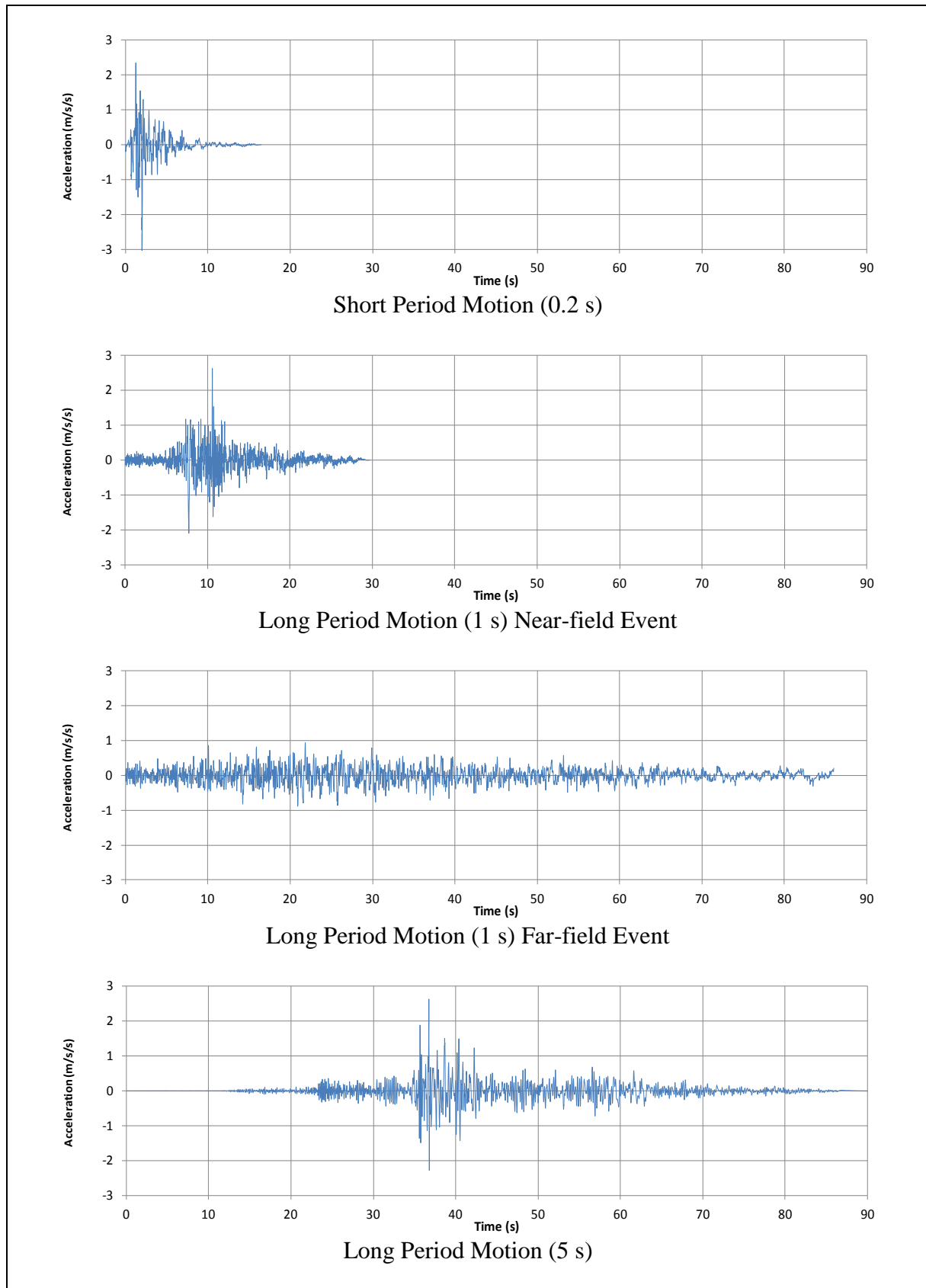
Figure 3.21   30 m Crest Spectrally Matched Time Histories of 1.4 Amplification Factor for 2% in 50 Years Ground Motion
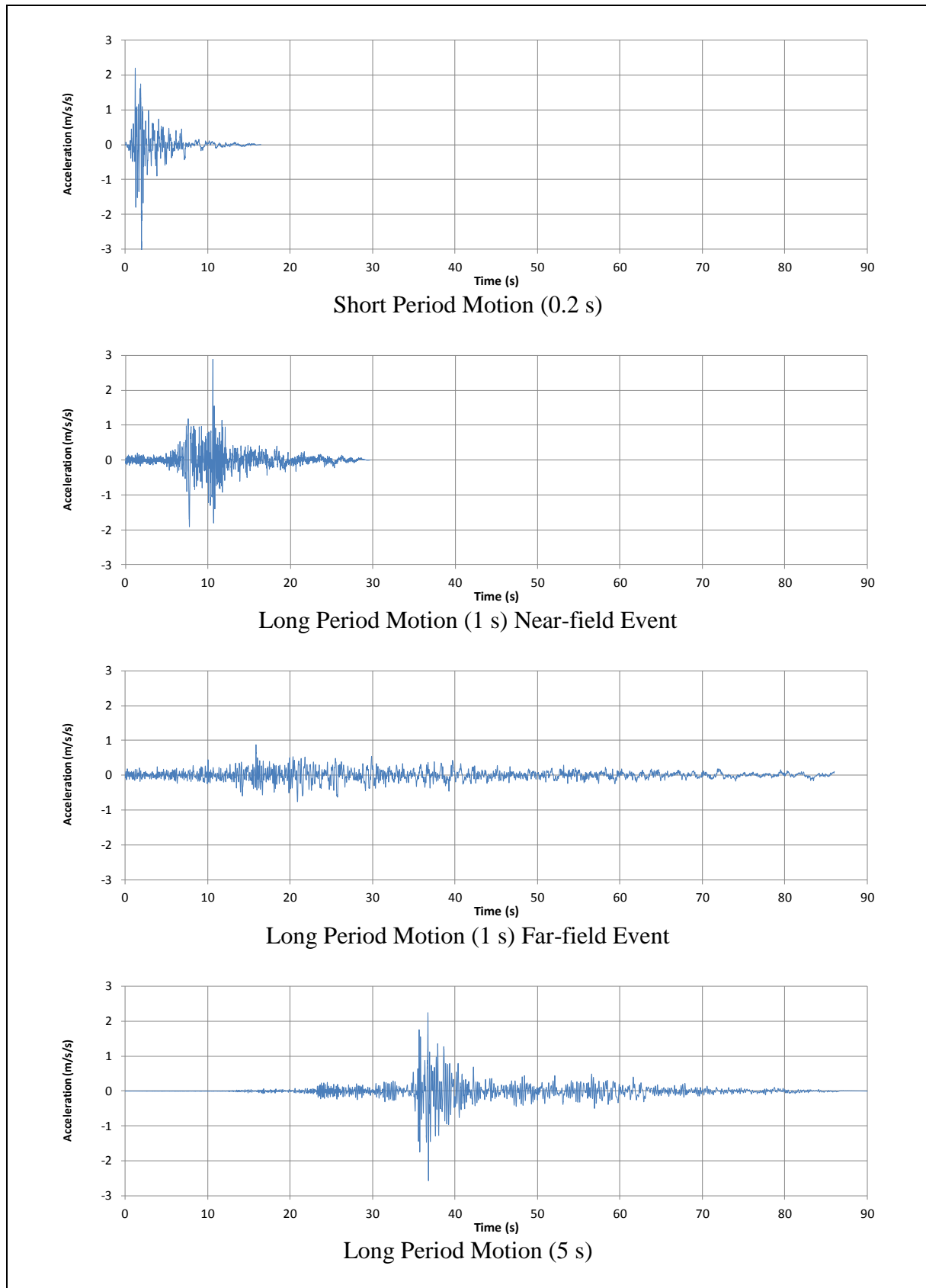
Figure 3.22   **100 m Crest Spectrally Matched Time Histories of 1.4 Amplification Factor for 2% in 50 Years Ground Motion**
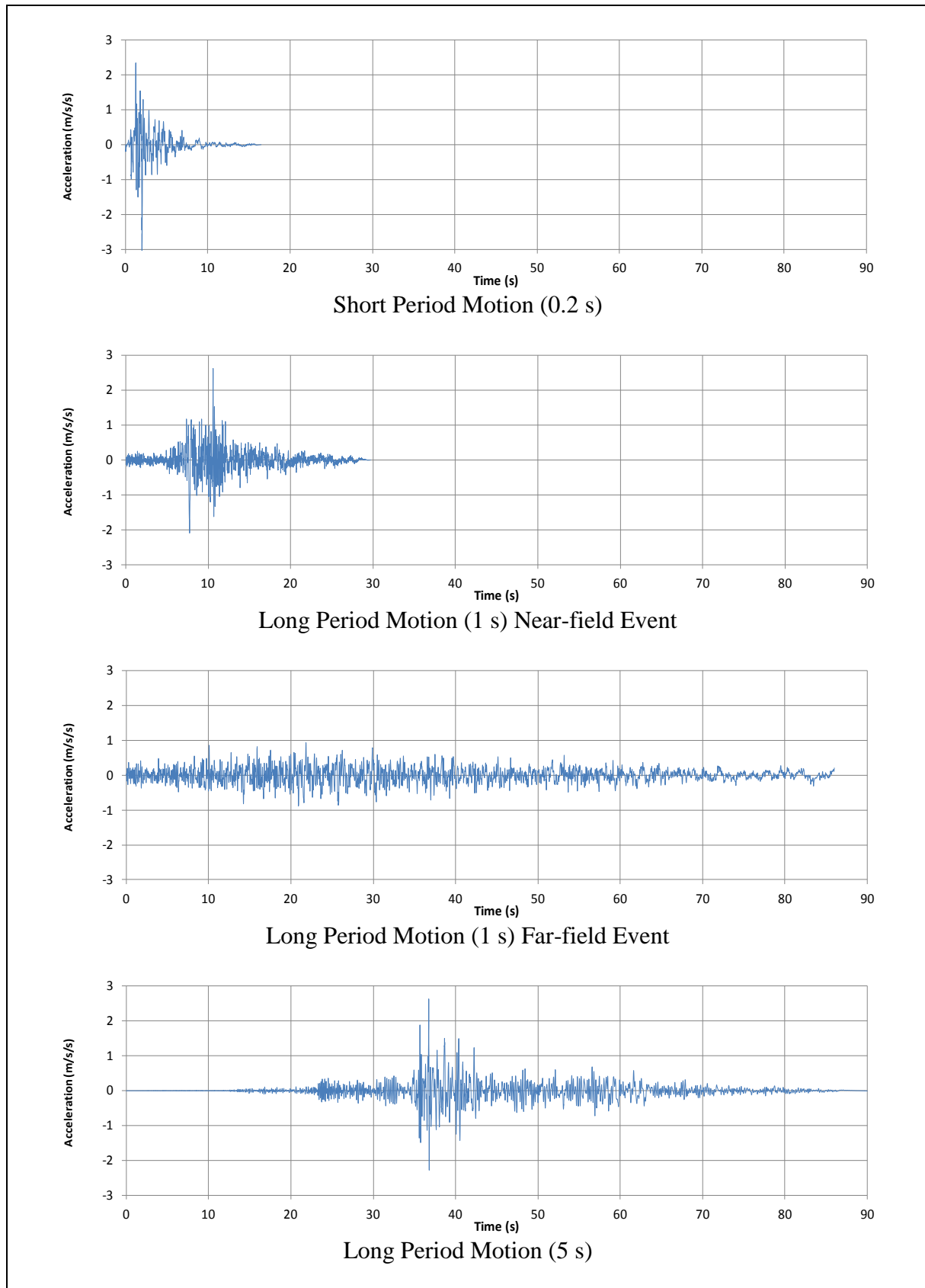
Figure 3.23   300 m Crest Spectrally Matched Time Histories of 1.4 Amplification Factor for 2% in 50 Years Ground Motion
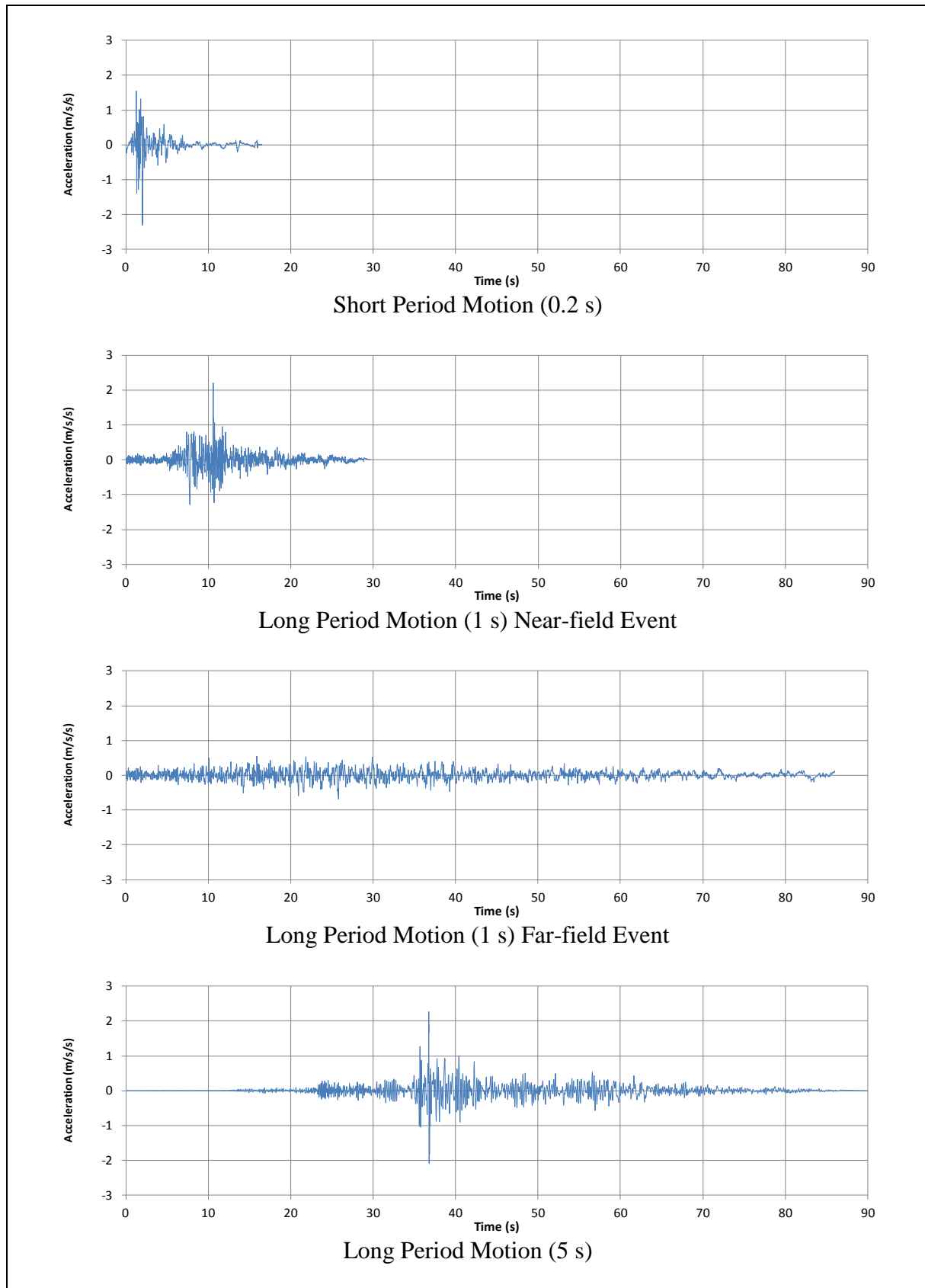
Figure 3.24   30 m Crest Spectrally Matched Time Histories of 1.2 Amplification Factor for 2% in 50 Years Ground Motion
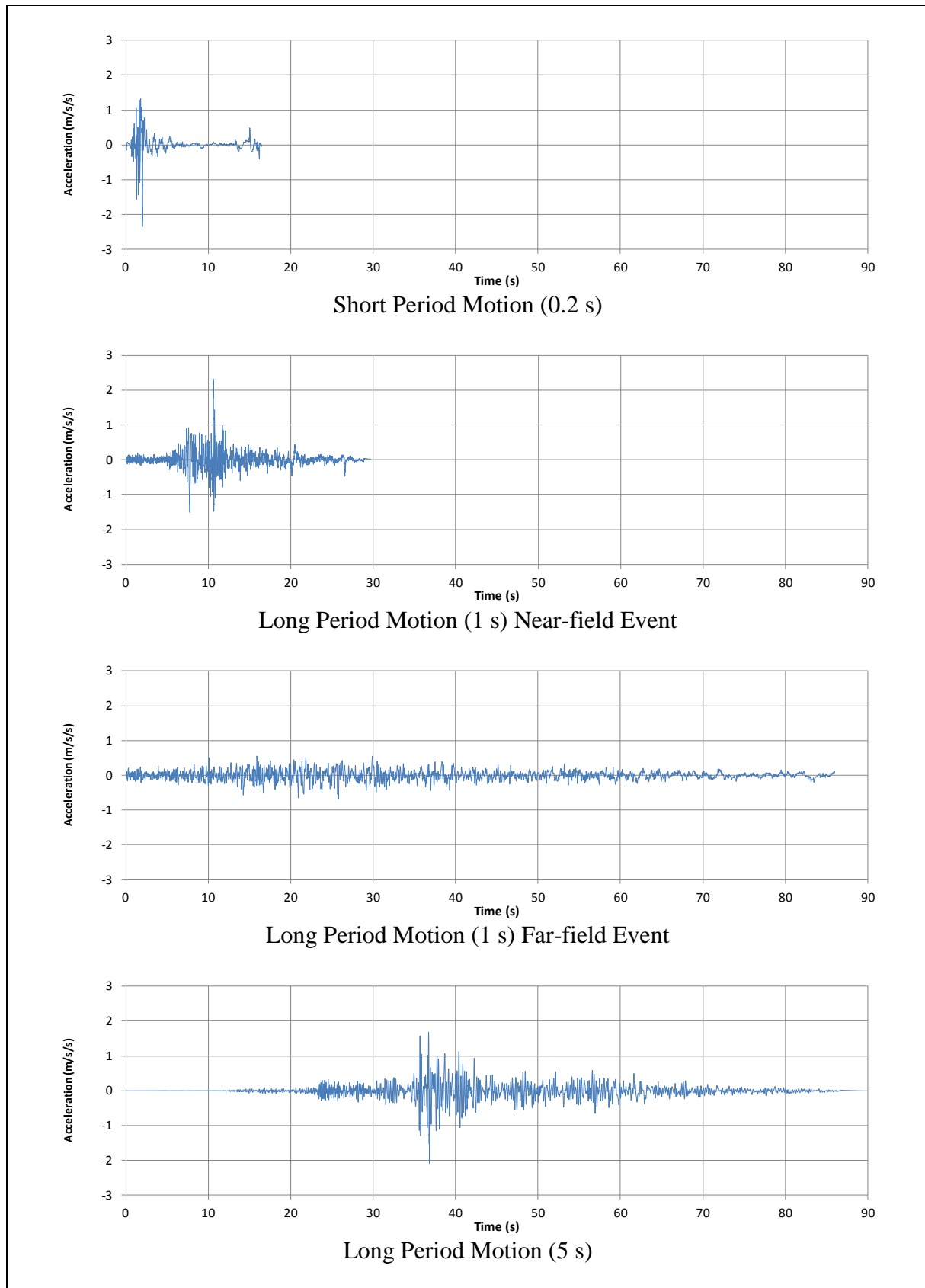
Figure 3.25   100 m Crest Spectrally Matched Time Histories of 1.2 Amplification Factor for 2% in 50 Years Ground Motion
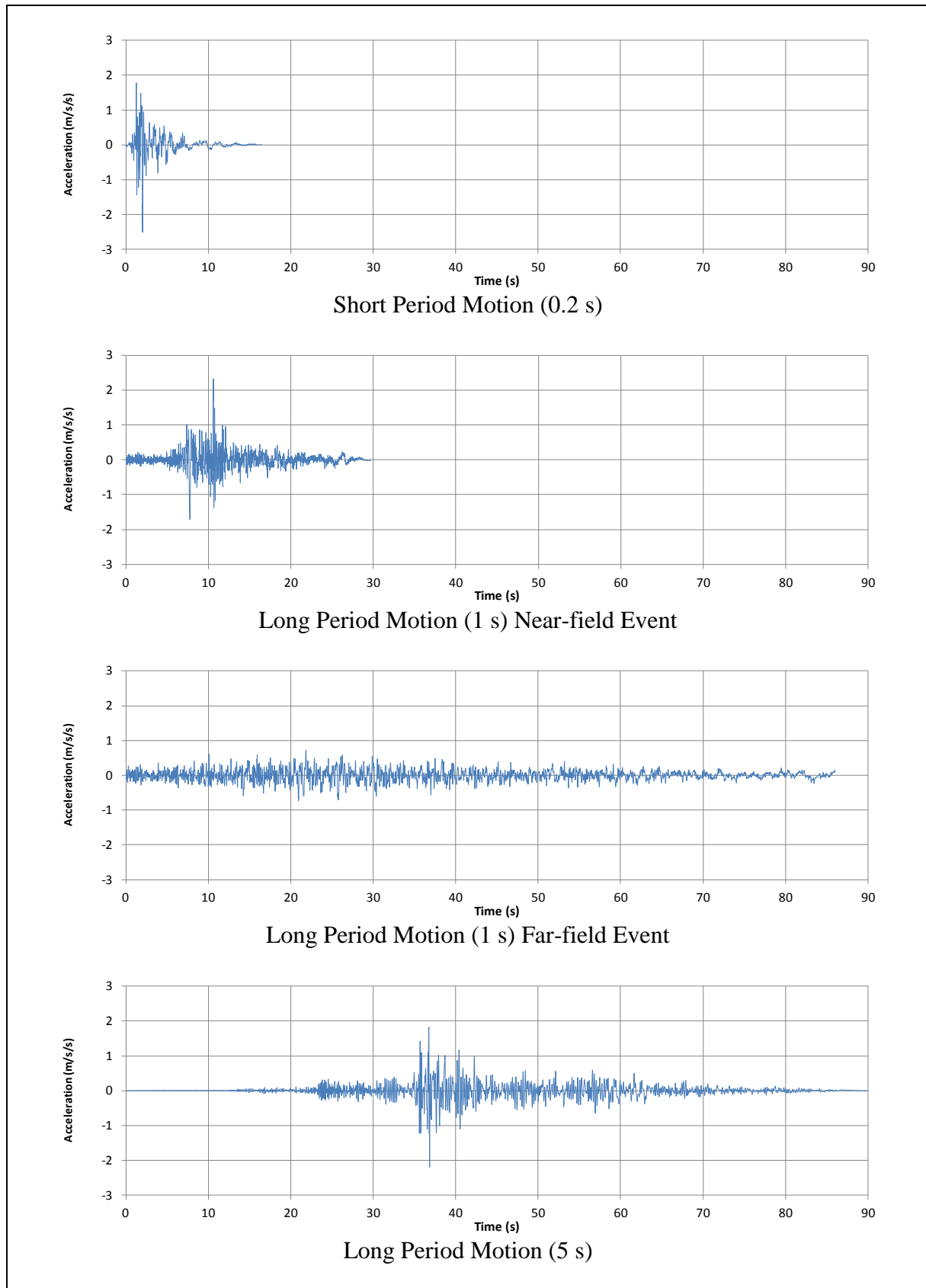
Figure 3.26   300 m Crest Spectrally Matched Time Histories of 1.2 Amplification Factor for 2% in 50 Years Ground Motion

3.2.3 Vertical Ground Motion

Attenuation equations specific for vertical ground motions are relatively scarce. Two recently published period-dependent spectral ratios between vertical and horizontal ground motions (*V/H*) are shown in Figure 3.27. The *V/H* ratio used as a basis to develop the vertical target response spectrum has been derived as the mean curve of those two curves plotted in Figure 3.27. The derived vertical target response spectrum is illustrated in Figure 3.28. The corresponding spectrally matched time histories (see Figure 3.29) have been generated from the vertical acceleration records of the same earthquake events as the ones selected for the 2% in 50 years horizontal ground motions for the periods of 0.2 s, 1 s (near-field) and 5 s.
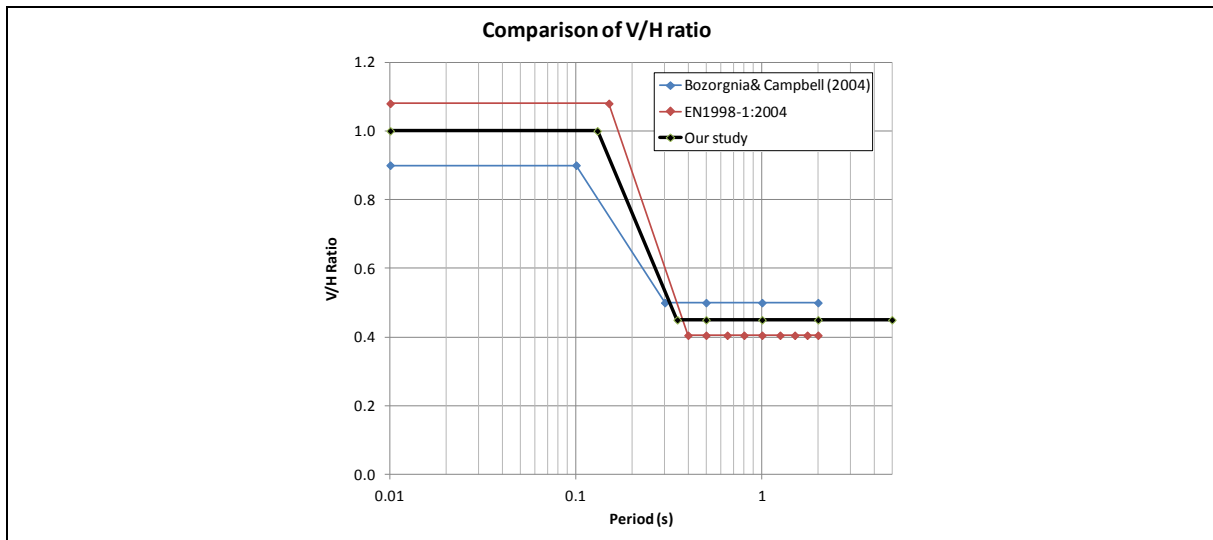
Figure 3.27   Spectral Ratio of Horizontal Ground Motion to Vertical Ground Motion
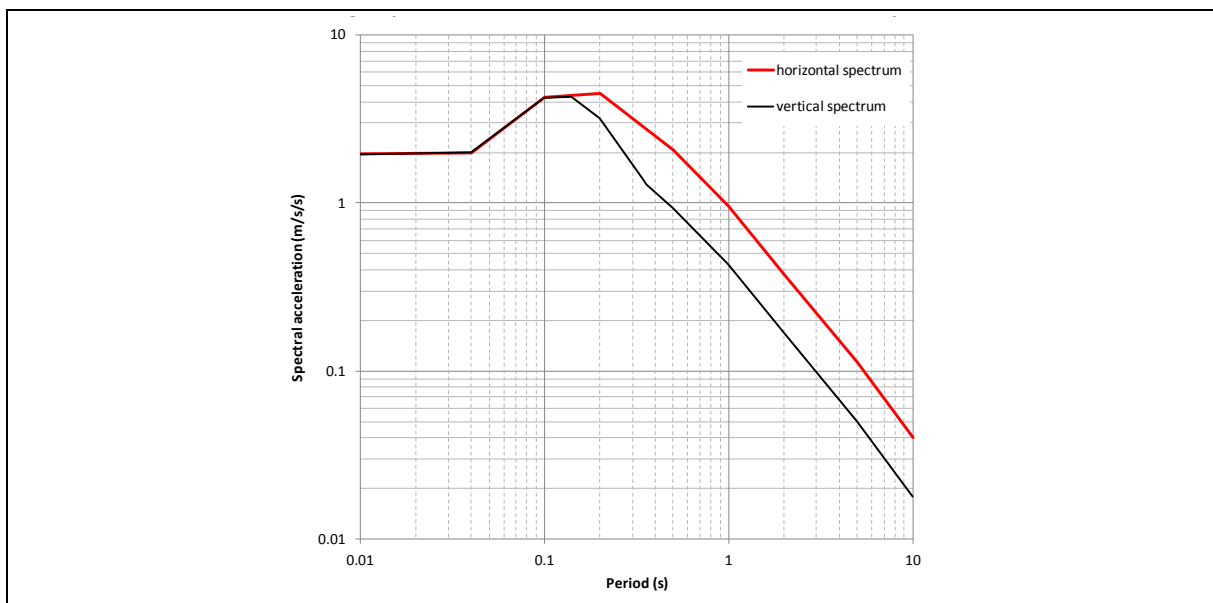
Figure 3.28   Target Response Spectra for Horizontal and Vertical 2% in 50 Years Ground Motion
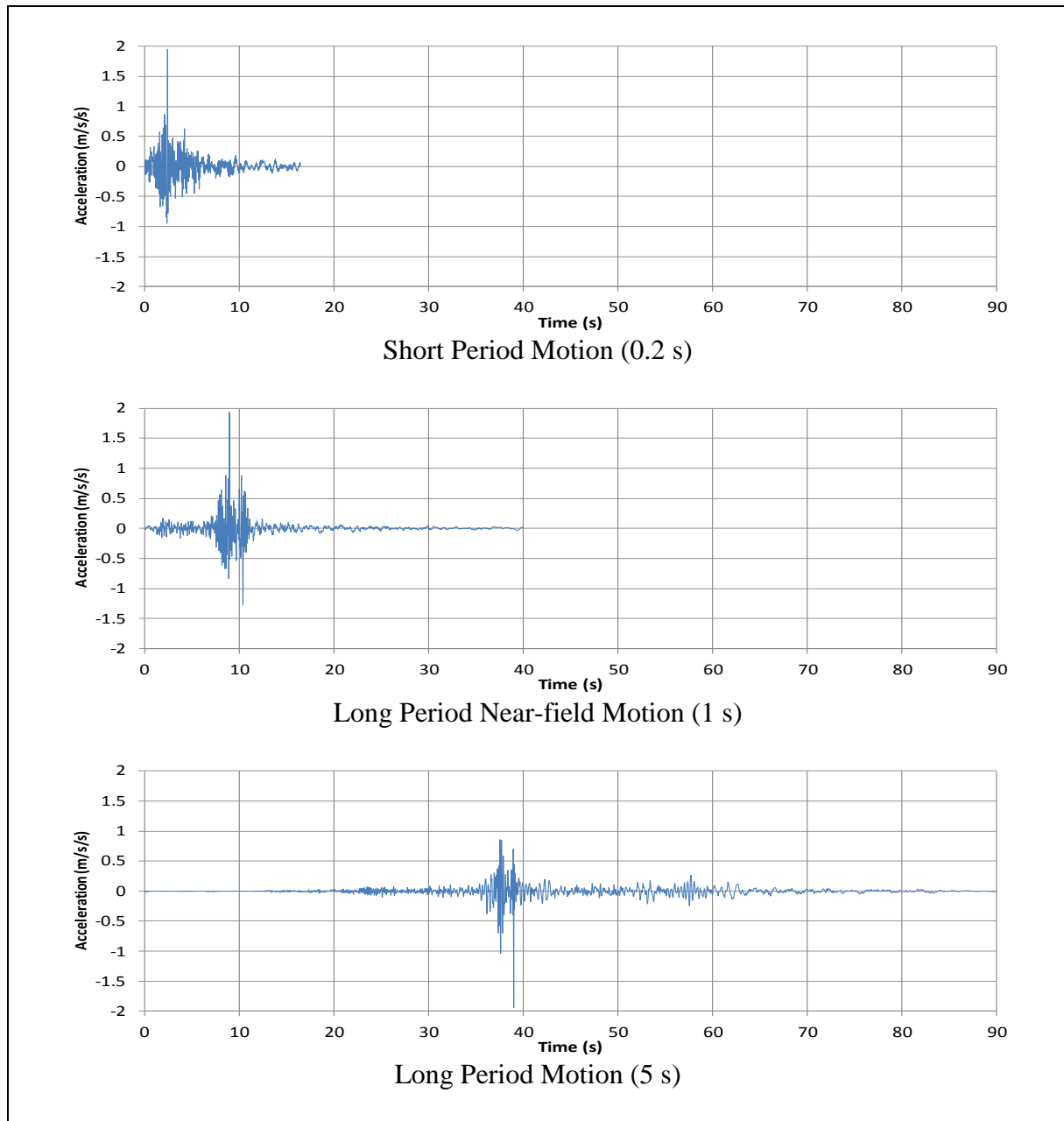
Figure 3.29   Spectrally Matched Time Histories for Vertical 2% in 50 Years Ground Motion

3.3   Numerical Modelling

One-dimensional and two-dimensional numerical modelling have been carried out using *Oasys* SIREN and dynamic FLAC respectively to calculate the downslope displacements of a shallow slope subjected to seismic ground motions.   The time histories described in Section 3.2 have been used as the input ground motions.   The shear strength of soils has also been considered.   Both analyses have adopted a high small strain shear stiffness that degrades with cyclic shear strain and generates hysteretic damping.   A small amount of viscous damping (0.5%) has been assigned to the soils in the analyses.   More details are described as follows.

3.3.1 One-dimensional Modelling by *Oasys* SIREN

The program *Oasys* SIREN has been used to perform a one-dimensional dynamic slope stability analysis. It is a finite difference program that analyses the horizontal response of a one-dimensional soil column subjected to a seismic ground motion at its base. The program has the advantage of modelling a system that is stronger in one direction than the other. As such, it has been used to simulate an infinite slope.

In this method, the maximum undrained shear strength, c, of the slope (with a given static FoS) is set by limiting the maximum stress level in the shear modulus degradation curve in the soil layer at a shallow depth. The back-calculated c-value is used to match a target static FoS for CDG at 2.5 m below ground level. The strength in the opposite direction is set to be ten times of this value. By inputting the earthquake time history in the model, permanent downslope displacements would automatically occur when the soil strength is exceeded.

The following equation shows the correlation between the maximum undrained shear strength of a slope and the static FoS for different soil thicknesses and slope angles:

$$\text{FoS} = \left(\frac{c}{\gamma h \cos \alpha \ \sin \alpha}\right) \dots\dots\dots\dots\dots\dots\dots\dots\dots\dots\dots(3.1)$$

where c = undrained shear strength of the soil
                 γ = unit weight of soil
                 h = depth of failure surface
                 α = slope angle.

In the analysis, a soil thickness of 2.5 m with slope angles of 20°, 30° and 40° have been modelled using different undrained shear strengths. The critical acceleration corresponding to this FoS is:

$$A_c = g \ (\text{FoS} - 1) \sin \alpha \dots\dots\dots\dots\dots\dots\dots\dots\dots\dots\dots(3.2)$$

where g = gravitational acceleration.

The topographic effect has also been considered using the time histories with topographic amplification described in Section 3.2.2.

3.3.2 Two-dimensional Modelling by Dynamic FLAC

The dynamic analysis option of FLAC Version 6.0 has been used to undertake two-dimensional fully non-linear dynamic analyses. It adopts explicit finite differences to solve equations of motion using lumped grid point masses derived from the density of surrounding zones. FLAC assumes a free-field boundary to prevent waves being reflected from the lateral boundaries of the model. The hysteretic damping model has also been used to account for the non-linear shear modulus degradation effect. A SHAKE type de-convolution analysis has been carried out to determine suitable input ground motions at depth within the bedrock.

In the model, a 30° soil slope with 10 m slope height is covered by a 2.5 m thick layer

of CDG (Figure 3.30). The CDG has been assigned with a shear modulus degradation curve according to Arup (2018). A shear wave velocity (V_S) of 300 m/s, which is equivalent to a SPT-N value of about 50 (based on the empirical correlation between V_S and SPT-N value of CDG presented in Arup (2018), has been used. It is also considered as a typical value for CDG in Hong Kong. The slopes having a static FoS of 1.04 and 1.10 have been modelled by assuming the shear strength of CDG as 15.8 kPa and 14.8 kPa respectively. The topographic amplification has not been considered when using this slope geometry.
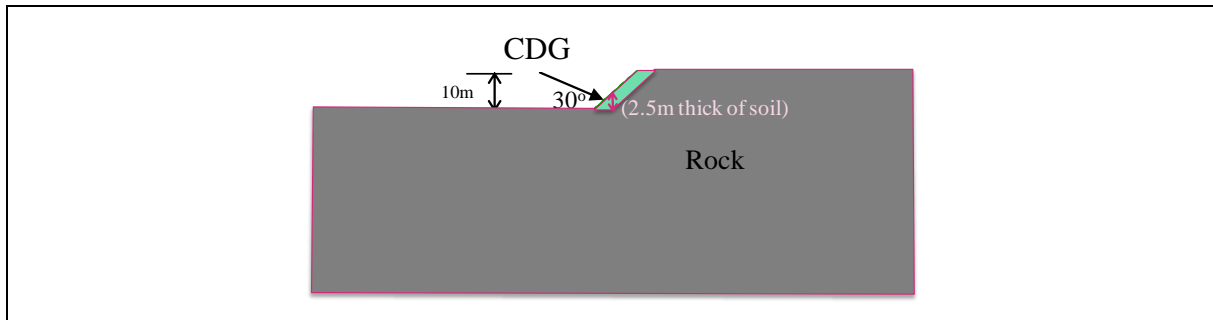
Figure 3.30 Soil Slope Modelled in FLAC

3.4 Empirical Correlations

Empirical correlations based on the simplified Newmark's method have been used to calculate the downslope displacements. In this method, time histories, which have been used to define seismic ground motions in the numerical models, could not be used. As discussed in Section 2, the Arias Intensity (I_a) has been found to correlate well to the downslope movements. This parameter has thus been adopted to represent the seismic ground motion. In addition to the simplified Newmark's method, correlations between the earthquake magnitudes and distances as well as the landslide occurrence have been used to evaluate the landslide likelihood in the Study Area for the earthquake scenarios derived from the probabilistic seismic hazard assessment (PSHA) as presented in Arup (2015).

3.4.1 Magnitude-distance Relationships

As summarised in Section 2, a few magnitude-distance relationships for landslide occurrence have been established based on earthquake-induced landslide inventories carried out around the world. These correlations can be compared with the earthquake scenario combinations of magnitude and distance derived from de-aggregation (see Table 3.1).

The magnitude-distance relationships derived by Tamura (1978), Yasuda & Sugitani (1988), Keefer & Wilson (1989) and ISSMFE (1993), which were reviewed by Halcrow (2009), have been used for comparison. The relative position of the magnitude-distance combinations from the PSHA of this study on different plots provides an indication of the likelihood of earthquake-induced landslides to occur for the considered ground motions.

Halcrow (2009) concluded that a maximum credible earthquake of magnitude between

6.5 and 7.5 could be envisaged, with an epicentre at the Dangan Islands (around 30 km away from Hong Kong). This event has been considered in the present analysis for the scenario earthquake (short period of 0.2 s) for 10% in 50 years ground motion.

The results based on the magnitude-distance combinations from the PSHA of this study or Dangan Islands scenario stated in Halcrow (2009) indicate that there is only a marginal likelihood of landslides. Based on the displacement calculations, it has been found that the static FoS is close to 1 if 100 mm is set as the threshold slope displacement. It means that earthquake-induced landslides are unlikely to occur except when the slope, at its initial state, is very close to failure.

3.4.2 Simplified Newmark's Method

Based on the literature review summarised in Section 2, the empirical correlations proposed by Jibson et al (1998) and Hsieh & Lee (2011) have been selected to calculate the Newmark displacements using the critical acceleration (A_c) of slopes and the Arias Intensity (I_a) of seismic ground motions. A_c, which represents the frictional resistance of a slope, can be calculated for a given static FoS using Equation 3.2. The selected empirical relationships for calculating the downslope displacements are summarised as follows:

(a) Jibson et al (1998)

$$\log D_n = 1.521 \log I_a - 1.993 \log A_c - 1.546 \pm 0.375 \quad \text{........................(2.14)}$$

(b) Hsieh & Lee (2011)

$$\log D_n = 0.847 \log I_a - 10.62 A_c + 6.587 A_c \log I_a + 1.84 \pm 0.295 \quad \text{..............(2.20)}$$

$$\log D_n = 0.788 \log I_a - 10.166 A_c + 5.95 A_c \log I_a + 1.779 \pm 0.294 \quad \text{.............(2.23)}$$

where D_n = Newmark downslope displacement (cm)
              I_a = Arias Intensity (m/s)
              A_c = critical acceleration (g).

Using the above correlations, the downslope displacements have been calculated and compared for different seismic ground motions.

3.4.2.1 Arias Intensity

The Arias Intensity (I_a) is a quantitative measure of the total shaking intensity which has been shown to possess remarkable correlation with the distribution of earthquake-induced landslides. It is directly related to the integral over time of the square of the ground acceleration as explained in Section 2.2.3.

Figures 3.31 and 3.32 show the I_a calculated using the original horizontal time histories for 10% and 2% in 50 years ground motions respectively. The I_a plots corresponding to the time histories modified for a PGA topographic amplification factor of 1.4 for 10% and 2% in

50 years ground motions are presented in Figures 3.33 to 3.35 and Figures 3.36 to 3.38 respectively. For the 2% in 50 years ground motions, the I_a plots corresponding to the time histories modified by a PGA topographic amplification factor of 1.2 are illustrated in Figures 3.39 to 3.41.

Short Period Motion (0.2 s)

Long Period Motion (1 s) Event

Long Period Motion (5 s)
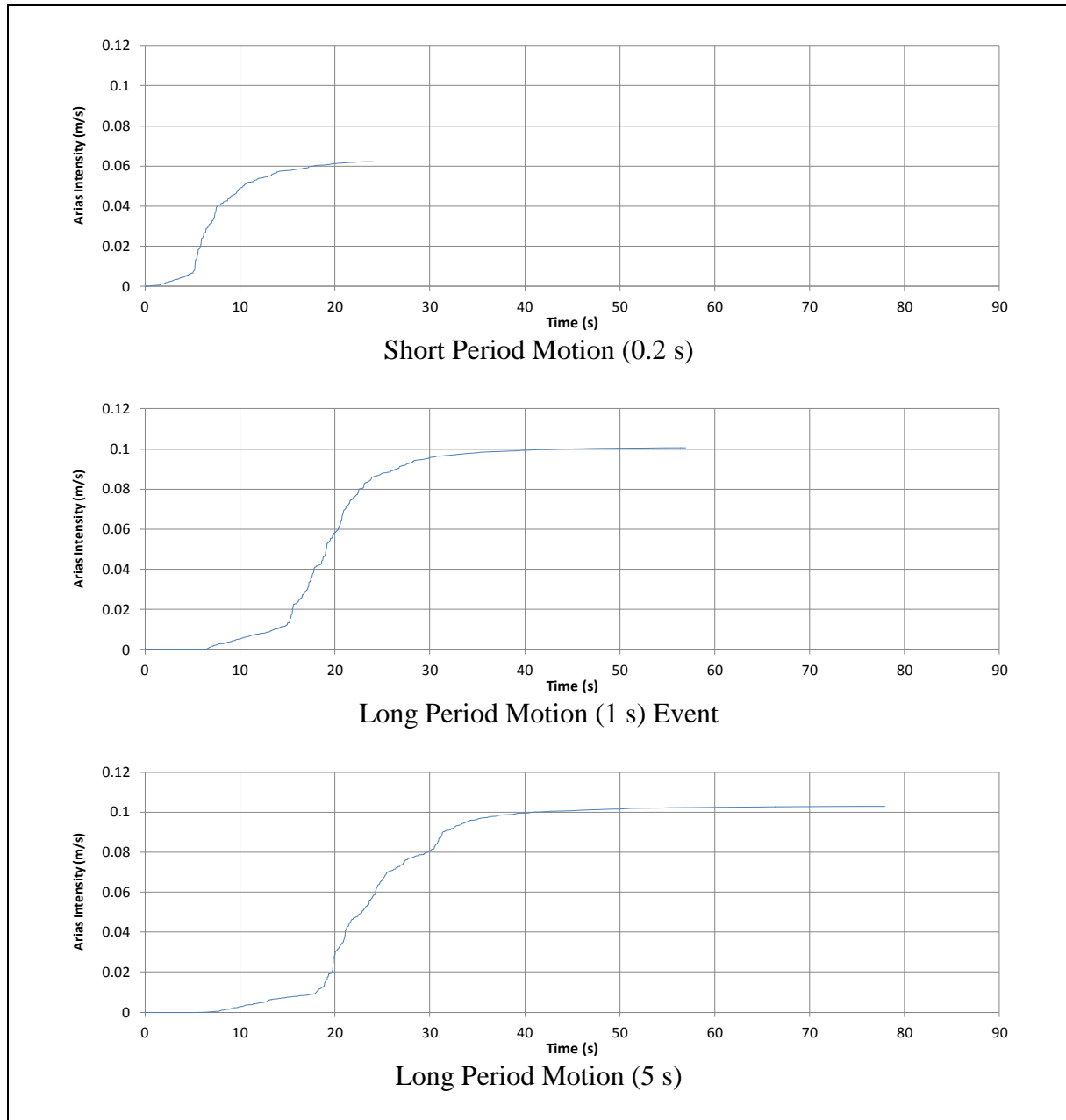
Figure 3.31   Arias Intensity for Time Histories for the 10% in 50 Years Ground Motion
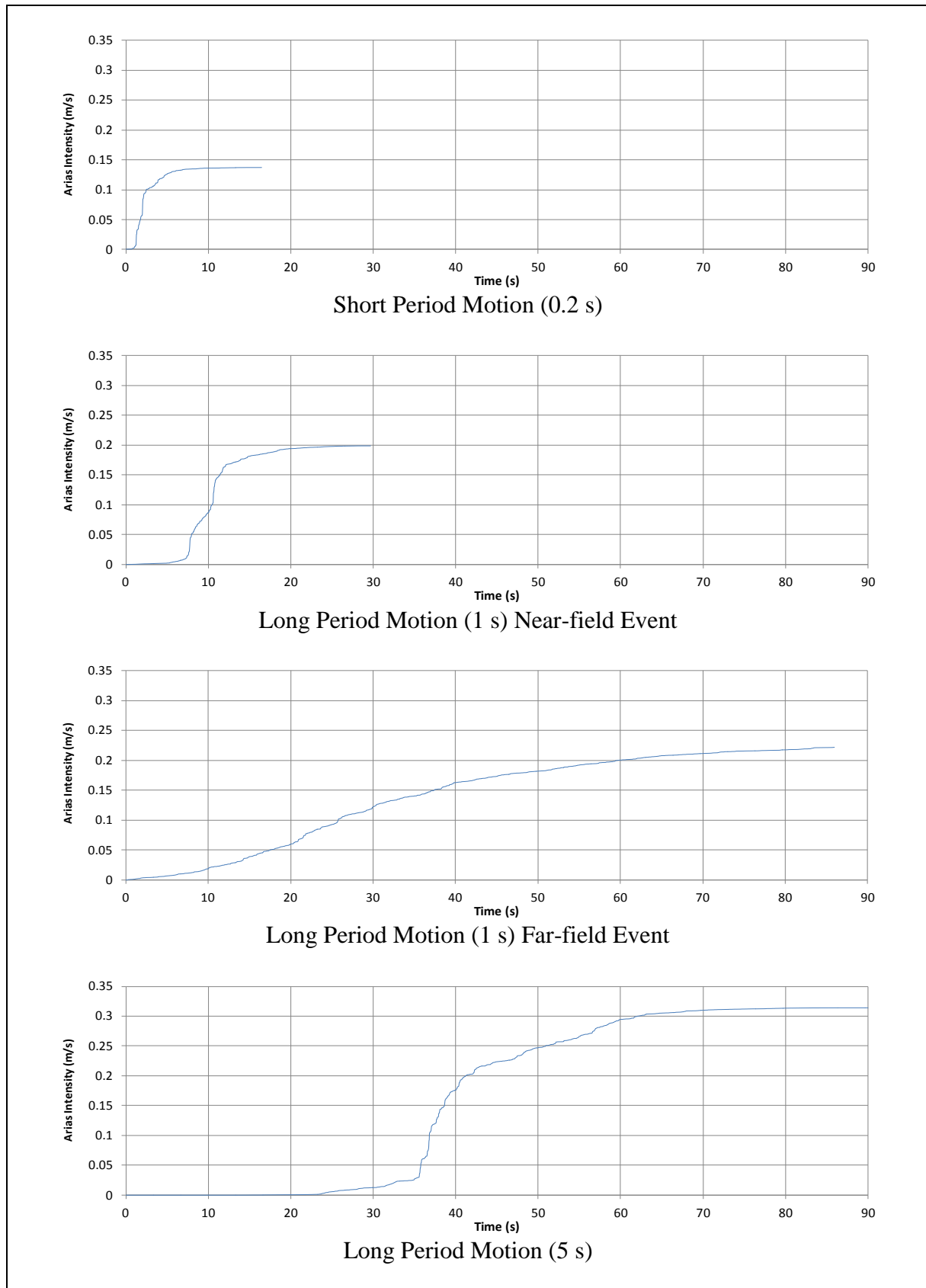
Figure 3.32   Arias Intensity for Time Histories for the 2% in 50 Years Ground Motion
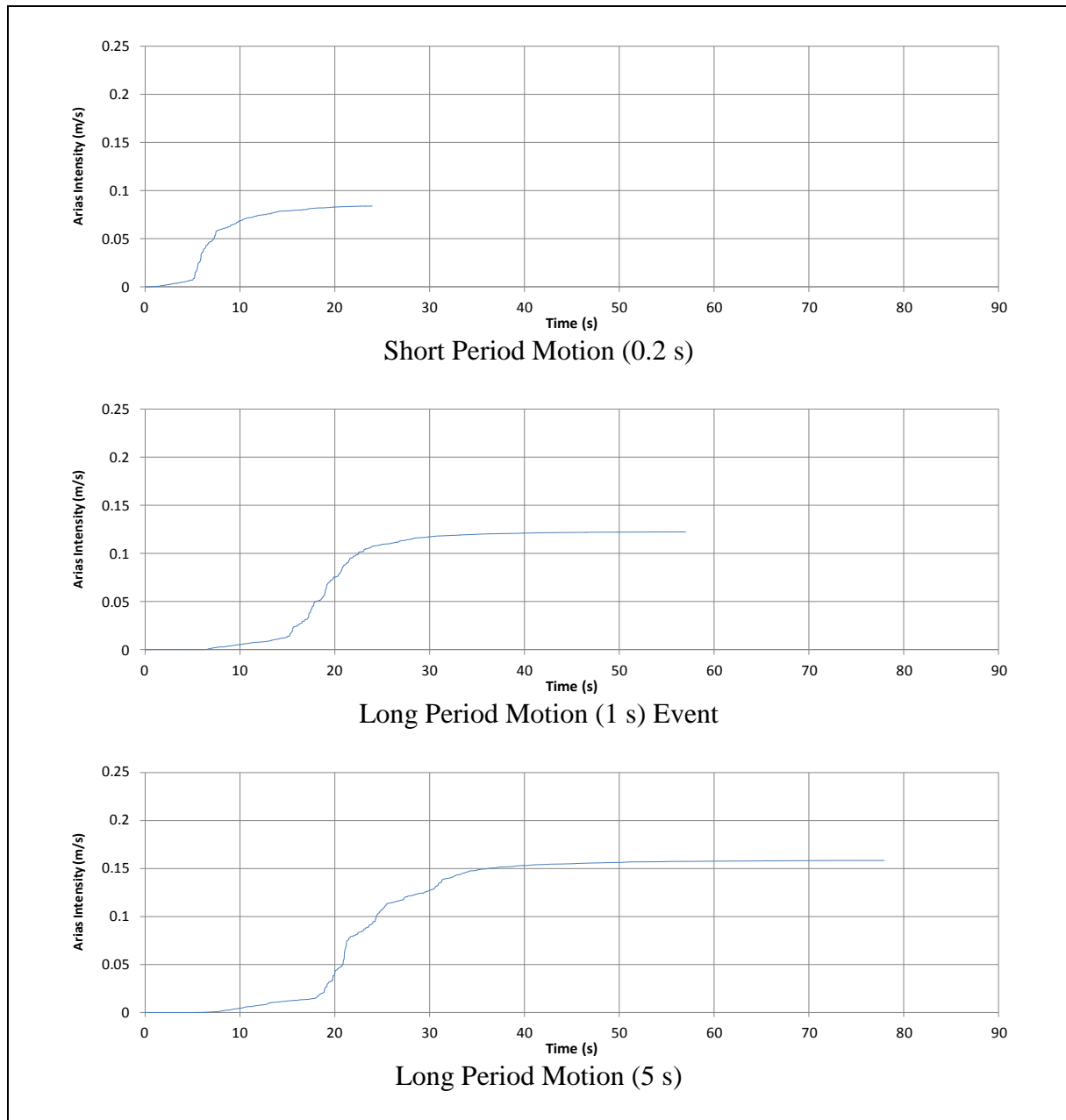
Figure 3.33 Arias Intensity for 30 m Crest Spectrally Matched Time Histories of 1.4 Amplification Factor for 10% in 50 Years Ground Motion
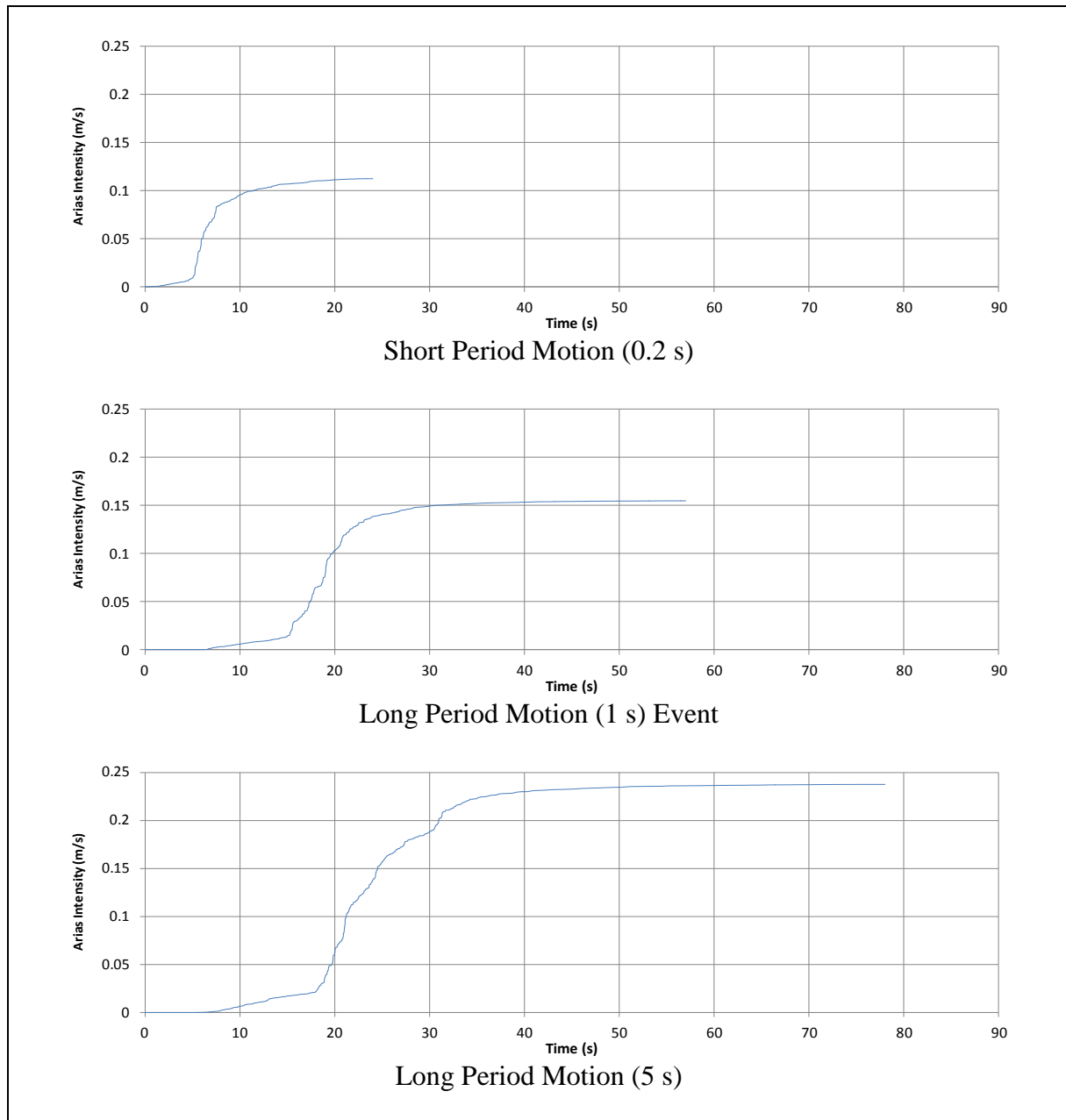
Figure 3.34   Arias Intensity for 100 m Crest Spectrally Matched Time Histories of 1.4 Amplification Factor for 10% in 50 Years Ground Motion
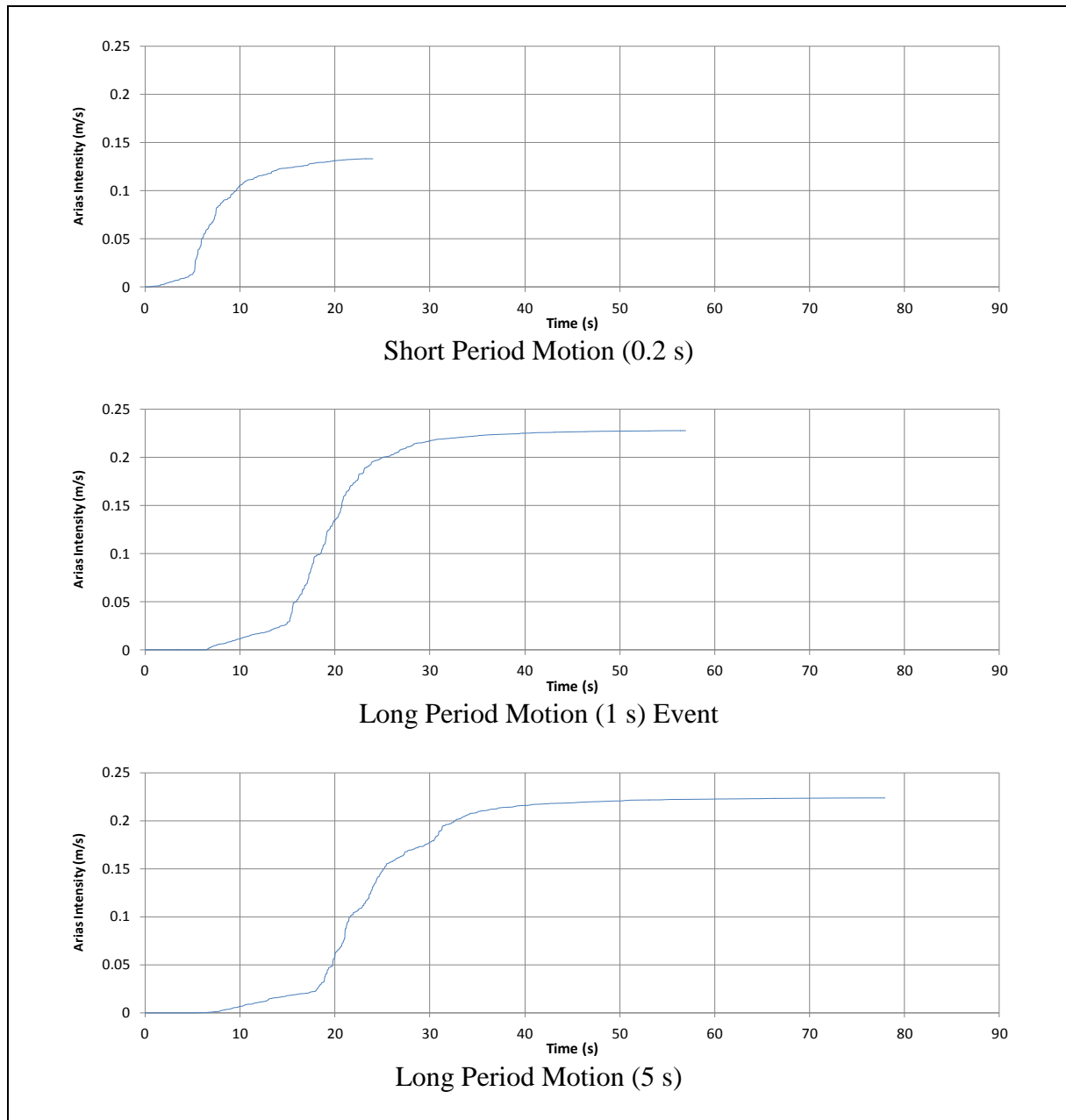
Figure 3.35   Arias Intensity for 300 m Crest Spectrally Matched Time Histories of 1.4 Amplification Factor for 10% in 50 Years Ground Motion
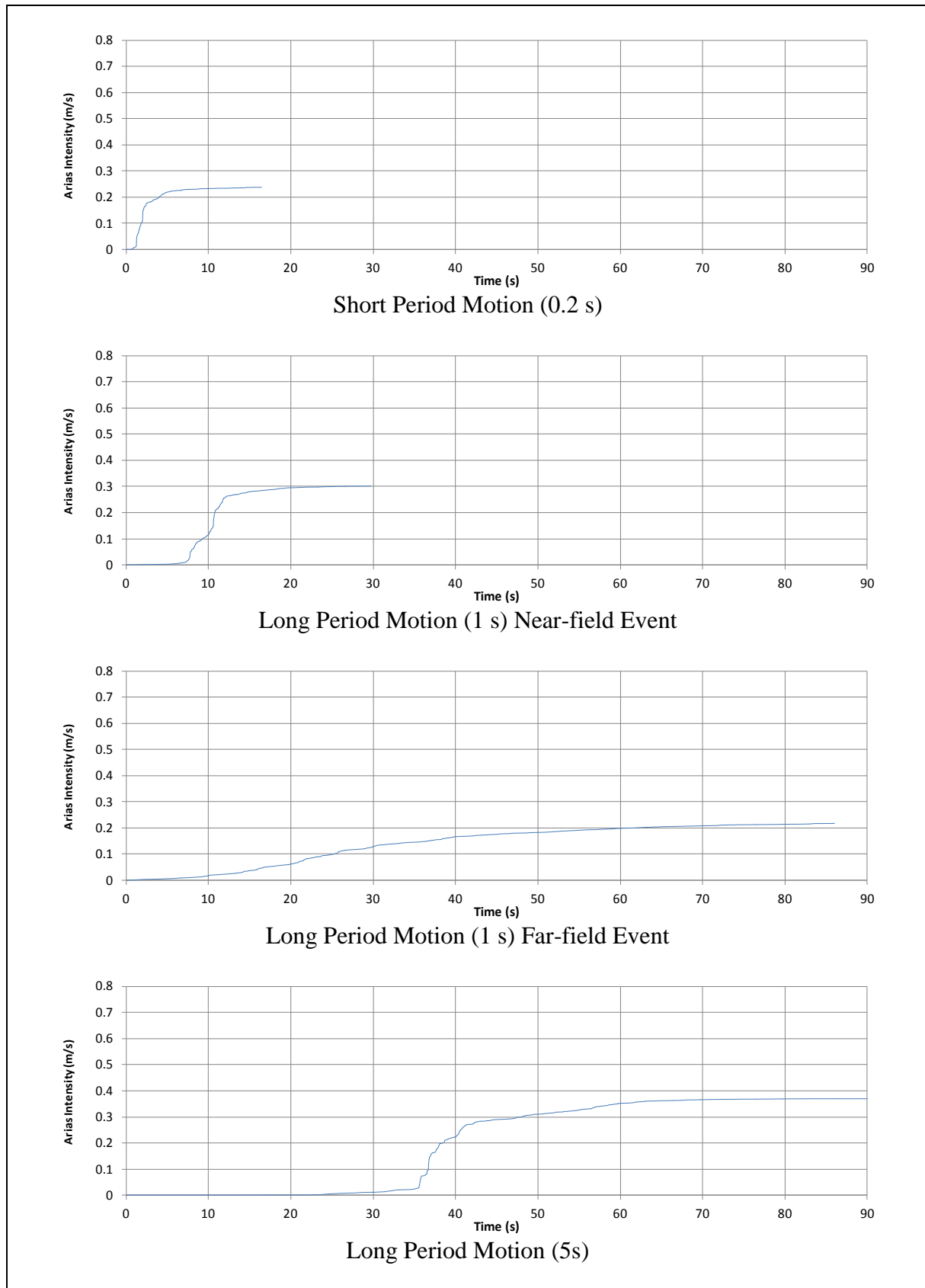
Figure 3.36   Arias Intensity for 30 m Crest Spectrally Matched Time Histories of 1.4 Amplification Factor for 2% in 50 Years Ground Motion
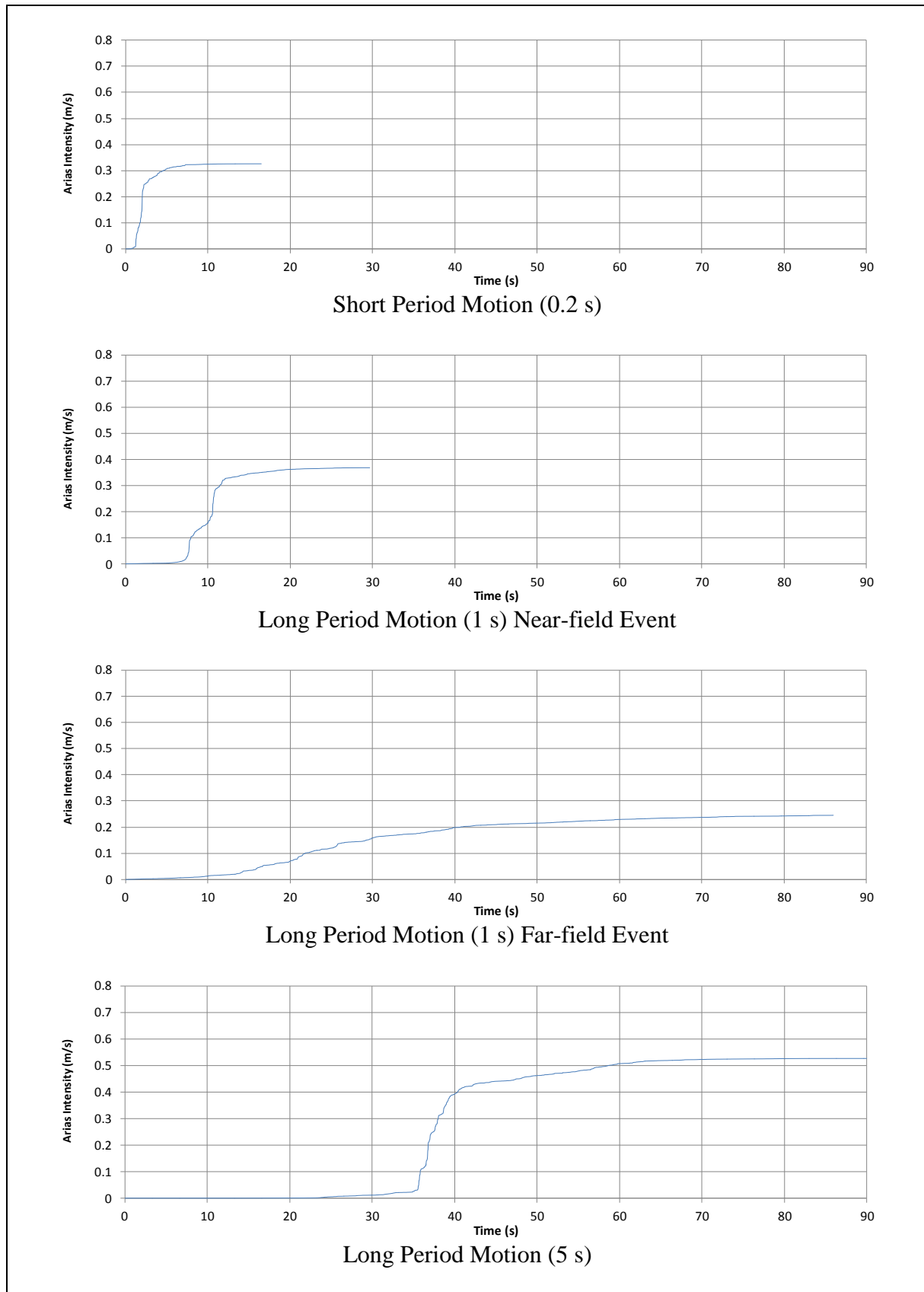
Figure 3.37   Arias Intensity for 100 m Crest Spectrally Matched Time Histories of 1.4 Amplification Factor for 2% in 50 Years Ground Motion
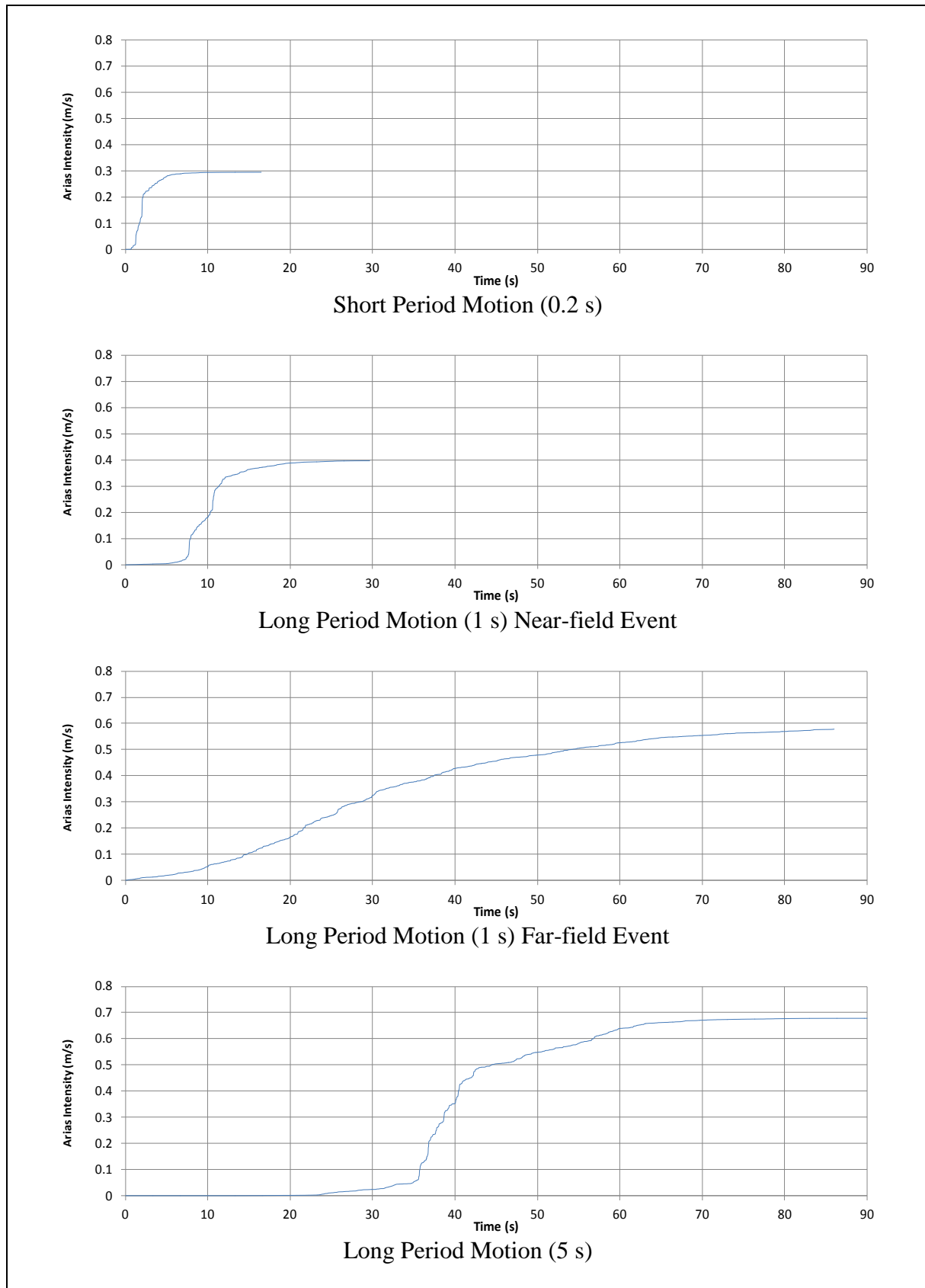
Figure 3.38 **Arias Intensity for 300 m Crest Spectrally Matched Time Histories of 1.4 Amplification Factor for 2% in 50 Years Ground Motion**

Short Period Motion (0.2 s)

Long Period Motion (1 s) Near-field Event

Long Period Motion (1 s) Far-field Event for 30 m Crest Height

Long Period Motion (1 s) Near-field Event for 100 m Crest Height
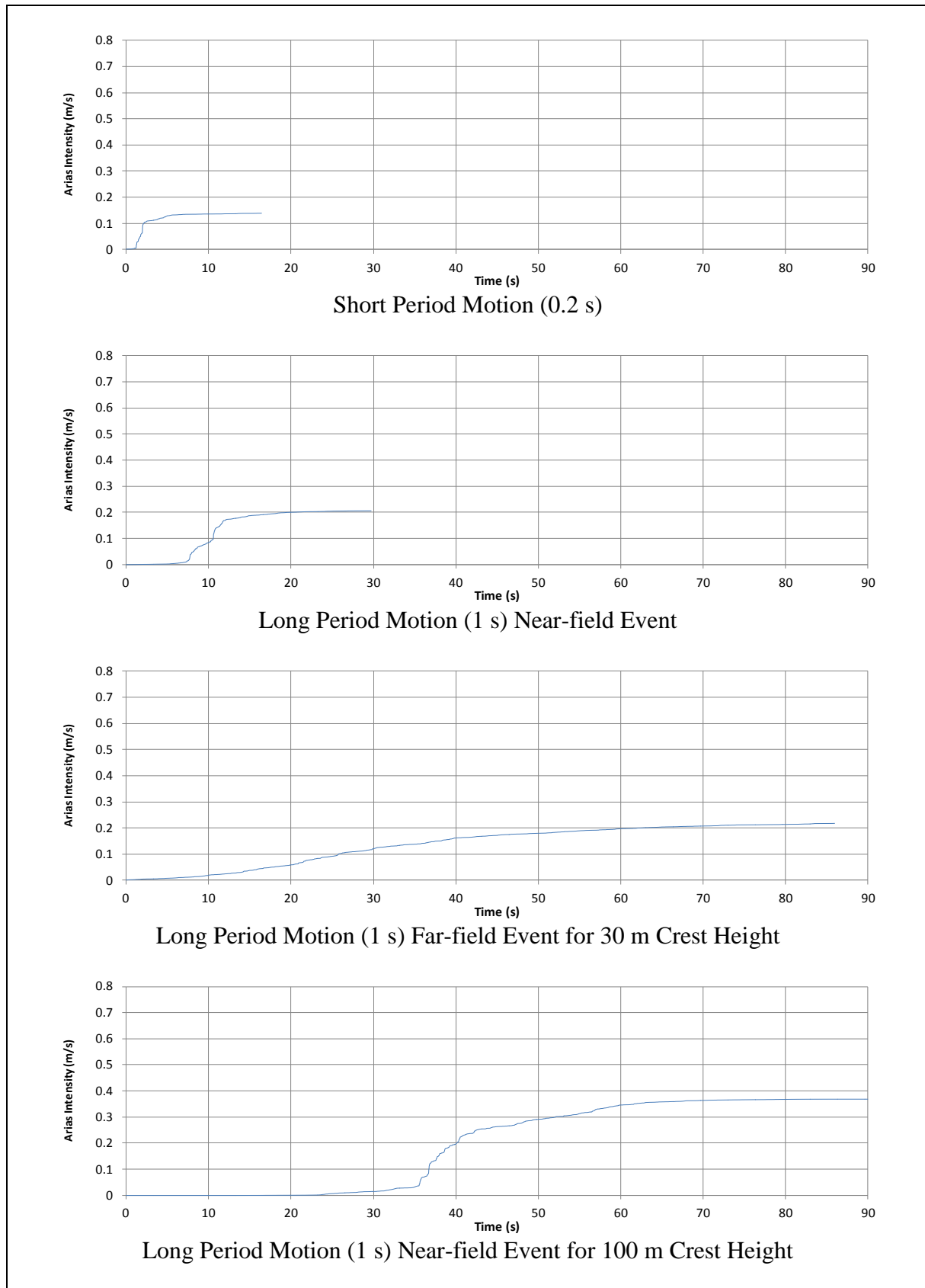
Figure 3.39   Arias Intensity for 30 m Crest Spectrally Matched Time Histories of 1.2 Amplification Factor for 2% in 50 Years Ground Motion
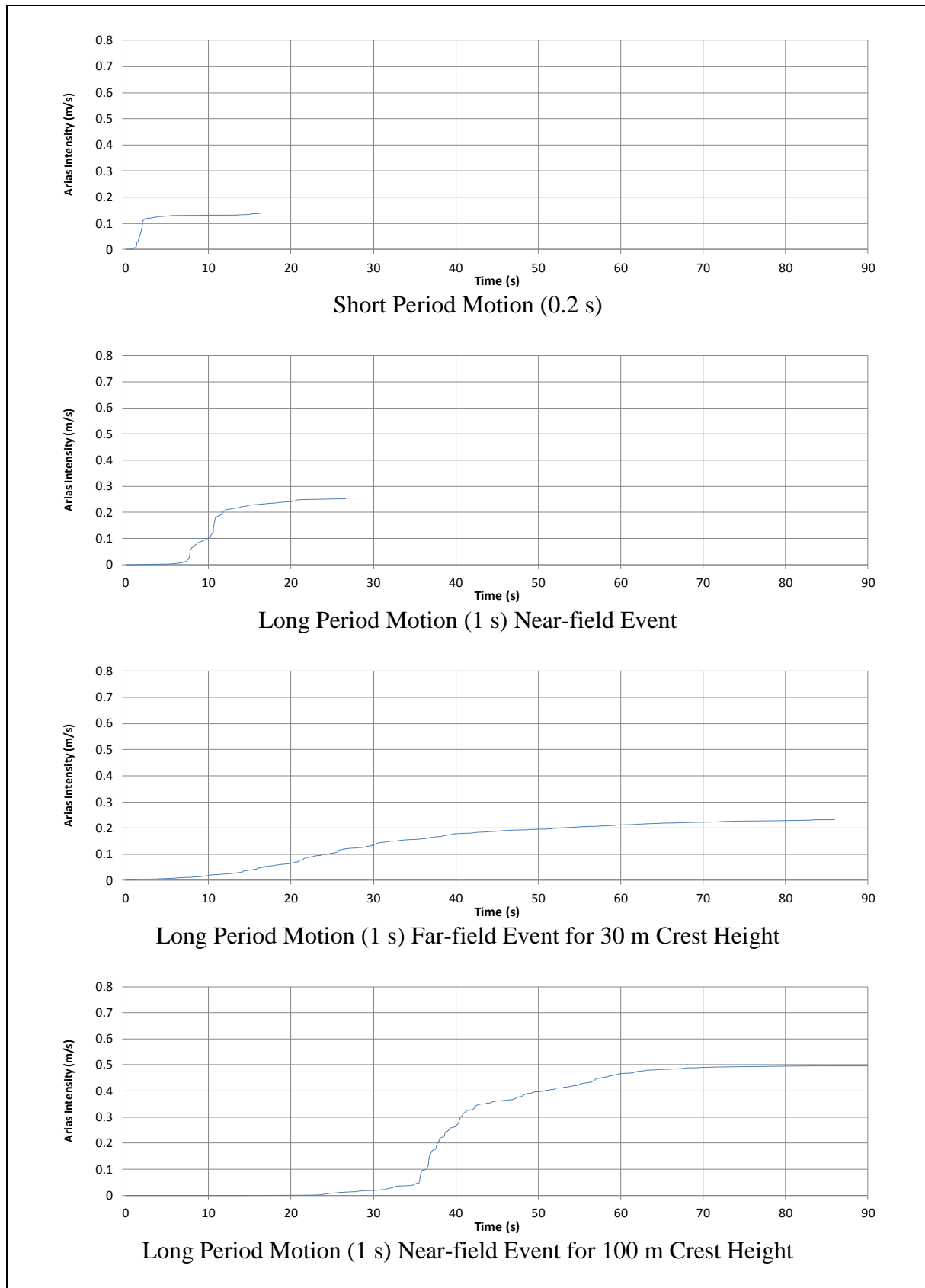
Figure 3.40   Arias Intensity for 100 m Crest Spectrally Matched Time Histories of 1.2 Amplification Factor for 2% in 50 Years Ground Motion
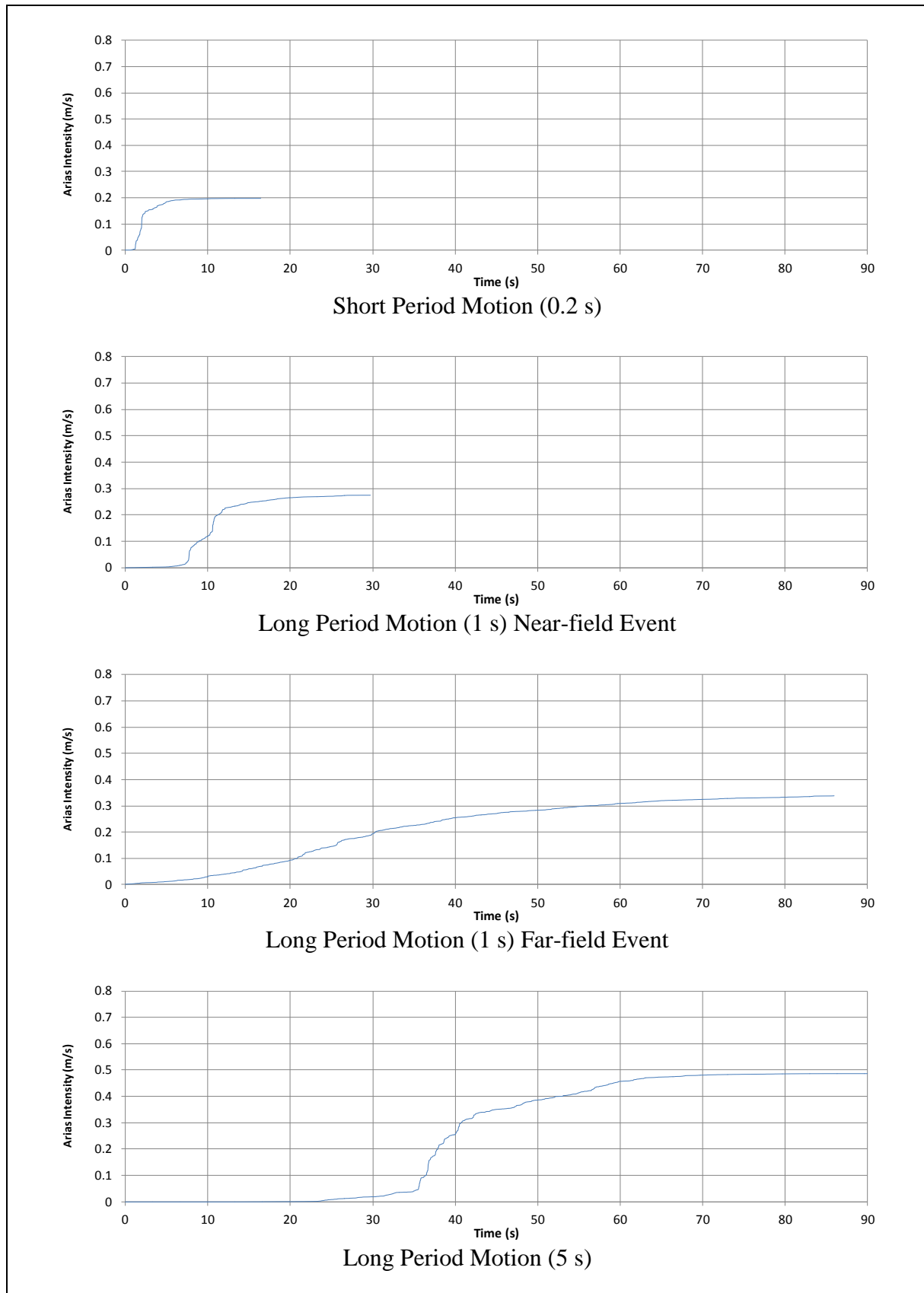
Figure 3.41 Arias Intensity for 300 m Crest Spectrally Matched Time Histories of 1.2 Amplification Factor for 2% in 50 Years Ground Motion

The variation of I_a has further been investigated for different scenarios. Figure 3.42 summarises the I_a values for 2% and 10% in 50 years ground motions respectively when different ridge heights are considered for a 1.4 PGA amplification factor. The I_a values increase with an increasing level of ground motions. For the 10% in 50 years ground motions, I_a increases with longer period ground motions and also generally with increasing ridge height. For the 2% in 50 years ground motion, I_a also generally increases with longer period ground motions. However, the 1 s far-field ground motions show almost no increase of I_a for 30 m and 100 m ridge heights but a significant amplification for the 300 m ridge height. As shown in Figure 3.5, only 300 m ridge height would amplify the longer period ground motion, which is expected to be present in this far-field ground motion. This is consistent with the trend observed in Figure 3.42.

The effect of varying the PGA amplification factor on I_a has also been investigated. The I_a values for the 2% in 50 years ground motions for the cases with no topographic effects and with PGA amplification factors of 1.2 and 1.4 respectively are plotted in Figure 3.43.

The I_a values subject to topographic effects have been compared with the empirical formula proposed by Lee et al (2008) (see Section 2.4.3). Equation 2.25 corrects I_a for the topographic amplification effect as a function of height and Table 2.17 shows the Arias Intensity amplification factor calculated for 30 m, 100 m and 300 m using this method. For the present study, the amplification factors of I_a have been calculated using I_a of 30 m, 100 m and 300 m ridge height ground motions divided by I_a without any topographic effects. The results are summarised in Table 3.3, which are similar to those derived by Lee et al (2008). They match especially well for the time histories obtained from the 1999 Chi-Chi earthquake (1 s for 10% and 5 s for 2% in 50 year ground motions). This comparison suggests that the Arias Intensities developed in the present study are reasonable.

It is well understood that a uniform hazard spectrum and an Arias Intensity are not directly related (i.e. two earthquake time histories with the same response spectrum could have very different values of Arias Intensity). For this reason, the time histories have been selected based on the earthquake scenario magnitude – distance combinations that are most likely to lead to various parts of the uniform hazard spectrum. These time histories, which should have reasonable durations appropriate to the hazard, have then been used to derive I_a as plotted in Figures 3.31 and 3.32 and again on Figures 3.42 and 3.43.

As an additional check that the ranges of values arising from the various earthquake scenarios are reasonable, PSHA has been used to directly derive Arias Intensity. The attenuation relationship by Travasarou et al (2003) has been used in this additional PSHA. The resulting hazard curve is shown in Figure 3.44. It shows a 2% in 50 years (0.0004 annual probability) Arias Intensity of about 0.2 m/s and a 10% in 50 year (0.0021 annual probability) Arias Intensity of about 0.06 m/s. These values compare well with the range of values used in the report of 0.14 to 0.32 m/s for the 2% in 50 years ground motions, and 0.06 to 0.104 m/s for the 10% in 50 years ground motions.

(a)

(b)
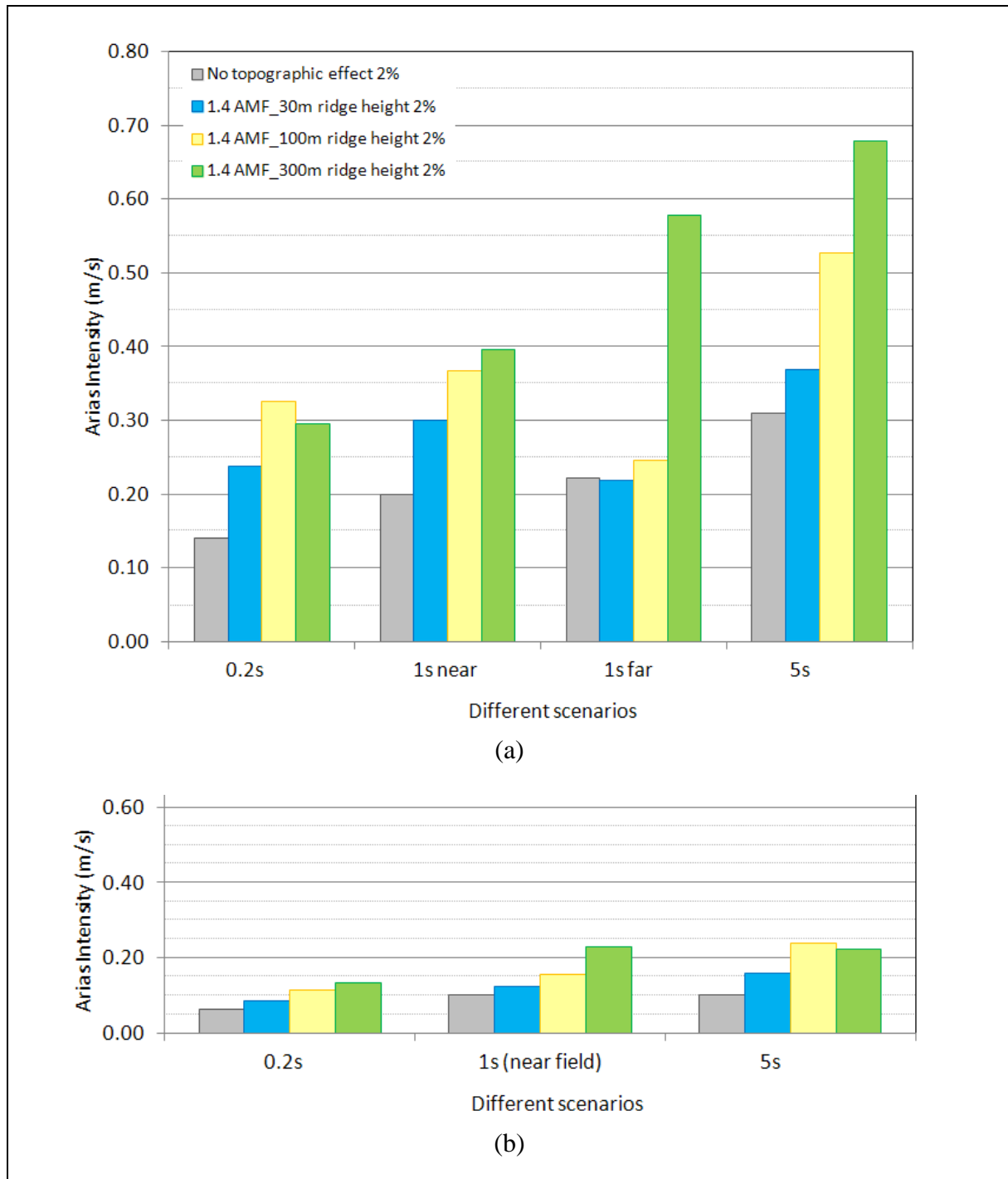
Figure 3.42 Arias Intensity for (a) 2% and (b) 10% in 50 Years Ground Motions (with No Topographic Effect and 30 m, 100 m, 300 m Ridge Heights with a 1.4 PGA Amplification Factor)
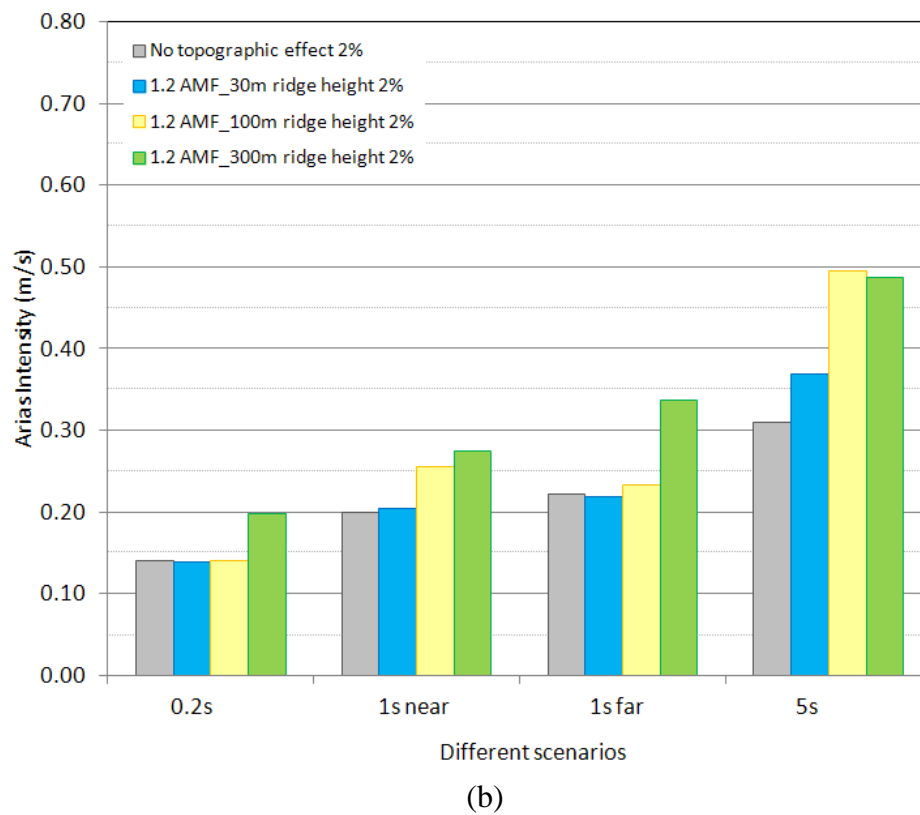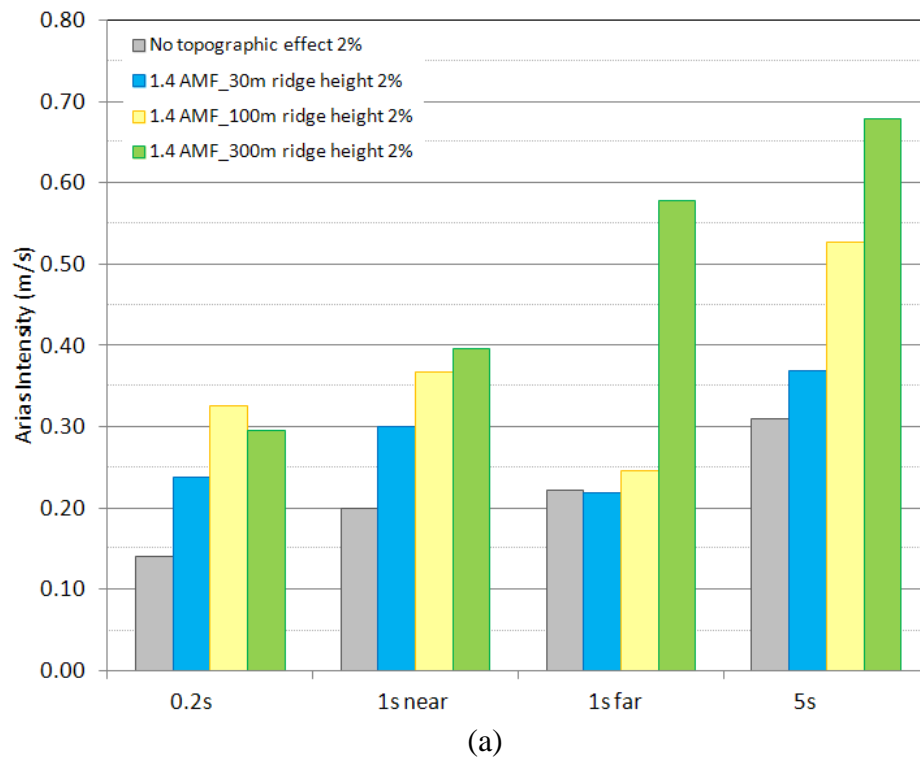
Figure 3.43 Arias Intensity for (a) 1.4 PGA Amplification Factor and (b) 1.2 PGA Amplification Factor (with No Topographic Effect and 30 m, 100 m, 300 m Ridge Heights) for 2% in 50 Years Ground Motions

Table 3.3 Calculated Arias Intensity Amplification Factors

PGA Amplification Factor	Probability of Being Exceeded in the Next 50 Years	Scenario	Original Time History	30 m	100 m	300 m
1.4	10%	0.2 s	Livermore-01	1.36	1.82	2.15
		1 s	Chi-Chi-Taiwan-05	1.23	1.55	2.28
		5 s	Kobe, Japan	1.58	2.38	2.23
	2%	0.2 s	Friuli-Italy-02	1.70	2.32	2.11
		1 s near-field	Loma Prieta	1.50	1.84	1.98
		1 s far-field	Denali, Alaska	0.99	1.11	2.60
		5 s	Chi-Chi-Taiwan	1.19	1.70	2.19
1.2	2%	0.2 s	Friuli-Italy-02	0.99	1.00	1.41
		1 s near-field	Loma Prieta	1.02	1.27	1.37
		1 s far-field	Denali, Alaska	0.98	1.05	1.52
		5 s	Chi-Chi-Taiwan	1.19	1.60	1.57
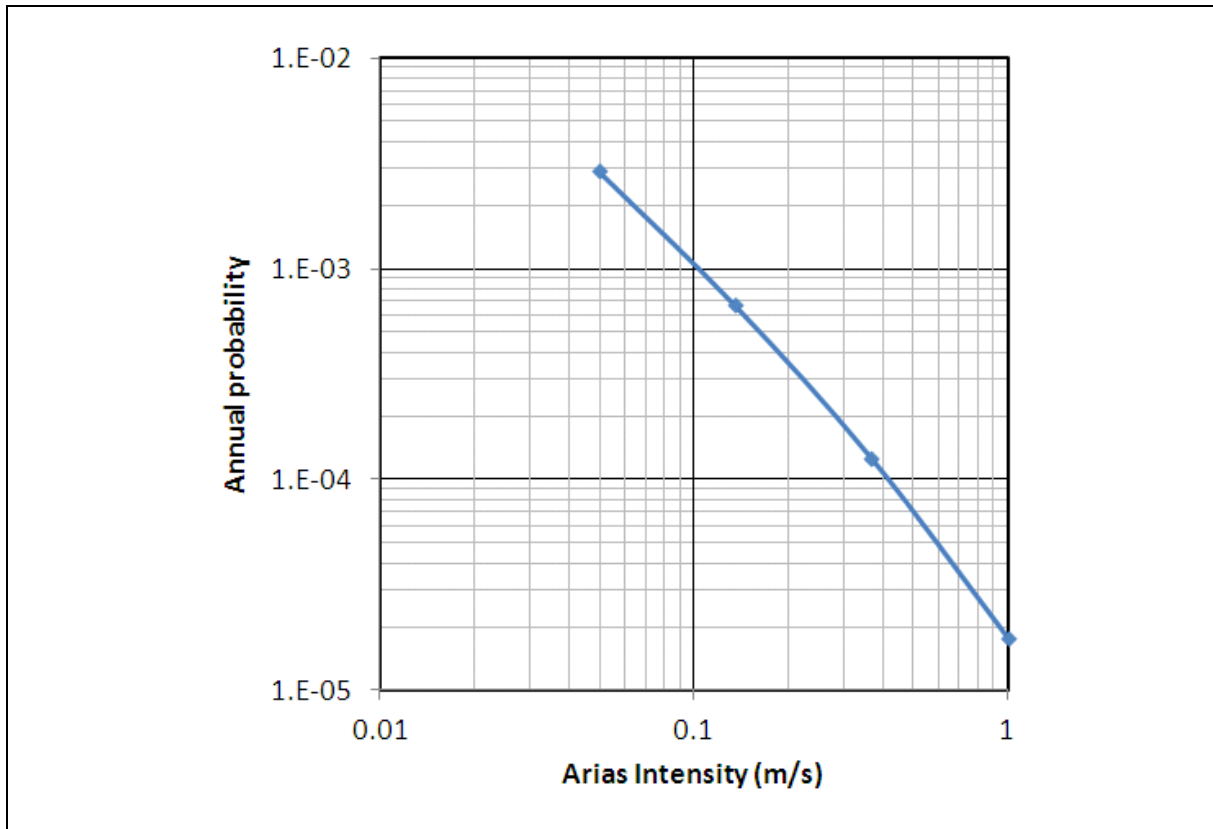
Figure 3.44   PSHA Results for Arias Intensity Using Travasarou et al (2003)

3.5   Results of the Slope Stability Analyses in Natural Terrain under Seismic Loading

3.5.1   Magnitude-distance Landslide Susceptibility

Using the findings of the literature review presented in Section 2 together with the combinations of magnitude and distance to epicentre for the probable ground motions derived from the PSHA in Arup (2015), the overall landslide susceptibility in the Study Area has been assessed.

Figures 3.45 to 3.48 show the comparison between the study dataset and the correlations from Keefer & Wilson (1989), Tamura (1978), Yasuda & Sagitani (1988) and ISSMFE (1993) respectively.

The comparisons indicate that the 10% in 50 years magnitude-distance combination appropriate to this study corresponds to the limiting case of landslide occurrence and that the 2% in 50 years would be expected to give rise to some landslides.   A comparison with Keefer & Wilson (1989) in Figure 3.45 shows that the likelihood of landslides is marginal especially for the 10% in 50 years ground motions.   Tamura (1978) and Yasuda & Sugitani (1988) both imply that some landslides are likely for the 2% in 50 years ground motions.   According to Figure 3.48, ISSMFE (1993) implies that destructive slope failures would not be expected, and that some slope failures may occur under 2% in 50 years ground motions.   However, the report did not explain what data they had used to distinguish between wet and dry countries.

Note: Category I: falls, disrupted slides, and avalanches; Category II: slumps, block slides, and earth flows; Category III: lateral spreads and flows.
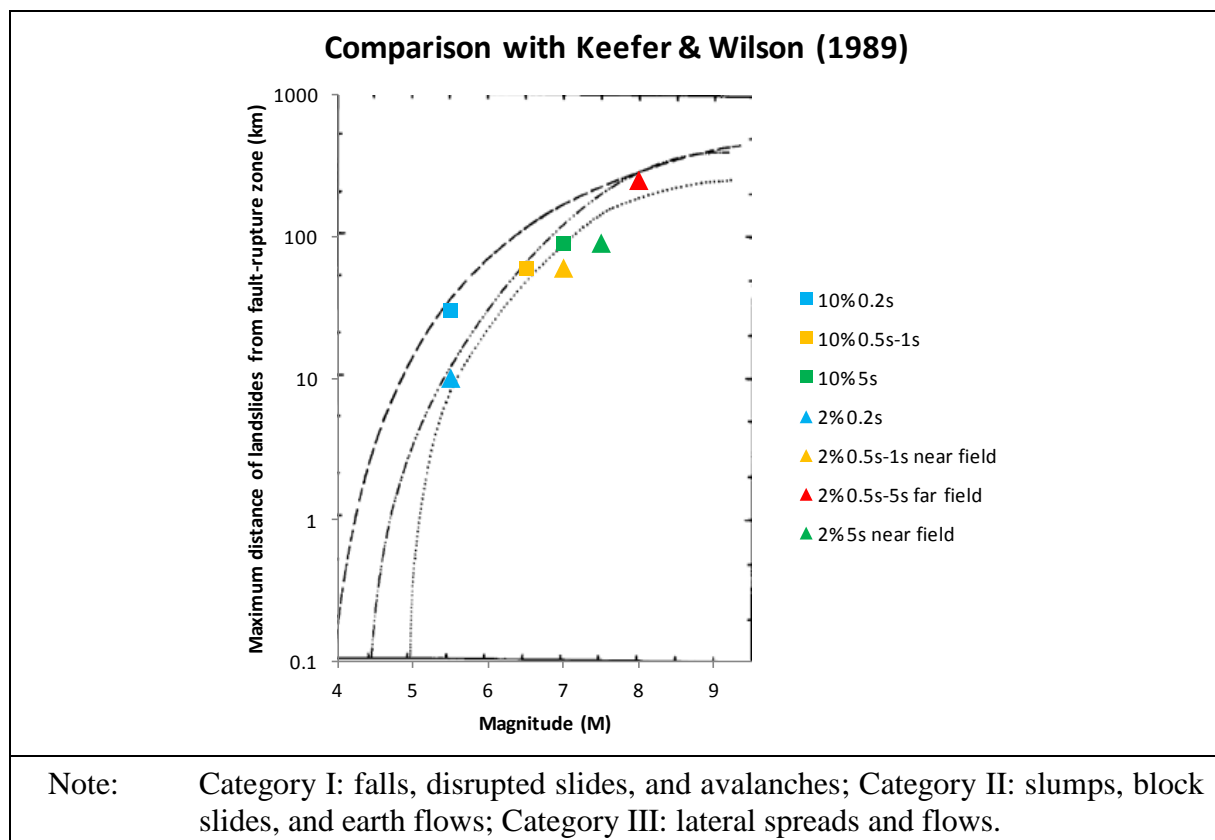
Figure 3.45   Magnitude-distance Comparison from Study Dataset to Keefer & Wilson (1989)

Comparison with Tamura (1978)

Legend:
- ■ 10% 0.2s
- ■ 10% 0.5s-1s
- ■ 10% 5s
- ▲ 2% 0.2s
- ▲ 2% 0.5s-1s near field
- ▲ 2% 0.5s-5s far field
- ▲ 2% 5s near field
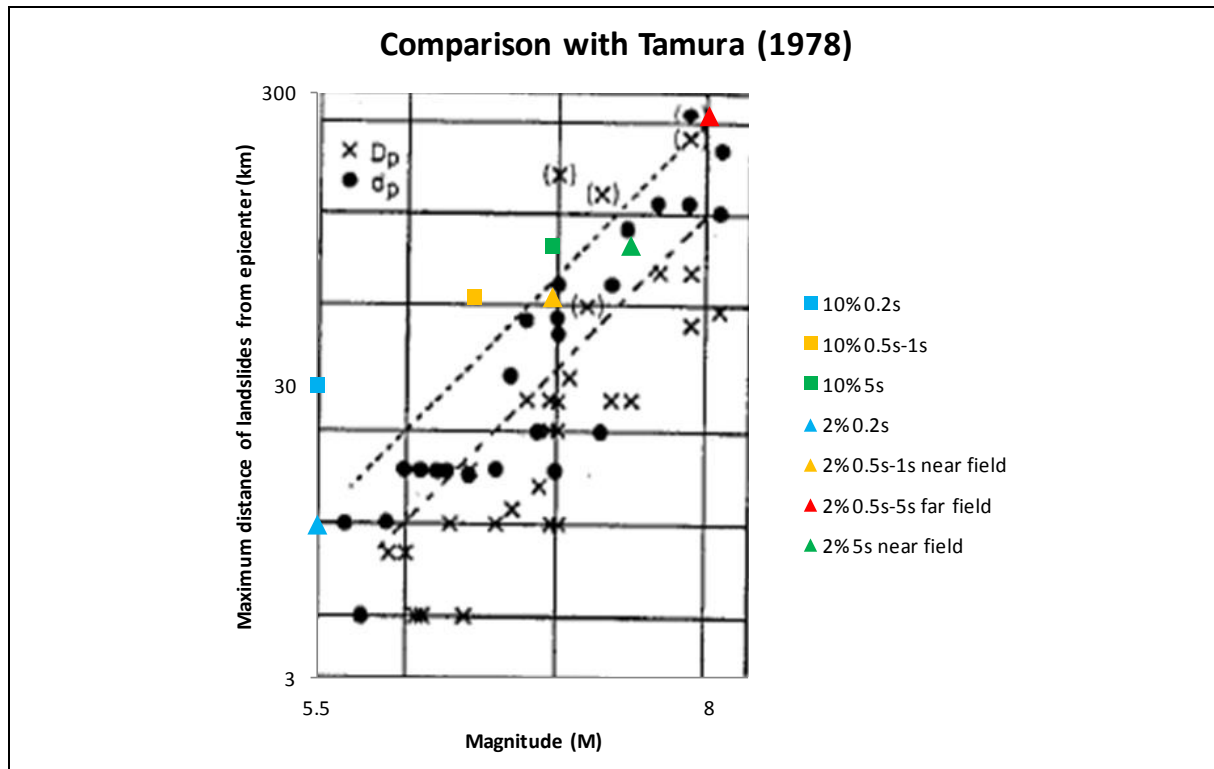
Figure 3.46   Magnitude-distance Comparison from Study Dataset to Tamura (1978)

Comparison with Yasuda &Sugitani (1988)

Legend:
- ■ 10% 0.2s
- ■ 10% 0.5s-1s
- ■ 10% 5s
- ▲ 2% 0.2s
- ▲ 2% 0.5s-1s near field
- ▲ 2% 0.5s-5s far field
- ▲ 2% 5s near field
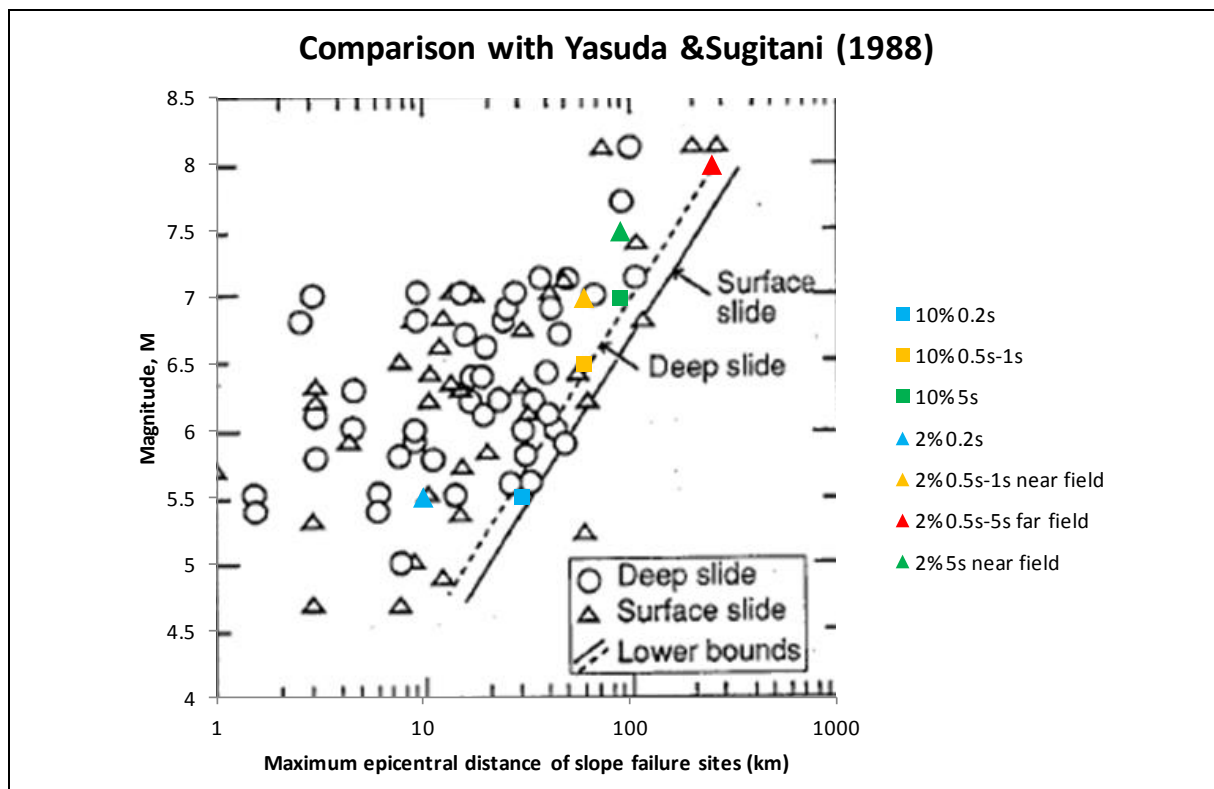
Figure 3.47   Magnitude-distance Comparison from Study Dataset to Yasuda & Sugitani (1988)
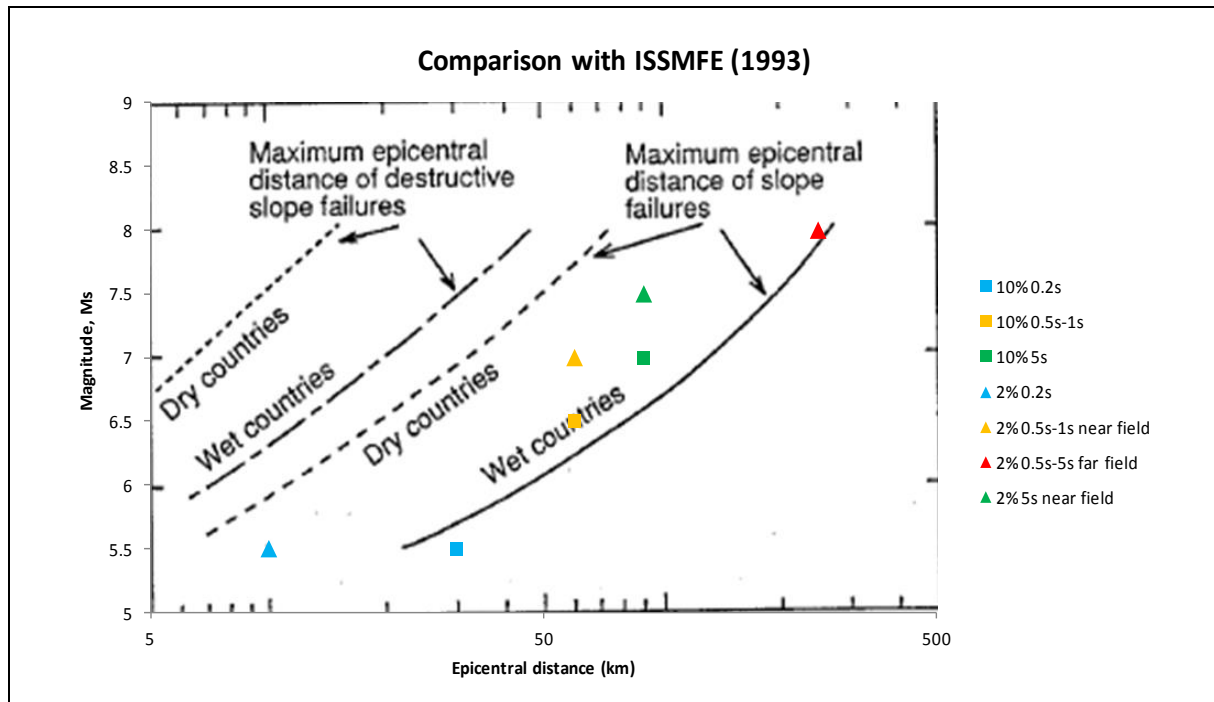
Figure 3.48   Magnitude-distance Comparison from Study Dataset to the Recommended Plot from ISSMFE (1993)

3.5.2   Earthquake-induced Slope Displacements

The natural terrain landslide hazard has been assessed in terms of the induced downslope displacements using both numerical and empirical methods as discussed in Sections 3.3 and 3.4 respectively.   Both 10% and 2% in 50 years ground motions have been considered. Additionally, calculations have been carried out for cases with topographic effects (i.e. ridge heights of 30 m, 100 m, and 300 m), in which the PGA amplification factors of 1.2 and 1.4 have been considered.   As regards the vertical ground acceleration, given that its effect on the seismic slope displacements is considered negligible for the ground motions appropriate to Hong Kong (see Section 2.2.4), this factor has not been considered in the analyses.

The earthquake-induced slope displacements have been calculated numerically using *Oasys* SIREN and dynamic FLAC (for the 2% in 50 years ground motions only), and empirically using the correlations from Jibson et al (1998), and that from Hsieh & Lee (2011) (see Section 3.4.2).   It has been found that the Jibson et al (1998) correlation would overestimate the induced displacement at very small A_c values (< 0.2 m/s^2) in comparison with others including the results obtained from *Oasys* SIREN and dynamic FLAC.

The calculated earthquake-induced slope displacements in different scenarios have been interpreted and compared.   The results would be integrated in the landslide susceptibility analyses in Section 5.   In the subsequent analyses, the A_c values are not derived by slope stability analyses.   It is assumed that the soil properties and groundwater conditions vary and thus the values of A_c would be varied with time.   The resulted A_c values are validated against those observed from other researchers.

Effect of the ground motion level on the induced slope displacements

Figure 3.49 shows the overall envelope (lower and upper bounds) of all the results for the critical acceleration, A_c, corresponding to the displacement required to trigger a landslide for the 10% and 2% in 50 years ground motions with and without topographic effects. It can be seen that the A_c values are significantly lower for the 10% in 50 years ground motions than those for the 2% in 50 years ground motions. The average and inferred A_c are found by approximately averaging the values of A_c at 100 mm displacement calculated using different empirical and numerical methods for all the scenario earthquakes. The A_c is judged graphically for better consideration for all cases rather than calculated using the lower and upper bound values. For the 10% in 50 years ground motions, the average FoS value corresponding to the triggering of landslides lies between 1 and about 1.05. It implies that such earthquake ground motions have barely any effect on the triggering of landslides compared to a static failure. For the 2% in 50 years ground motions, the average FoS corresponding to landslide triggering lies between 1.05 and 1.10 for 20° slopes, and around 1.05 for 30° to 40° slopes. When no topographic effect is considered, the 2% in 50 years ground motions only have limited effect on the slope stability.
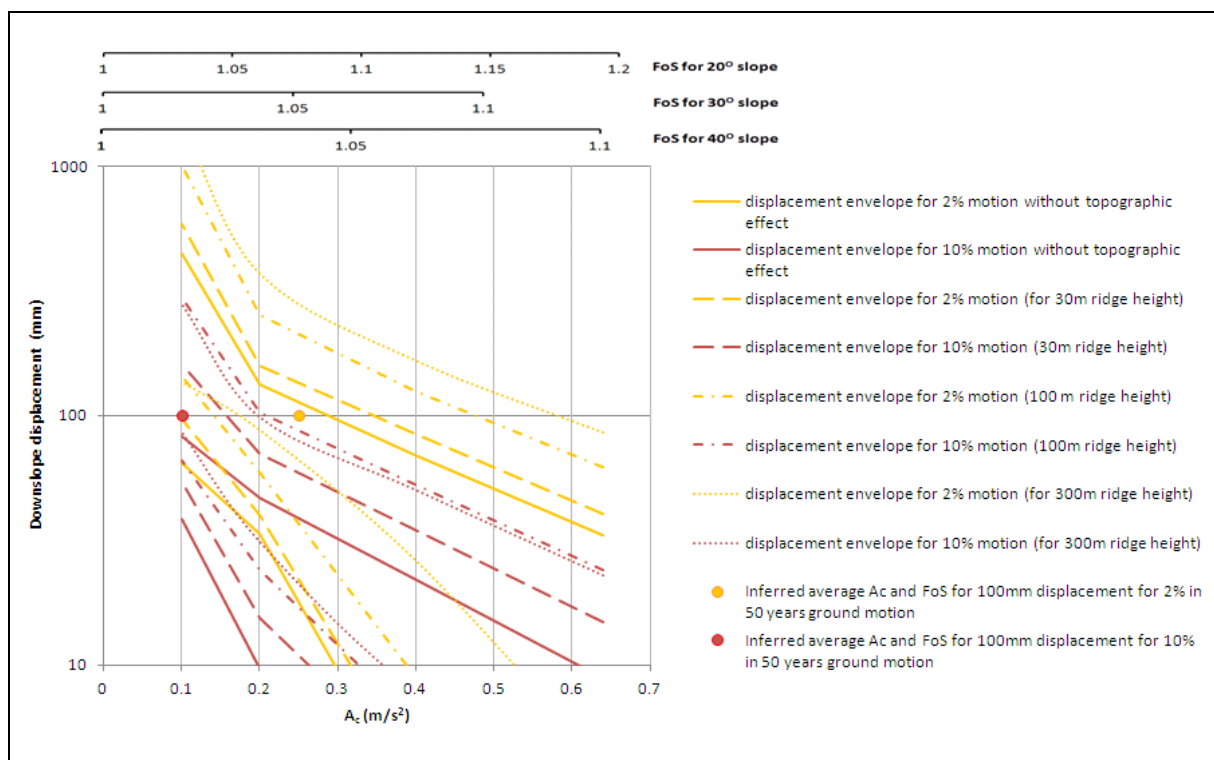
Figure 3.49   Effect of Ground Motion on Induced Downslope Displacement for 2% and 10% in 50 Year Ground Motions

The detailed results for the 2% and 10% in 50 years ground motions (with no consideration for topographic effects) are presented in Figures 3.50 and 3.51 respectively. As can be seen, the 5 s long period ground motion gives rise to the largest downslope displacements whereas the 0.2 s short period ground motion results in the least displacements. For the 2% in 50 years ground motions, the *Oasys* SIREN analyses give lower displacement values than the dynamic FLAC analyses, which are in good agreement with the results of empirical correlations.

Detailed plots for the 2% in 50 years ground motions (1 s far-field and 5 s) are shown for topographic effects of 30 m, 100 m and 300 m crest heights in Figures 3.52 to 3.57 respectively. The topographic effect is reflected on the calculated downslope displacements. More discussions are provided in the following section.
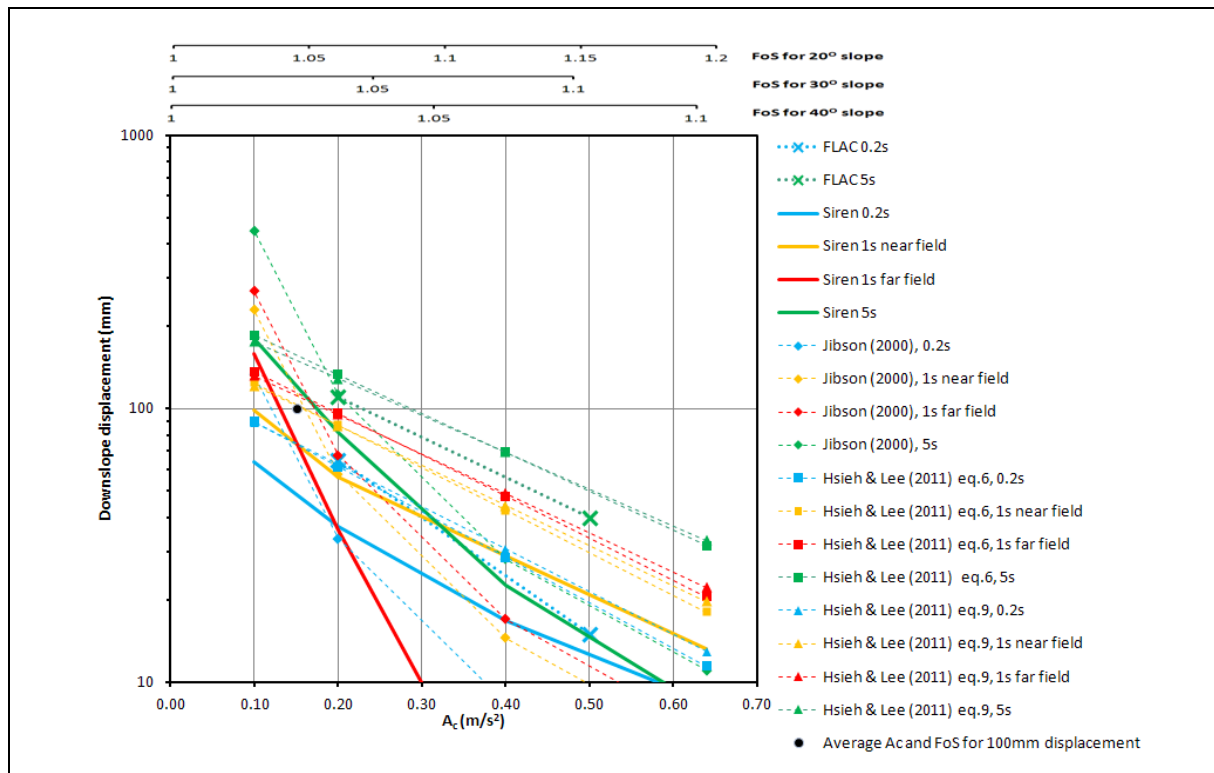
Figure 3.50 Downslope Displacements Calculated by *Oasys* SIREN, Dynamic FLAC and Empirical Correlations for 2% in 50 Years Ground Motion (without any Topographic Effect)
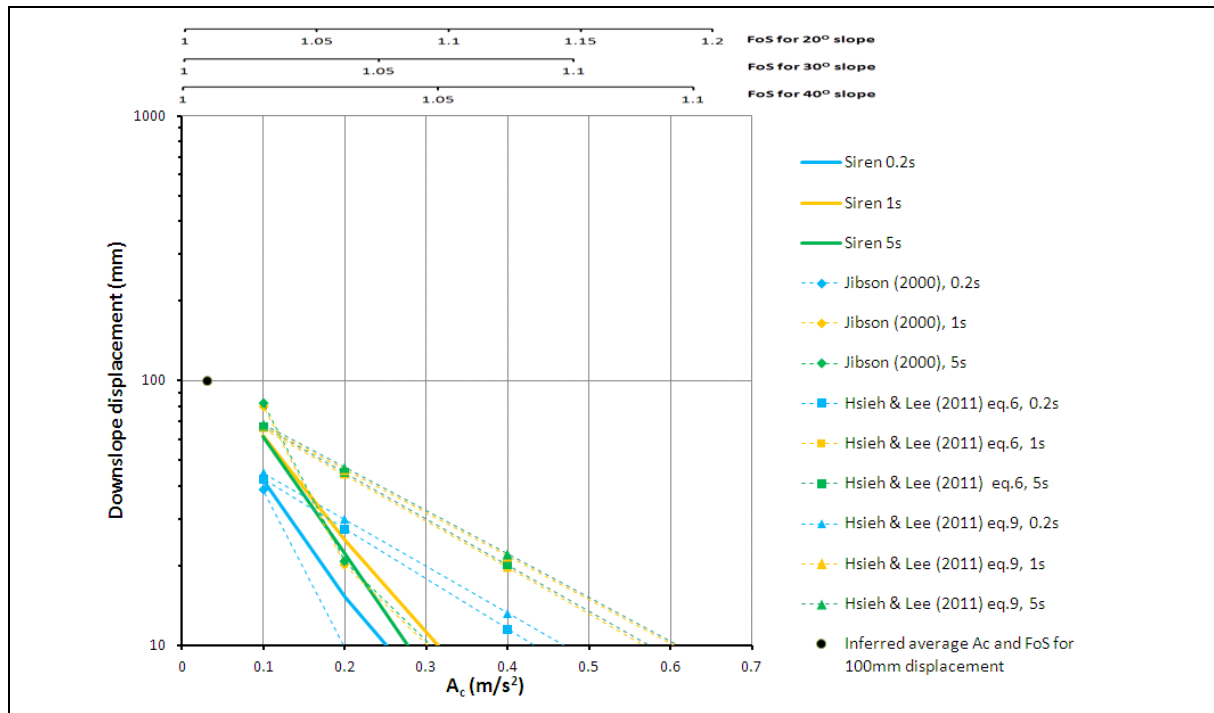
Figure 3.51   Downslope Displacements Calculated by *Oasys* **SIREN, Dynamic FLAC and Empirical Correlations for 10% in 50 Years (without any Topographic Effect)**
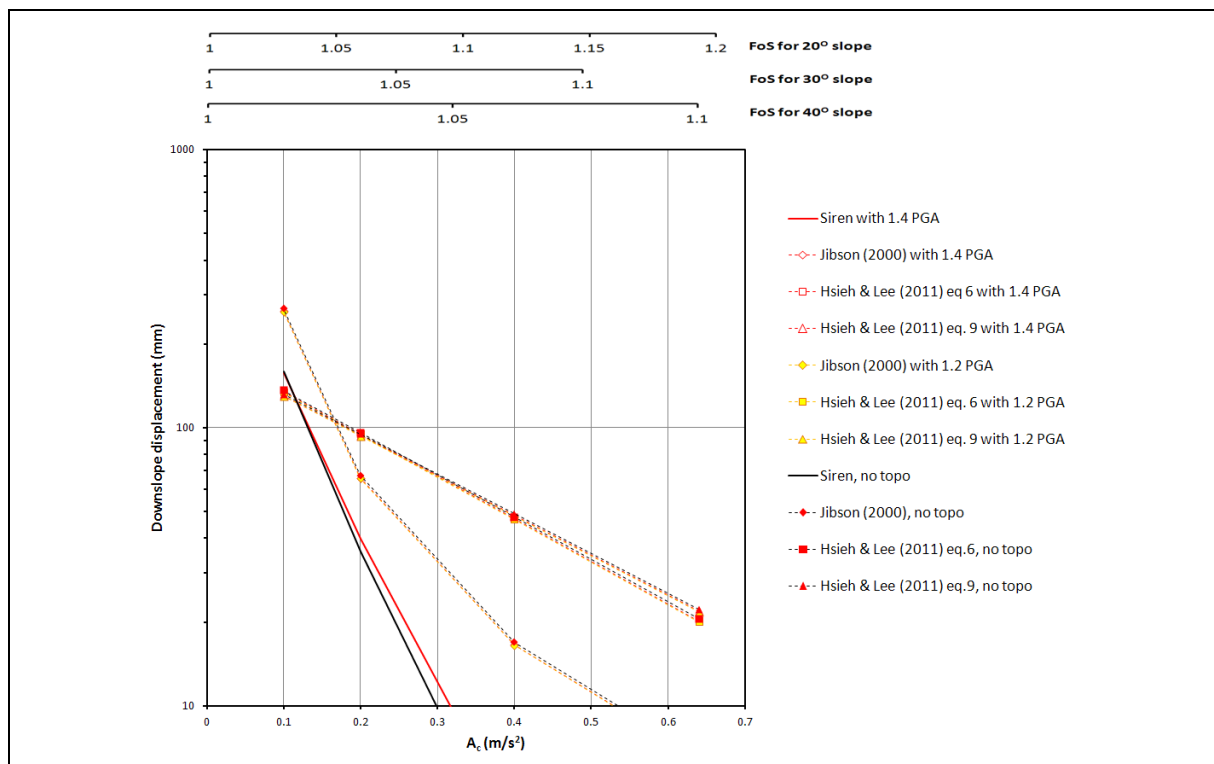
Figure 3.52   Downslope Displacements Calculated for 2% in 50 Years, 1 s Far-field, with No Topographic Effect and 30 m Crest Height Effect
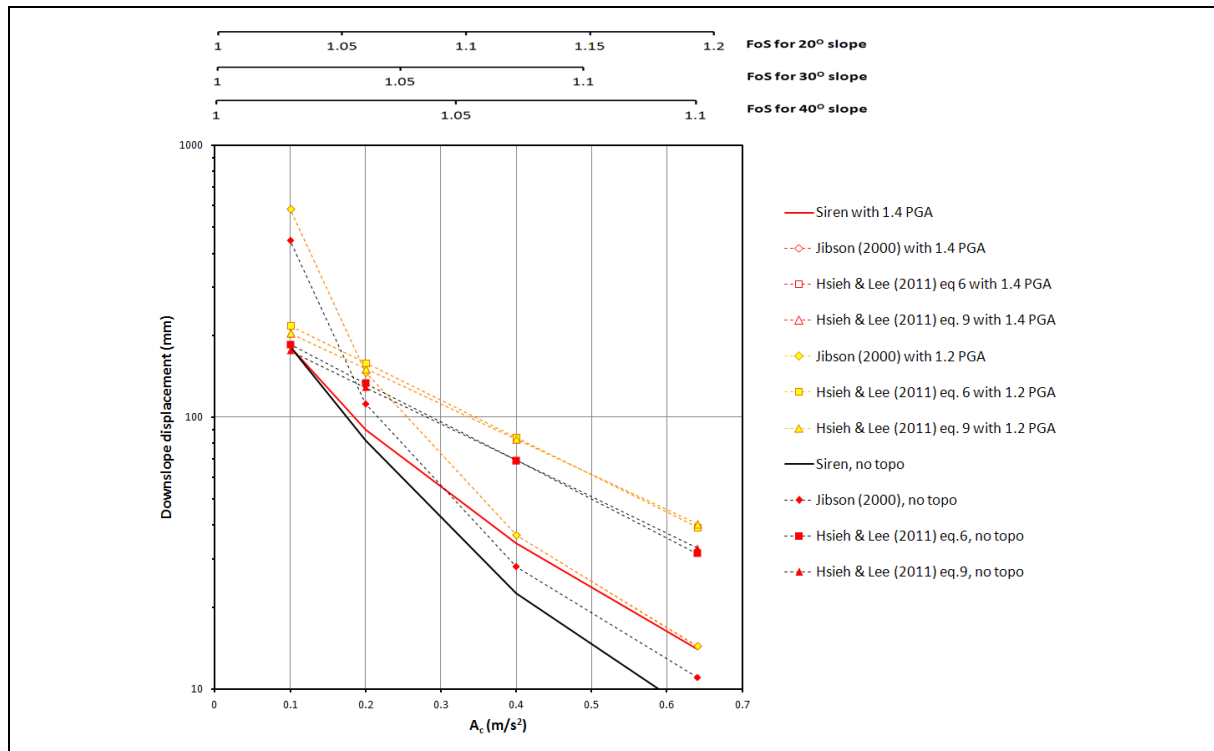
Figure 3.53 Downslope Displacements Calculated for 2% in 50 Years, 5 s, with No Topographic Effect and 30 m Crest Height Effect
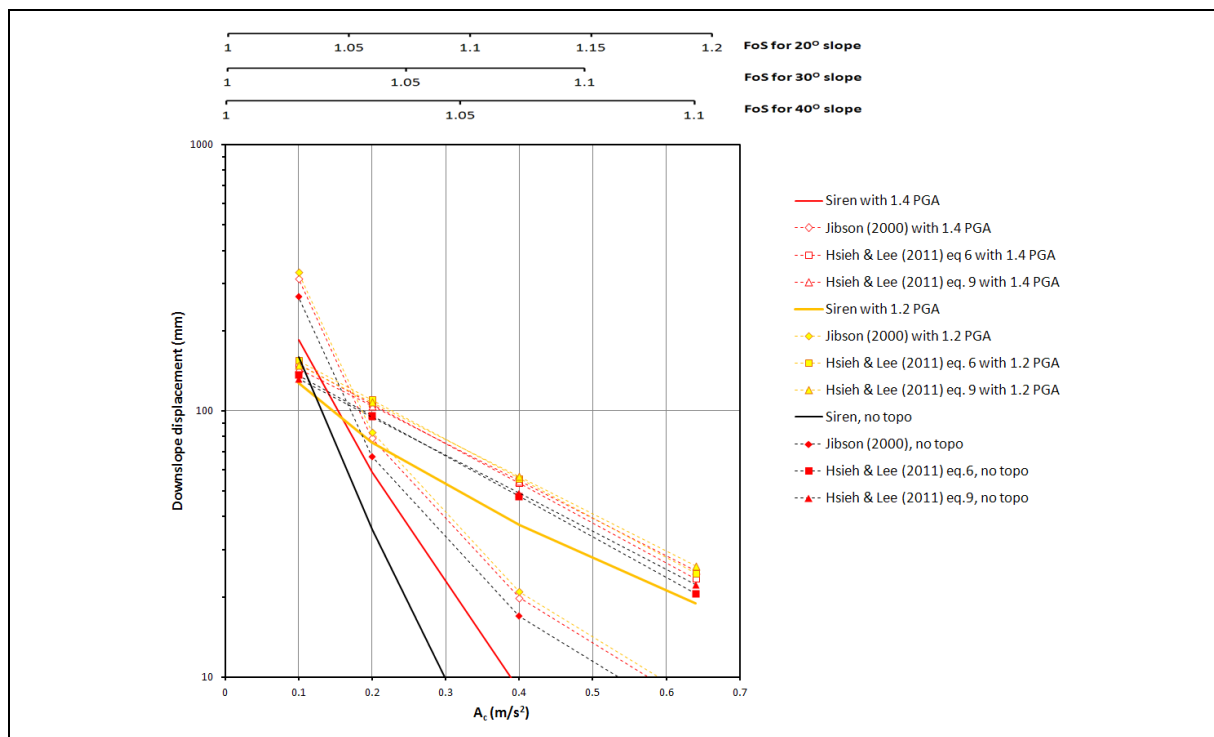
Figure 3.54 Downslope Displacements Calculated for 2% in 50 Years, 1 s Far-field, with No Topographic Effect and 100 m Crest Height Effect
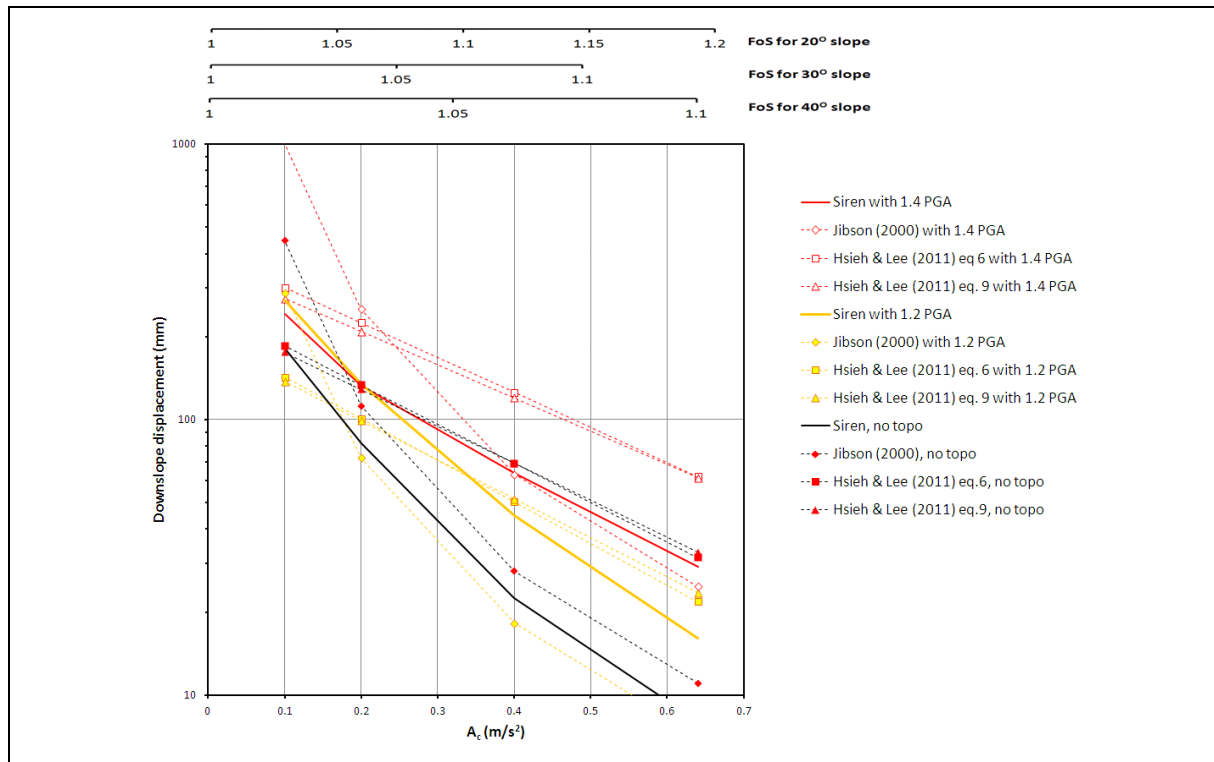
Figure 3.55   Downslope Displacements Calculated for 2% in 50 Years, 5 s, with No Topographic Effect and 100 m Crest Height Effect
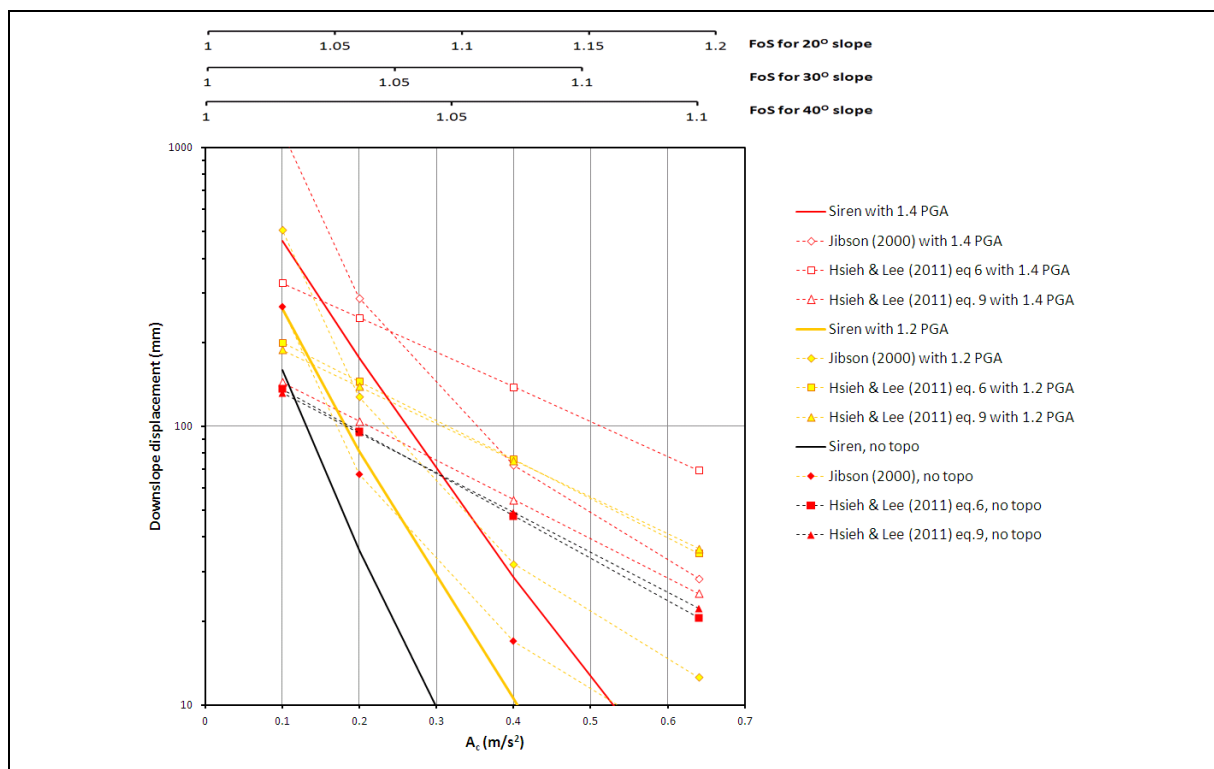
Figure 3.56   Downslope Displacements Calculated for 2% in 50 Years, 1 s Far-field, with No Topographic Effect and 300 m Crest Height Effect
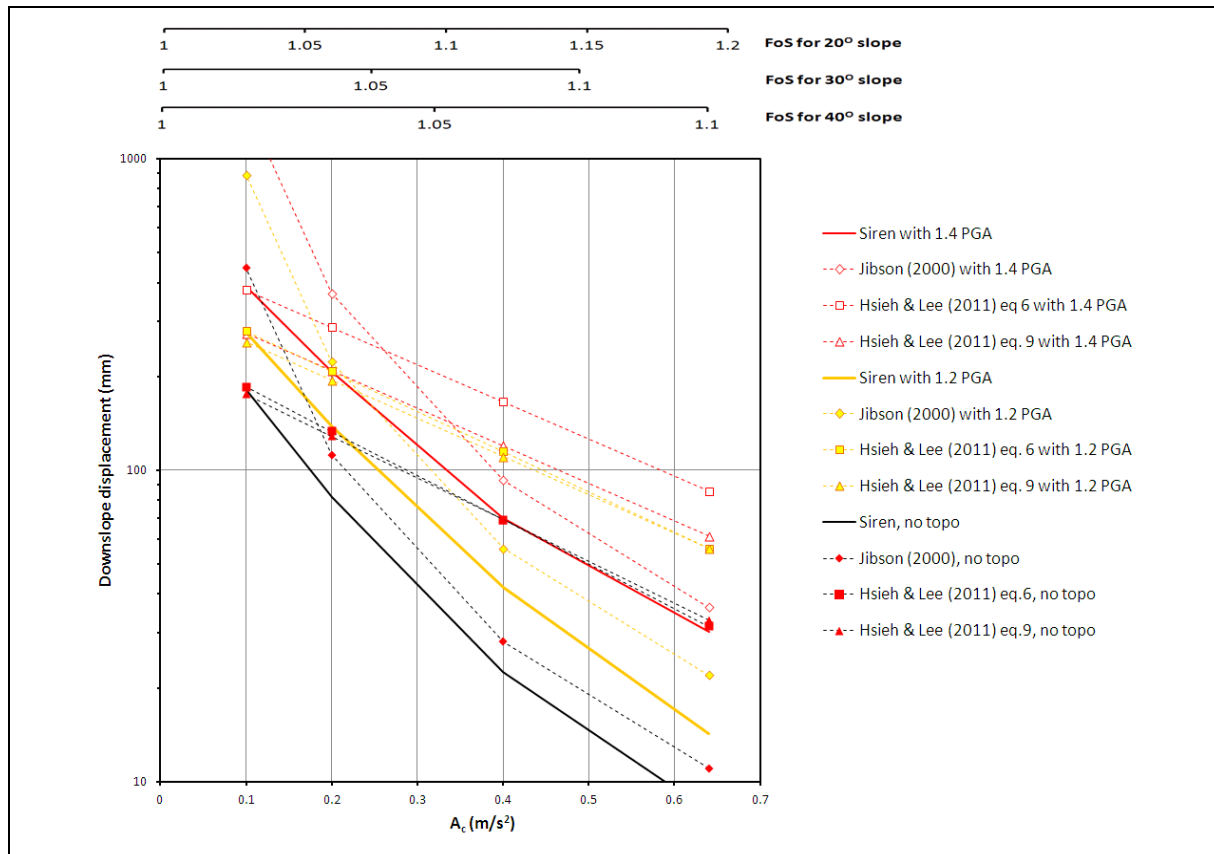
Figure 3.57   Downslope Displacements Calculated for 2% in 50 Years, 5 s, with No Topographic Effect and 300 m Crest Height Effect

Topographic effects on the induced slope displacements

The topographic effects on the induced seismic slope displacements have been studied for the 10% and 2% in 50 years ground motions respectively.

Figures 3.58 to 3.60 show the summary plots of the results from the empirical correlations as well as from *Oasys* SIREN analyses for the 2% in 50 years ground motions, considering topographic effects of 30 m, 100 m and 300 m crest heights (for a PGA amplification factor of 1.4) respectively. Overall, it is found that the higher the crest is, the greater the induced displacements would be. Therefore, a 300 m crest height is considered the most critical case. For a 30 m crest height, the average FoS corresponding to the threshold displacement for landslide triggering lies between 1.06 for a 20° slope, to 1.03 to 1.04 for 30° to 40° slopes. For 100 m and 300 m crest heights, the average FoS lies between 1.10 for 20° slopes, to 1.06 for 30° slopes and 1.05 for 40° slopes. The effect of earthquakes on the natural terrain slope stability is therefore not negligible when considering topographic effects. Such an effect becomes stronger with larger crest heights.
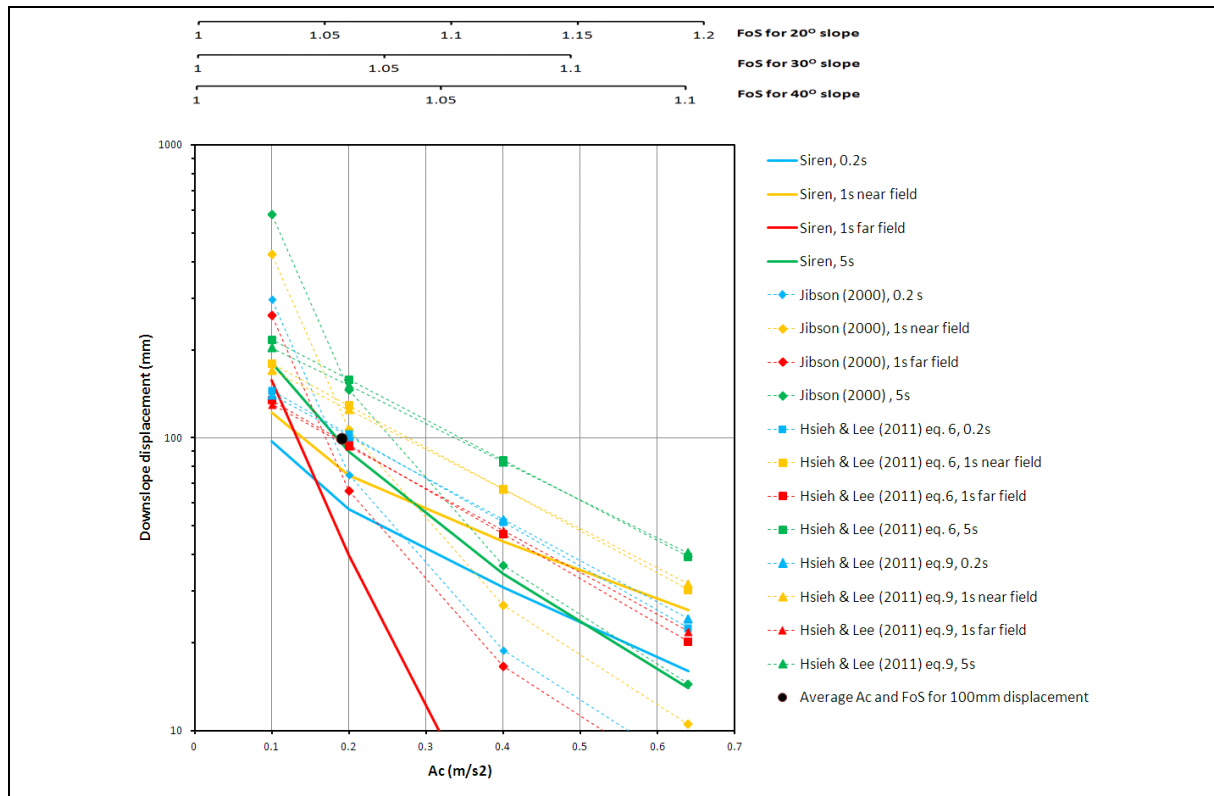
Figure 3.58 **Downslope Displacements Calculated for 2% in 50 Years, and 30 m Crest Height Effect (1.4 PGA Amplification Factor)**
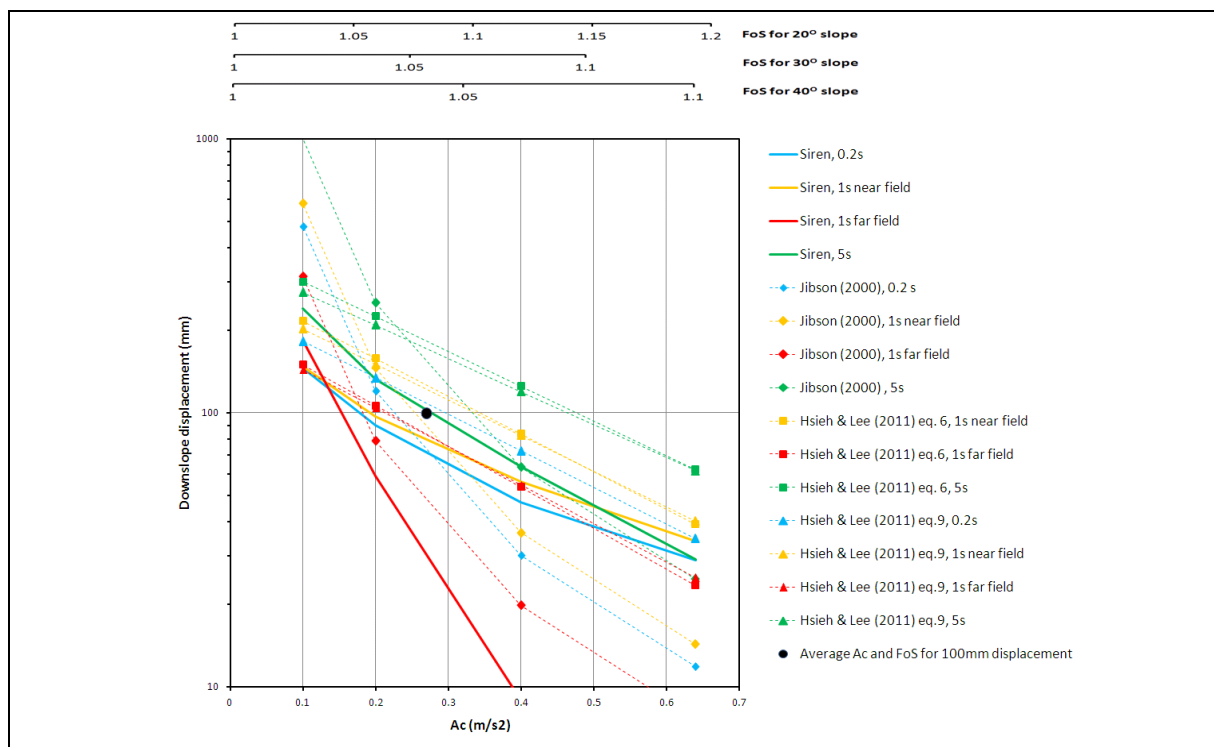
Figure 3.59 **Downslope Displacements Calculated for 2% in 50 Years, and 100 m Crest Height Effect (1.4 PGA Amplification Factor)**
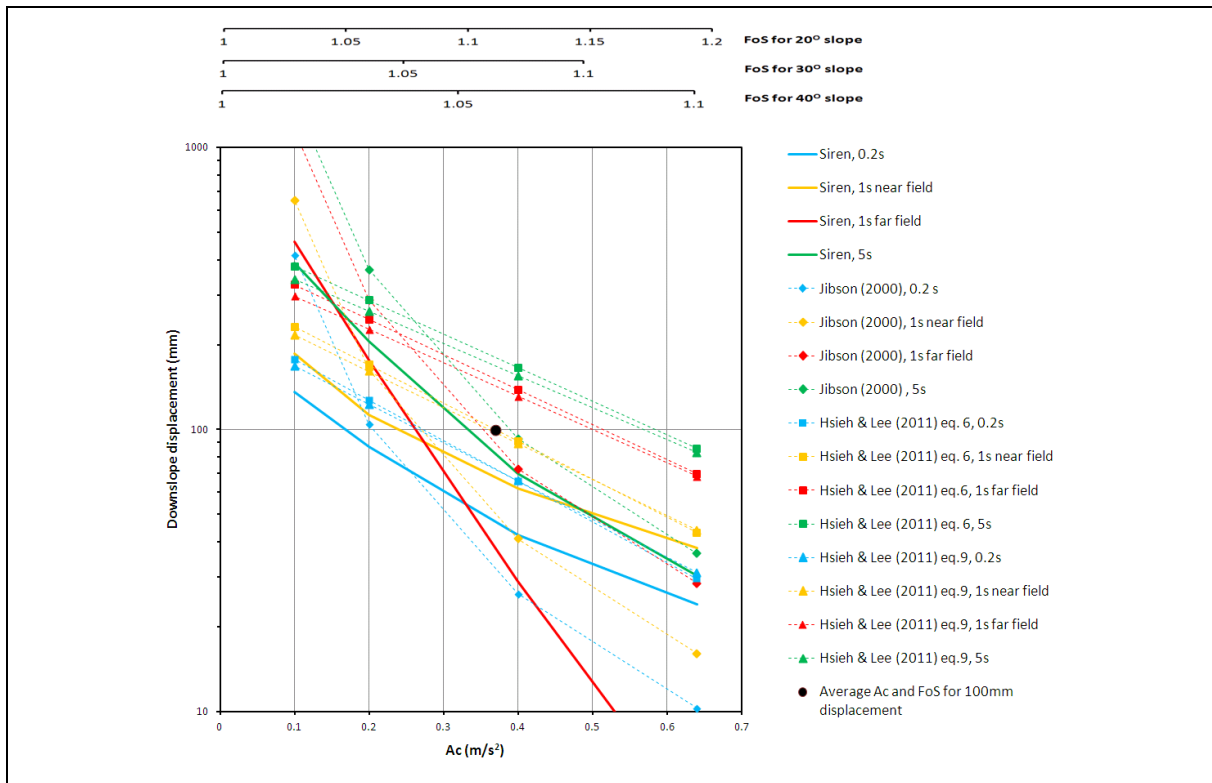
Figure 3.60   Downslope Displacements Calculated for 2% in 50 Years, and 300 m Crest Height Effect (1.4 PGA Amplification Factor)

Figures 3.61 to 3.63 show the same results for the 10% in 50 years ground motions. It can be seen that the topographic effects are greatly reduced. Even for the largest crest height, the static FoS to prevent a slope failure is less than about 1.05.

In order to investigate the effects of different PGA amplification factors on induced slope displacements, calculations have been repeated for a PGA amplification factor of 1.2. Figures 3.64 to 3.66 show the comparison between the results for the 2% in 50 years ground motions.   The average FoS corresponding to the threshold displacement for landslide triggering in the case of an amplification factor of 1.2 lies between 1.05 and 1.10 for a 20° slope, and between 1.02 and 1.06 for 30° to 40° slopes.   Figure 3.67 shows the lower and upper bounds of the results for a 2% in 50 years ground motion for cases with no topographic effect, and with topographic effects (including 30 m, 100 m, and 300 m ridge heights with 1.2 and 1.4 amplification factors used).   This shows more clearly the shift of the FoS and A_c corresponding to the threshold displacement for different cases of amplification factors.   Table 3.4 summarises the values of critical accelerations that correspond to the 100 mm threshold displacement for different combinations of seismic ground motions, ridge heights and PGA amplification factors.
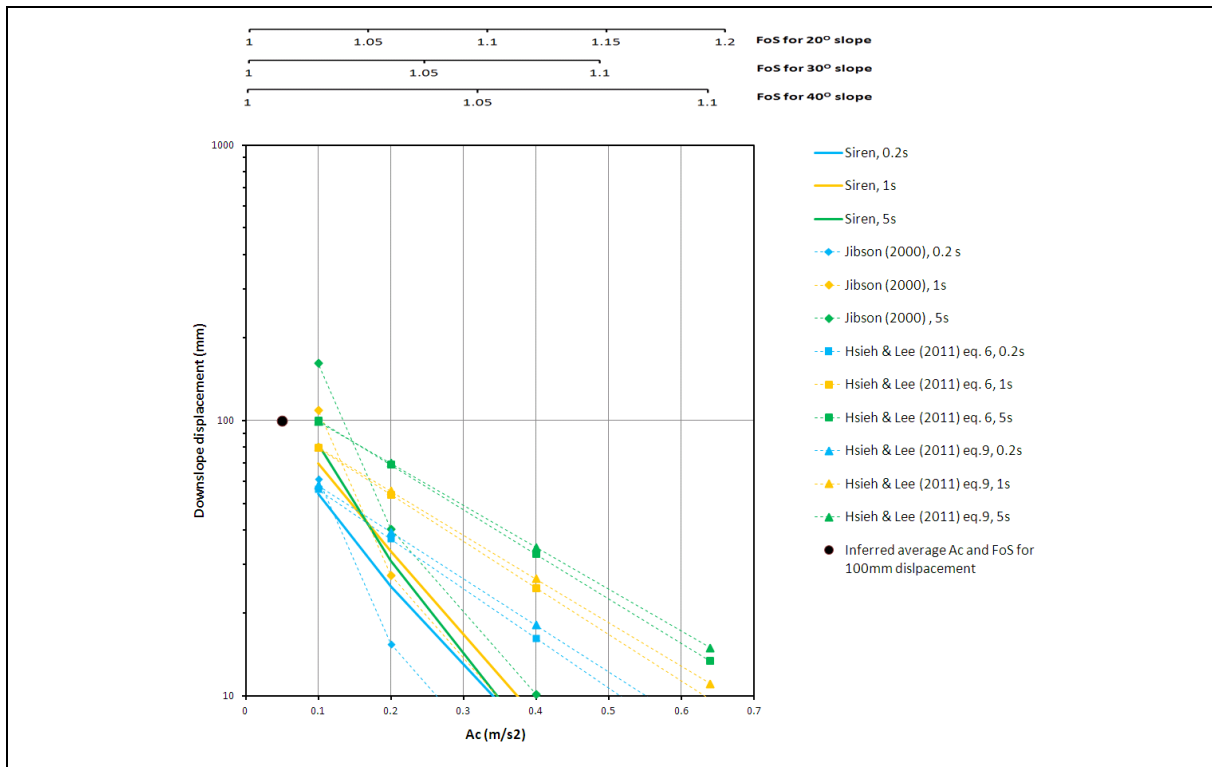
Figure 3.61   Downslope Displacements Calculated for 10% in 50 Years, and 30 m Crest Height Effect (1.4 PGA Amplification Factor)
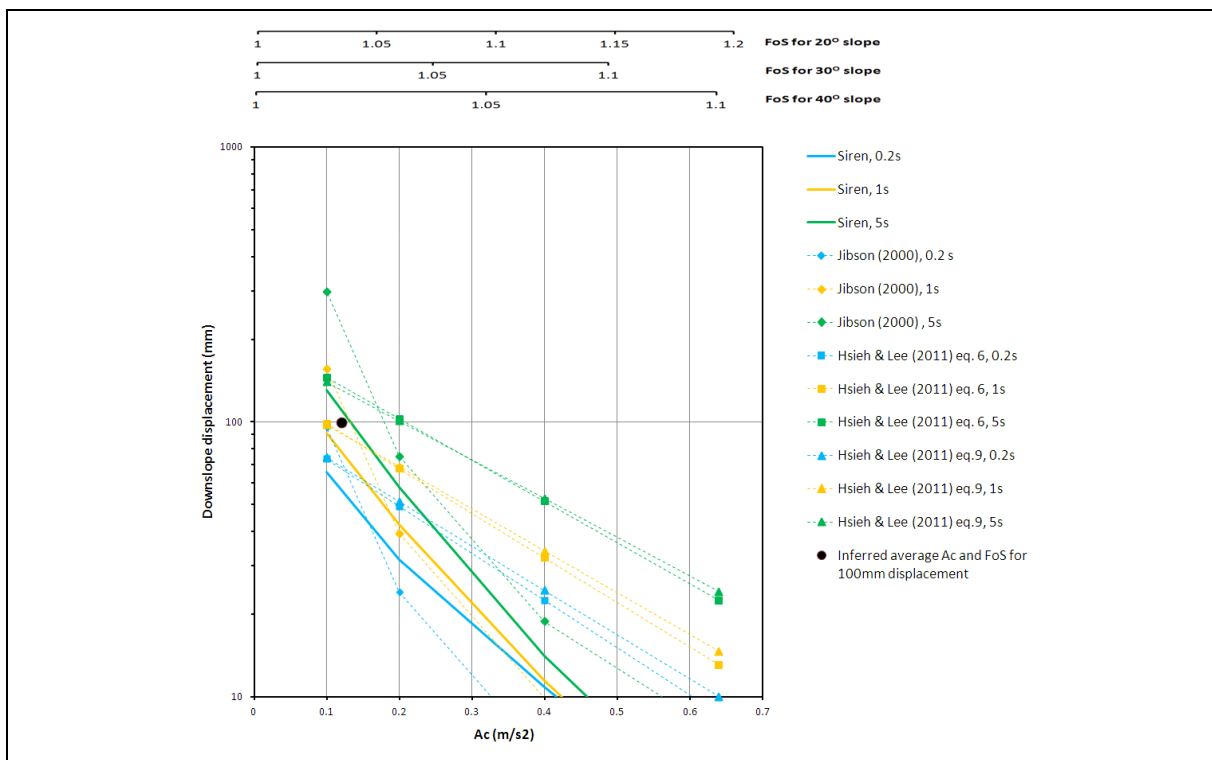
Figure 3.62   Downslope Displacements Calculated for 10% in 50 Years, and 100 m Crest Height Effect (1.4 PGA Amplification Factor)
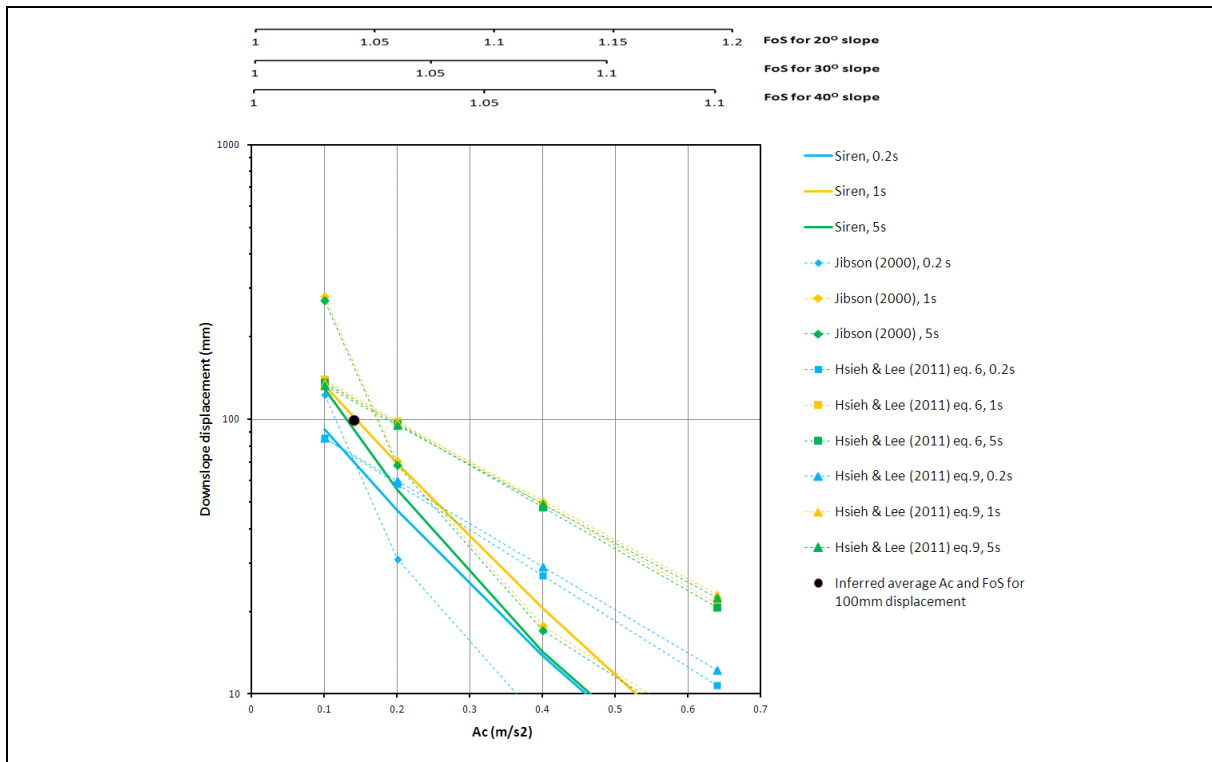
Figure 3.63 Downslope Displacements Calculated for 10% in 50 Years, and 300 m Crest Height Effect (1.4 PGA Amplification Factor)
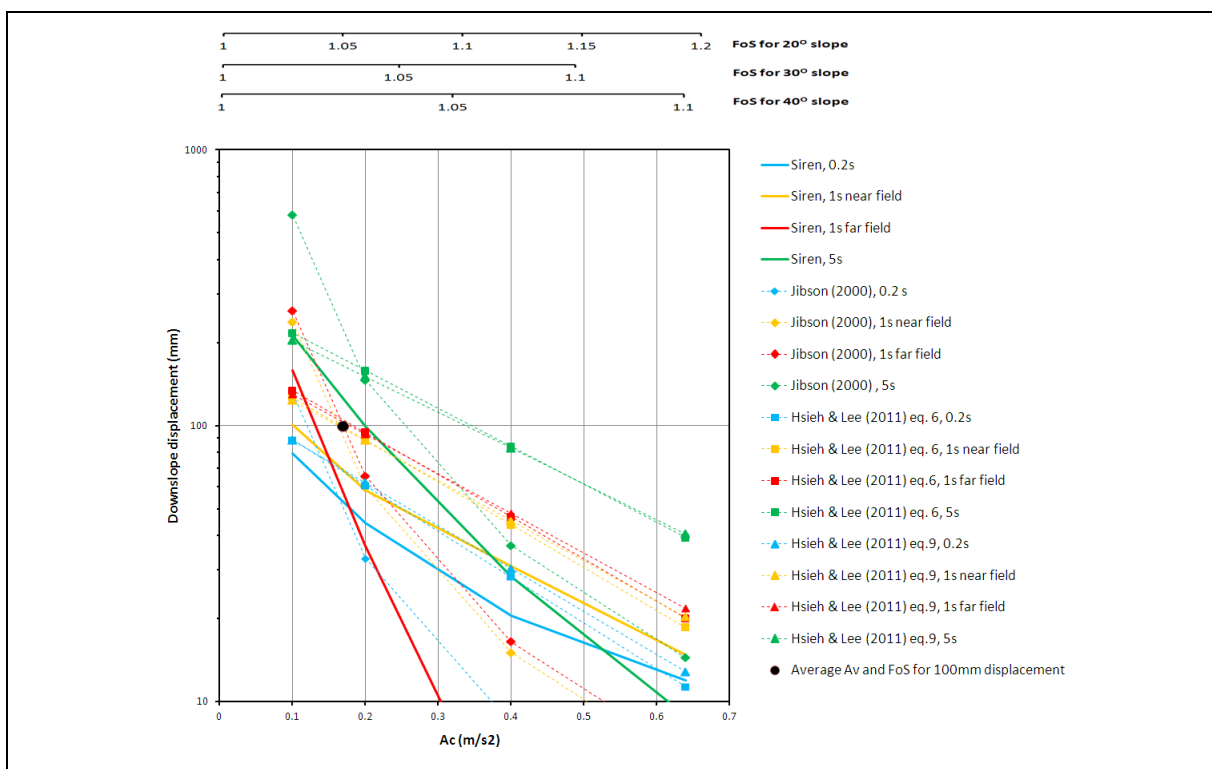
Figure 3.64 Downslope Displacements Calculated for 2% in 50 Years, and 30 m Crest Height Effect (1.2 PGA Amplification Factor)
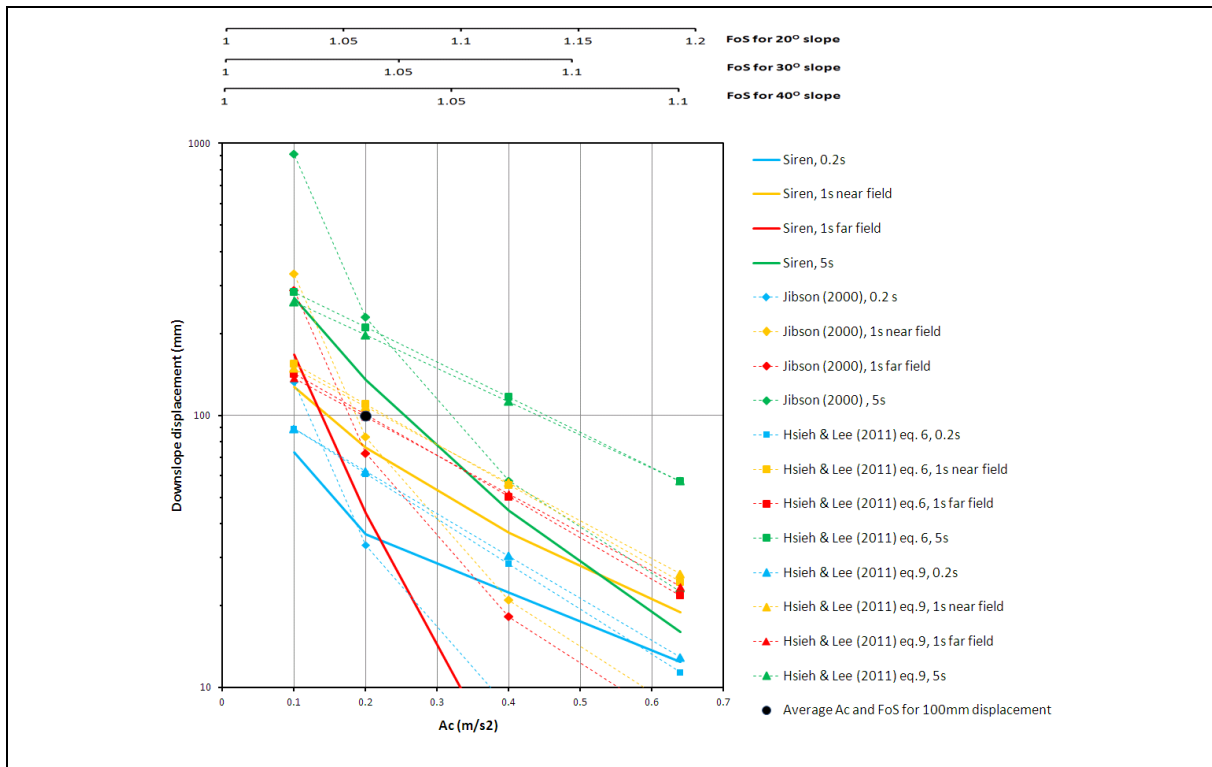
Figure 3.65   Downslope Displacements Calculated for 2% in 50 Years, and 100 m Crest Height Effect (1.2 PGA Amplification Factor)
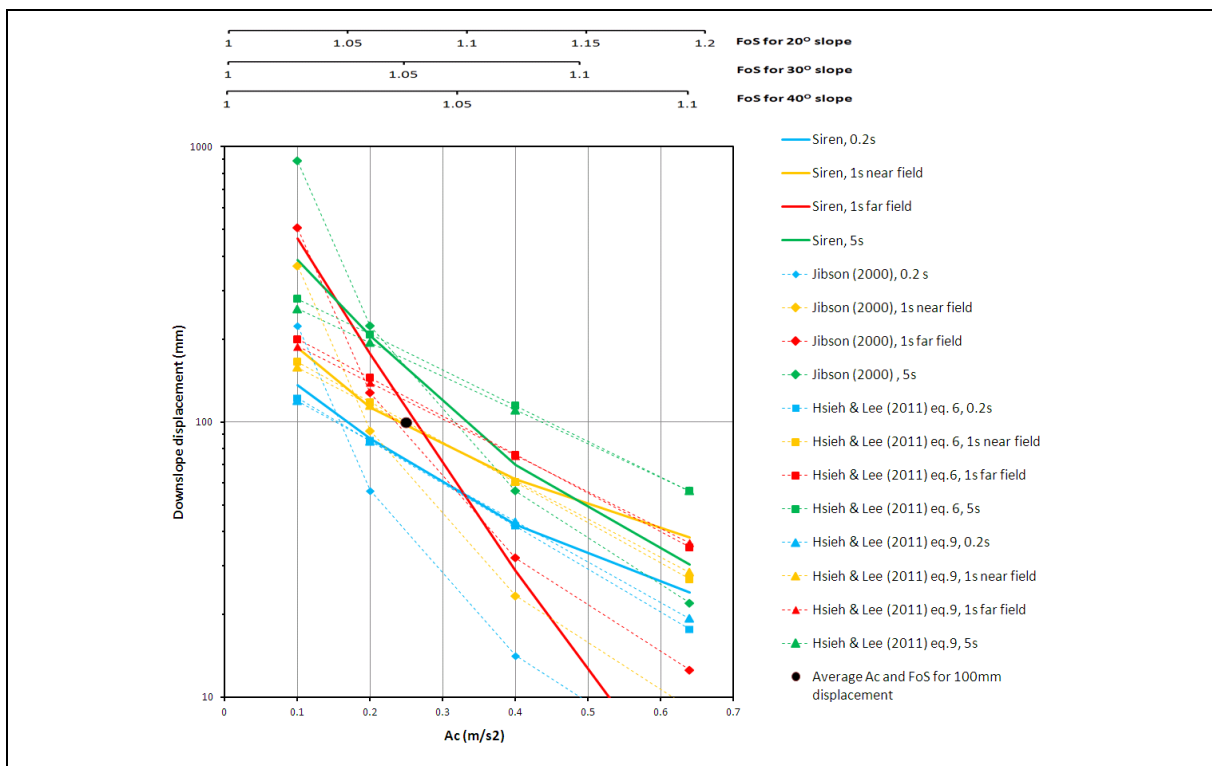
Figure 3.66   Downslope Displacements Calculated for 2% in 50 Years, and 300 m Crest Height Effect (1.2 PGA Amplification Factor)
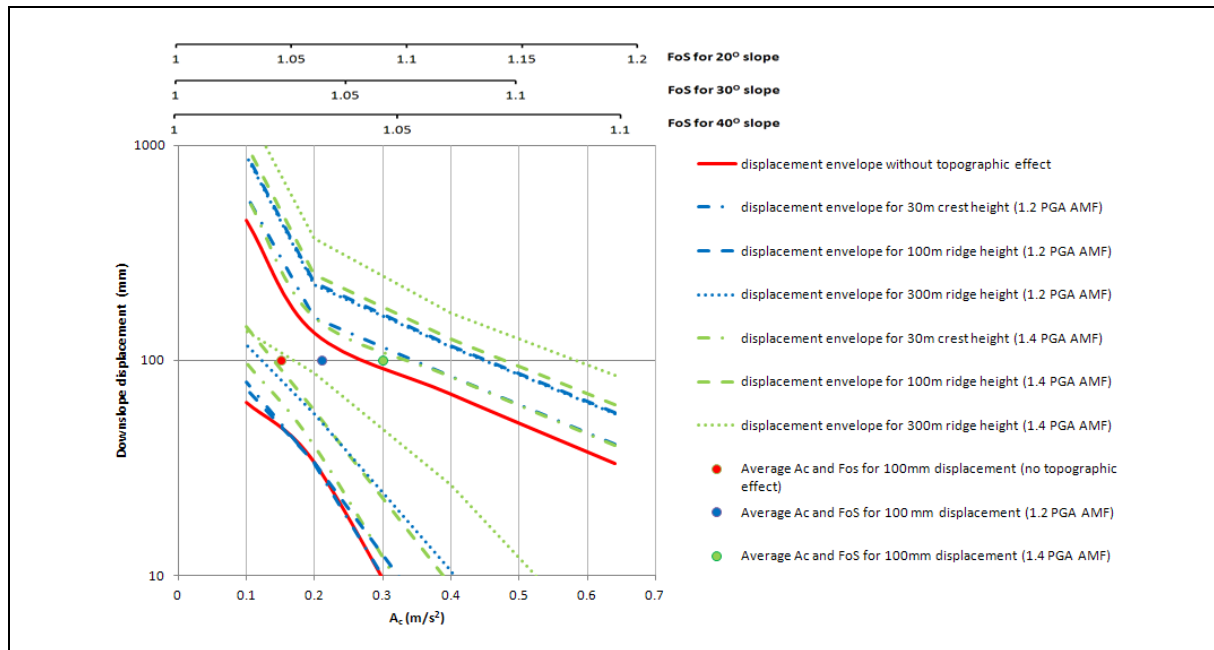
Figure 3.67 Topographic Effect on Earthquake-induced Landslides Displacement for 2% in 50 Years Ground Motion (No Topographic Effect and Topographic Effect with 1.2 and 1.4 PGA Amplification Factors)

Table 3.4 A_c (m/s^2) Corresponding to the 100 mm Threshold Displacement for Triggering of Landslide

PGA Amplification Factor	Probability of being Exceeded in the Next 50 Years	A_c (m/s^2) Considering a Ridge Height (m) of			
		0	30	100	300
1.4	10%	0.03	0.05	0.12	0.14
1.4	2%	0.15	0.19	0.27	0.37
1.2	2%	0.15	0.17	0.20	0.25

Summary

Based on the above seismic slope displacement assessments, it is found that both numerical models (*Oasys* SIREN and Dynamic FLAC) and empirical correlations produce comparable results. The findings help identify the most critical scenario for earthquake-induced landslides i.e. a long period (1 s far-field or 5 s) event of the 2% in 50 years seismic ground motions. The topographic effect significantly affects the induced slope displacements, especially for a ridge higher than 100 m. However, the threshold displacement of 100 mm required to trigger landslides is reached for a relatively low static FoS, implying that earthquakes likely to happen in Hong Kong will generally have a limited effect on landslide triggering even under 2% in 50 years ground motions. In high ridge areas, the topographic amplification effects will be more significant. More discussions will be provided in the susceptibility microzonation mapping in Section 5.

4 Seismic Stability Analysis for Boulders

4.1 General

To study the seismic stability of boulders, a one-dimensional (1-D) dynamic stability analysis program has been created to assess the boulder fall hazard under seismic loadings.   In the present study, the horizontal acceleration time histories derived from site response analyses (Arup, 2018), the time histories with topographic effects considered for 30 m, 100 m and 300 m crest heights as well as the vertical acceleration time histories for the 2% in 50 years ground motions have been used.

The results of the dynamic stability analysis have been compared with those obtained using an energy approach.   This approach considers the amount of energy required for a boulder to fall under a certain peak ground velocity.   The equation used for the energy approach that accounts for the effects of vertical ground motions is based on Wong & Pang (1991) for multi-directional blasting vibration (see Section 2).

The stability of boulders is dependent on the geometry of the boulder, the characteristics of its position on the ground, and the surrounding soil/rock conditions.   In this study, spherical boulders of 100 kg, 1,000 kg and 10,000 kg have been considered.   It is further assumed that the boulders are sitting on rock and the primary falling mode of the boulder is by tipping.

The results of the analyses are presented in terms of the limiting eccentricity necessary for the boulder to fall under a given acceleration time history.   The eccentricity of a boulder sitting on a slope is defined in Figure 4.1.   It corresponds to the horizontal distance between the centre of gravity of the boulder and the point around which it will rotate or tip.
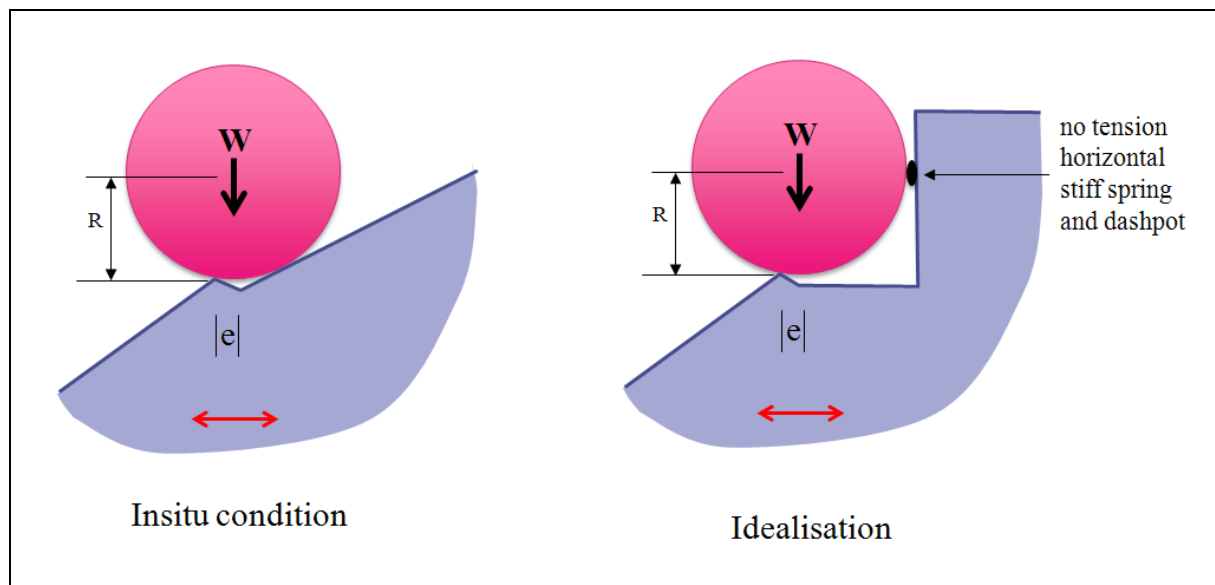
Figure 4.1   Analysis Model for Seismic Stability of Boulders

4.2 Dynamic Stability Analysis Methodology

The 1-D dynamic stability analysis program that has been used to assess the limiting eccentricity necessary for a boulder to fall under seismic loadings is based on the calculation of the relative displacement of the boulder to that of the ground at each time step of 0.001 s of the seismic accelerations time histories:

$$d_r = (d_g - d_b) \times 10^3 \dots\dots\dots\dots\dots\dots\dots\dots\dots\dots\dots\dots(4.1)$$

where d_r = relative displacement of the boulder (in mm)
              d_g = displacement of the ground (in m), and is defined as follows:

$$d_{g\ i+1} = a_{gi} \times \Delta T^2 + 2 \times d_{gi} - d_{gi-1}$$

$$d_{g0} = 0 \text{ m}$$

       where ΔT = time step (= 0.001 s) (in s)
                       i = number of time steps considered
                     a_{gi} = imposed seismic ground acceleration at that time step (in m/s/s)

     d_b = displacement of the boulder (in m), and is defined as:

$$d_{b\ i+1} = a_{bi} \times \Delta T^2 + 2 \times d_{bi} - d_{bi-1}$$

$$d_{b0} = 0 \text{ m}$$

$$a_{bi} = \Sigma F_i / m_b$$

       where F_i = the forces applied to the boulder at the time step i (in N)
                      m_b = the mass of the boulder (in kg).

F_i is defined as illustrated in Figure 4.1 and calculated as:

(i) The spring force (F_s):

         if $d_g < d_b$, $F_s = K (d_g - d_b)$

         or else $F_s = 0 \text{ N}$

K being the spring coefficient (in N/m) to give a small displacement under the static restoring of the boulder and has the values listed in Table 4.1.

(ii) The dashpot force (F_d):

         if $v_g < v_b$ and $F_s \neq 0$, $F_d = D (v_g - v_b)$

         or else $F_d = 0 \text{ N}$

D being the dashpot coefficient (in N/m/s) to obtain critical damping of the boulder when it reconnects with the spring after lifting off. It has been assigned the values listed in Table 4.1.

Table 4.1 Spring (K) and Dashpot (D) Coefficients for Boulder Seismic Stability Analysis

Boulder Mass	K (N/m)	D (N/m/s)
100 kg	1,000,000	20,000
1,000 kg	10,000,000	200,000
10,000 kg	100,000,000	2,000,000

(iii) The gravitational force of the boulder (F_g):

$$F_g = 9.81 \times m_b \times (e + d_b - d_g) / R$$

where e (m_b) is the eccentricity of the boulder, and R is its radius.

In order to consider the effect of the vertical acceleration on the boulder stability as well, the gravitational force equation can be modified as follows:

$$F_{gv} = (9.81 - a_{vi}) \times m_b \times (e + d_b - d_g) / R$$

where a_{vi} (in m/s^2) is the imposed vertical acceleration at the ith time step.

The limiting eccentricity of the boulder required for it to move under a certain ground motion has been deduced using the above equations. It corresponds to the eccentricity at which the relative displacement of the boulder diverges to a very large value with time as illustrated in an example shown in Figure 4.2.
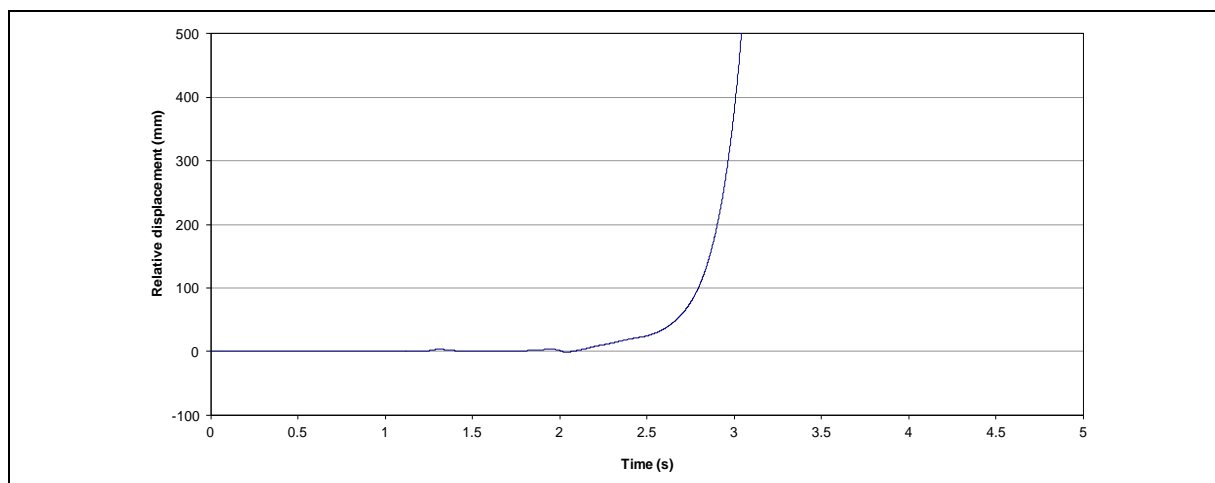
Figure 4.2 Calculated Relative Displacement when the Limit Eccentricity is Reached for a 100 kg Spherical Boulder, under the 2% in 50 Years, 0.2 s Horizontal Ground Motion

4.3 Energy Approach

The results presented above have been compared with the results of an energy approach that considers how much energy delivered by the ground motion is required to move a boulder.

The energy to cause the boulder to tip (E_t) is defined as:

$$E_t = F_h \times d_t \dotfill (4.2)$$

where F_h (N) is the average horizontal force applied to the boulder, and d_t is the distance that the boulder has to move for it to tip ($= e$).

$$F_h = 0.5\, m_b \times g \times e\, /\, R$$

The eccentricity can therefore be derived from the fundamental energy equilibrium equation as:

$$0.5\, m_b\, V^2 = 0.5\, m_b\, g\, e^2\, /\, R$$

i.e.

$$e = V\, (R\, /\, g)^{0.5}$$

where V (m/s) is defined as the peak horizontal particle velocity of the ground motion PPV.

When considering the effects of the vertical ground acceleration on the seismic stability of boulders, the energy equation can be modified as recommended by Wong & Pang (1991) by taking:

$$V = 1.35 \max (PPV_h, PPV_v)$$

It should be noted that the horizontal PPV exceeds the vertical PPV as expected from the response spectra shown in Figure 3.28.

4.4 Results of Boulder Fall Analysis

Based on the methodology described above, a boulder seismic stability analysis has been carried out using the 1-D dynamic stability method and the energy approach. The results of both methods have been compared in terms of the limiting eccentricity of the boulder, that is required for it to tilt under a given seismic ground motion.

4.4.1 1-D Dynamic Stability Analysis

The 1-D dynamic stability analysis has been carried out for 2%, 10% and 63% in 50 years seismic ground motions. The topographic effects have also been taken into account. Figures 4.3 to 4.5 show the calculated limiting eccentricity for different ground motions for a spherical boulder with different masses (100 kg, 1,000 kg and 10,000 kg). The results show

that the limiting eccentricity required for the boulder to tip under seismic loadings significantly increases with the level of ground motion.   However, even for a 1 s near-field, 2% in 50 years ground motion, the highest limiting eccentricity for a 10,000 kg boulder is only 27 mm, which is considered as a small value.   The results indicate that under the probable earthquake ground motions in Hong Kong, boulders do not have any likelihood to fall unless they are already very close to toppling.
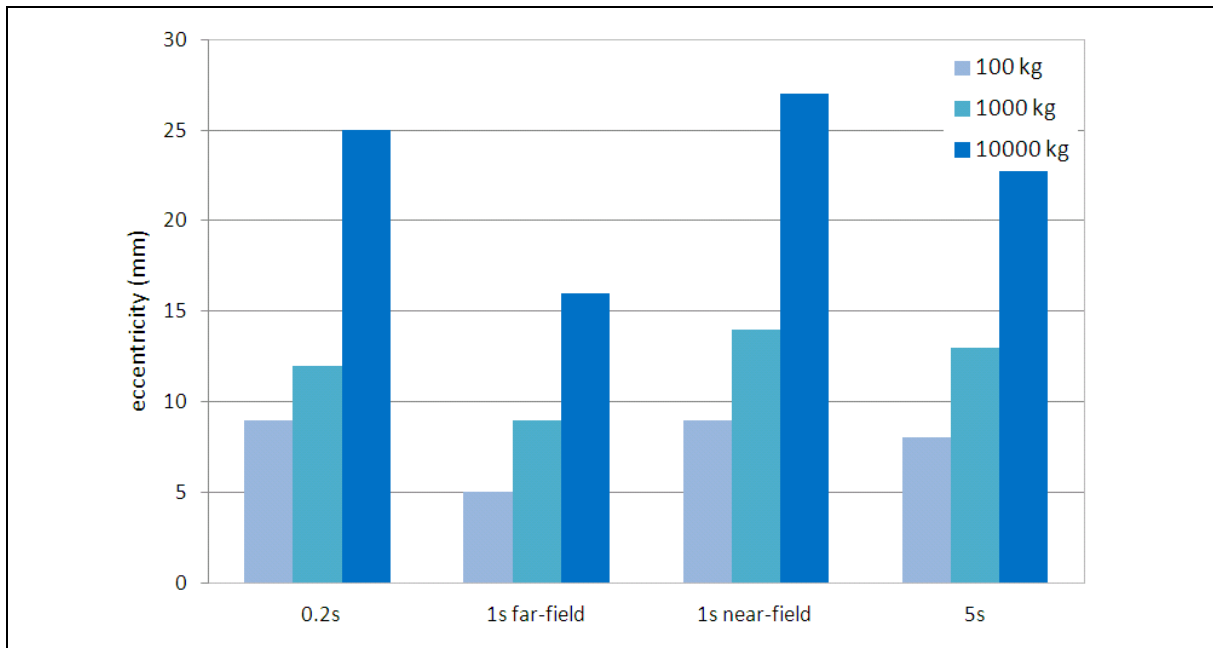
Figure 4.3   Limiting Eccentricity Required for the Boulder to Fall, for 2% in 50 Years Ground Motion
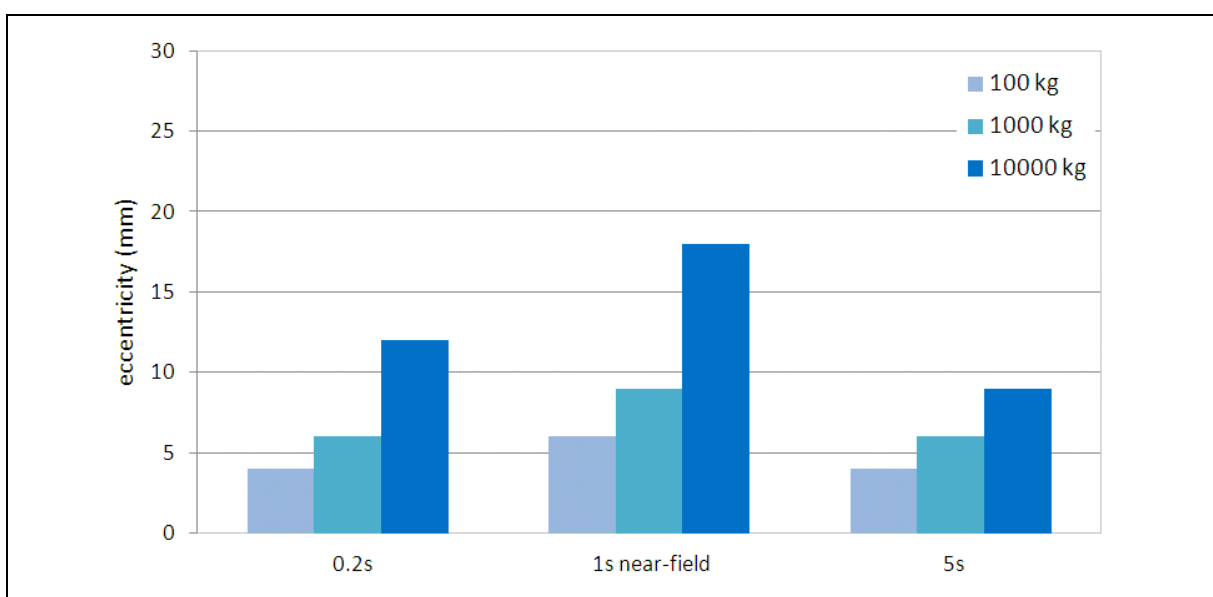
Figure 4.4   Limiting Eccentricity Required for the Boulder to Fall, for 10% in 50 Years Ground Motion
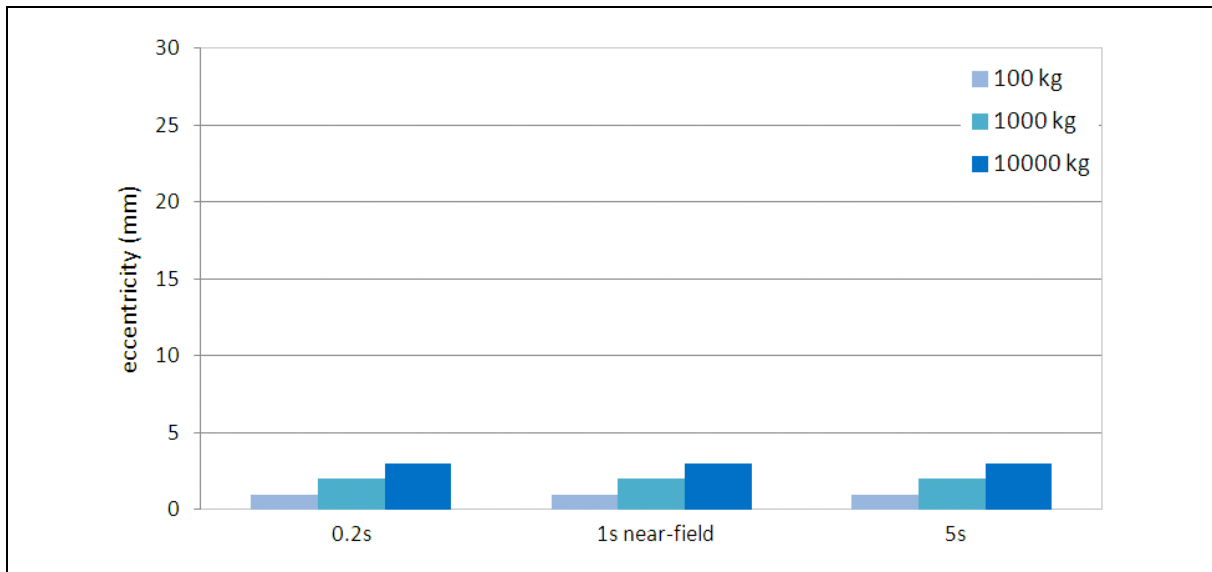
Figure 4.5   Limiting Eccentricity Required for the Boulder to Fall, for 63% in 50 Years Ground Motion

In order to investigate the topographic effects on the seismic stability of boulders, the 1-D dynamic stability analysis has been carried out for a 10,000 kg boulder with the 2% in 50 year time histories that account for the topographic effects for 30 m, 100 m, and 300 m ridge heights (see Figure 4.6).   It shows that higher crests tend to result in higher limiting eccentricity values.   As the crest height increase from 30 m to 300 m, the limiting eccentricity increases to 31 mm, 24 mm, 36 mm and 40 mm for the 0.2 s short period, 1 s far-field, 5 s near-field , and 1 s near-field ground motions respectively.   For a 10,000 kg spherical granitic boulder of about a metre radius, theses values considered as very small.
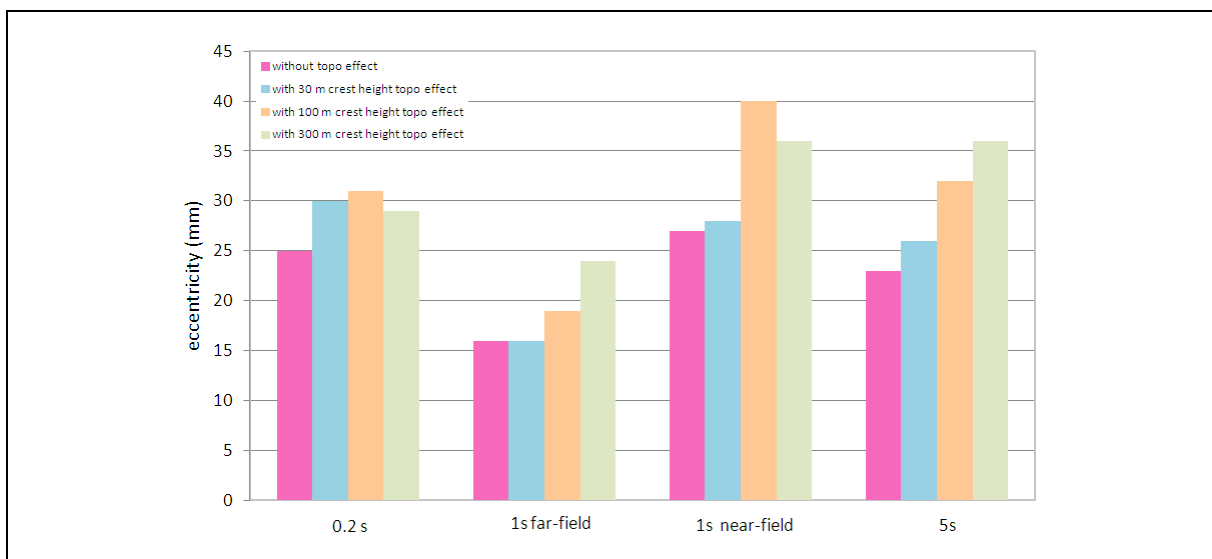
Figure 4.6   Limiting Eccentricity Required for the Boulder of 10,000 kg to fall for 2% in 50 Years Ground Motion, with Topographic Effect (30 m, 100 m, and 300 m Crest Height)

In addition, the effect of the vertical acceleration has been checked. Figure 4.7 shows the comparison between the horizontal ground motion results (without topographic effect) and the ones calculated by taking the vertical acceleration into account. Clearly, the effect of the vertical acceleration is negligible.
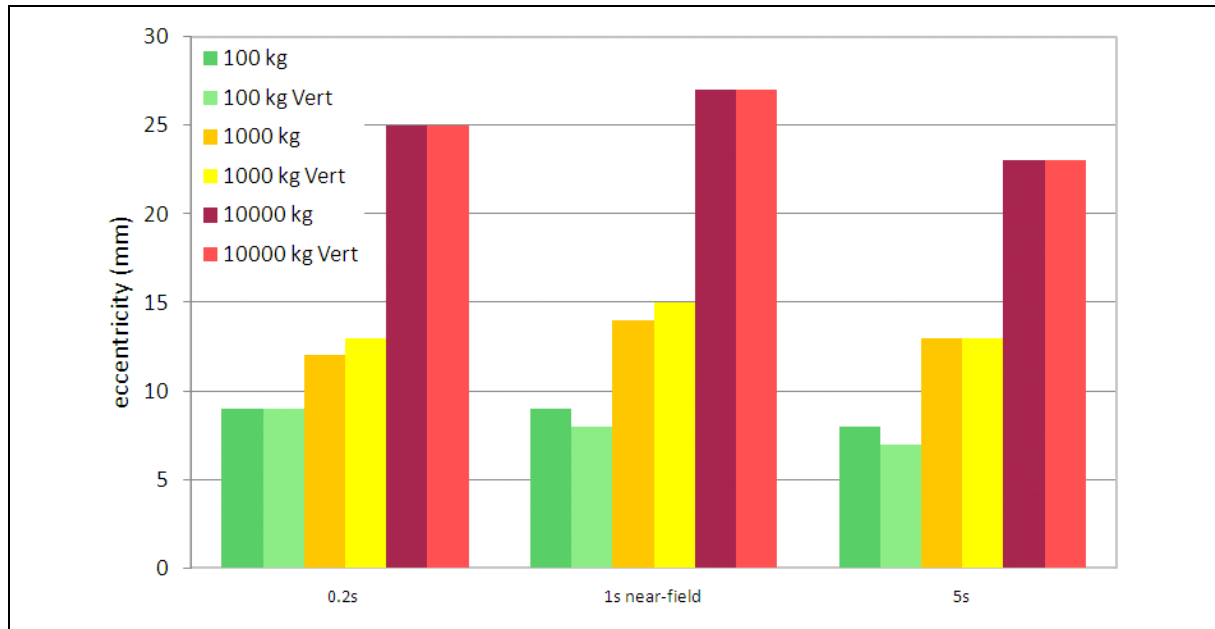
Figure 4.7   Effect of the Vertical Motion on the Limiting Eccentricity Necessary for Boulders of 100 kg, 1,000 kg and 10,000 kg to Fall Under a 2% in 50 Years Ground Motion

4.4.2   Comparison with the Energy Approach

The results between 1-D dynamic stability analysis and the energy approach have been compared. Figures 4.8 to 4.11 compare the eccentricity calculated by the energy approach and that calculated by the dynamic analysis for cases with no topographic amplification effect, and with 30 m, 100 m, and 300 m ridge height effects considered respectively. In general, the correlations are good, although there is a consistent trend that the energy approach would predict a larger eccentricity to retain equilibrium.

When comparing the results of both methods modified to account for the vertical acceleration effect, Figure 4.12 shows that the energy approach gives a slightly higher required eccentricity than the dynamic analysis. The results are consistent with the cases in which vertical acceleration has been ignored. This implies that the recommendations of Wong & Pang (1991) who suggested that the velocity would be increased by 35% (i.e. $V = 1.35$ max (PPV$_x$, PPV$_y$)) would give much higher limit eccentricity values than the dynamic stability approach. Therefore, this additional coefficient appears not appropriate to account for the vertical ground motion effect in the seismic stability assessment for boulders.
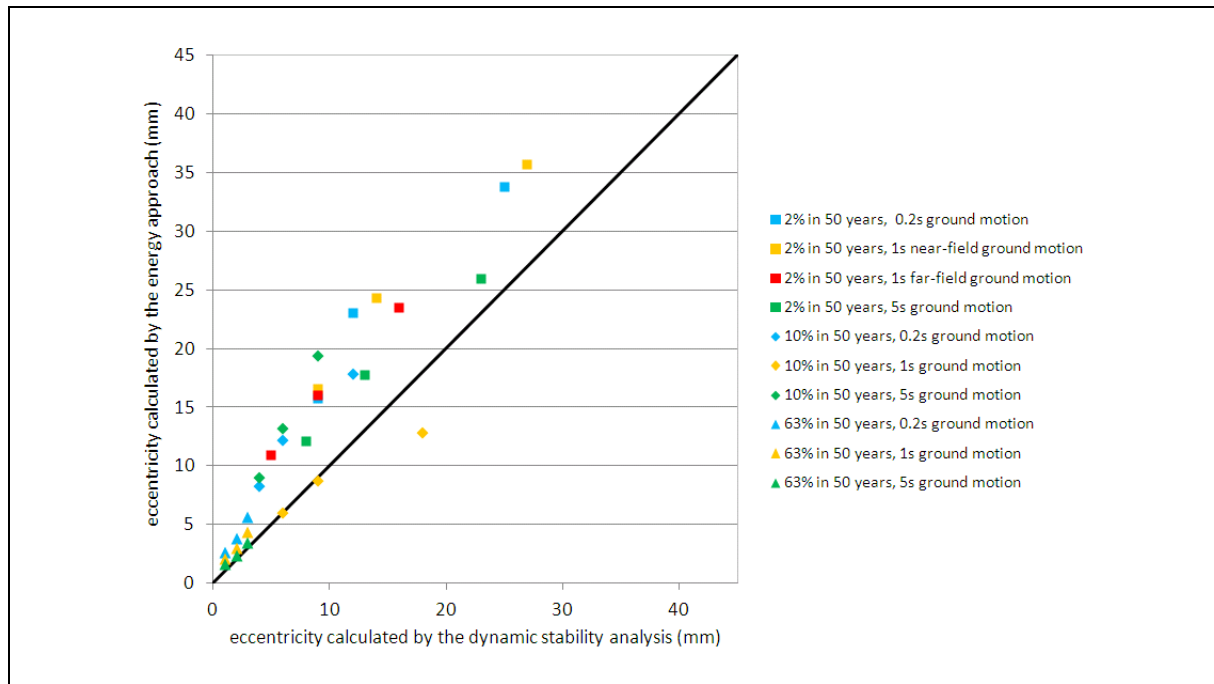
Figure 4.8 Comparison between Limiting Eccentricity of Boulder Fall Calculated by the Energy Approach and by Dynamic Stability Analysis for No Topographic Effect
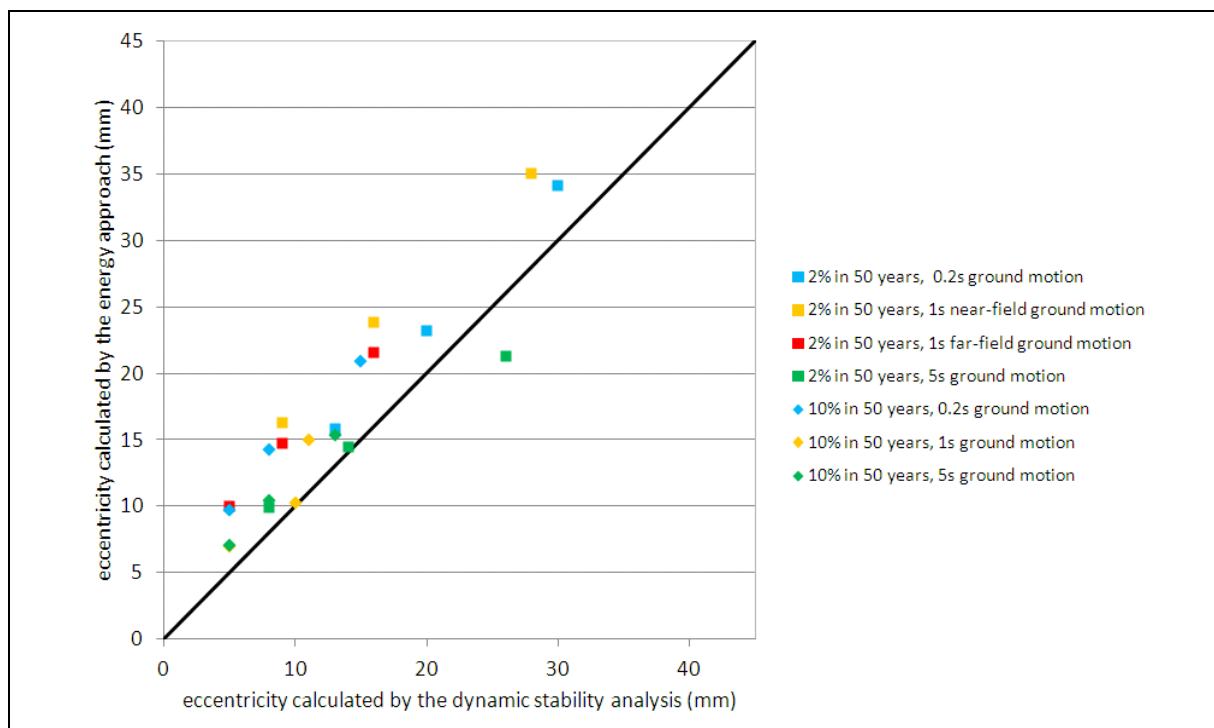
Figure 4.9 Comparison between Limiting Eccentricity of Boulder Fall Calculated by the Energy Approach and by Dynamic Stability Analysis for a 30 m Crest Height Topographic Effect
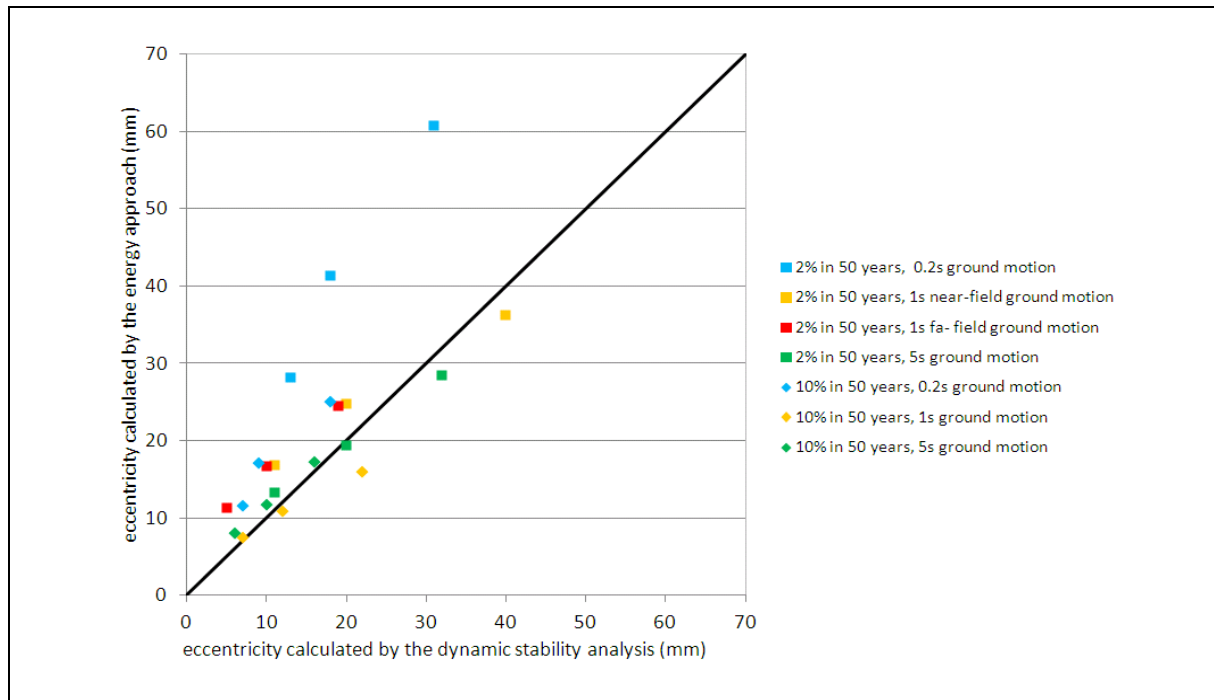
Figure 4.10   Comparison between Limiting Eccentricity of Boulder Fall Calculated by the Energy Approach and by Dynamic Stability Analysis for a 100 m Crest Height Topographic Effect
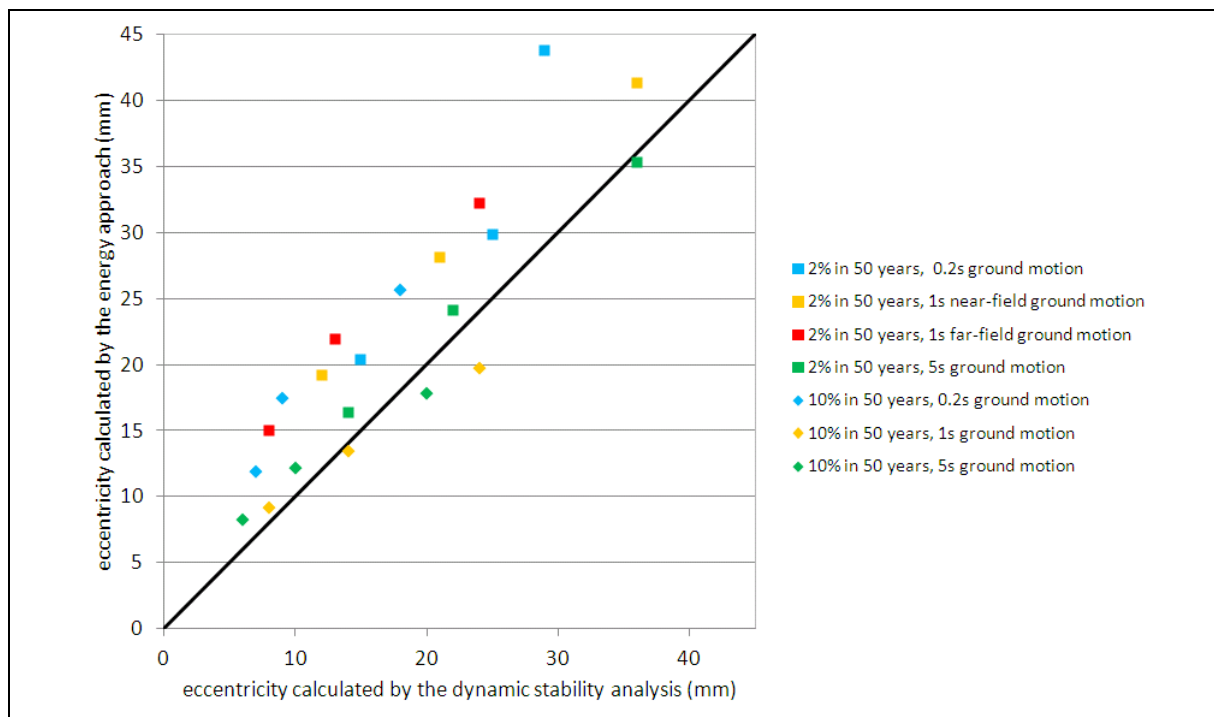
Figure 4.11   Comparison between Limiting Eccentricity of Boulder Fall Calculated by the Energy Approach and by Dynamic Stability Analysis for a 300 m Crest Height Topographic Effect
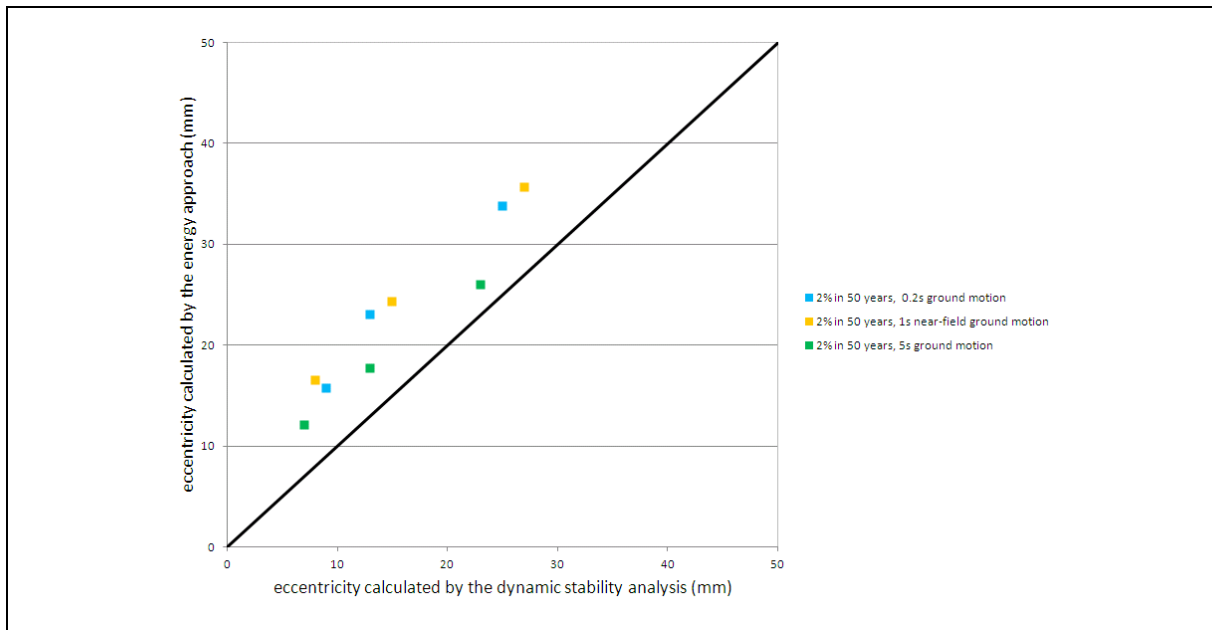
Figure 4.12   Comparison between Limiting Eccentricity of Boulder Fall Calculated by the Energy Approach and by Dynamic Stability Analysis Accounting for the Vertical Acceleration (and No Topographic Effect)

4.4.3   Effect of Boulder Shape

As discussed in Section 2.5.2, Haneberg (2009) showed that boulders with higher aspect ratios would require lower eccentricities to topple.   The energy approach gives a direct indication to the effect of aspect ratios in that the equation shows that the limiting eccentricity is directly related to the square root of the height of the centre of mass of the boulder above its base.   Therefore, for example, for a prismatic boulder having a height four times its width, the height of its centre of mass would double that of a spherical boulder.   It means that the eccentricity required would be about 1.4 times that that required for a sphere.

It is therefore concluded that while boulders with high vertical to horizontal aspect ratios will require larger eccentricities to limit falling, the eccentricity is not likely to be more than about 1.5 times that of a spherical boulder.

4.4.4   Other Failure Modes

Apart from rolling and falling, sliding of a boulder, which is initially resting on an inclined surface, is another possible failure mode under earthquake shaking.   In principle, this mode of failure is essentially the same as the sliding failure of a slope, where the failure mass is assumed as a rigid block.   Thus, the same conclusions reached regarding the natural terrain slope failure (e.g. the critical acceleration values shown in Figure 3.67) should also be applicable to boulders when sliding failure is concerned.   In addition, there is essentially no chance of pore water pressure build up in boulders during rainstorms.   Therefore, for a boulder to fail in sliding mode, the static FoS against sliding will have to be very low at the time of earthquake loading.

5 Landslide Susceptibility Analysis

5.1 General

A regional landslide susceptibility model has been developed for the natural terrain areas within the Study Area of this study. The susceptibility model adopts a landslide hazard zonation approach to identify and document those areas considered the most susceptible to the initiation of landslides. Varnes (1984) recommended three key principles for consideration in the landslide hazard zonation process:

> (a) Natural slope failures in the future will most likely be in similar geological, geomorphic and hydrological situations that have led to past and present failures (i.e. predisposition factors).
>
> (b) The main conditions and processes that cause the landslides (i.e. triggering factors) should be identified and understood.
>
> (c) The relative contributions of the identified predisposition and triggering factors should be evaluated to give a measure of the factors and reflect their importance in contributing to landslides.

To conduct the landslide susceptibility analysis with reference to the three principles, a statistical approach has been adopted for this study. The Enhanced Natural Terrain Landslide Inventory (ENTLI) has been used to represent the past instability locations. Some key general possible susceptibility factors have been identified and the landslide density has been calculated within each particular factor. The landslide density for each class of the initiation factors has been compared to assess the importance of those factors which contribute to landslides. The landslide susceptibility map has subsequently been generated by a matrix method which included the selection and combination of different rankings of the selected susceptible factors.

Geographical Information System (GIS) has been used as a tool to analyse different initiation factors based on the existing information. Each initiation factor has been compared with the landslide density, which is considered as a direct measure of the probability of landslide occurrence, to give the susceptibility ranking of each factor. The ranking of each factor has been overlaid in the GIS to classify the susceptibility when combining all factors. The reliability of the final susceptibility class has also been checked by the landslide density to ensure that the classification could measure the expected probability of landslide occurrence.

The susceptibility map produced by analysing the ENTLI data only presents the susceptibility of landslides triggered by rainfall. Over most of the area, this susceptibility is also directly indicative of the susceptibility of the natural terrain to earthquake-induced landslides as will be discussed in Section 5.5. For areas where the topographic effects are applicable, there would be a slight increase in the earthquake-induced landslide susceptibility. As a result, the overall susceptibility map has been modified.

5.2 Desk Study Data

In view of the regional scale of the present study and in order to develop a systematic approach that could readily be adopted elsewhere within the territory of Hong Kong, the developed approach has made use of existing available digital datasets.   These include:

(a) Topographic information contained within the Lands Department 1:1,000 and 1:5,000 scale LIC Maps.

(b) Topographic information contained within the GEO 2010 LiDAR Survey Dataset.

(c) The location of built structures based on the BLDPOLY Polygon contained within the 1:1,000 scale LIC Maps.

(d) The location of roads based on the ROAD Polygon contained within the 1:10,000 scale LIC Maps.   (Note: the 1:10,000 scale maps have been used in favour of the 1:1,000 scale maps as these maps contain information on road type and classification).

(e) Information on the location and extent of man-made slope features and retaining walls within the GEO Slope Information System.

(f) Geological information contained within the Hong Kong Geological Survey 1:20,000 Solid and Superficial Geology Map Sheets.

(g) Information on the form and geomorphological setting of the natural hillside areas from the Landform Map developed under the Geotechnical Area Studies Programme (GASP).

(h) Information on the distribution and density of boulders and rock outcrops from the GEO Boulder Field Inventory.

(i) Information on the location, size (plan area only) and age of landslides from the GEO Enhanced Natural Terrain Landslide Inventory (ENTLI), up to 2009 only.

(j) Ortho-rectified aerial photographs for the years 1963 and 2010 have also been collected and reviewed to validate the findings of the above datasets.

(k) Rain gauge information for Gauge Nos. N07, N12, N28, N29, N31, N32 and N49 for the years 1984 to 2010.

The above information provides a wealth of information concerning the location and the scale of past instability in the Study Area as well as information on the topography, geology,

hydrology, geomorphology and extent of anthropogenic activity.   Whilst these datasets are of a variety of scales and resolutions, they are considered sufficiently accurate for a regional scale assessment, the main purpose of which is identifying those areas of high susceptibility from those with significantly lower susceptibility.

In addition, a natural terrain hazard study previously carried out for the Tsing Shan Foothill Area by MFJV (2003) has been used as a further reference as their study area is a part of the Study Area being assessed in the present study.   Their work included a susceptibility analysis and generation of site-specific susceptibility maps.

5.3   Delineation of Natural Terrain Boundary

In order to identify the susceptibility of natural terrain landslides within the Study Area, it is necessary to differentiate between those areas that comprise predominantly natural terrain hillside (natural terrain) and those areas that have been significantly affected by anthropogenic activities (urban area).   The methodology adopted to differentiate between these two areas is summarised below and presented graphically on Figures 5.1 to 5.6.
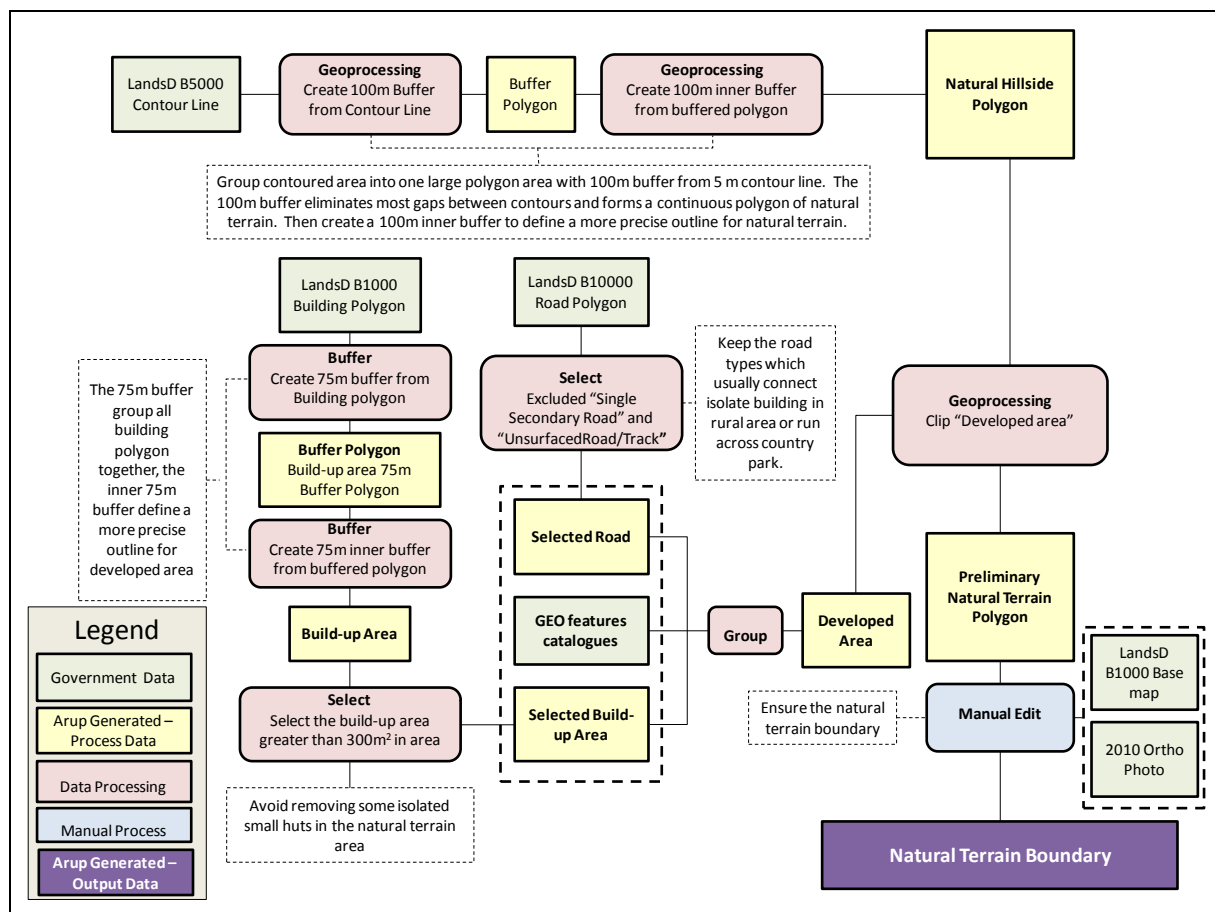
Figure 5.1   Flow Chart of Development of Natural Terrain Boundary
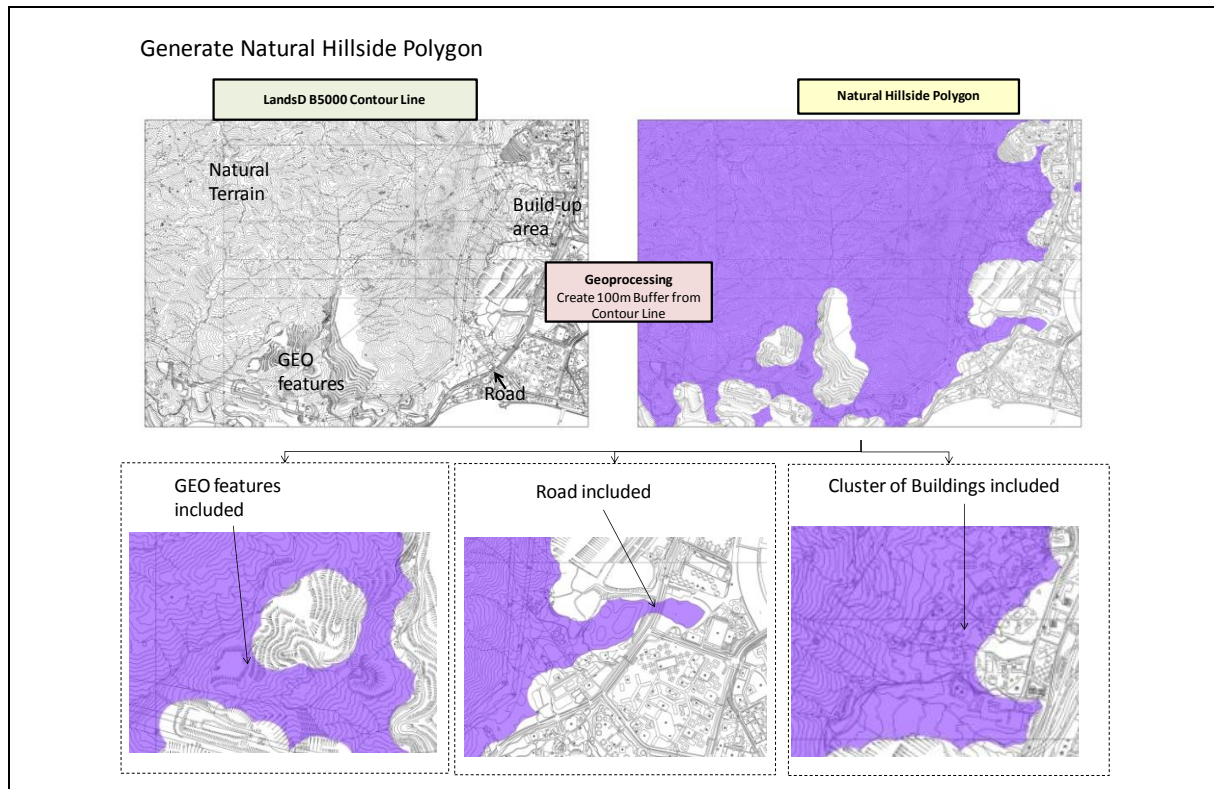
Figure 5.2   Flow Chart of Generating Natural Polygon
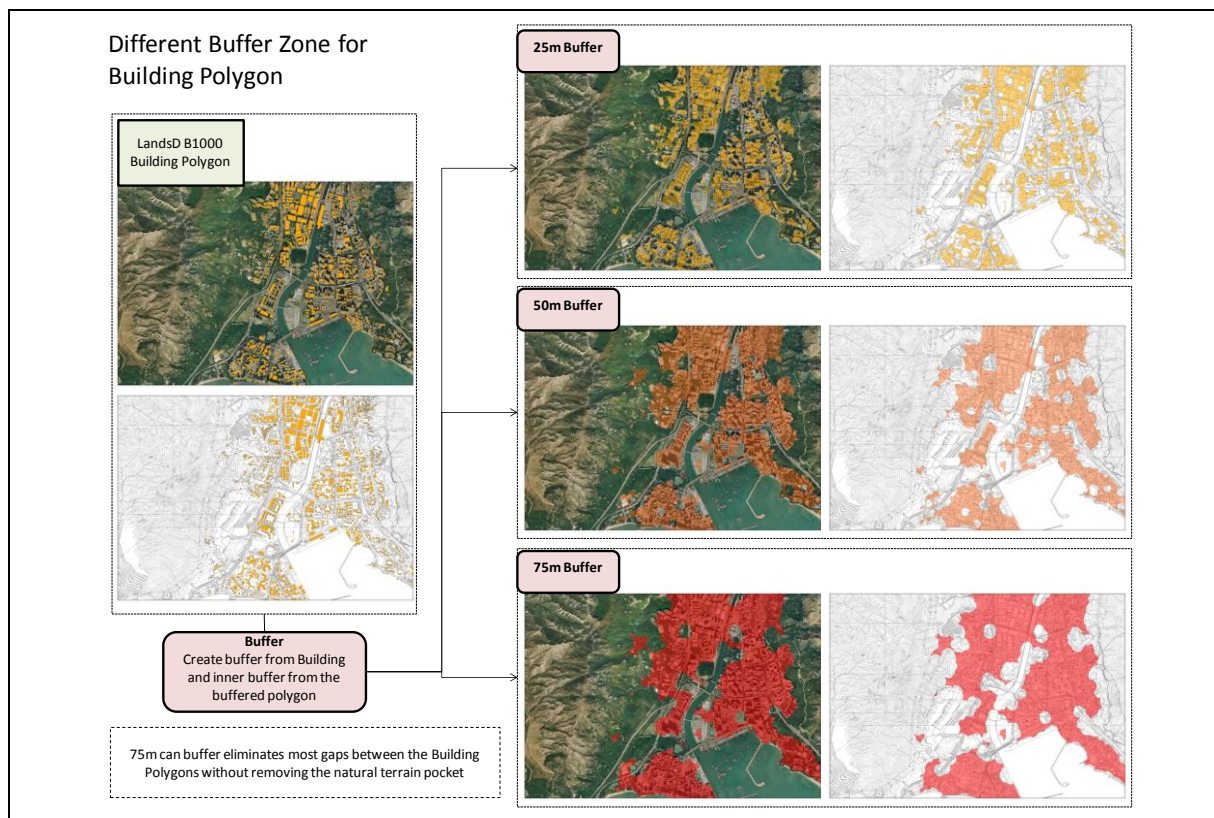
Figure 5.3   Flow Chart of Generating Building Polygon
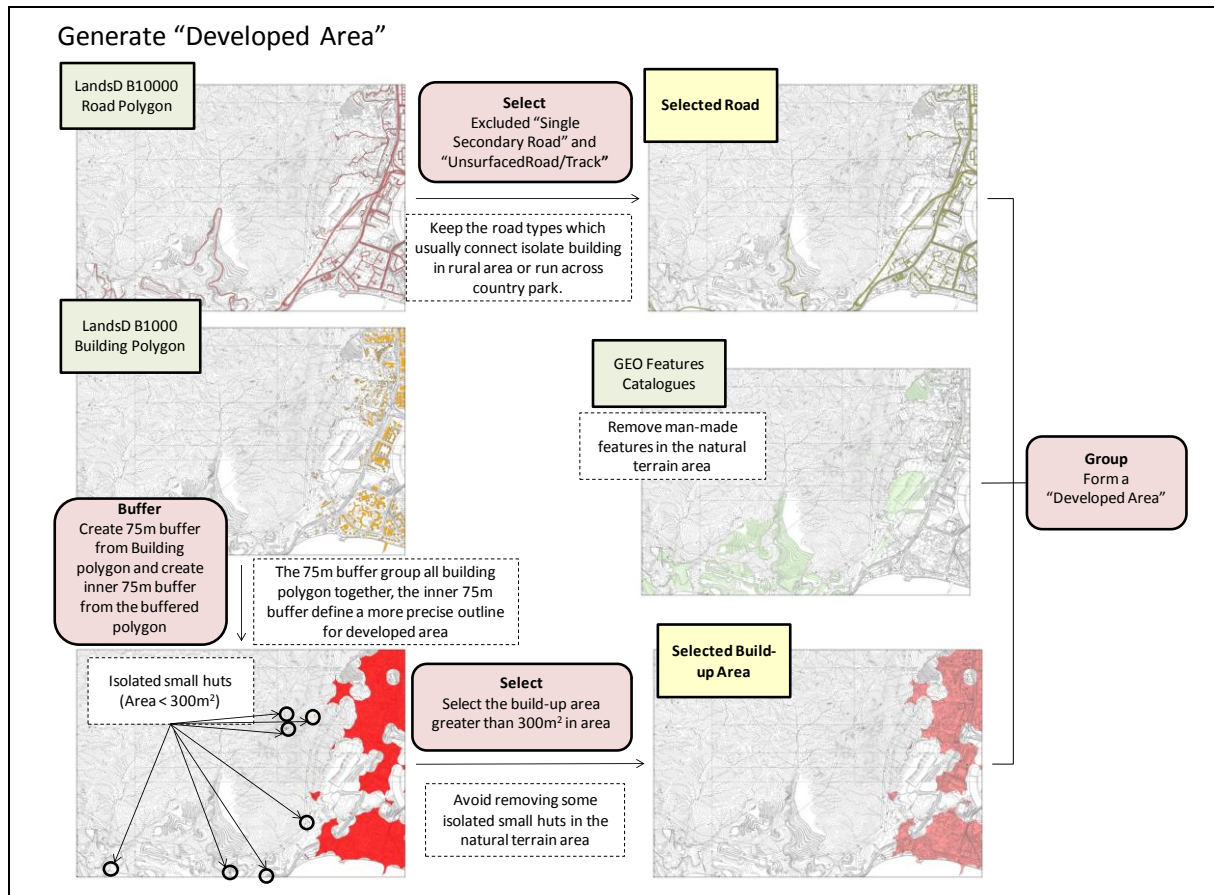
Figure 5.4   Flow Chart of Generating "Developed Area"
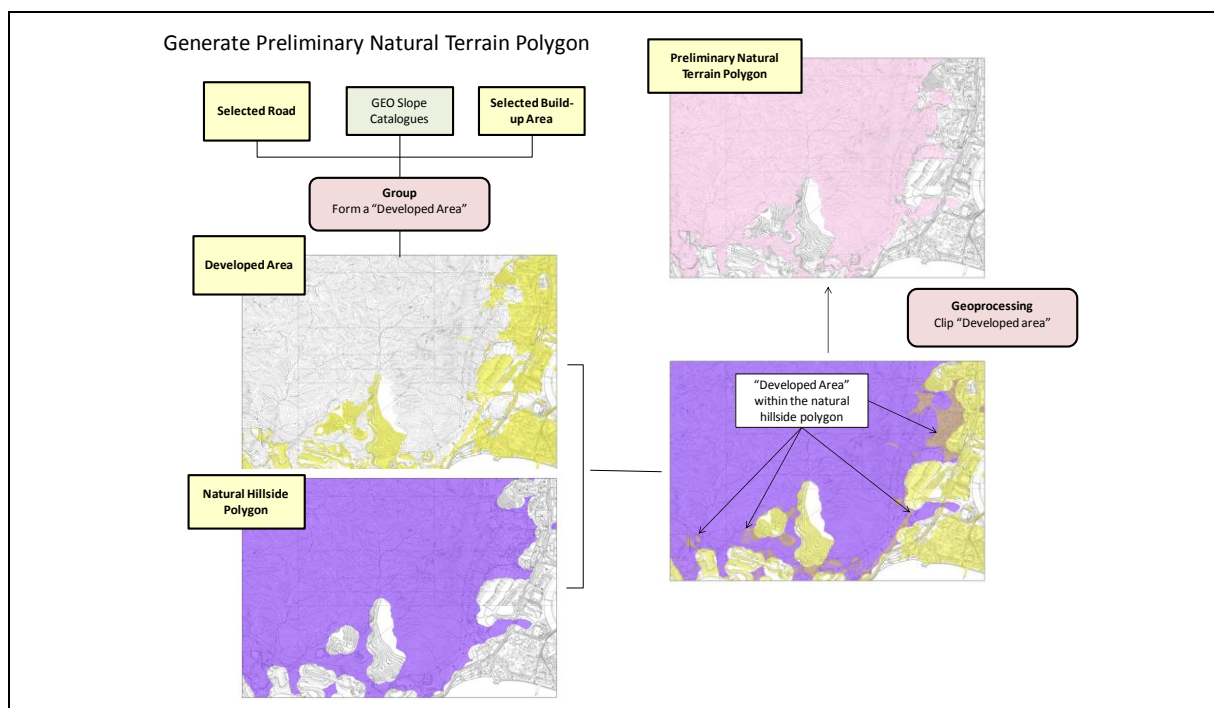
Figure 5.5   Flow Chart of Generating Preliminary Natural Terrain Polygon
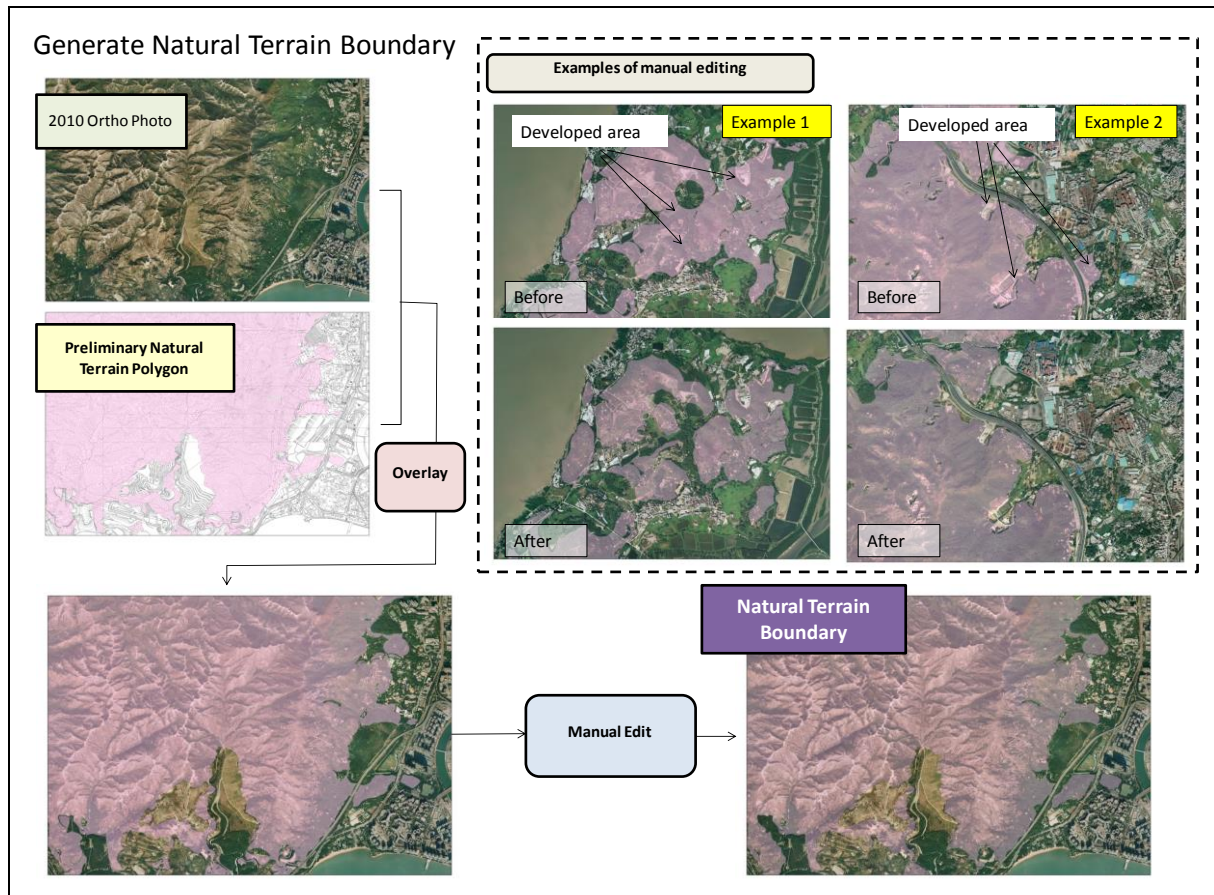
Figure 5.6   Flow Chart of Generating Final Natural Terrain Boundary by Manual Editing

(a) The contour lines shown in 1:5,000 scale topography maps have been used as a basis to define the general areas of natural terrain.   These contour lines typically present only on the LIC Maps within areas of natural hillside and are absent in urban or disturbed areas.   The contour line areas have been linked by the buffer function of GIS in order to roughly generate a polygon that represents predominantly the natural terrain area, as shown in Figure 5.2.

(b) Anthropogenic features have been clipped from the predominate natural terrain areas based on the locations of buildings, roads and man-made slope features recorded in the LIC Maps (BLDPOLY & ROAD Polygons) and the GEO Slope Catalogue, as shown in Figures 5.3 to 5.5.

(c) Validation of the predominant natural terrain areas generated under Steps 1 and 2 above has been carried out through a review of the 2010 ortho-rectified aerial photograph and 1:1,000 LIC maps of the Study Area.   Any necessary manual refinements to the polygon have then been carried out to

> remove obvious areas of anthropogenic disturbance and finalise the natural terrain boundary (Figure 5.6).

The final natural terrain boundary presented in Figure 5.7 would be used for further analyses of natural terrain landslide hazards. The data for those areas outside the boundary, including those ENTLI data, would be discarded.

It should be noted that the natural terrain boundary is not the same as that for the boundary of the rock site class defined in the seismic microzonation study (Arup, 2018) as their definitions are different. Natural terrain is defined as the area that has not been developed, whereas the rock site class is defined mainly based on slope gradient.
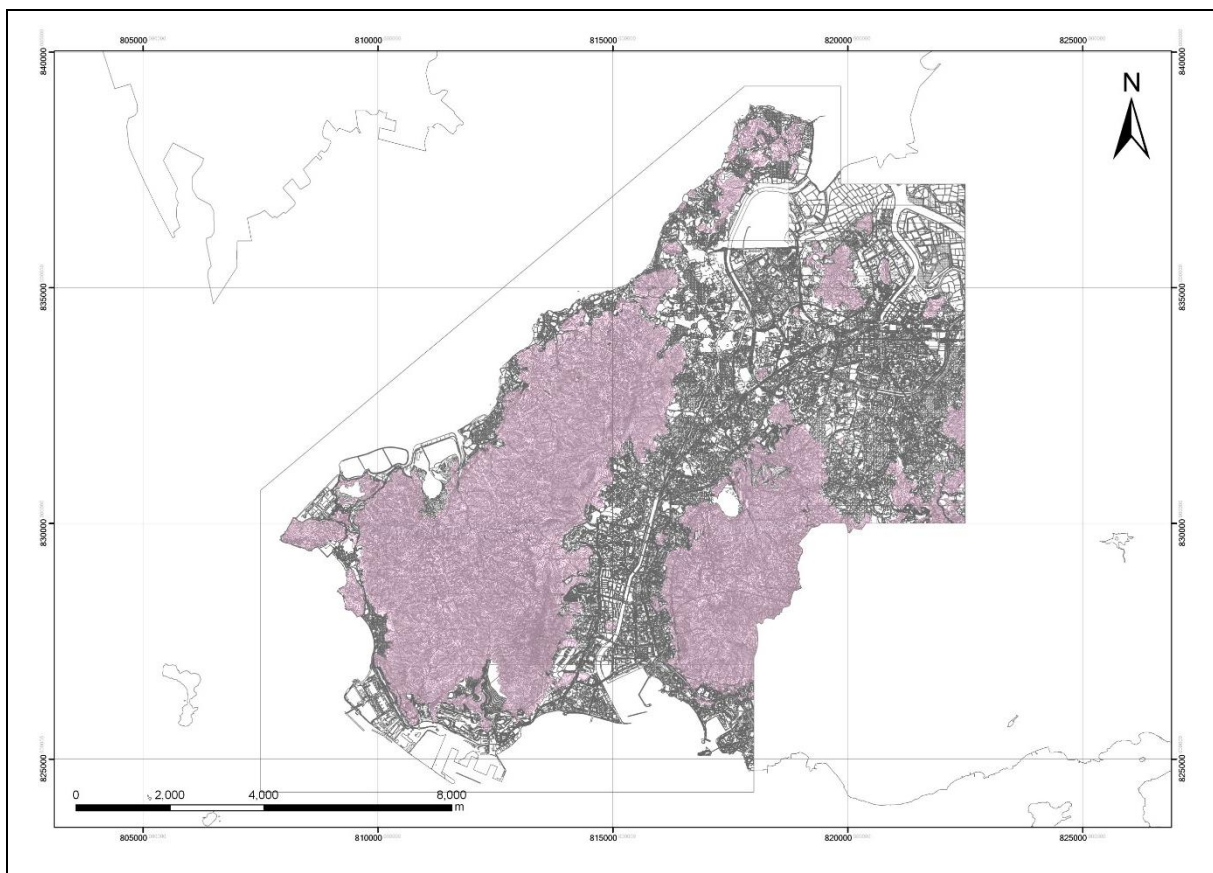
Figure 5.7   Final Natural Boundary in the Study Area

5.4   Past Instability

5.4.1   Landslide Datasets

The ENTLI consists of an inventory of historical natural terrain landslides compiled using available aerial photographs between 1924 and 2009. This inventory has been used as the primary source of information for the location and size (plan area) of the landslide sources, and the age of past landslides within the natural terrain area (Figure 5.8).
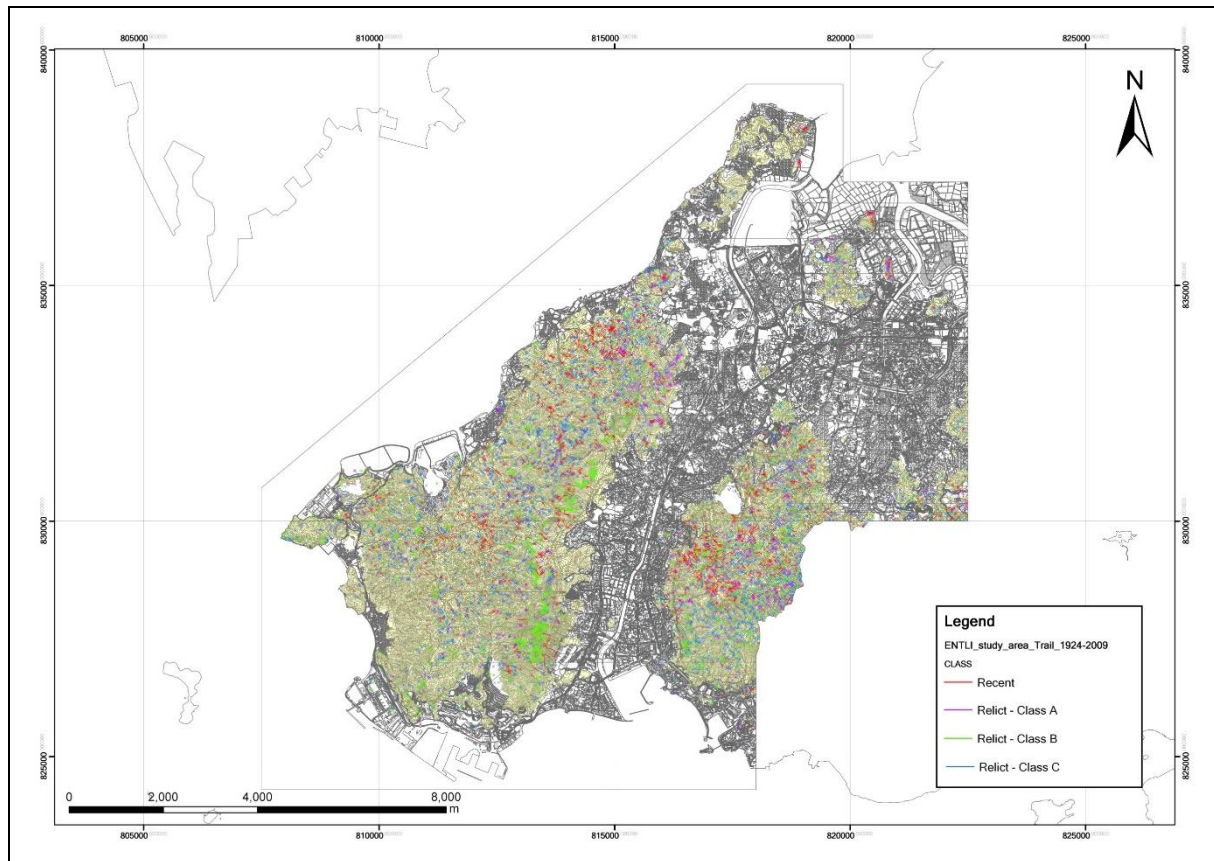
Figure 5.8   ENTLI Record up to 2009 with the Natural Boundary

The landslide records within the ENTLI have been broadly classified into two groups with regard to the date of occurrence, namely, recent landslides and relict landslides, defined as follows.

      (a) Recent landslides

           Recent landslides are those that clearly occurred within the time scale of the available aerial photographs.   For the majority of Hong Kong, they refer to landslides that occurred after about 1961.

           The year of aerial photographs in which landslide was first identified, as well as the date of the preceding available aerial photographs, are also recorded in the ENTLI.

      (b) Relict landslides

           Relict landslides are those that occurred earlier than the time scale of the available aerial photographs.   In general, they refer to landslides that occurred before 1962.

           The relict landslides in the ENTLI have been further

classified as Relict Class A, Class B or Class C features. These classifications relate to the degree of confidence that the features interpreted from aerial photographs actually represent a landslide. Class A, Class B and Class C refer to a probability of being a landslide of 80%, 50% and 10% respectively.

To ensure a high degree of confidence in the susceptibility models derived for the Study Area, calibration against the available landslide data has been carried out with reference to following three groupings of data from the ENTLI dataset:

(i) Total landslides (Recent + all Relict landslides).

(ii) Recent landslides.

(iii) Recent + Relict Class A landslides.

In general, there are some intrinsic differences between "Recent" and "Relict" landslides in terms of the scale and correlation with geomorphological settings, especially when the highly degraded Relict Class B and Relict Class C landslide features are concerned. However, the typically sharp and well-defined nature of the back scarps for Relict A landslides suggests that these features are quite young in terms of landform development and thus should be occurred under similar climatic conditions to those present nowadays. In order to increase the number of landslides for statistical analyses, both "Recent" and "Relict Class A" landslides have been regarded as reliable. Based on the previous experience in reviewing the ENTLI data for natural terrain hazard studies, these two datasets could typically be relied upon as being reasonably accurate. On the other hand, Relict Class B and Relict Class C landslides could often be questionable and could represent geomorphic features rather than actual landslide scars.

Therefore, the grouping of "Recent + Relict Class A" landslides is considered to provide the most reliable dataset on past landslide occurrence. This has been used as the key dataset for calibration of the various susceptibly factors adopted. However, "Total landslides" and "Recent landslides" have also been plotted for references. This allows the intrinsic differences in the setting and distribution of various landslide classes to be checked together with an identification of whether or not notable variations exist.

5.4.2 Modification of ENTLI Data

When reviewing the ENTLI data, it has been noted that the landslide source location recorded in the dataset comprises point information (i.e. grid coordinates) at the crown of the landslide scars. This means that the actual landslide scar itself is located downslope of the coordinates recorded in the dataset and that direct adoption of this information to represent landslide locations may result in inaccuracy and misinterpretation. In order to overcome this problem, the source location for the landslide scar has been shifted 5 m downslope from the crown and along the runout trail recorded in the ENTLI. This results in a modified ENTLI dataset in GIS that is considered to more accurately represent the conditions of the area in which actual landslides had taken place. The value of 5 m has been chosen because the average landslide width is about 10 m to 12 m among the > 8,000 ENTLI records in the Study Area. The radius of the landslide could generally be considered as being half of the width, i.e. about

5 m. Nevertheless, the results for both shifted and non-shifted data are presented in this study for the sake of comparisons.

5.4.3 Landslide Records

A total of 8,475 Recent and Relict (all classes) landslides within the natural terrain boundary has been identified in the ENTLI, including 1,980 Recent landslides and 999 Relict Class A landslides. As previously discussed, the remaining 5,496 ENTLI landslides, classified as Relict Class B or Class C, are considered to be of lower reliability. As such, these landslides have been excluded from the calibration exercise. The modified locations of the 2,979 Recent and Relict Class A landslides recorded in the ENTLI up to 2009 are shown in Figure 5.9.
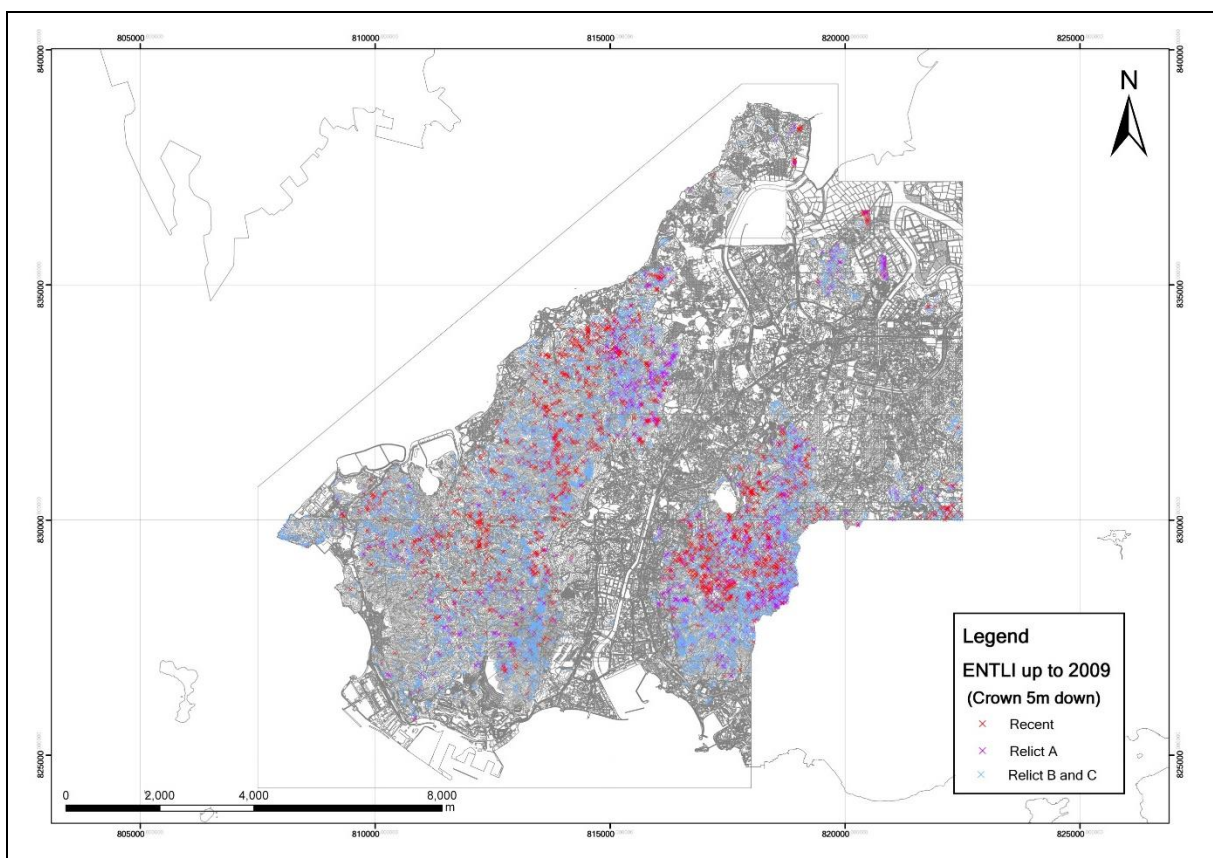
Figure 5.9   Location of 5 m down of the Crown in ENTLI Record up to 2009 within the Natural Boundary

In addition to the location of landslides, the year in which the landslides were first identified has also been reviewed. It is found that significant landslide swarms occurred within the Study Area in 1982 (208 landslides), 1989 (284 landslides) and 2000 (730 landslides). A plot of the total number of landslides occurring annually since 1963 is shown in Figure 5.10.
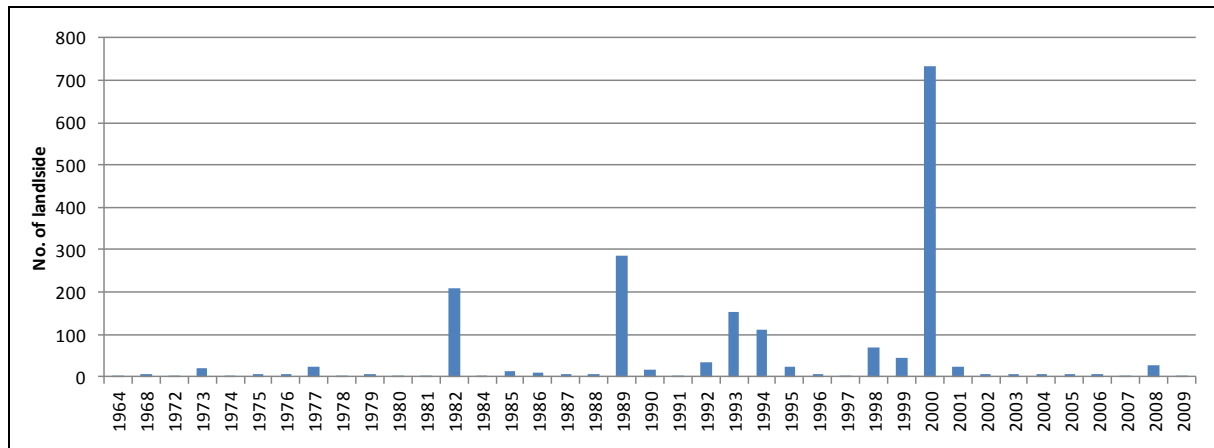
Figure 5.10   Annual Record of Number of Landslides from ENTLI Data

5.4.4   Landslide Density

The data contained within the ENTLI, with modifications and groupings as discussed in the preceding sections, has been used to determine the landslide density (in terms of the number of landslides per unit area in km^2) for various susceptibility factors.   This information has been used as a measure of the probability of landslide occurrence for rating various parameters to the landslide susceptibility.   Similar approach was used by MFJV (2003) to identify the key initiation factors for landslides.

In the present study, the landslide density is expressed in terms of the area affected by landslides per unit are in km^2.   This area is calculated using the landslide length and width recorded in the ENTLI.

5.5   Potential Susceptibility Factors

As noted in AGS (2007), landslide susceptibility zoning involves a degree of interpretation that is often based upon the spatial distribution and the rating of region-specific terrain units according to their propensity to produce landslides.   The susceptibility zoning is dependent on the topography, geology, geotechnical properties, climate, vegetation and anthropogenic factors affecting the area.

MFJV (2003) considered slope angle, regolith types, lithological boundaries, regolith downslope of rock outcrop and the head of a drainage line as potential factors that affect the landslide occurrence.   With respect to the Study Area and considering the results of MFJV (2003), the key initiation factors with the potential to predispose an area to landsliding mainly include the geology, geological structure, topography, geomorphology, hydrology and hydrogeology.   The regolith types and lithological boundaries have not been considered because they require detailed field mapping to obtain the information.   While this was applicable for the site-specific Tsing Shan Foothill Area, it is not appropriate for the present study, which is of a regional scale.   These two factors have been analysed indirectly through the geological condition assessment.

These various parameters have largely been accounted for by consideration of the following aspects within the susceptibility model.

5.5.1 Slope Angle

The slope angle is known to be an important factor in controlling the occurrence of landslides. This factor is probably the most commonly reviewed and adopted parameter for landslide susceptibility analyses.

The gradients of the natural terrain hillside within the Study Area have been calculated in GIS based on a Triangulated Irregular Network (TIN) model generated from the 1:5,000 scale LIC Maps. The slope angles within the TIN model have subsequently been "smoothed" to overcome potential problems associated with localised irregularities. The "smoothing" process is presented as follows:

> (i)   A slope angle has been calculated for a 1 m cell size across the whole Study Area.

> (ii) A circular area within a radius of five cells has been used to calculate the average value of each cell. This averaged slope angle has then been adopted in that grid cell to provide a smoothed slope angle map with a 1 m resolution.

The results of the slope angle smoothing exercise are presented in Figure 5.11. The smoothing attempts to reduce the sensitivity of the slope angle determination arising from those contours being extremely close together horizontally (note that the contour spacing of 1: 5,000 LIC map is 10 m vertically). Hence, it makes only a minor difference to the resulting slope angle map with the smoothing only applied to very localised irregularities.

There are limitations in the use of the 1:5,000 LIC maps as they may not be as accurate as the 1:1,000 LIC maps when the generation of slope angle maps is concerned. In order to review the implications, a comparison of the landslide density for a number of key slope classes using slope angle maps generated from both 1:1,000 LIC and 1:5,000 LIC maps have been carried out for a small test area (about 3 km x 3 km) as shown in Figure 5.12. The results of this review indicate that the densities computed using both LIC maps are largely comparable, provided that the data for any areas less than 0.1 km^2 have been screened out (see Figure 5.13).
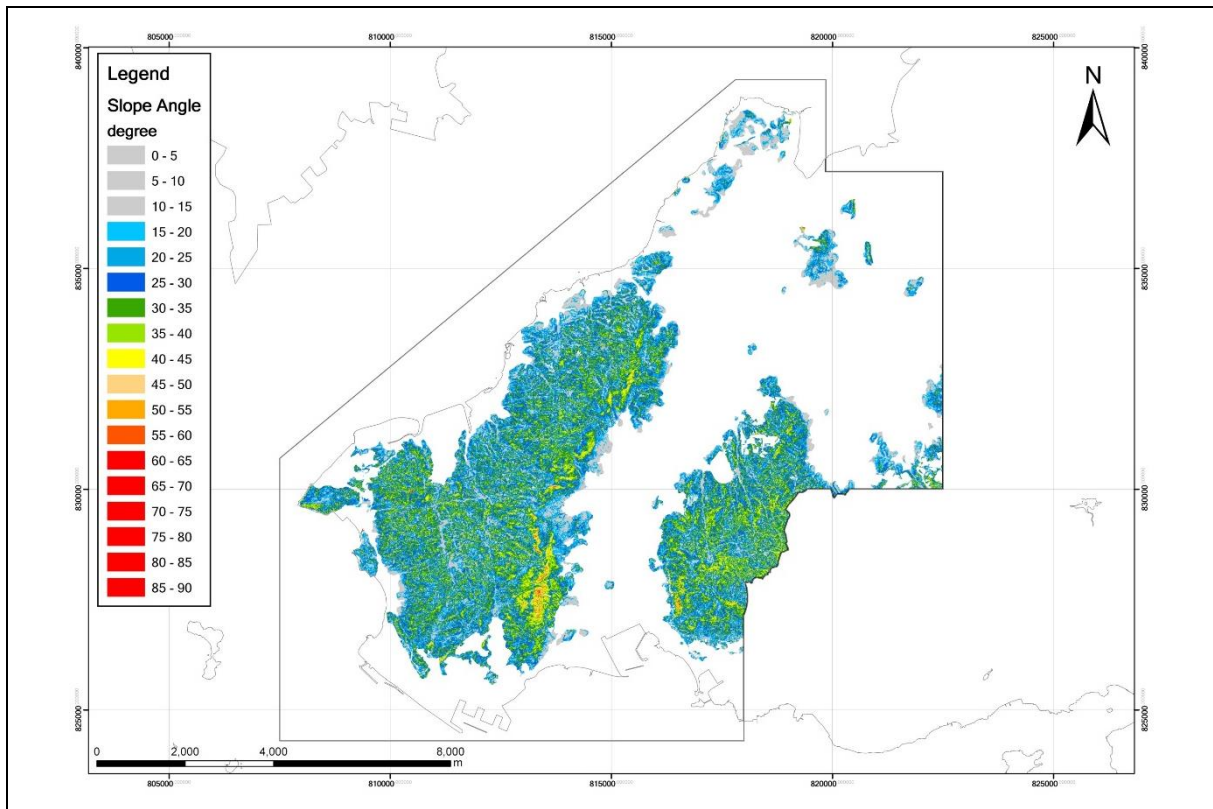
Figure 5.11   Smooth Slope Angle within Natural Terrain Boundary
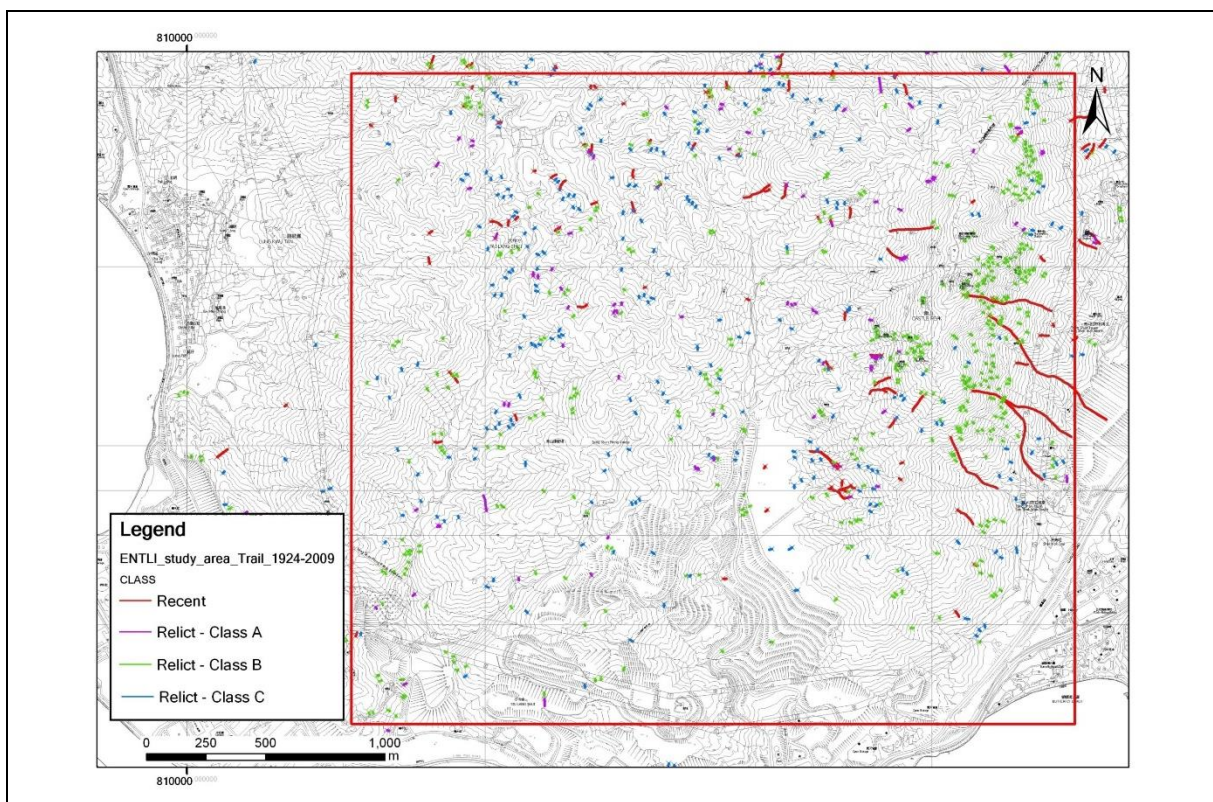
Figure 5.12   ENTLI Record in the Test Area
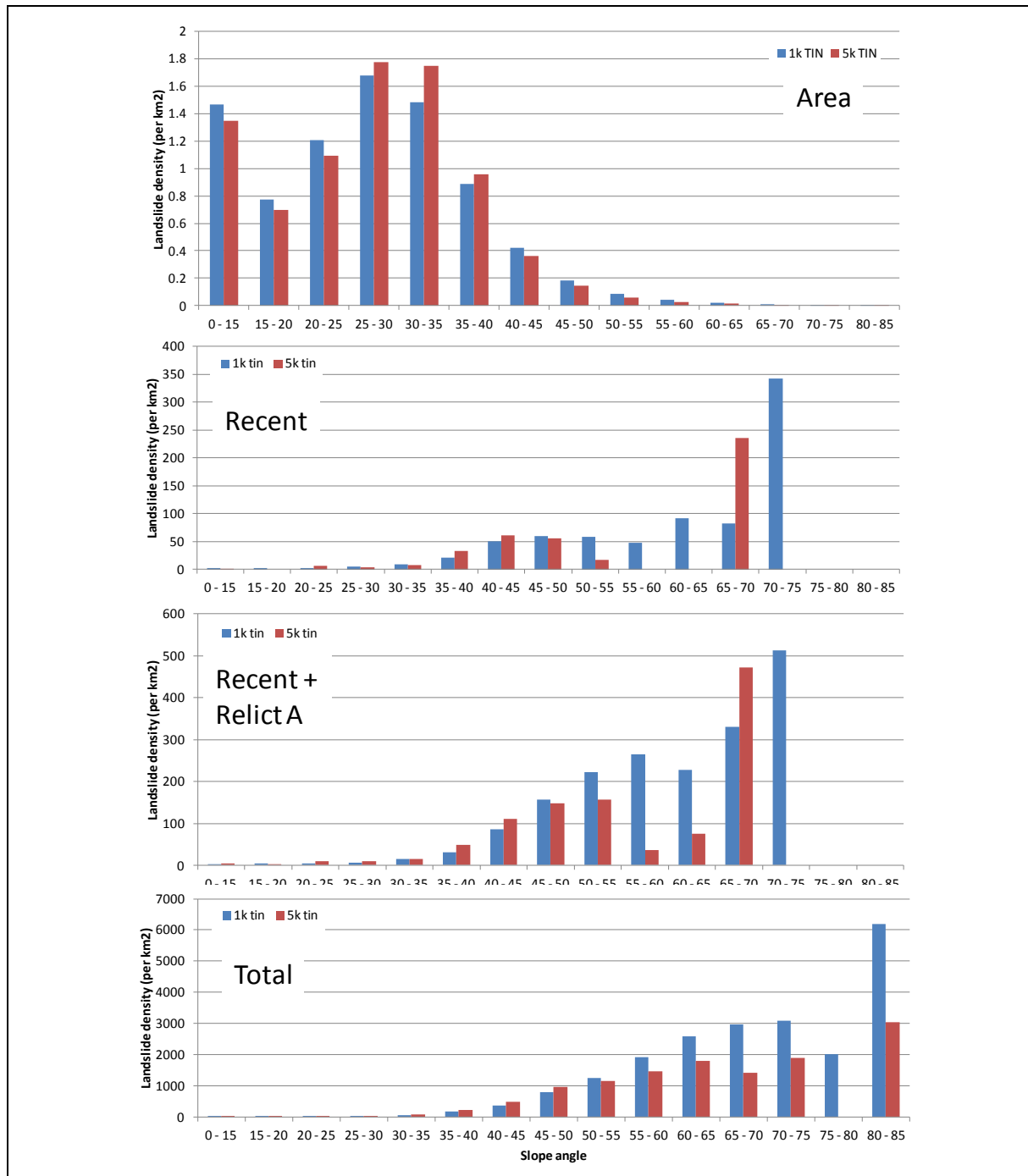
Figure 5.13 Plots of ENTLI of Non-shifted Landslide Crown up to 2009 against Slope Angle for TIN Model Generated from 1:1,000 (1 k) and 1:5,000 (5 k) LIC Maps

With the above considerations, the use of the 1:5,000 LIC dataset is considered acceptable for the present regional-scale assessment. However, for a detailed site-specific study, the use of the 1:1,000 LIC or LiDAR datasets is recommended.

The landslide density of shifted and non-shifted landslide crown has then been reviewed for each 5° slope angle increment within the natural terrain area (see Figures 5.14 and 5.15

respectively). The density of "Recent and Relict Class A" landslides is relatively low within areas with slope gradients less than 30° and increases significantly for areas with gradients above 40°. Whilst there is an apparent drop in the density of Recent and Relict Class A landslides above slope angles of 50°, this can largely be attributed to small areas ($< 1 \text{ km}^2$) occupied by these slope angle classes. Table 5.1 presents the susceptibility factor classes recommended with regard to the influence of the slope angles.
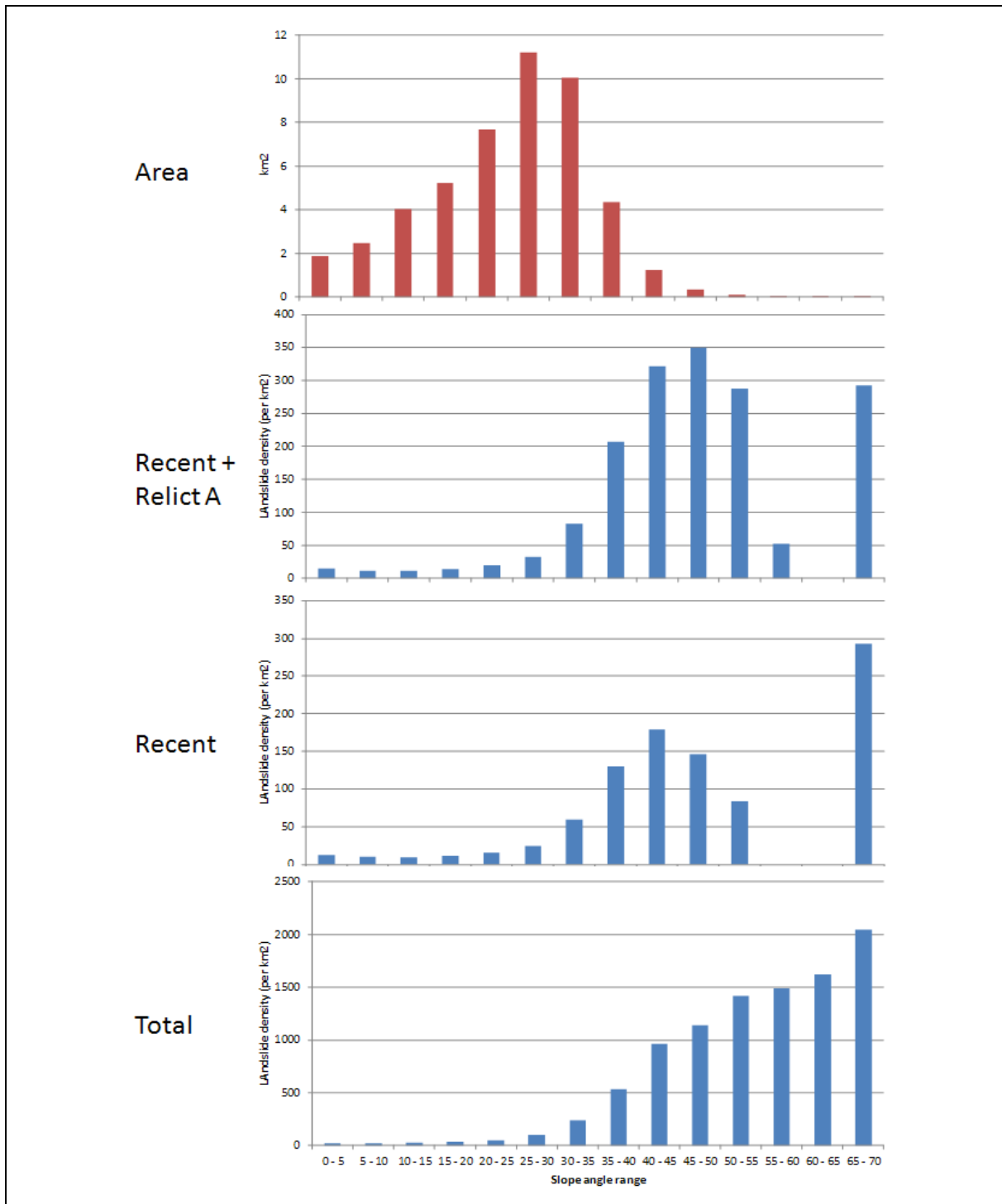
Figure 5.14   Plots of ENTLI of Shifted Landslide Crown up to 2009 against Slope Angle
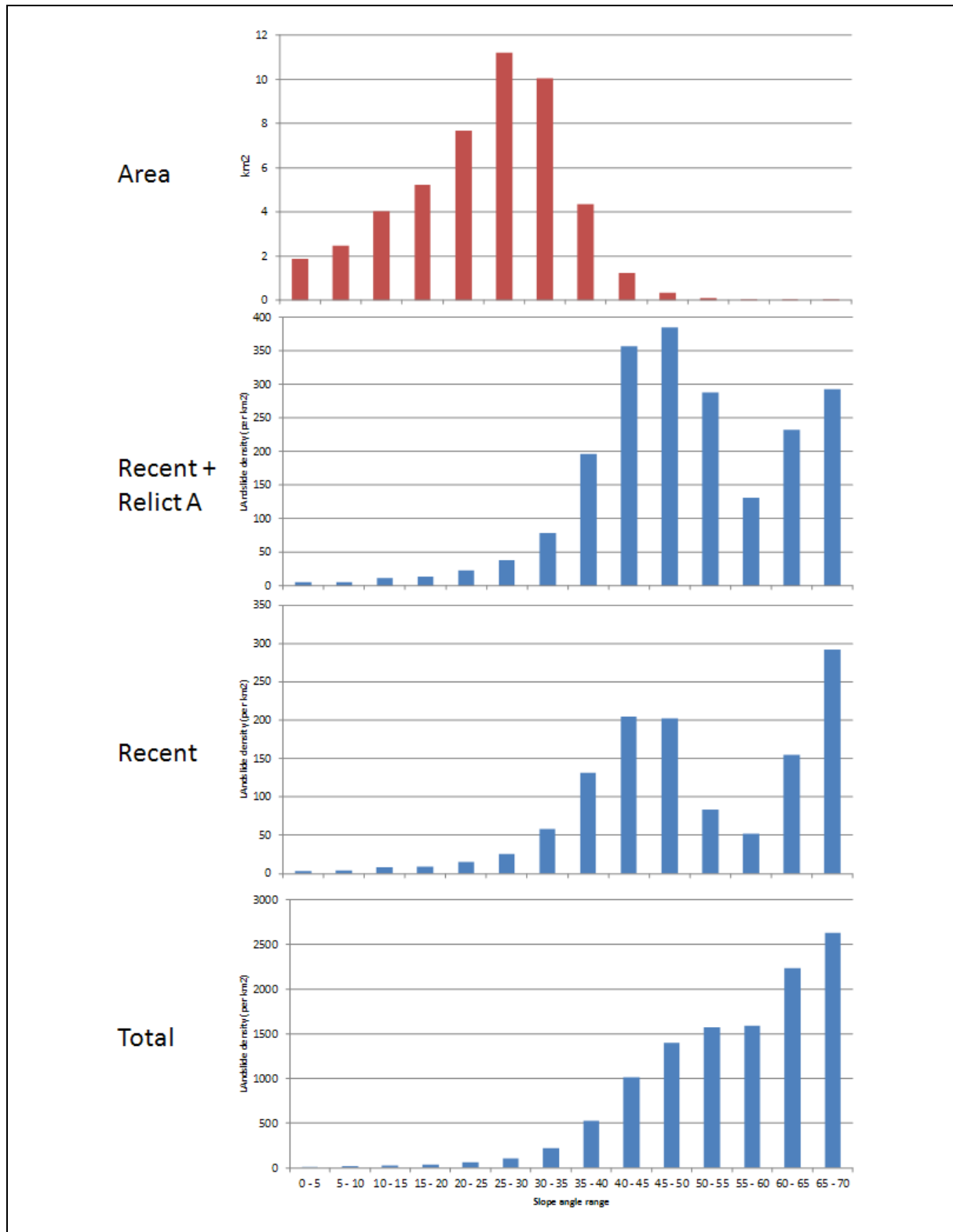
Figure 5.15   Plots of ENTLI of Non-shifted Landslide Crown up to 2009 against Slope Angle

Table 5.1   Susceptibility Factor Classes with Regard to Slope Angle

Slope Angle Class	Descriptor	Slope Angle Range	Landslide Density
Class A	Very Steep	≥ 40°	316.04 per km²
Class B	Moderately Steep	30° to 40°	120.43 per km²
Class C	Gentle	< 30°	21.39 per km²

Figure 5.16 shows the distribution of different slope classes described above within the Study Area.
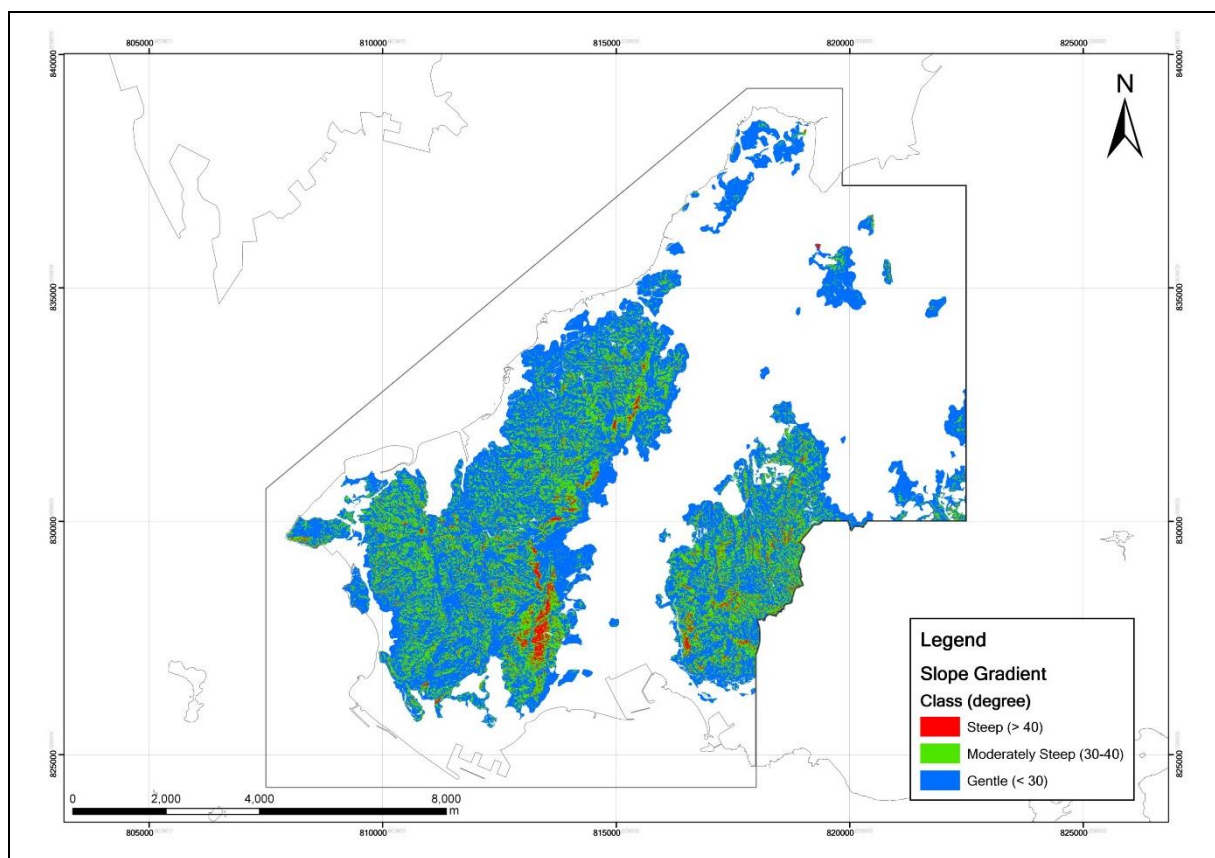
Figure 5.16   Map Showing Susceptibility Classes for Slope Angle

5.5.2   Geological Conditions

The distribution of past landslides within the Study Area has been reviewed against the published geological data at the landslide source area based on the 1:20,000 scale Solid and Superficial Geological Map (Figure 5.17).   The geological map shows geological boundaries, different types of Quaternary deposits and rocks (which can be implied as different saprolites). It is understood that the map could be oversimplified as compared with information obtained from field mapping but it is still considered applicable for this regional study.
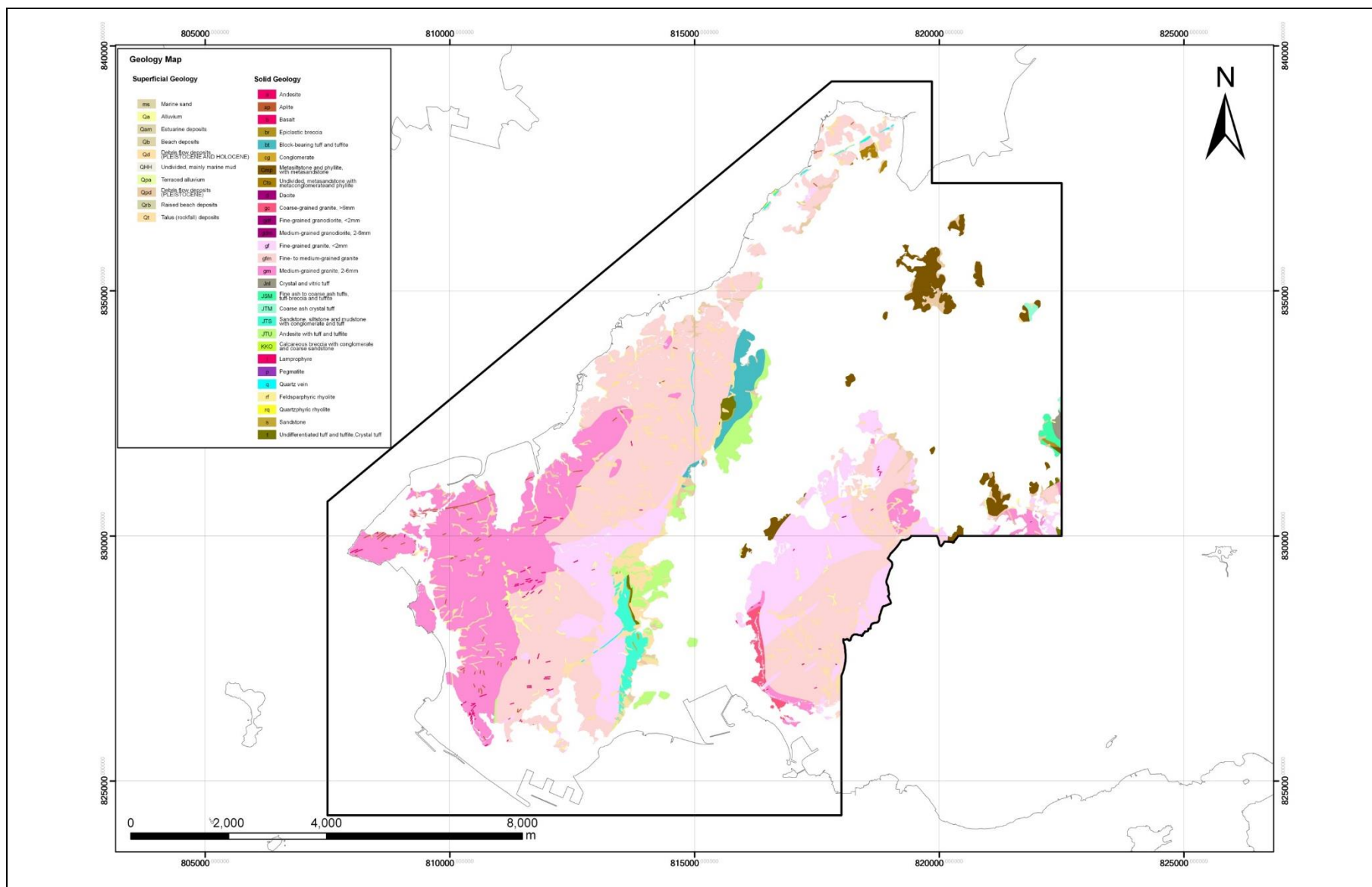
Figure 5.17   1:20,000 Scale Solid and Superficial Geology Map (GCO, 1987a & 1987b)

The results of this review indicate that the landslide densities are higher within areas recorded as fine-grained granite (gf), fine-to-medium grained granite (gfm), block bearing tuff and tuffite (bt), undifferentiated tuff and tuffite (t), siltstone with thin bedded limestone (Cmp) and sandstone, siltstone and mudstone with conglomerate and tuff (JTS) (see Figure 5.18). Figure 5.19 shows the equivalent non-shifted landslide results.
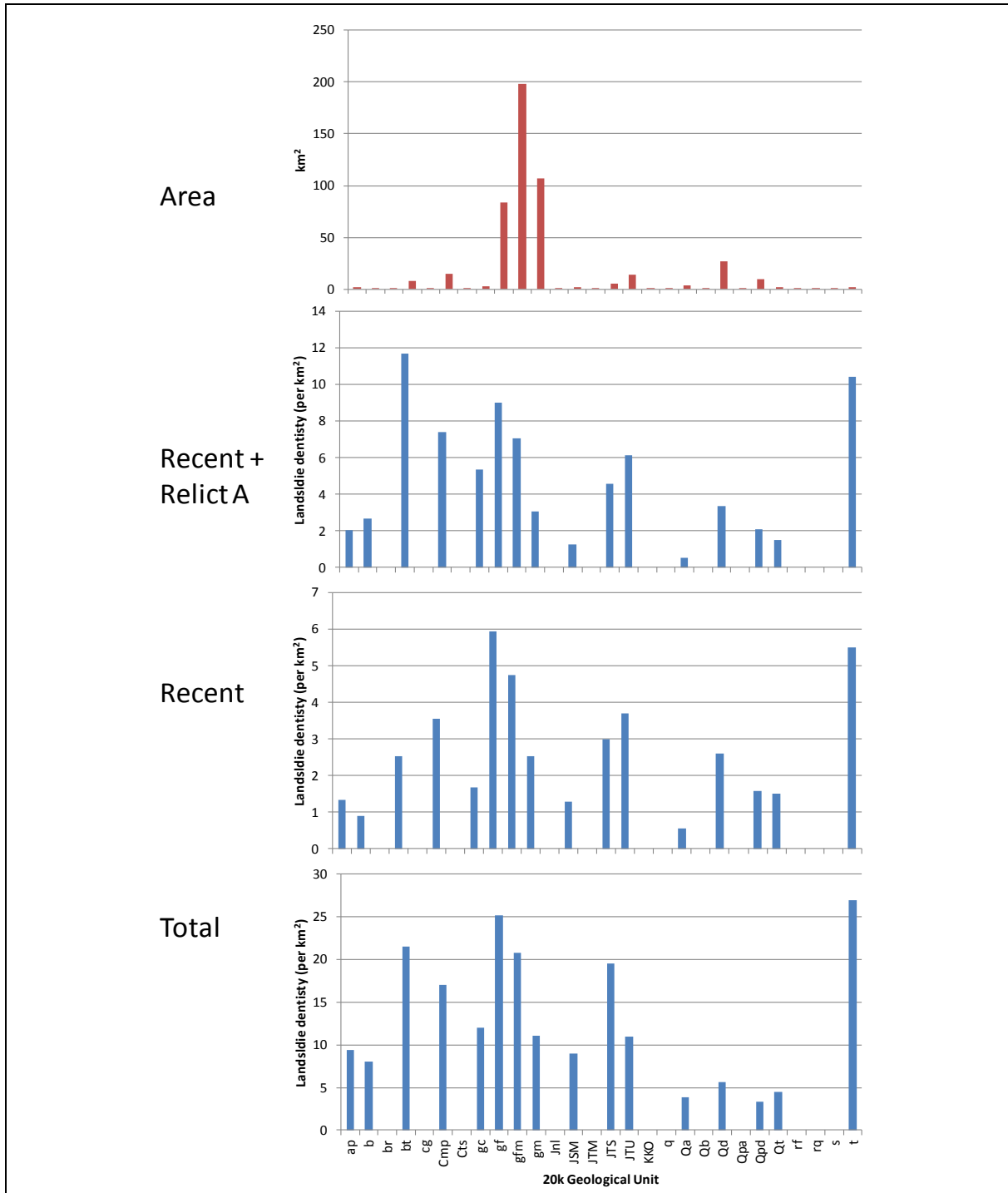
Figure 5.18   Landslide Density of Shifted Landslide Crown in Different Geological Units in 1:20,000 Geological Map
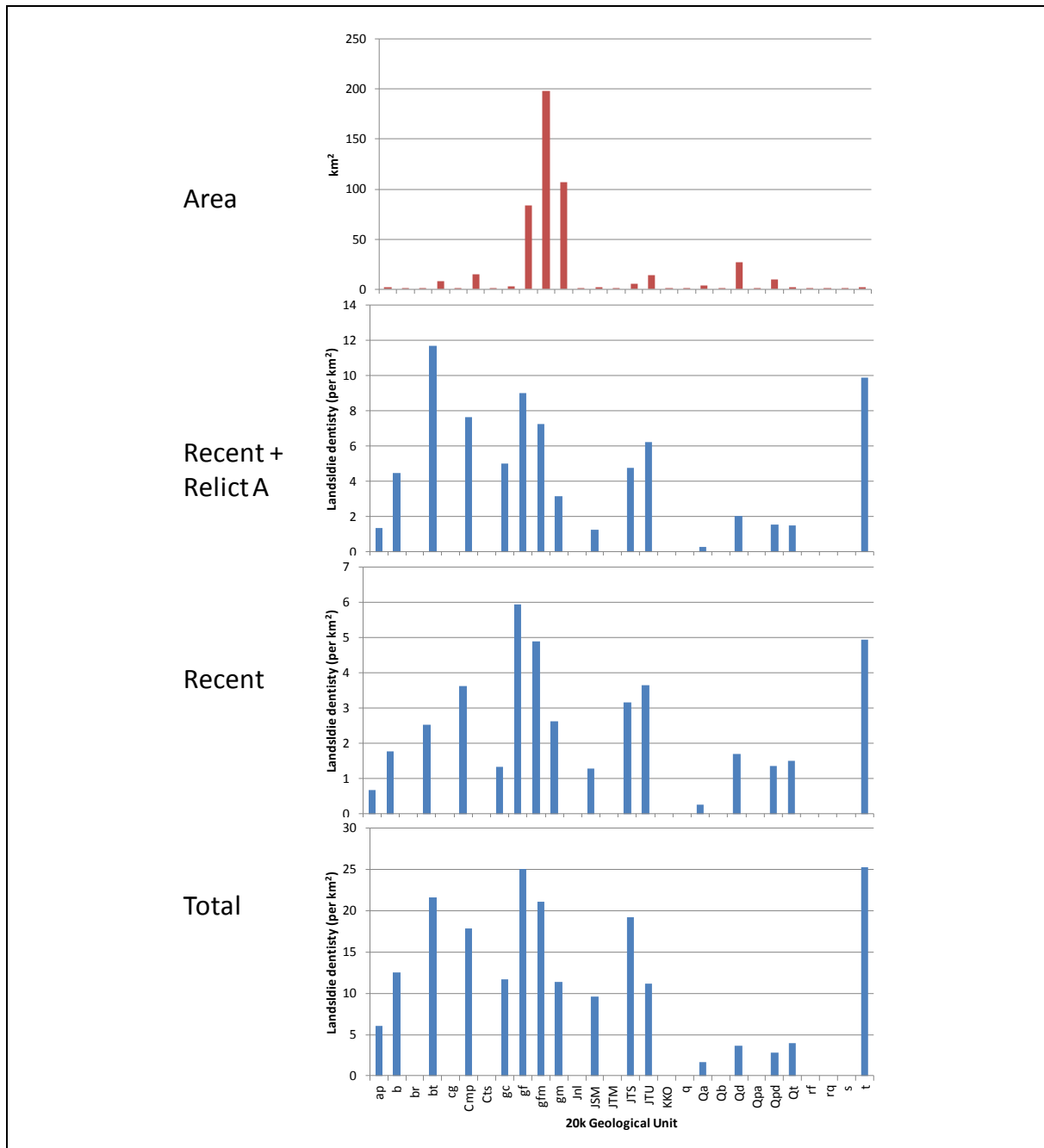
Figure 5.19   Landslide Density of Non-shifted Landslide Crown in Different Geological Units in 1:20,000 Geological Map

Apparently, these geological units give rise to a higher predisposition to landsliding than others.   However, it has been found that the locations of these units are coincident with other topographic and geomorphological indicators of landslide susceptibility.   It is considered reasonable as the development of the landforms is related to the underlying geological characteristics.   As such, other factors considered in the susceptibility model, in particular, Slope Angle (see Section 5.5.1) and Terrain Unit (see Section 5.5.3), have already accounted for the variance resulted from the solid geological conditions.   On the other hand, the Study Area is mainly exposed with granite (about 80% within the natural terrain boundary) and

slightly with tuff (only occupied about 5%). The weak sedimentary and volcanic rocks, which have been considered to be more prone to landslide occurrence, are not considered in the present study as the geology does not vary a lot spatially. To conclude, it is considered not necessary to specifically include the geological strata in the susceptibility model.

5.5.3 Geological Structure

Geological structure is another potential susceptibility factor for earthquake-induced landslides. For example, fractured rocks could be more erodible and provide weak points triggering failures. Thus, they would be more prone to landsliding. It is, therefore, of interest to examine the relationship between the geological structure and the landslide density.

The pertinent geological structure mainly includes faults and joints. For the purpose of a regional-scale assessment, the analysis of joint sets is considered not applicable. Instead, the fault proximity has been checked against the landslide density to assess if geological structure is a controlling factor. The faults, inferred faults and photo-lineaments shown in 1:100,000 Hong Kong Geological map (GEO, 2000) and GASP report III and IV (GCO, 1987a & 1987b) have been used to represent the geological structure (Figure 5.20) and buffering of 10 m, 25 m, 50 m and 100 m has been carried out to review whether there exists any strong correlation between the location of past landslides and the proximity of the geological structure.
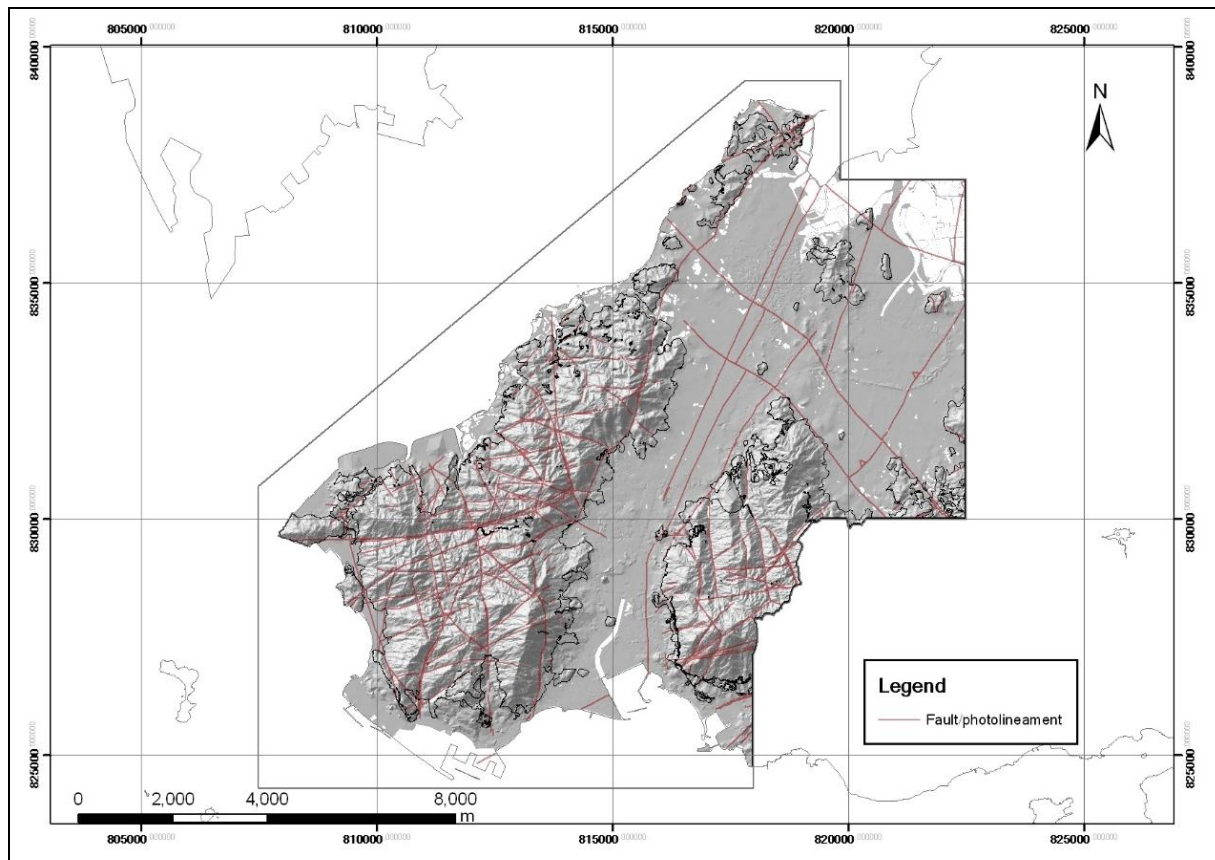
Figure 5.20 Geological Structure Extracted from 1:100,000 Hong Kong Geological Map and the GASP Reports

The results of shifted and non-shifted landslide crowns, as shown in Figures 5.21 and 5.22 respectively, show that the landslide densities for all buffer distances are generally comparable. It indicates that the geological structure is unlikely a controlling factor in this case.
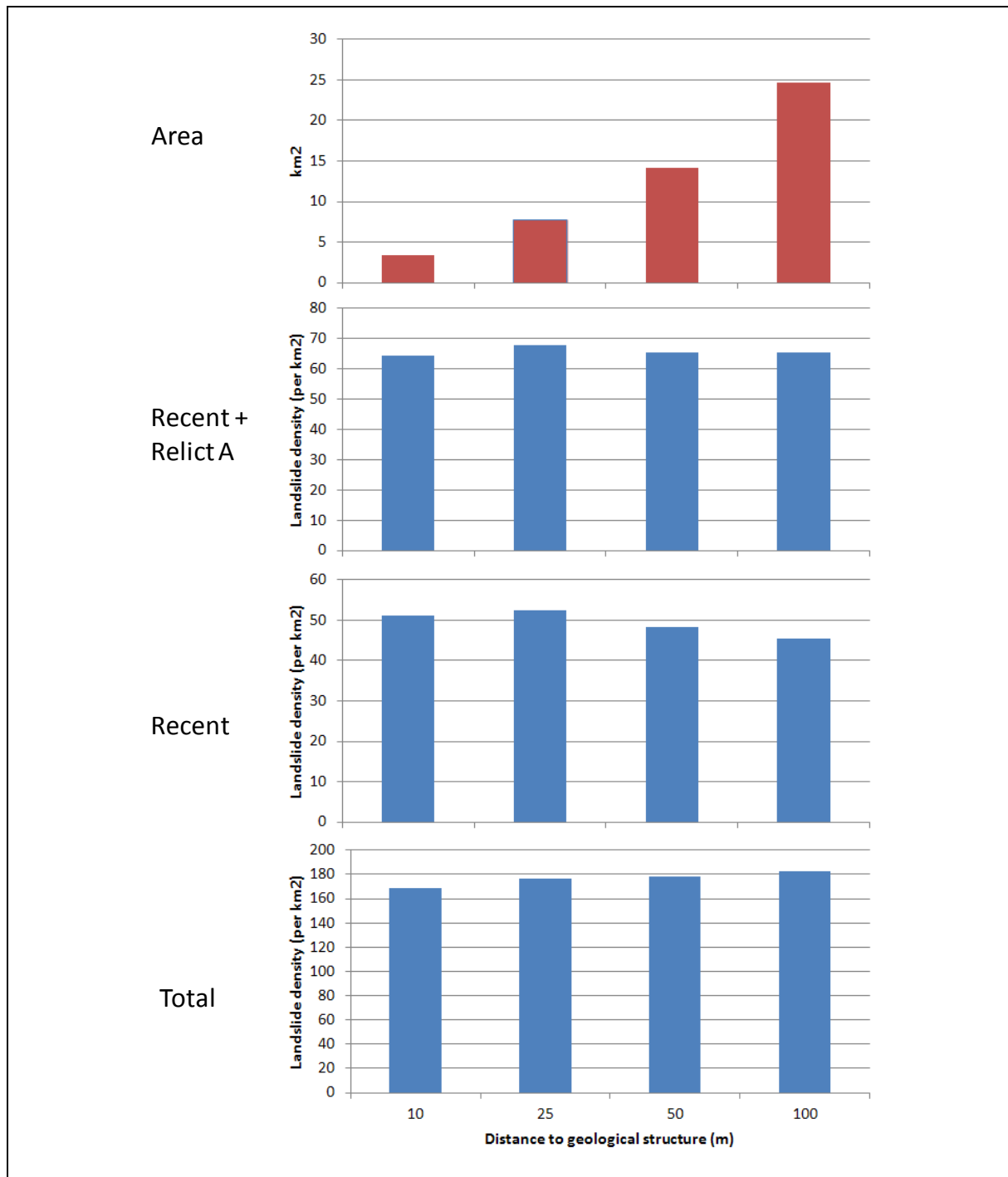
Figure 5.21 Landslide Density of Shifted Landslide Crown in Geological Structure Proximity
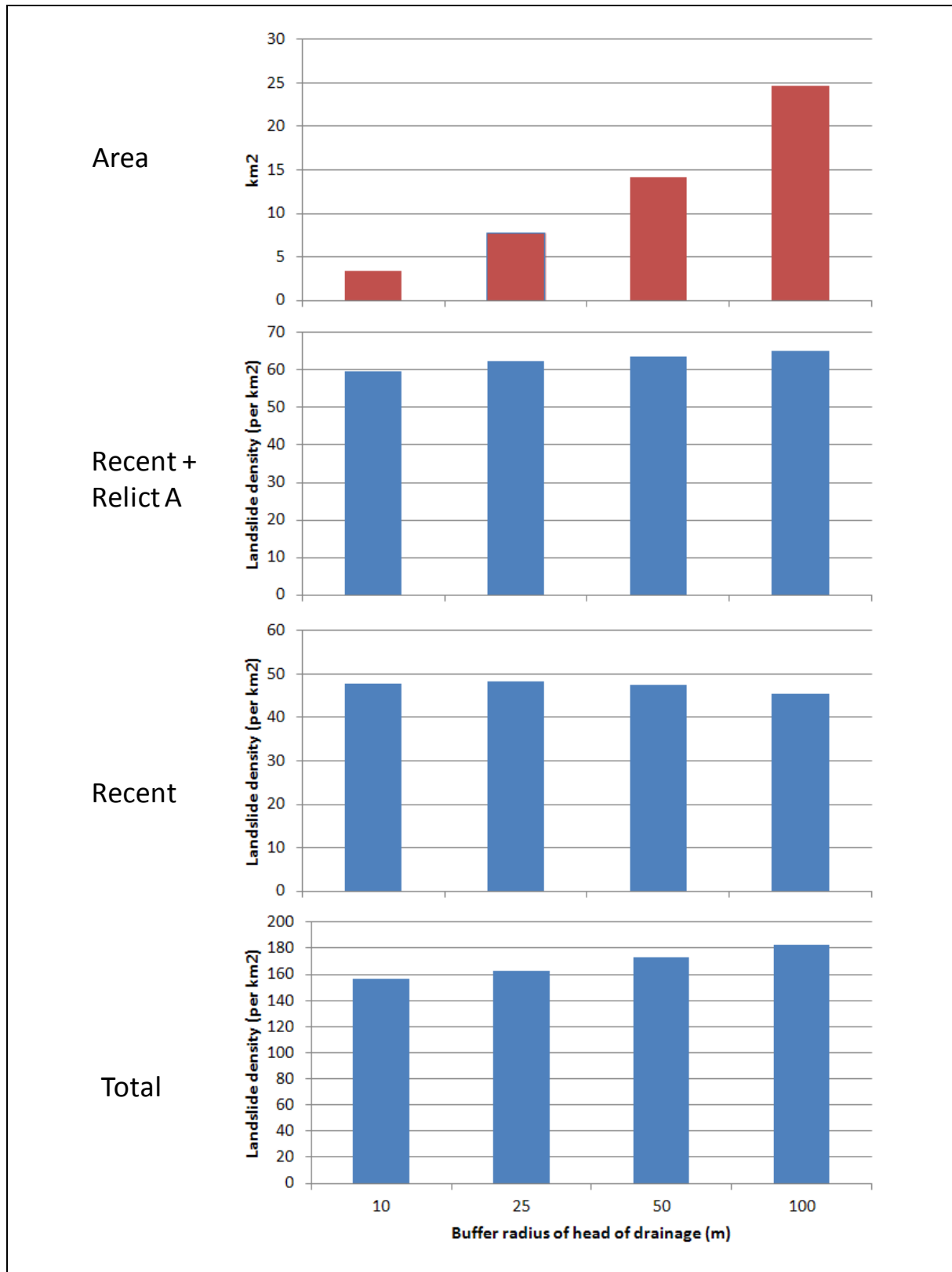
Figure 5.22   Landslide Density of the Non-shifted Landslide Crown in Geological Structure Proximity

5.5.4 Geomorphology (Terrain Unit)

The geomorphological setting of the natural terrain within the Study Area has been characterised using the terrain component of the Landform Maps from the Geotechnical Area Studies Programme (GASP) Reports (Figure 5.23). The various terrain components documented in these maps, which are generally based on the slope form and process, have been reviewed and grouped to develop a simplified terrain model based on the method developed by Dalrymple et al (1968) (Figure 5.24).

The simplified terrain model provides a general reference of the geomorphological conditions, with specific emphasis on the slope morphology and process on a hillslope. The various units adopted to characterise natural terrain hillsides within the Study Area are summarised in Table 5.2, which also lists the corresponding terrain components from GASP Maps that have been used to delineate the extent of the terrain unit.
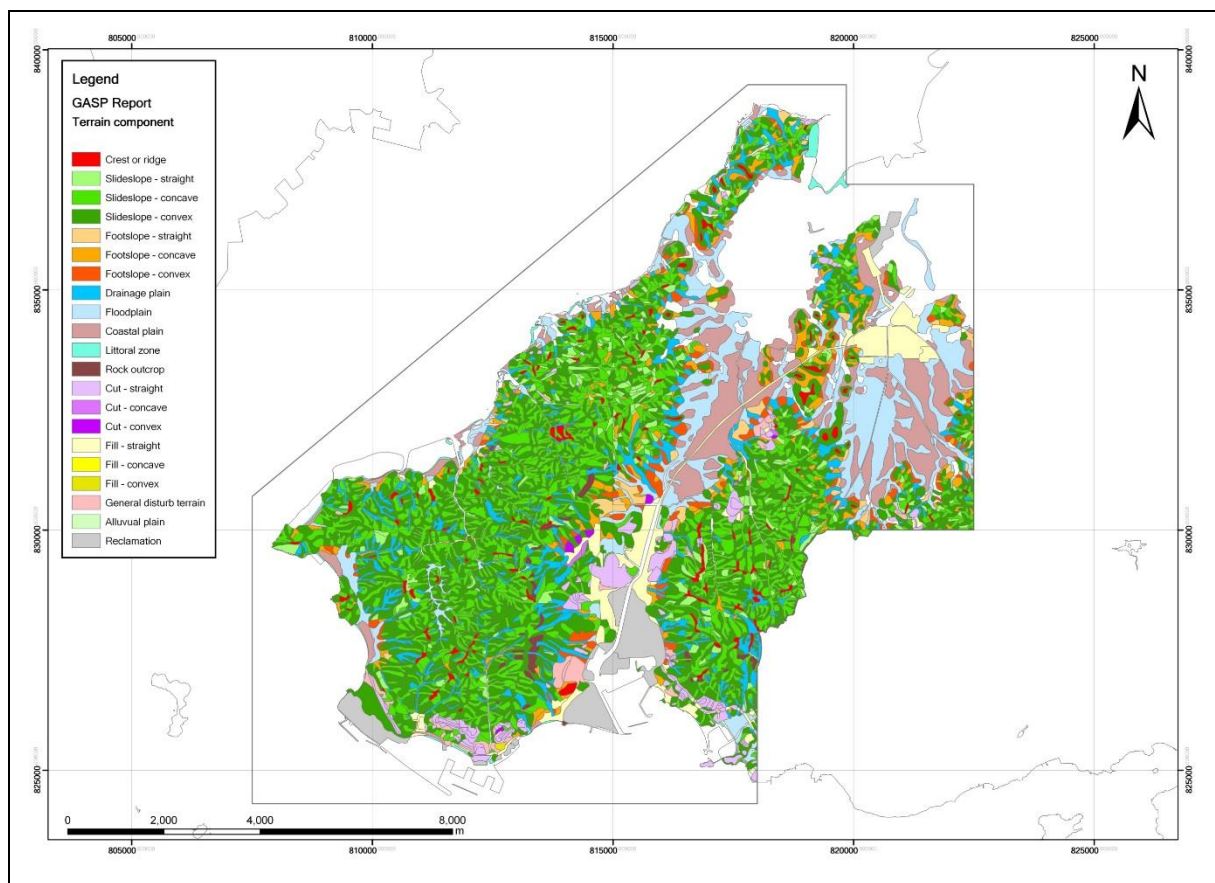
Figure 5.23   Terrain Components in Landform Map in GASP Reports
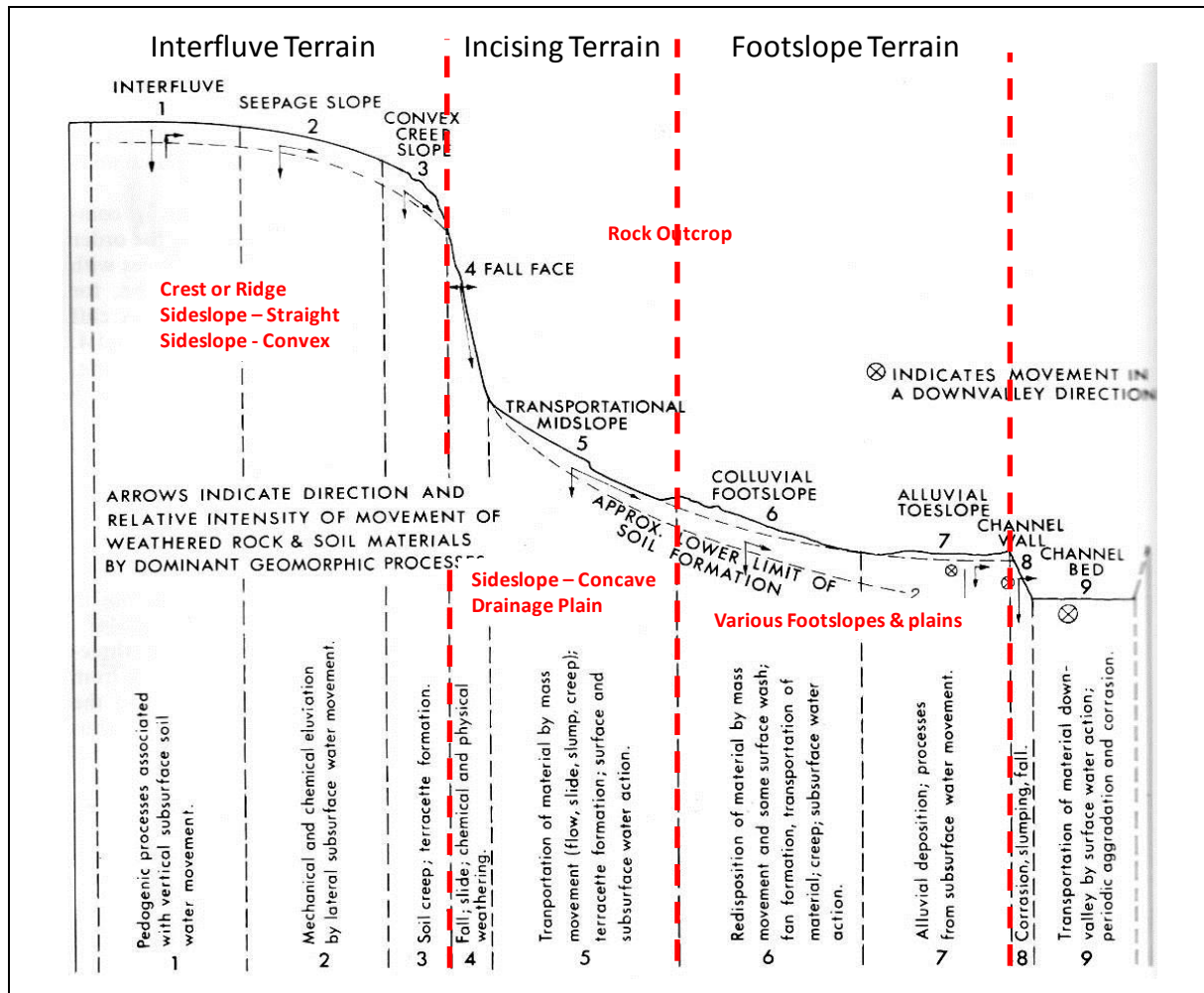
Figure 5.24 The Hypothetical Nine-unit Land Surface Model by Dalrymple et al (1968) and the Simplified Terrain Model in Our Study

Table 5.2 Terrain Unit Developed in Simplified Terrain Model

Terrain Unit	Terrain Characteristics	Terrain Components in Landform Maps in GASP Report
Interfluve Terrain	• rounded/undulating terrain and planar hillslope areas • moderate-to-low erosion rates	Crest or Ridge Sideslope - Straight Sideslope - Convex
Incising Terrain	• concave terrain including numerous drainage valleys • high rates of erosion	Sideslope - Concave Drainage Plain
Footslope Terrain	• shallow gradient footslope areas and alluvial plains etc. • primarily depositional terrain	Various Footslopes and Plains
Rock Outcrop	• exposure of rock	Rock Outcrop

The terrain units developed based on the published GASP Maps have been validated using ortho-rectified aerial photographs and Digital Terrain Models (DTM) of the Study Area. This process has confirmed that the model is broadly acceptable, with an exception of several areas, which have previously been classified in the GASP Maps as footslope terrain but is considered more representative of either incising or interfluve terrain (Figure 5.25).
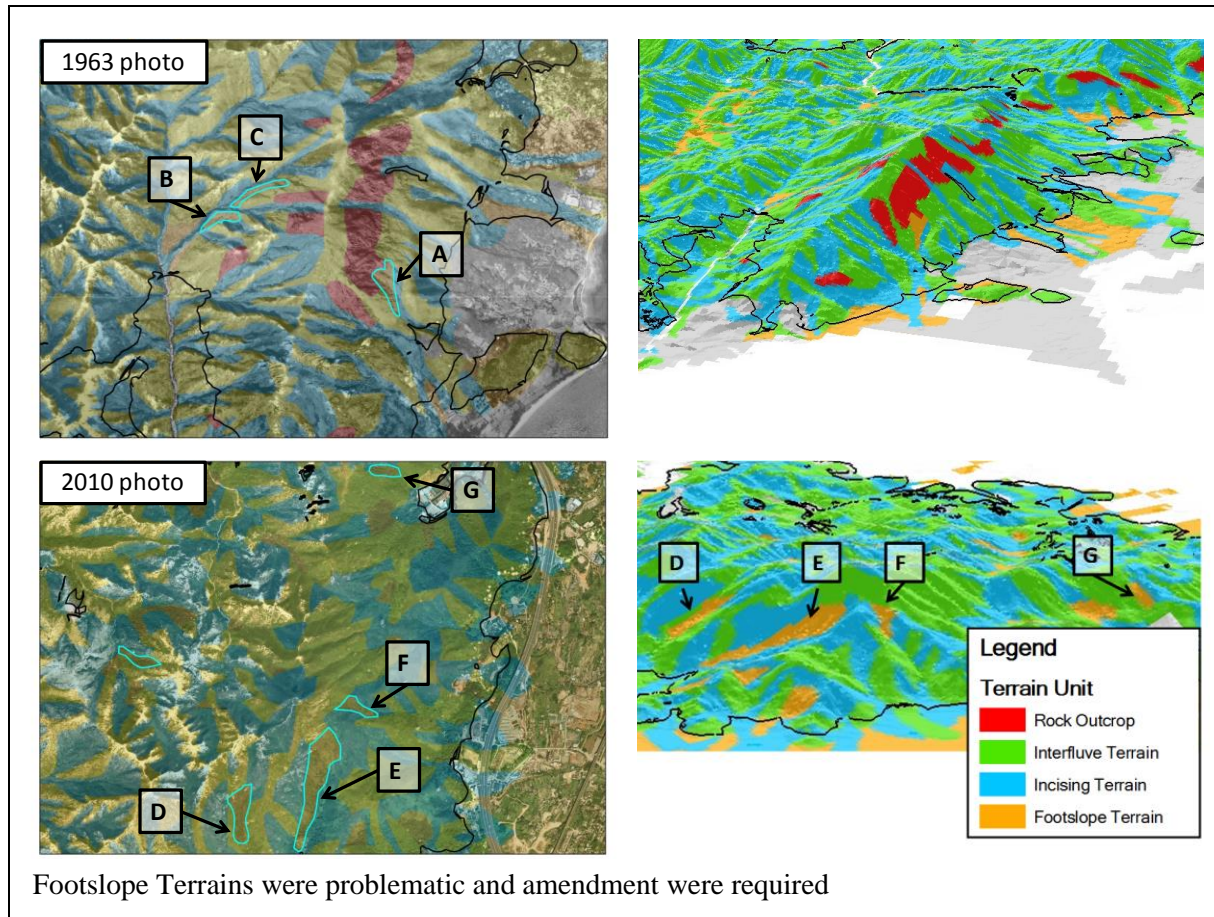
Figure 5.25 Terrain Components in Landform Map in GASP Reports

It is noted that, in a number of areas, the extent of the Incising Terrain does not fully capture the areas of incised and over-steepened channel banks and valley side slopes associated with significant drainage line activities.   These inaccuracies in the model have been overcome by expanding the Incising Terrain area into the surrounding Interfluve Terrain areas through the application of a 10 m buffer.

The validation exercise has confirmed that whilst the published GASP Maps provide a valuable starting point for the assessment of Terrain Units, careful review by an experienced engineering geologist or geomorphologist is still required to validate the model.

A review of the landslide densities of shifted and non-shifted landslide crown for various terrain units derived by the model shows that the Incising Terrain has a relatively higher landslide density than Interfluve Terrain, which in turn has a higher density than the Footslope

Terrain (see Figures 5.26 and 5.27 respectively).   The areas recorded as Rock Outcrop are also noted to result in high landslide densities.   With due consideration given to the above points, three key Terrain Classes related to landslide susceptibility have been derived as summarised in Table 5.3.
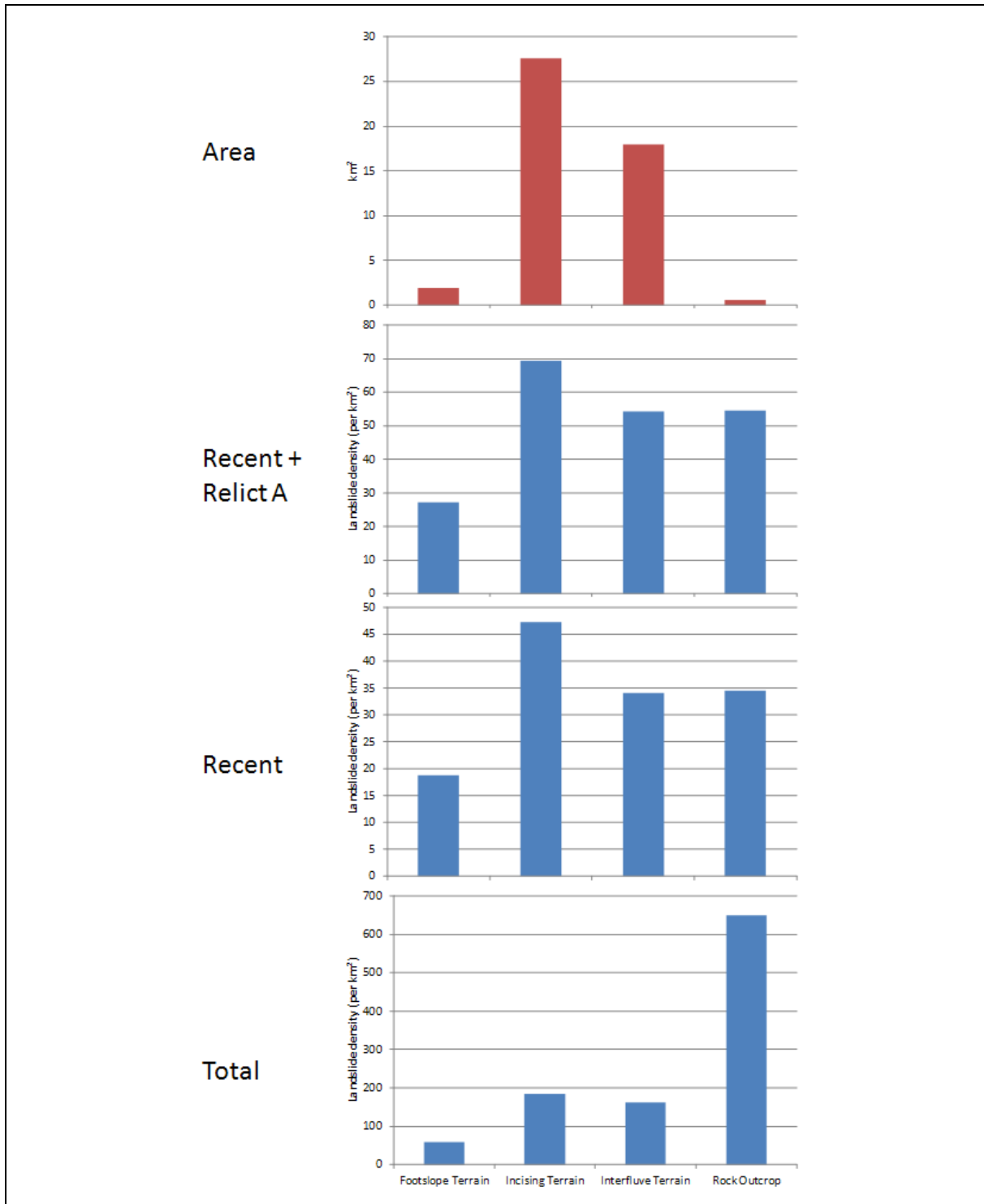
Figure 5.26   Landslide Density of Shifted Landslide Crown with Terrain Unit
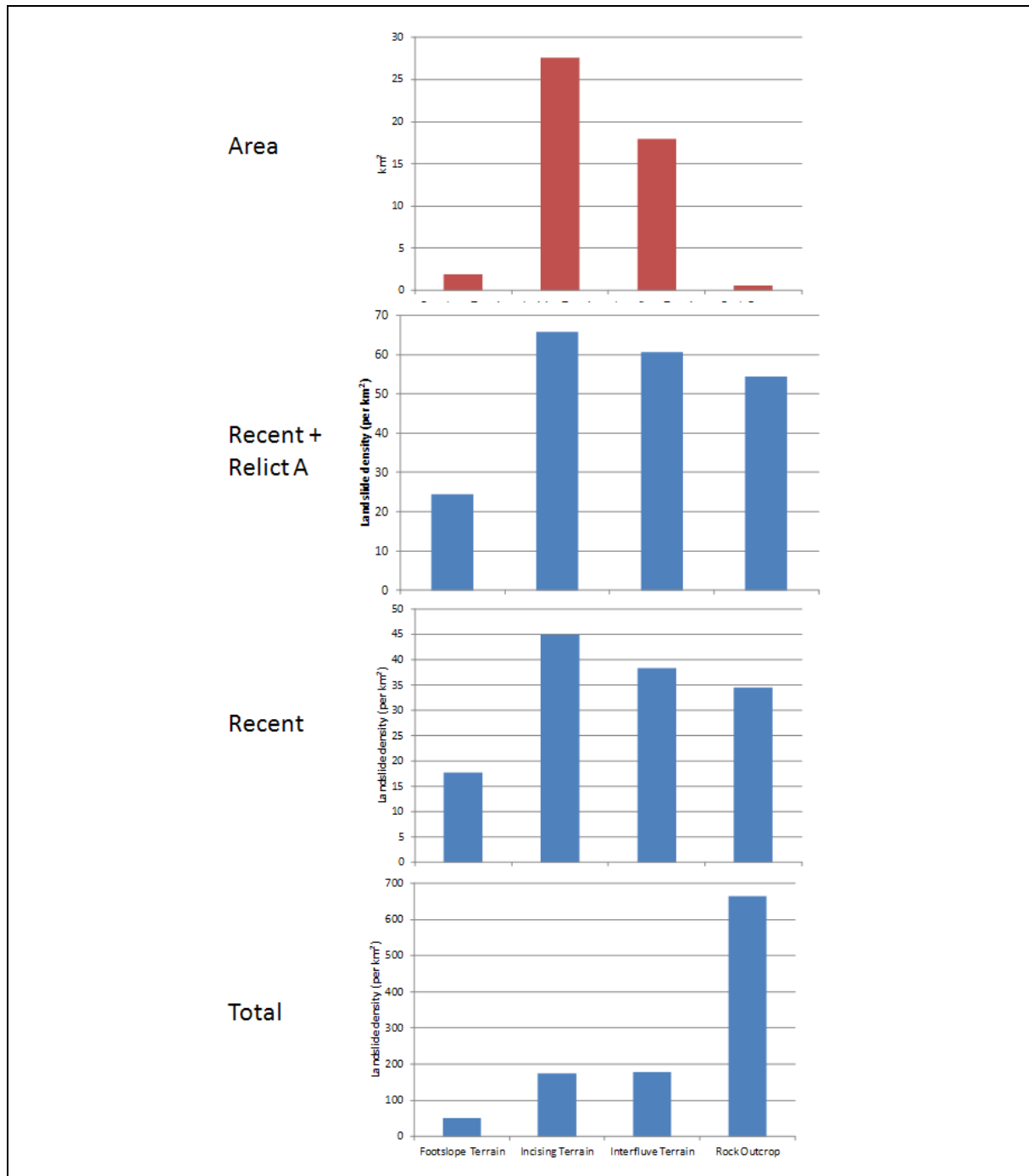
Figure 5.27 Landslide Density of Non-shifted Landslide Crown with Terrain Unit

Table 5.3 Susceptibility Factor Classes with Regard to Terrain Unit

Terrain Class	Terrain Unit	Landslide Density
Adverse	Incising Terrain Rock Outcrop	68.98 per km²
Moderate	Interfluve Terrain	54.38 per km²
Favourable	Footslope Terrain	27.12 per km²

Figure 5.28 shows the distribution of the susceptibility classes for terrain unit within the Study Area.
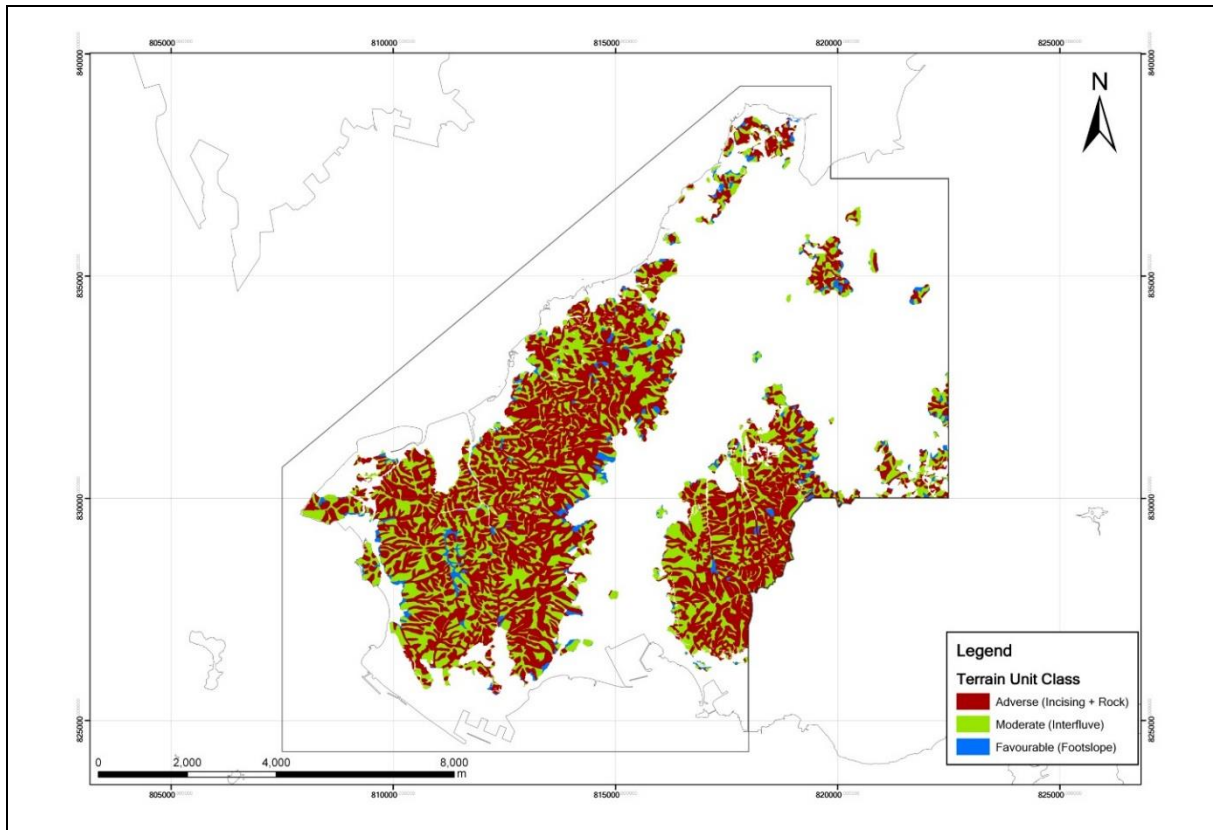
Figure 5.28 Susceptibility Classes for Terrain Unit

5.5.5 Drainage

Taking cognisance of the fact that landslides often occur at the head or along the banks of natural drainage lines, the location of such features within the Study Area have been extracted from 1:5,000 scale LIC Maps (Figure 5.29). These drainage lines have then been buffered at distances of 10 m, 25 m, 50 m and 100 m to review whether there exist any correlations between the location of past landslides and the proximity of the terrain to the natural drainage system.

Apart from drainage lines, the heads of drainage have also been buffered at radii of 10 m, 25 m, 50 m and 100 m to review if there exist any correlations with landslide densities (Figure 5.30).

Based on this review, there appears no specific correlation between the landslide locations of shifted and non-shifted landslide crowns and the proximity to drainage lines (Figures 5.31 and 5.32 respectively) and to heads of drainage (Figures 5.33 and 5.34 respectively), with the landslide densities for all buffer distances considered showing broadly comparable results. As such, it is considered that the Incising Terrain Unit derived under the geomorphological assessment provides a more reliable means of defining the influence of the hydrological system.
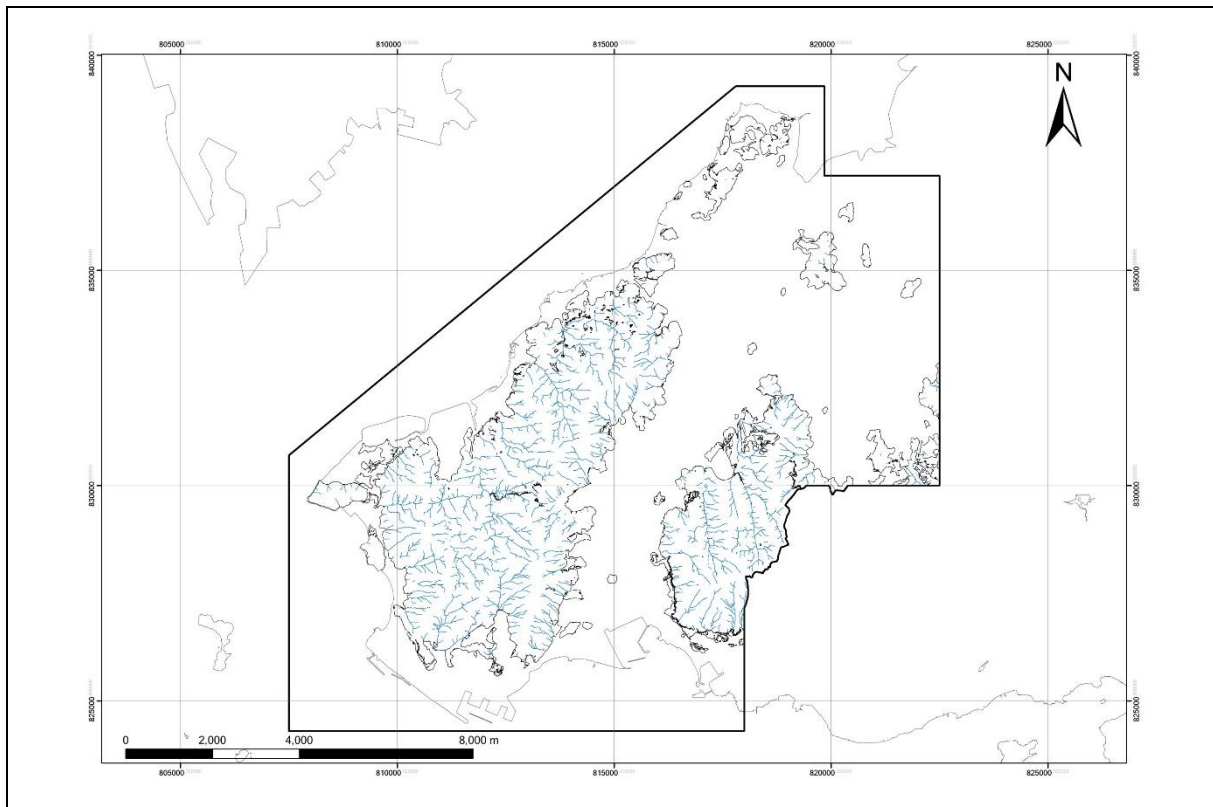
Figure 5.29   Drainage Lines in 1:5,000 Scale Topographic Map
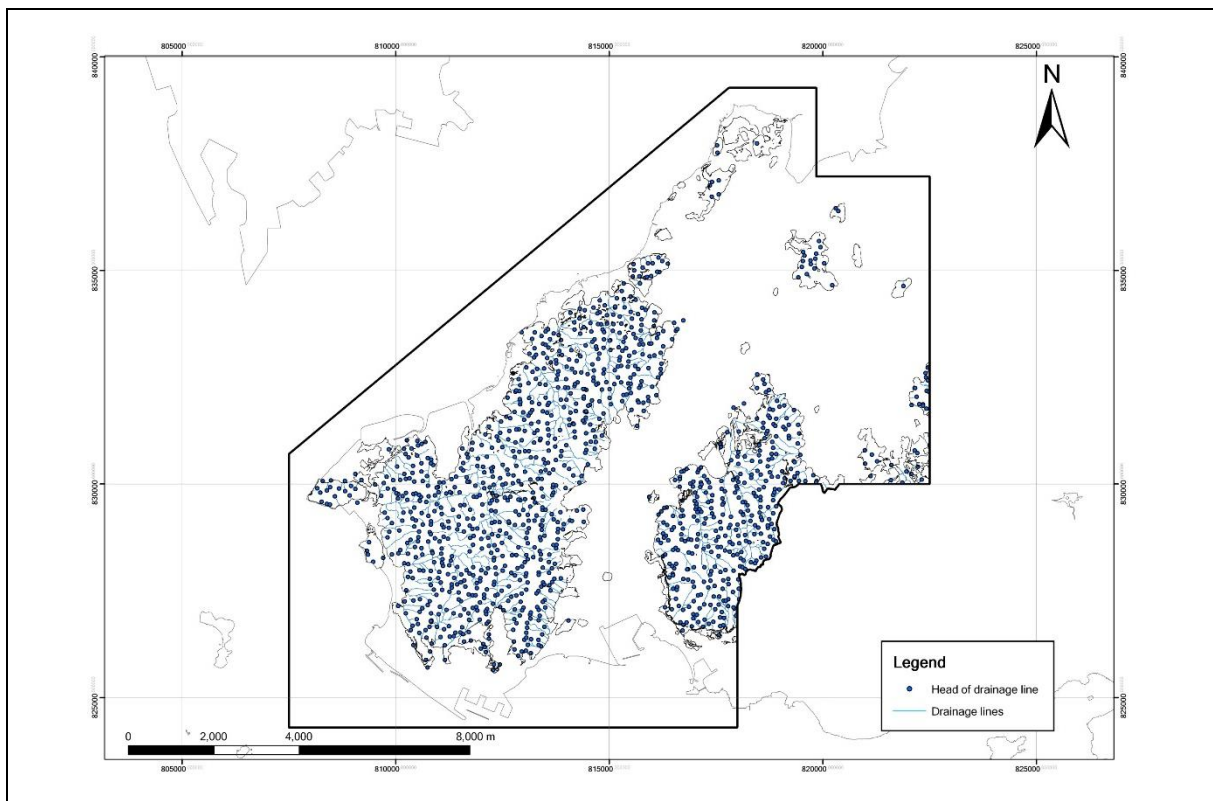
Figure 5.30   Head of Drainage Lines in 1:5,000 Scale Topographic Map
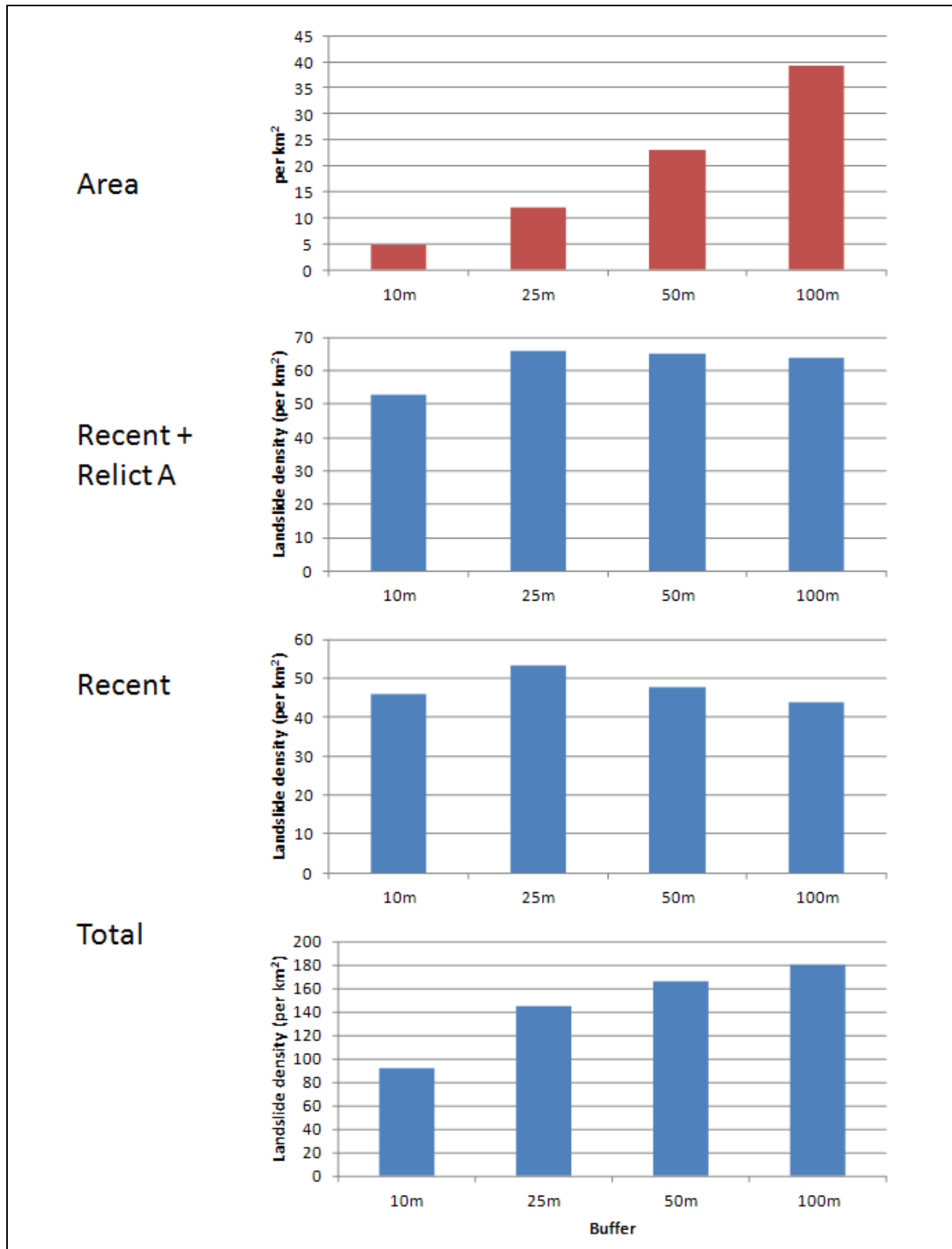
Figure 5.31   Landslide Density of Shifted Landslide Crown for Different Proximities to Drainage Lines
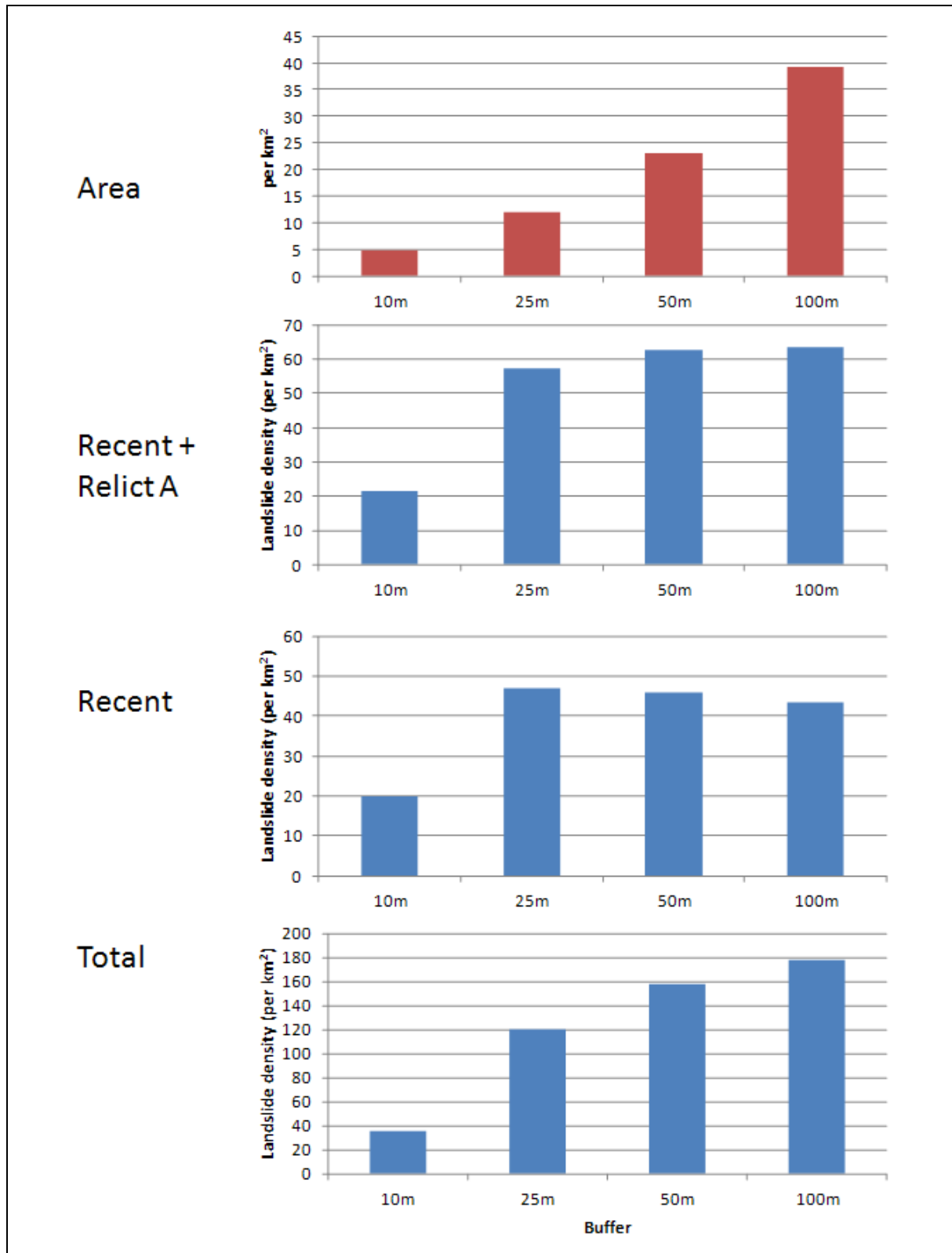
Figure 5.32 **Landslide Density of Non-shifted Landslide Crown for Different Proximities to Drainage Lines**
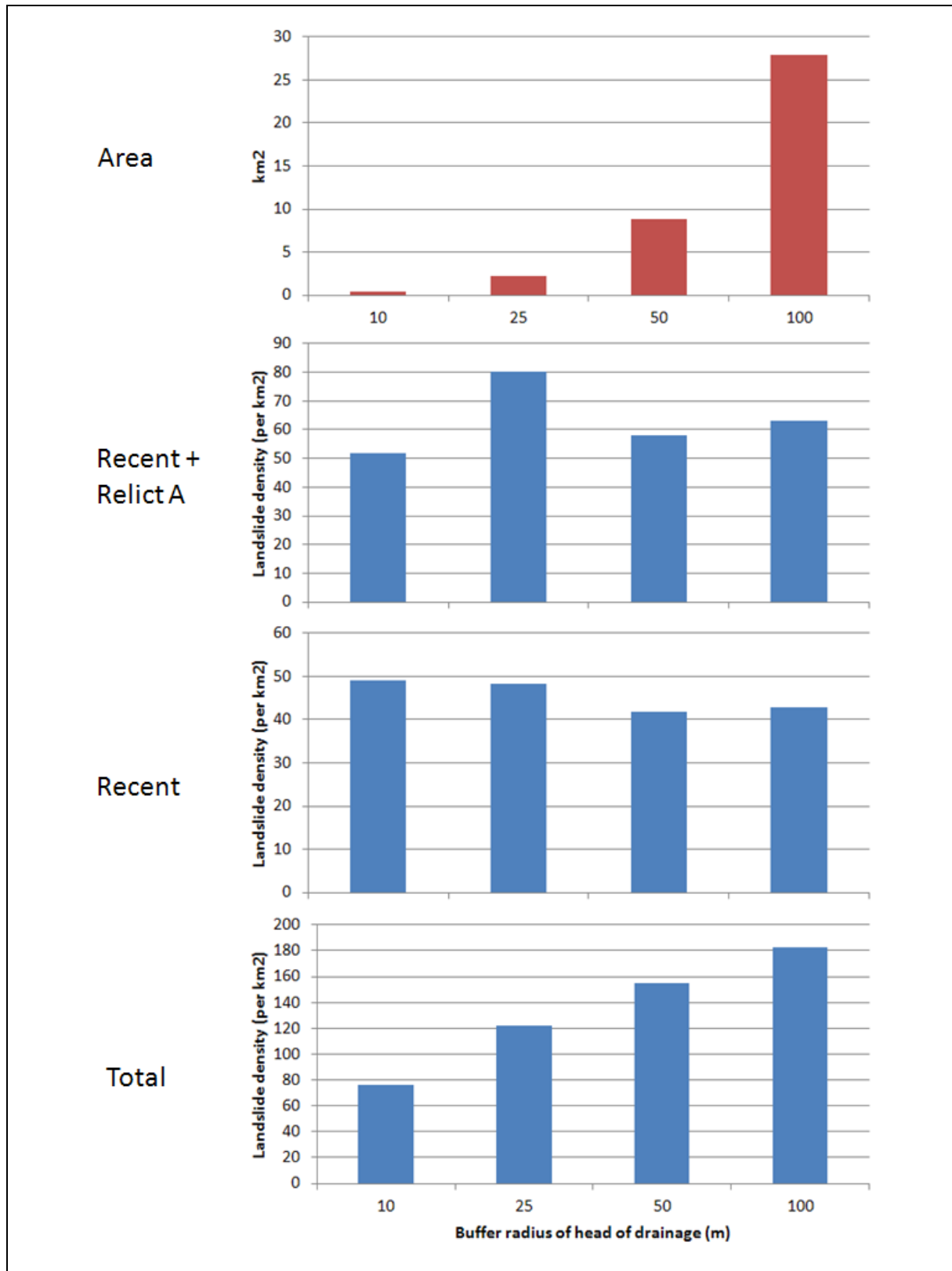
Figure 5.33 Landslide Density of Shifted Landslide Crown for Different Buffers to the Head of the Drainage Line
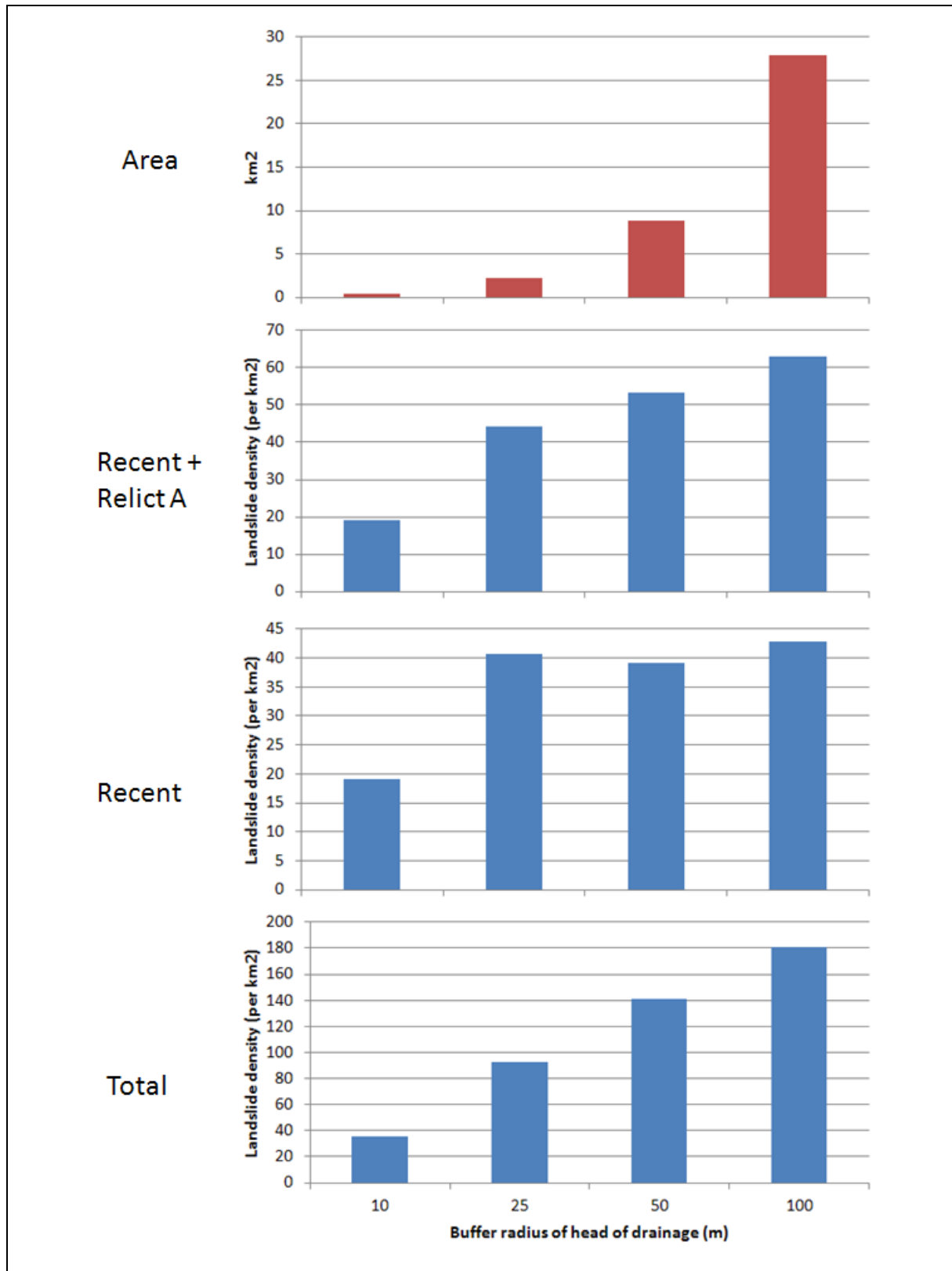
Figure 5.34   Landslide Density of Non-shifted Landslide Crown for Different Buffers to the Head of the Drainage Line

5.6 Susceptibility Assessment

5.6.1 Preliminary Susceptibility Model

A preliminary susceptibility model has been developed in order to combine the influence of various susceptibility factors identified in the previous section as key contributors to the predisposition of hillsides to landsliding. Based on a statistical review of various datasets discussed in Section 5.5 against the published ENTLI data, the Slope Angle and the Terrain Unit are considered as the most relevant indicators for a regional-scale screening of potential landslide hazards. The combined influence of these two parameters has been assessed using a matrix approach to provide a qualitative indicator of the landslide susceptibility within the Study Area. Using this matrix (as shown in Table 5.4), a susceptibility map for the Study Area has been generated in GIS to graphically present those areas falling within different landslide susceptibility classes as shown in Figure 5.35.

Table 5.4 Combined Influence of Slope Angle and Terrain Unit on Landslide Susceptibility

Terrain Class Slope Class	Adverse	Moderate	Favourable
Steep (> 40°)	Very High	High	Moderate
Moderately Steep (30° - 40°)	High	Moderate	Low
Gentle (< 30°)	Moderate	Low	Low
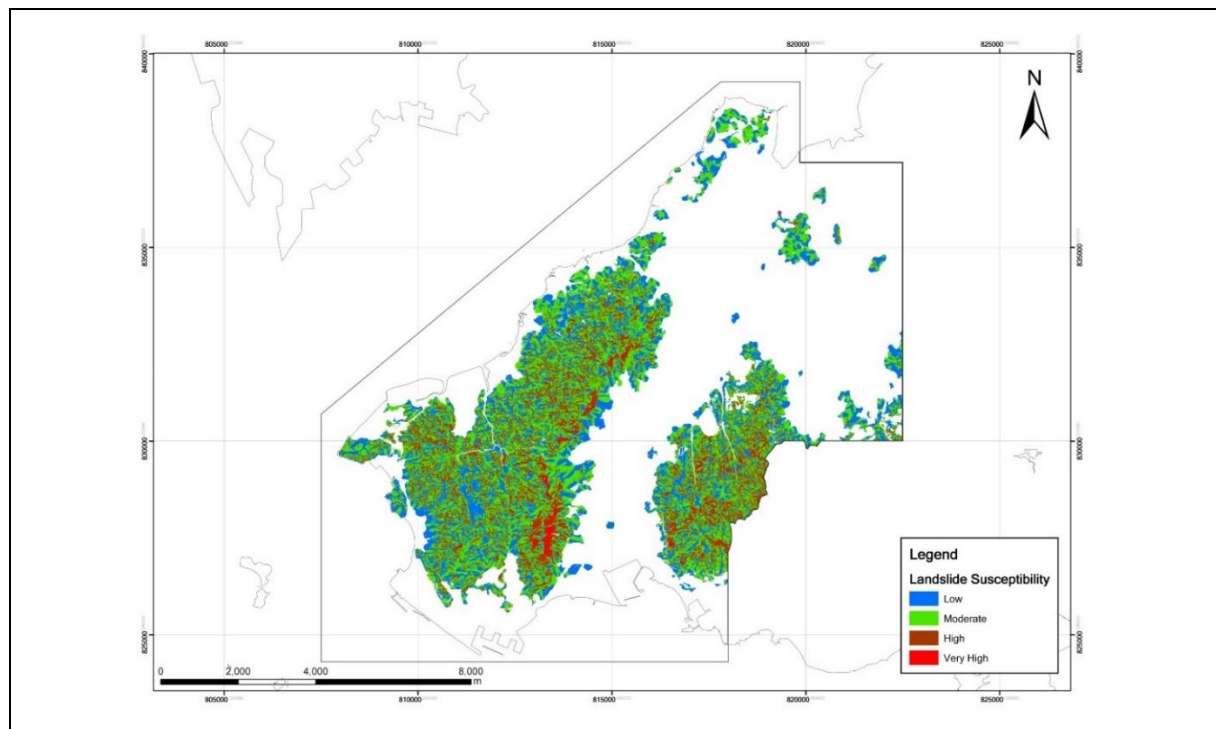
Figure 5.35 Susceptibility Map Based on Terrain Unit and Slope Angle

5.6.2 Susceptibility Model Validation

The landslide susceptibility model has been checked and calibrated against the available landslide information contained in the ENTLI. As indicated below and in Figures 5.36 and 5.37 for shifted and non-shifted landslide records, the model shows a good correlation between the qualitative landslide susceptibility class and the corresponding density of past landslides within those areas.   The corresponding landslide densities are listed in Table 5.5.
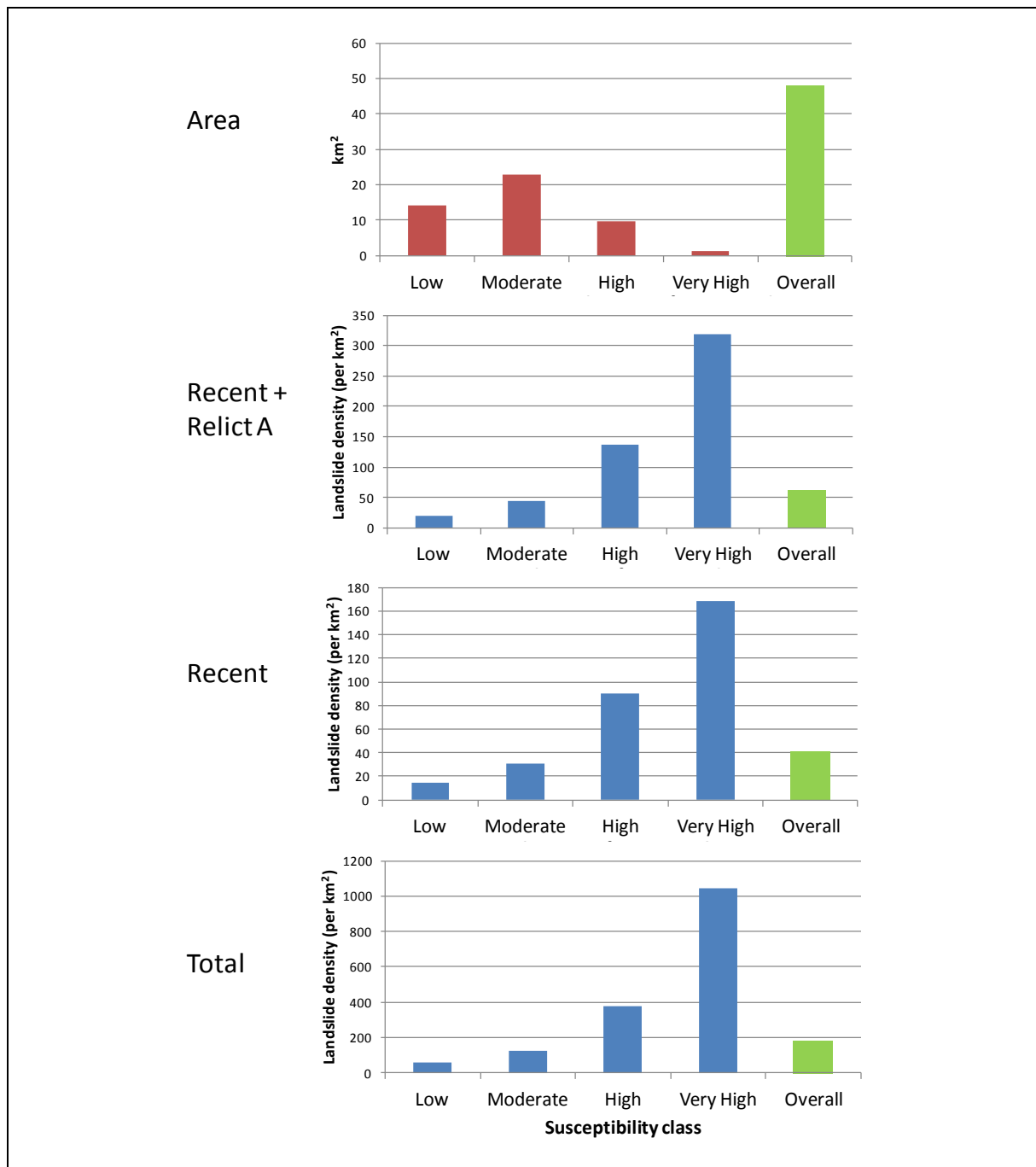
Figure 5.36   Landslide Density of Shifted Landslide Crown with Susceptibility Class up to 2009
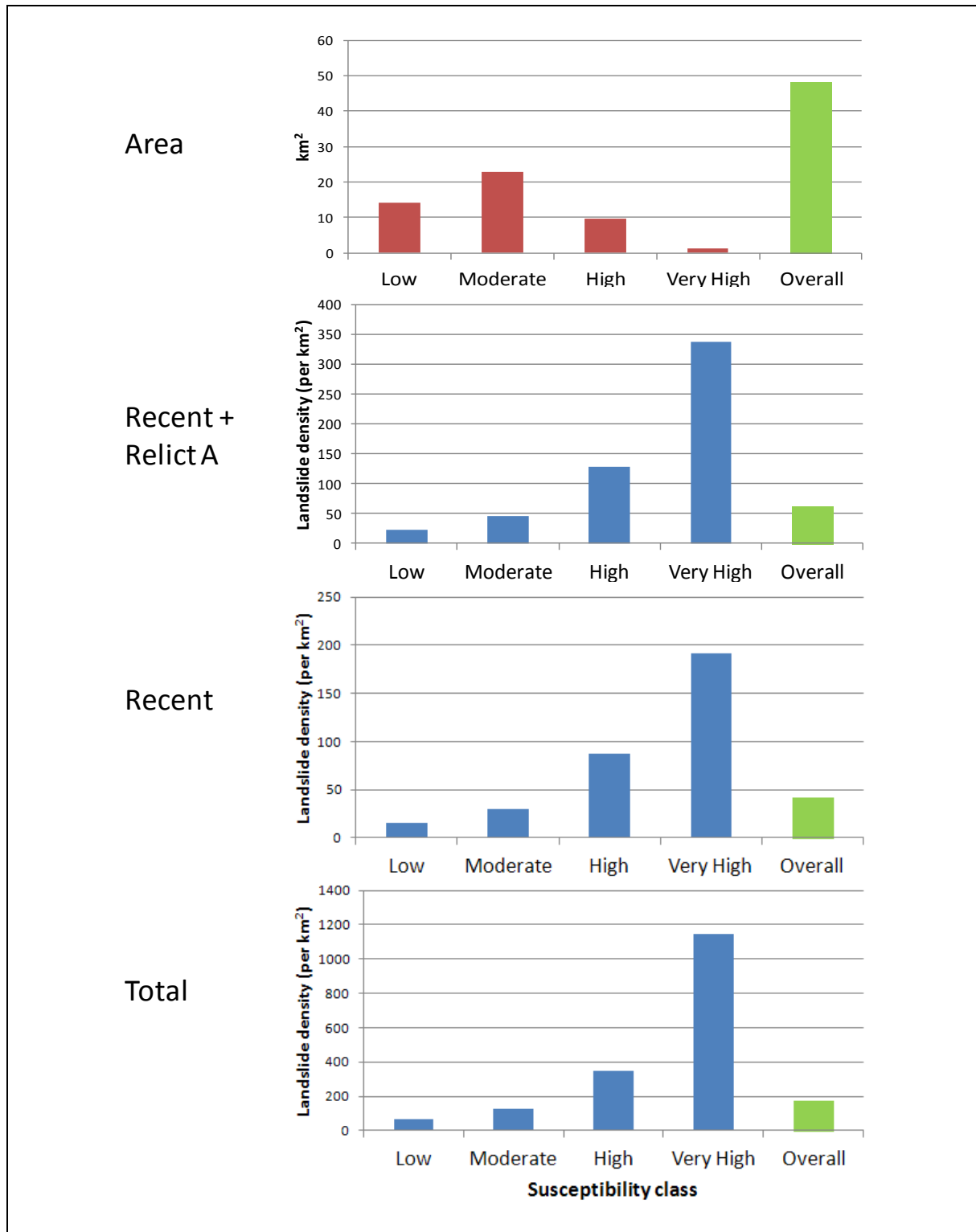
Figure 5.37   Landslide Density of Non-shifted Landslide Crown with Susceptibility Class up to 2009

Table 5.5 Susceptibility Class and the Corresponding Density of Past Landslides

Susceptibility Class	Landslide Density (No. of Landslides per km²) for		
	Recent ENTLI	Recent + Relict Class A ENTLI	All ENTLI
Very High	168.77	318.04	1,044.88
High	80.72	136.24	377.80
Moderate	30.77	43.83	121.31
Low	14.42	19.66	56.75
Overall	41.08	61.85	176.06

As noted in Section 5.4.3 and highlighted in Figure 5.10, a significant number of landslides observed in the area occurred in three swarms. In order to check whether these landslides reinforce or contradict the susceptibility model, the ENTLI data have been examined for each of them. The results of shifted and non-shifted landslide densities are shown in Figures 5.38 and 5.39 respectively.   These figures show that the landslide density with respect to the susceptibility class is remarkably consistent for all three swarms. This implies that landslides occurring within any of these major events do not significantly affect the overall validity of the model.

Further validation of the model has also been carried out by examining the ENTLI data within 10-year intervals. The results of the shifted and non-shifted landslide densities, presented in Figures 5.40 and 5.41 respectively, show that the qualitative landslide susceptibility class gives very similar and consistent trends for each decade and reinforces the stability over time of the susceptibility classes.

5.6.3 Landslide Occurrence Probability

The total landslide area of each susceptibility class has been normalised to the total area of each class and the time period of the landslide record to give the landslide occurrence probability.   The landslide area has been estimated by multiplying the length and width recorded in the ENTLI inventory.   As the recent ENTLI records started from 1963 i.e. when aerial photographs were available, and those landslide scars occurred one to two years before 1963 as observed in the aerial photographs were also classified as recent landslides, it follows that the time period for recent landslides up to 2009 is approximately equal to 50 years. Figures 5.42 and 5.43 present the landslide area as a fraction of the total area for each susceptibility class for shifted and non-shifted landslides respectively for the ENTLI data recorded in that 50-year period.
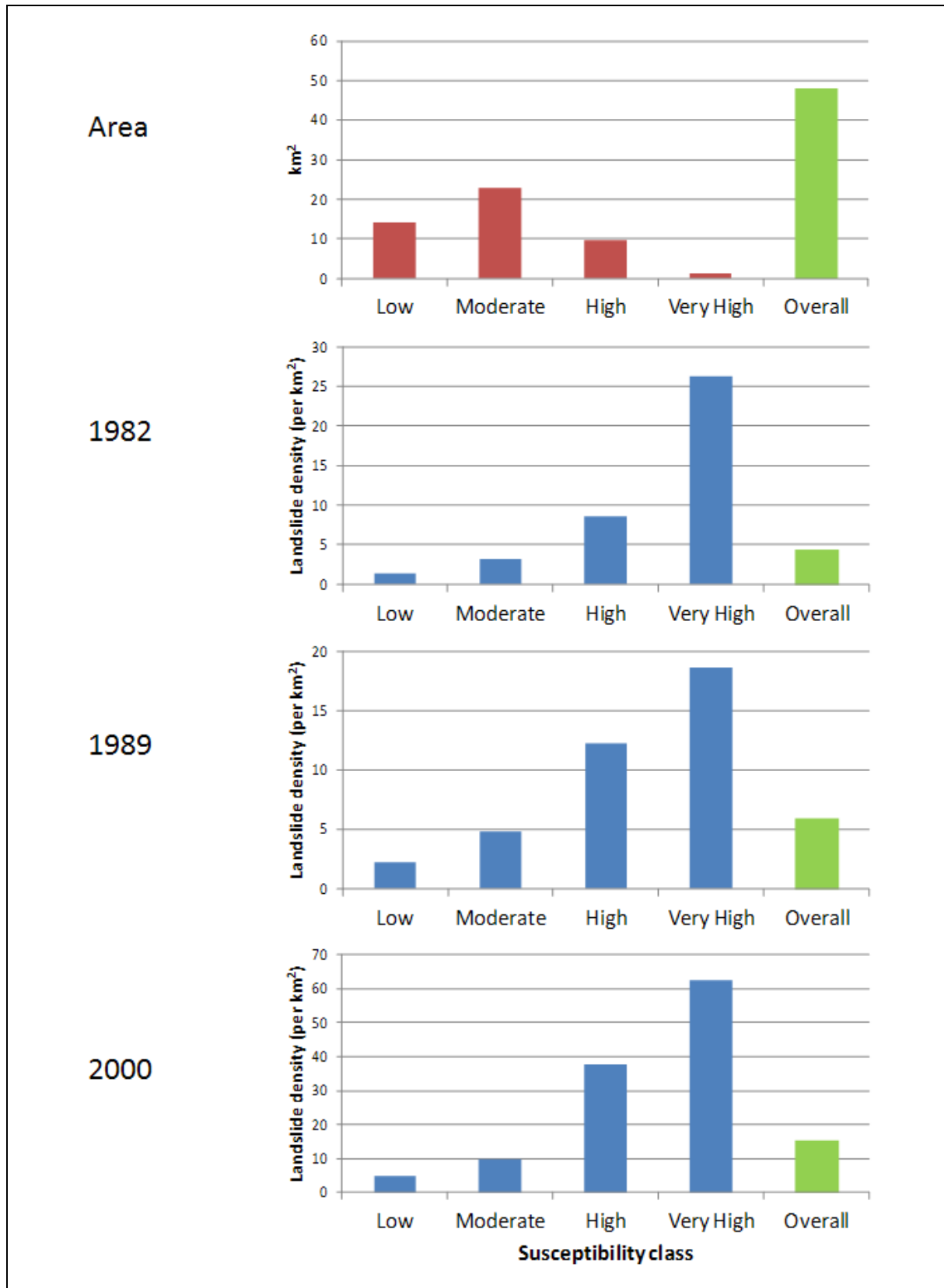
Figure 5.38   Landslide Density of Shifted Landslide Crown with Susceptibility Class in Particular Years
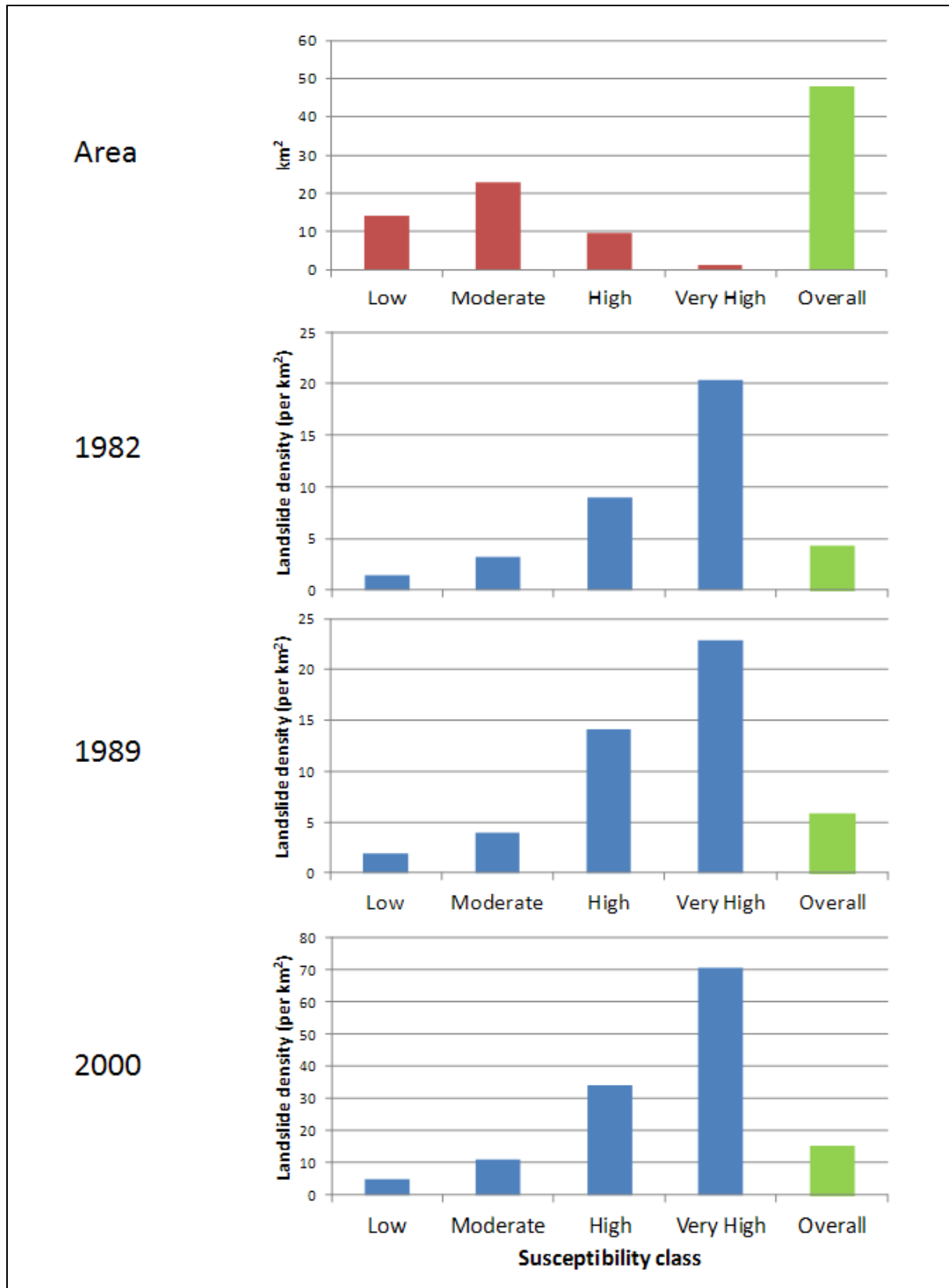
Figure 5.39   Landslide Density of Non-shifted Landslide Crown with Susceptibility Class in Particular Years
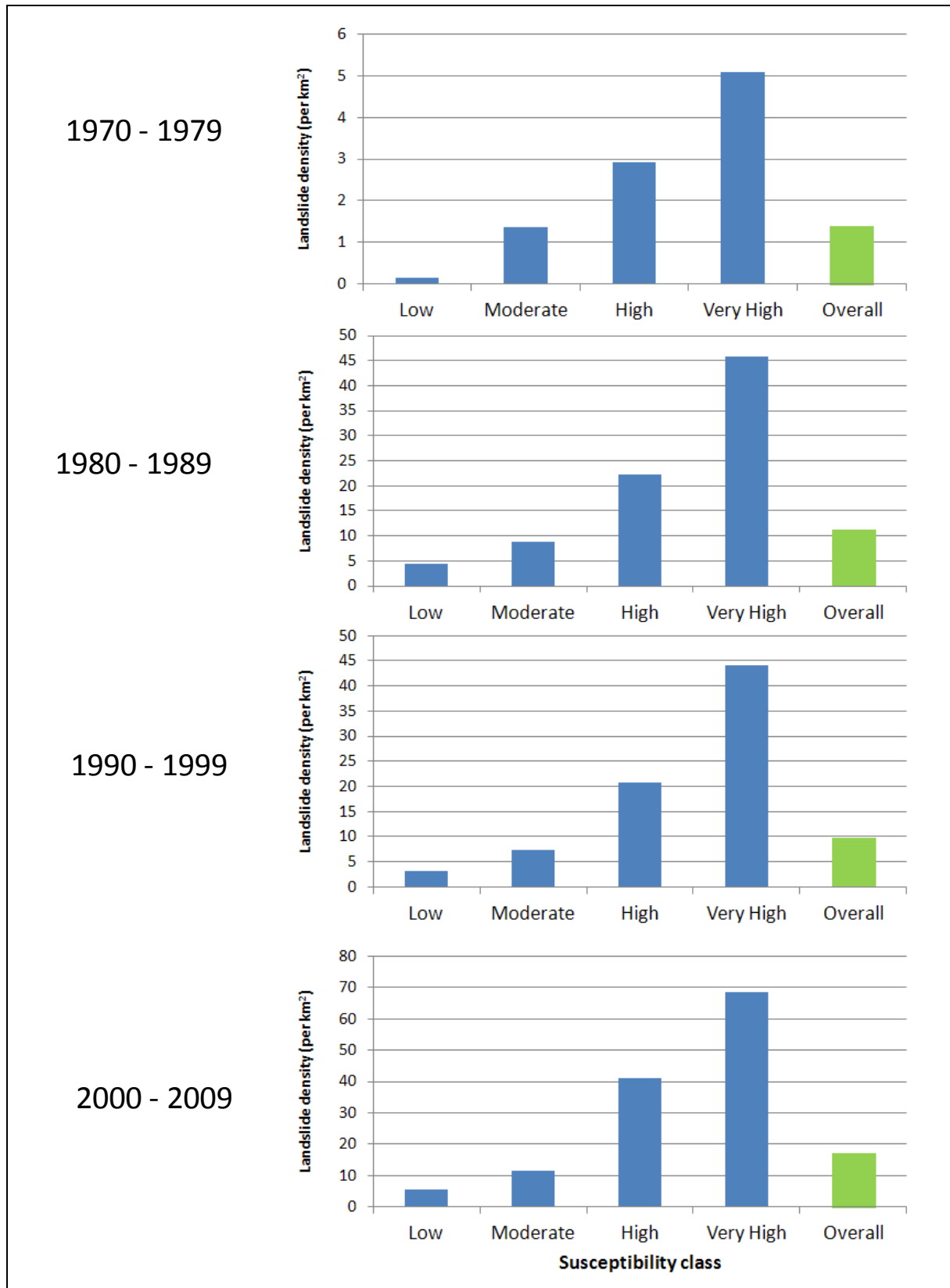
Figure 5.40   Landslide Density of Shifted Landslide Crown with Susceptibility Class in 10 Year Intervals
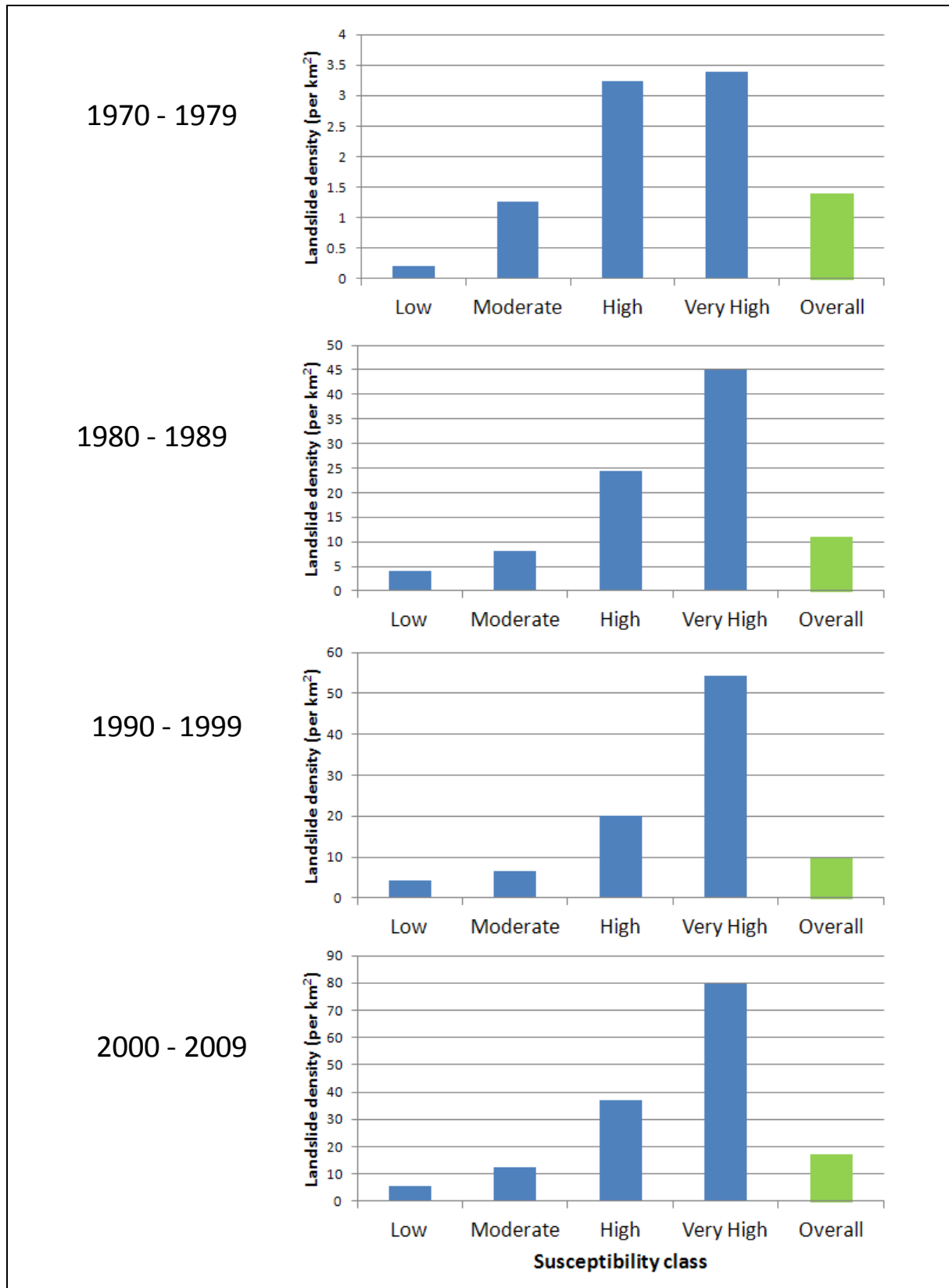
Figure 5.41   Landslide Density of Non-shifted Landslide Crown with Susceptibility Class in 10 Year Intervals
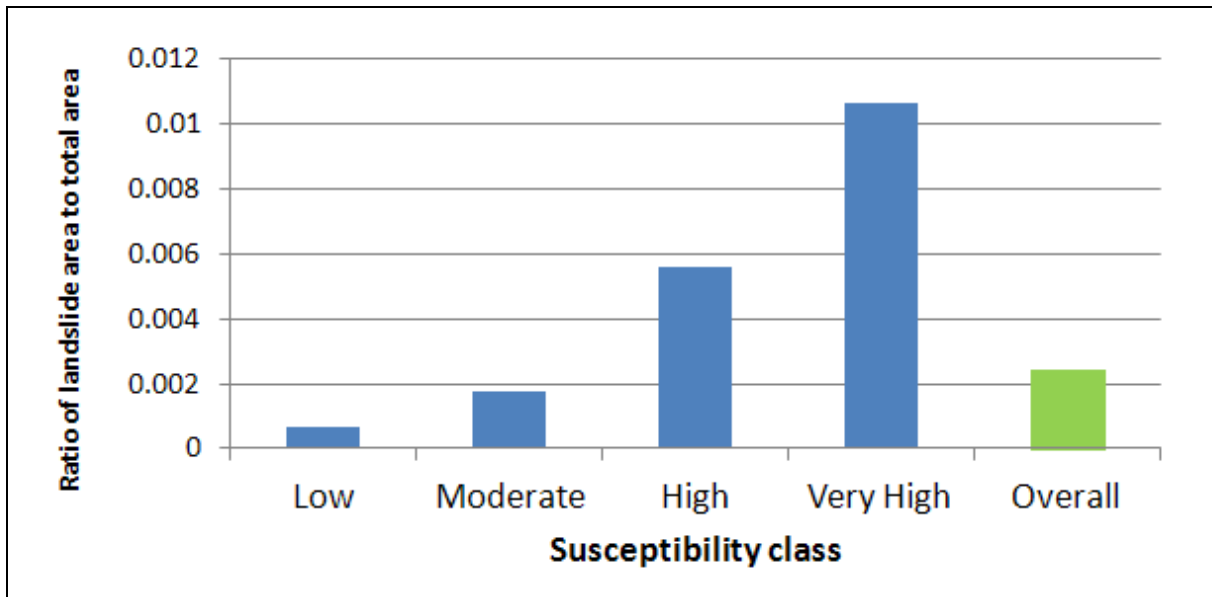
Figure 5.42   Ratio of Landslide Area to Total Area of Shifted Landslide Crown with Susceptibility Class for Recent Landslides up to 2009
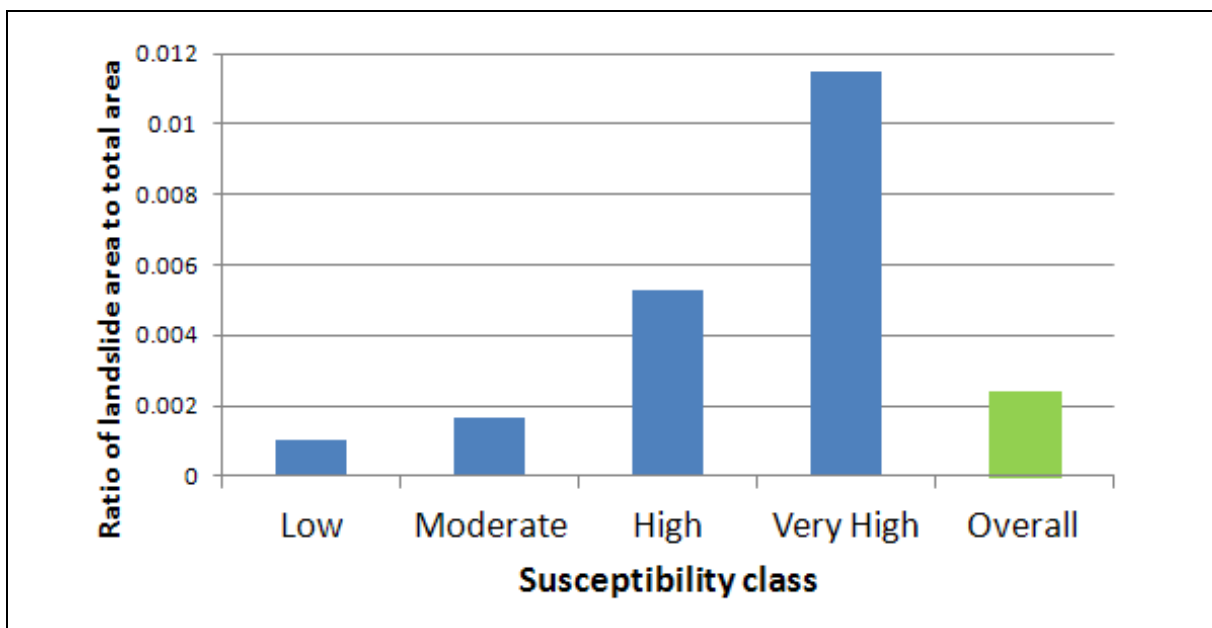
Figure 5.43   Ratio of Landslide Area to Total Area of Non-shifted Landslide Crown with Susceptibility Class for Recent Landslides up to 2009

6 Seismic Microzonation Maps

6.1 Slope Susceptibility

The susceptibility map presented in Figure 5.35 comprises an assessment of the predisposition of natural terrain hillsides to landsliding irrespective of the triggering event that may have induced the failures. In Hong Kong, there is no evidence of other triggering events except for rainfall.

As concluded in Section 3, the potential of earthquake-induced landslides is significant only if the slope, at its initial state, has a very low static factor of safety (FoS) i.e. it is close to failure at the time when an earthquake takes place. As such, the susceptibility map in Figure 5.35 forms a good starting point for the assessment of earthquake-induced landslide susceptibility.

To assess the additional effects of earthquakes on the landslide susceptibility, the likelihood of seismic ground motions occurring at the same time when a slope is close to failure (because of rainfall) needs to be analysed. In Section 3, the seismic ground motions used for slope stability analyses are pertinent to rock sites. As mentioned in Section 5.3, the natural terrain boundary is not exactly the same as the rock boundary. However, most of the area within the natural terrain boundary is defined as "rock and thin soil" as discussed in Arup (2018) and delineated in Figure 6.1. Comparatively, areas with a thicker soil layer are small. Overlaying with the slope angle map, as shown in Figure 6.2, it can be seen that these thicker soil areas are mainly located in gently sloping areas (less than 20°). It is considered that these are depositional areas where landslides are unlikely to occur. Therefore, if the ground motion amplification due to localised soil deposits occurs, it would only affect a small area that will not have a significant effect on the overall hazard assessment. With the above considerations, the seismic ground motions pertinent to rock sites is appropriate to this study.

Wong & Ho (2000) discussed the effects of earthquakes on man-made slopes and addressed the issue of the occurrence of seismic ground motions concurrently with a slope being in a weakened state due to precedent rainfall. Based on the wetting front theory, it was concluded that if the daily rainfall exceeded 50 mm, there would be a moderate degree of saturation, and if the daily rainfall exceeded 380 mm, there would be a high degree of saturation. By studying the rain gauge data for Hong Kong, it was concluded that there would be a 4.5% likelihood of moderate saturation, and a 0.5% likelihood of high saturation. In the remainder of the time (i.e. 95% likelihood), the slope would be at a low degree of saturation. It was also concluded that the static FoS of the slope would be enhanced by about 0.3 for low saturation, and by 0.15 for moderate saturation.
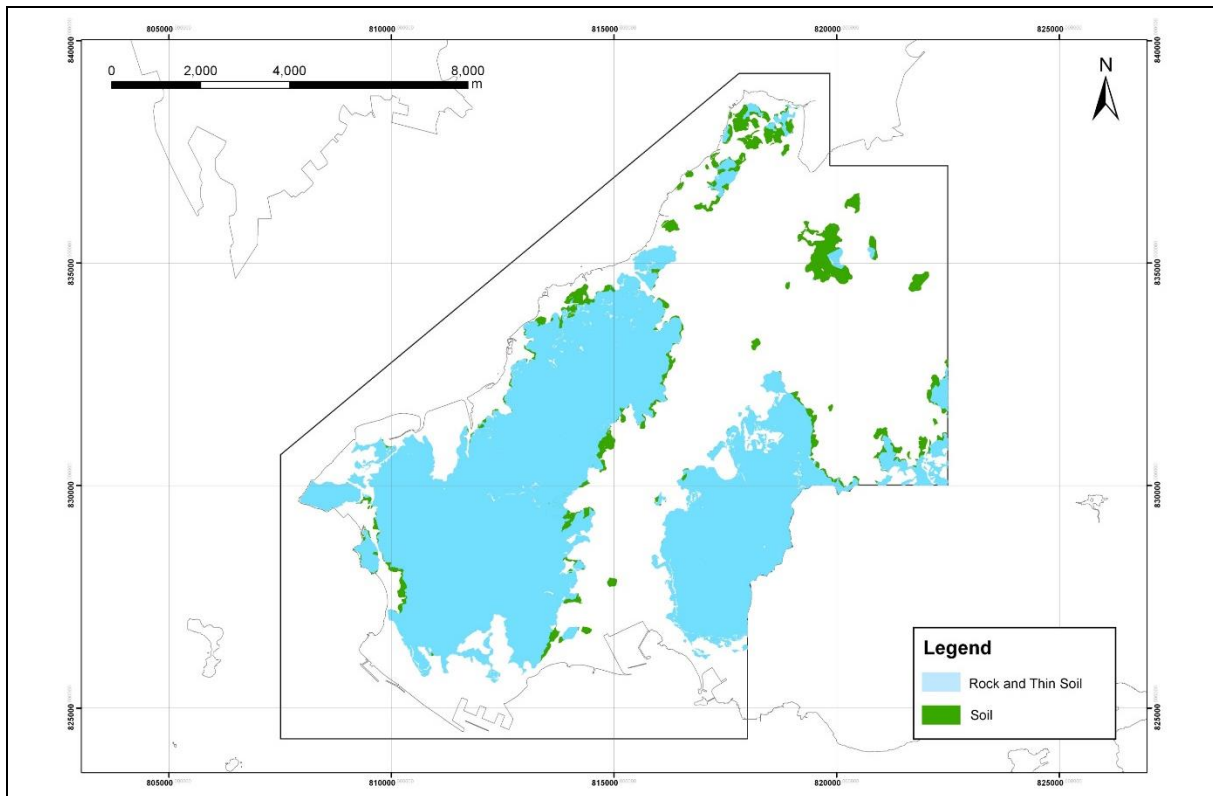
Figure 6.1   Soil and Rock Distribution within Natural Terrain Boundary
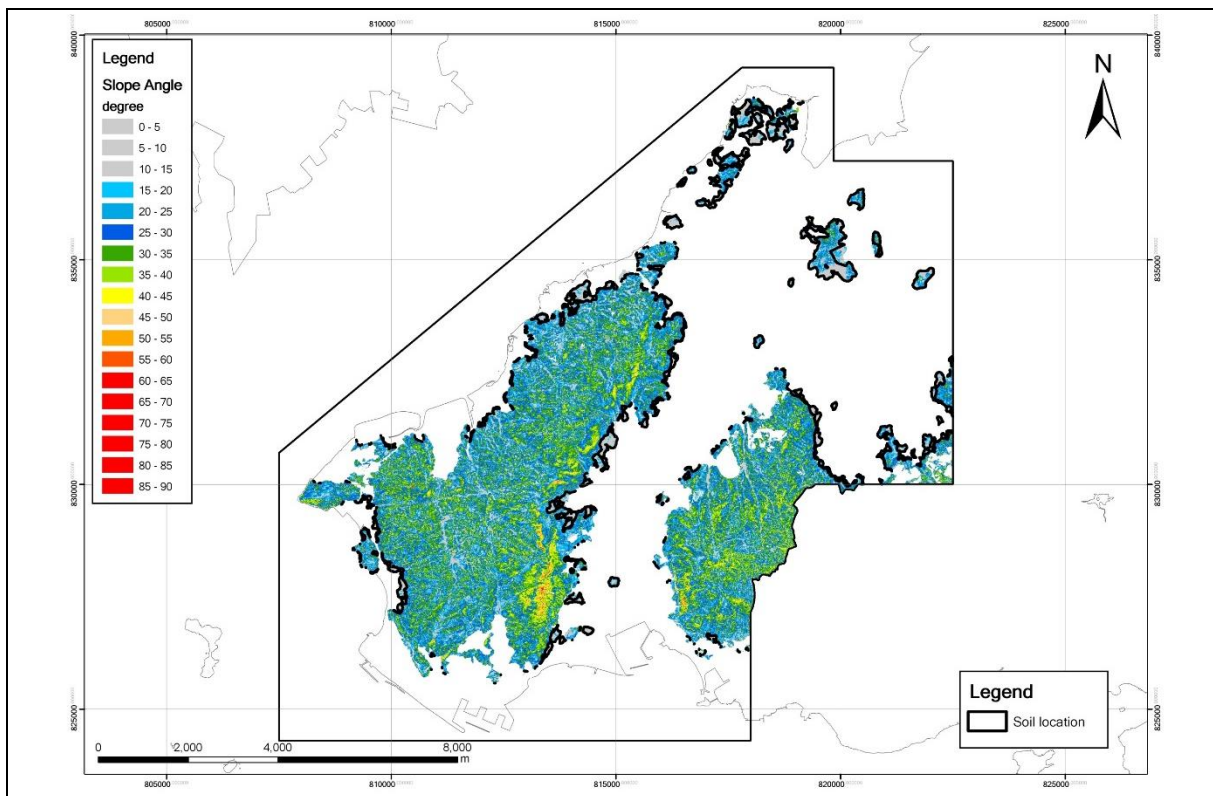
Figure 6.2   Soil Distribution Compared with Slope Angle

In this study, the durations and the static FoS reported by Wong & Ho (2000) have been combined with the observed failure rates from the ENTLI data as shown in Figure 6.3. For the Average curve, it is assumed that the FoS reduces to 1.05 when the soil is at a high level of saturation for 0.5% of the time, and the FoS is 1.2 and 1.35 at 5% and 20% of the time respectively. For the remaining 80% of the time, the FoS is much larger and beyond the level of concern. For the purpose of plotting the ENTLI data on a logarithmic scale, it is assumed that the soil slopes actually fail when their FoS is 1.001. The "% time" values plotted on the *x* axis are those observed for various susceptibility classes (see Figure 5.42) divided by the 50-year observation period. These values along the *x*-axis (i.e. at a FoS of 1.001) is interpreted as the annual chance that any particular location will fail due to rainfall. These points have then been extrapolated over time to show the likely FoS as a function of duration for each of the susceptibility class.
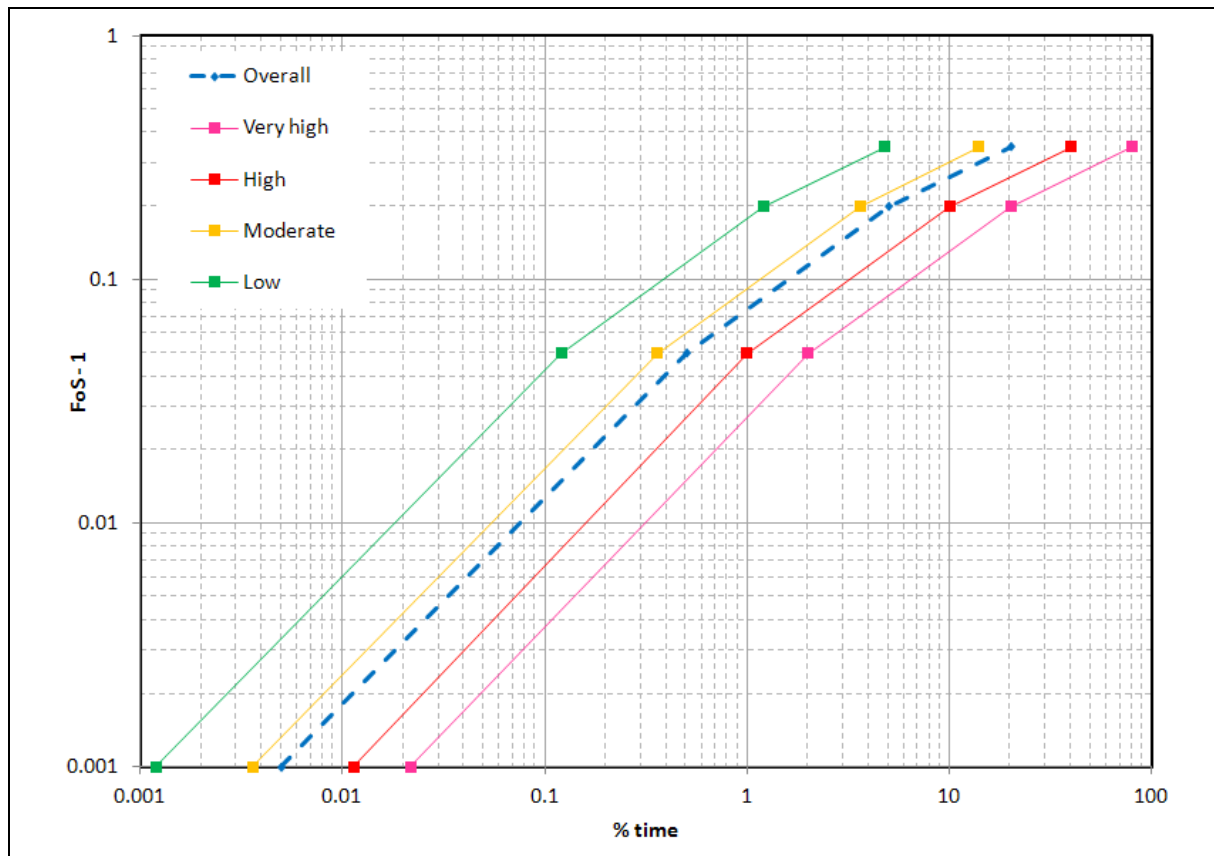
Figure 6.3   Factor of Safety and Percentage Time Relationship for the Susceptibility Classes

Figure 6.3 can be used to estimate the additional likelihood of failure induced by seismic ground motions. For example, for a 2% in 50 years ground motion with no topographic amplification, Figure 3.50 implies that, on average, slopes with an A_c value of 0.15 m/s^2 would be at the onset of failure. This A_c value corresponds to a FoS of about 1.03 (see Figure 6.3). It can be seen to have an average chance of occurrence for 0.3% of the time. It, therefore, implies that over 50 years, the enhanced hazard of slope failure is 2% times 0.3% i.e. 0.006%.

The effect of how likely earthquakes would take place also needs to be considered. Figure 3.51 shows that under the 10% in 50 years ground motion, a slope with a FoS of about 1.01 would be at the onset of failure.   Based on Figure 6.3, this FoS is likely to exist over about 0.08% of the time.   By approximately integrating the ground motions between 10% and 2% in 50 years, the overall hazard is increased by about 0.018% in the next 50 years.   Given that the average landslide area ratio hazard from rainstorms in the past 50 years is 0.25% at present (see Figure 5.42), the overall hazard in the next 50 years is therefore likely to increase to 0.268%.

For areas assessed as being of very high susceptibility, using the same approach, it has been evaluated that the landslide area ratio hazard is increased by about 4 times to a value of 0.07% in the next 50 years.   As a result, the overall hazard increases from 1.08% to 1.15% in the next 50 years.   Similar assessments have been undertaken for other susceptibility classes and the results are summarised in Figure 6.4.   This figure also shows the additional influence of topographic effects derived using the same procedures.   For example, for the case of 1.4 PGA amplification, Figure 3.67 shows that the FoS needs to be about 1.07 for the onset of failure for the 2% in 50 years ground motion.   From Figure 6.3, thitaFoS would occur at about 4% of the time for very highly susceptible slopes leading to an enhanced landslide area ratio hazard of 0.08%.   For more frequent seismic ground motions, it is increased to about 0.24% leading to a total value of 1.32% as shown in Figure 6.4.
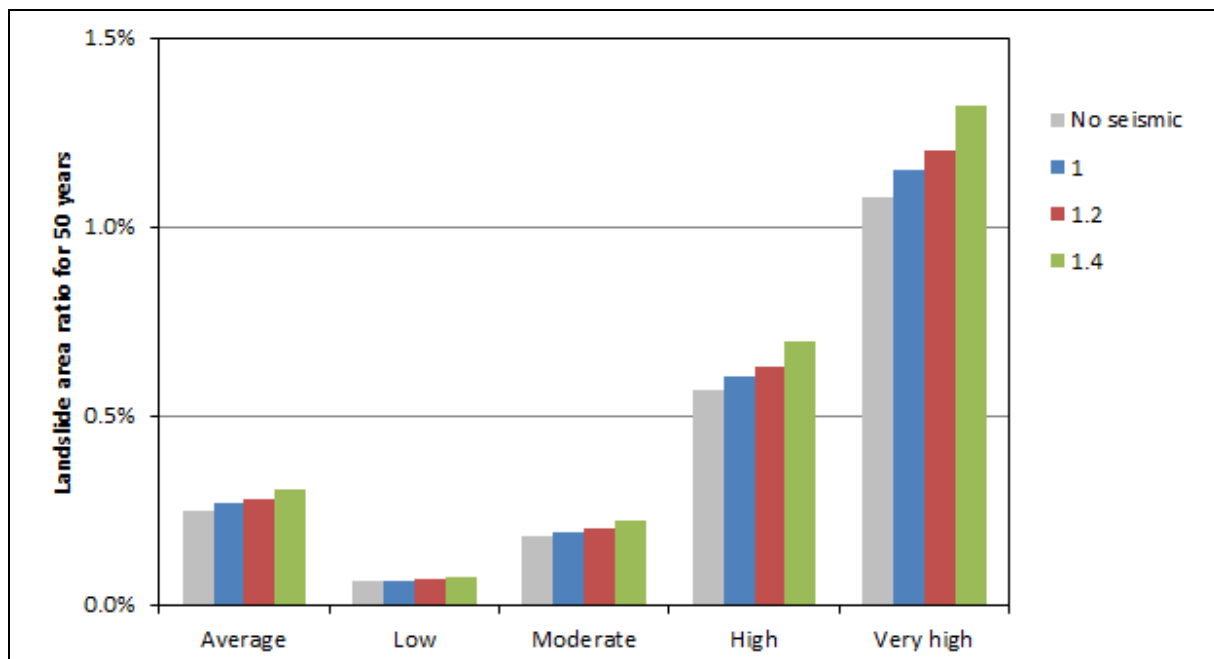
Figure 6.4   Landslide Area Ratio in 50 Years for Different Amplification Factors and Susceptibility Classes

These enhanced overall susceptibility values have been added to the susceptibility map in Figure 5.23 and plotted as colours representing the likelihood of failure in the next 50 years (in steps of 0.1%).   The resulted natural terrain landslide microzonation map is shown in Figure 6.5.   For comparison, the same contours have been mapped for rainstorms only as shown in Figure 6.6.
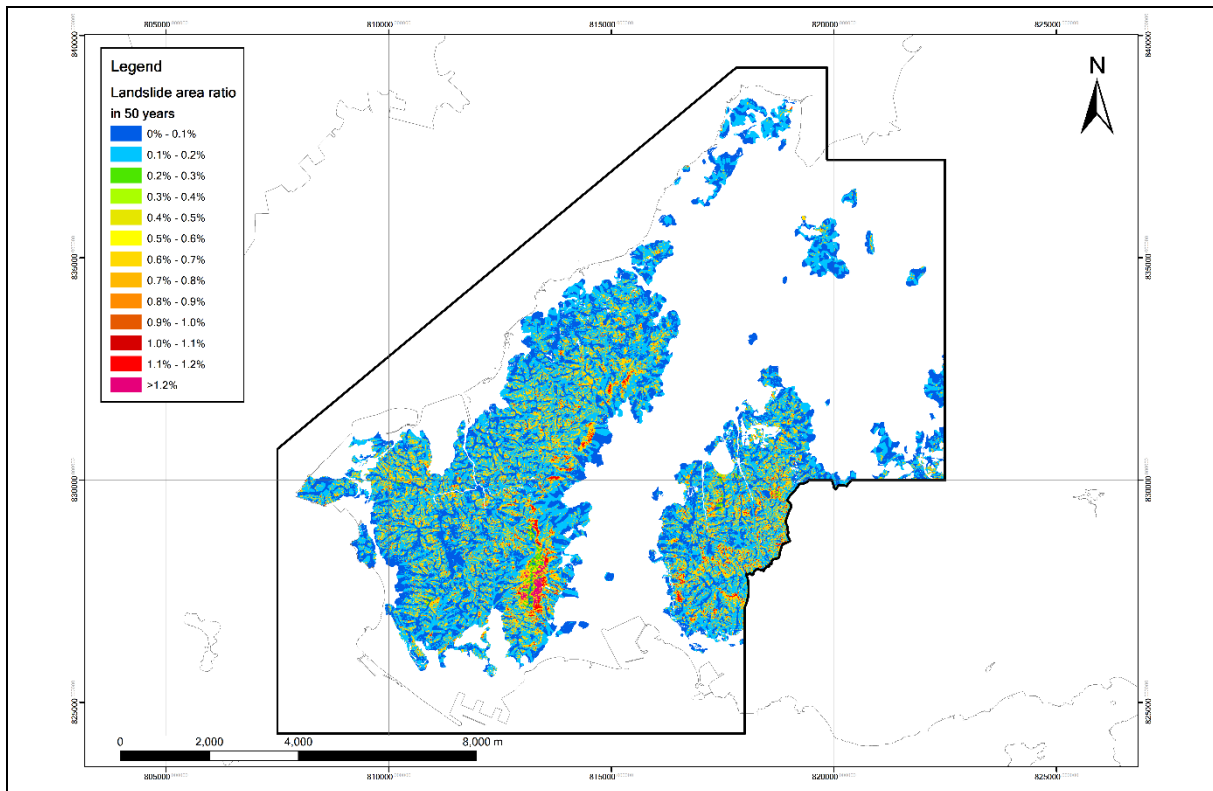
Figure 6.5   Susceptibility Map for Landslide Density Considering Earthquake and Rainfall Effect
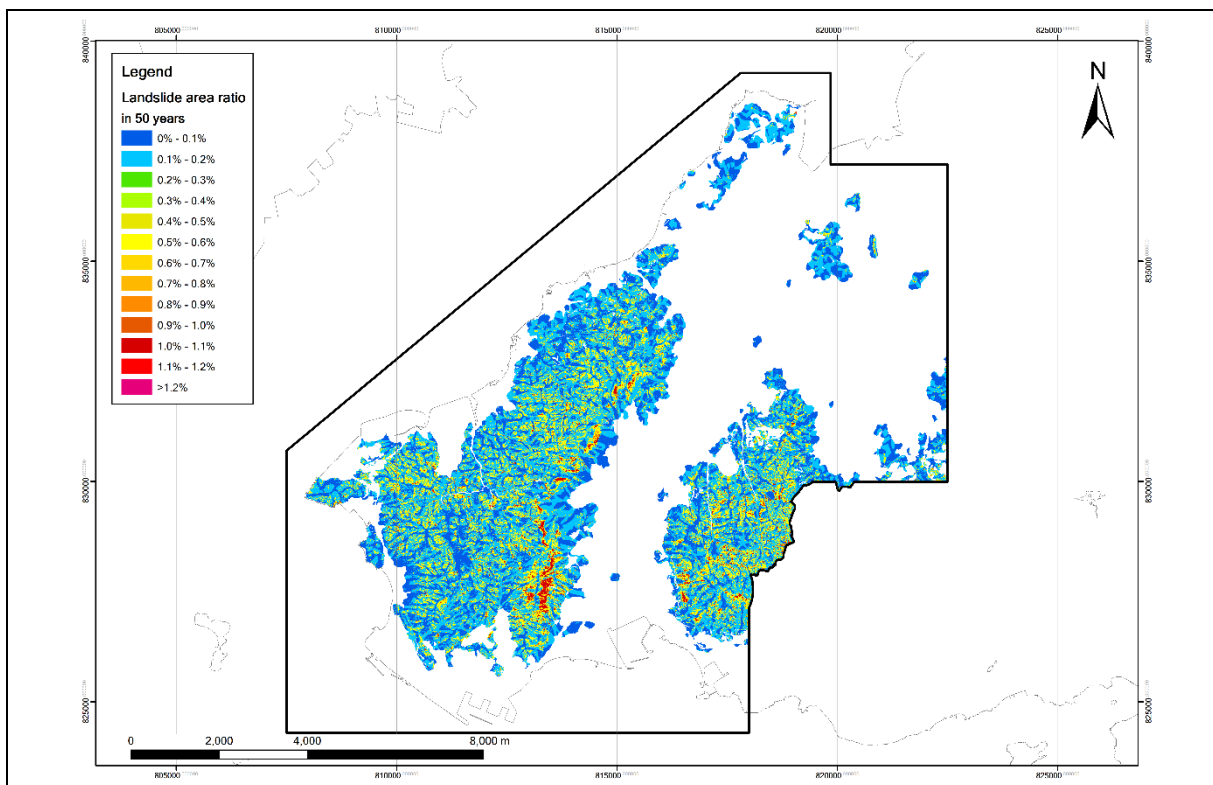
Figure 6.6   Susceptibility Map Only Considering Rainfall

The increase in the overall landslide hazard has been determined by multiplying the natural terrain hazard factors shown in Figure 6.4 by the areas associated with each classification and the pertinent PGA amplification factor. Table 6.1 shows these areas of natural terrain. Table 6.2 shows the total area of natural terrain that is likely to fail within the Study Area together with the overall average hazard in the next 50 years for cases where seismic loading is ignored, and where it is considered. It can be seen that the overall hazard in the next 50 years increases from the rainfall-induced value of 0.244% to 0.261% if seismic effects are included. It should be noted that this modest increase is less than one tenth and within the error of prediction for the amount of failure due to rainfall alone.

Table 6.1   Areas of Natural Terrain (m^2) Associated with Susceptibility Class and with PGA Amplification Factor

Susceptibility Class	PGA Amplification Factor							Total
	1.0	1.0 - 1.1	1.1 - 1.2	1.2 - 1.3	1.3 - 1.4	1.4 - 1.5	> 1.5	
Low	12,754,946	1,017,691	436,893	53,165	10,069	16,869	475	14,290,109
Moderate	19,374,690	2,374,390	1,010,173	155,774	28,726	30,130	666	22,974,549
High	7,272,766	1,344,515	749,320	165,944	48,300	26,907	439	9,608,192
Very High	765,399	115,620	146,889	85,826	48,710	16,600	42	1,179,086
Total	40,167,802	4,852,216	2,343,276	460,709	135,805	90,507	1,622	48,051,936

Table 6.2   Area of Natural Terrain Likely to Fail (m^2) and Average % Area Ratio in the Next 50 Years

Susceptibility Class	Seismic Effect		
	None	Expected	Worst credible
Low	8,574	9,163	10,337
Moderate	41,354	44,225	49,729
High	54,615	58,424	66,119
Very High	12,734	13,770	15,852
Total (m^2)	117,277	125,582	142,037
Av. Area Ratio	0.244%	0.261%	0.296%

6.1.1   Sensitivity Analysis

The microzonation map shown in Figure 6.5 can be considered to be the best estimate. As shown in Figure 6.4, the effect of seismic ground motions, compared with the effect of rainfall only, is relatively small and does not have a major effect on the overall zoning. It is, however, admitted that many assumptions have been made in combining the effects of rainfall and earthquake. There is also uncertainty in the derivation of the effects of seismic ground motions.

To address this issue, the maximum credible effect has been assessed. This has been considered by assuming that the FoS of an average slope reduced from 1.05 to 1.02 for 0.5% of the time and that the 5% value has reduced from 1.2 to 1.1. The effect of this on the plot of FoS against % time is shown in Figure 6.7. This adjustment effectively increases the effects of the seismic ground motion by a factor of three. The resulted landslide area ratio hazard in the next 50 years is shown in the lower diagram of Figure 6.8. The best estimate values derived previously are shown in the upper diagram of the figure as a direct comparison. As can be seen, the overall result is not greatly changed. However, for the peak values for areas of high and very high susceptibility with topographic effects, some noticeable increases are observed. The resulted seismic zonation map, drawn using the same contours as Figures 6.5 and 6.6, is shown in Figure 6.9.

The area of natural terrain likely to fail and the overall average hazard in the next 50 years under this worst credible seismic effect is shown in Table 6.2. It can be seen that the current expected hazard of 0.244% increases by 0.052% (or by about one fifth) to 0.296%.
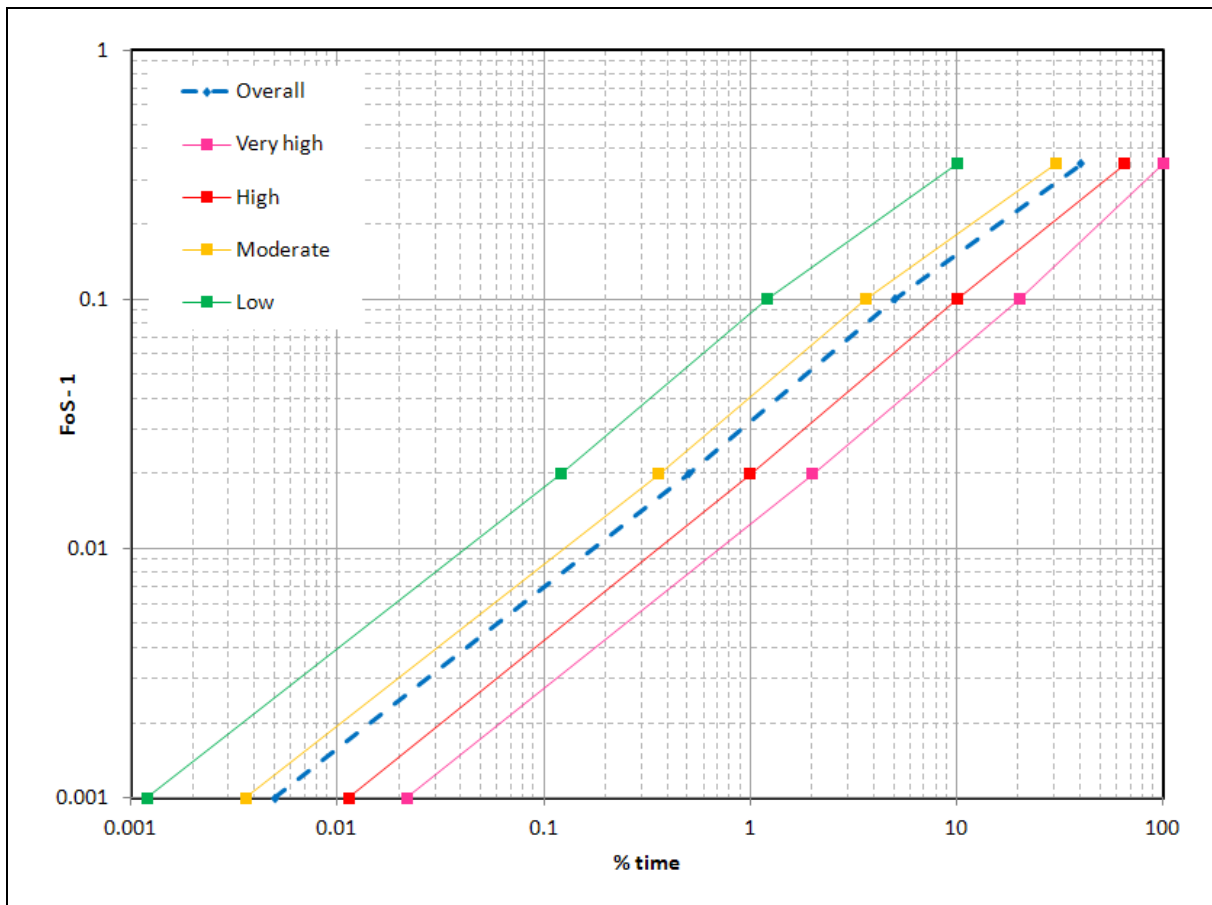
Figure 6.7   Worst Credible Factor of Safety and Percentage Time Relationship
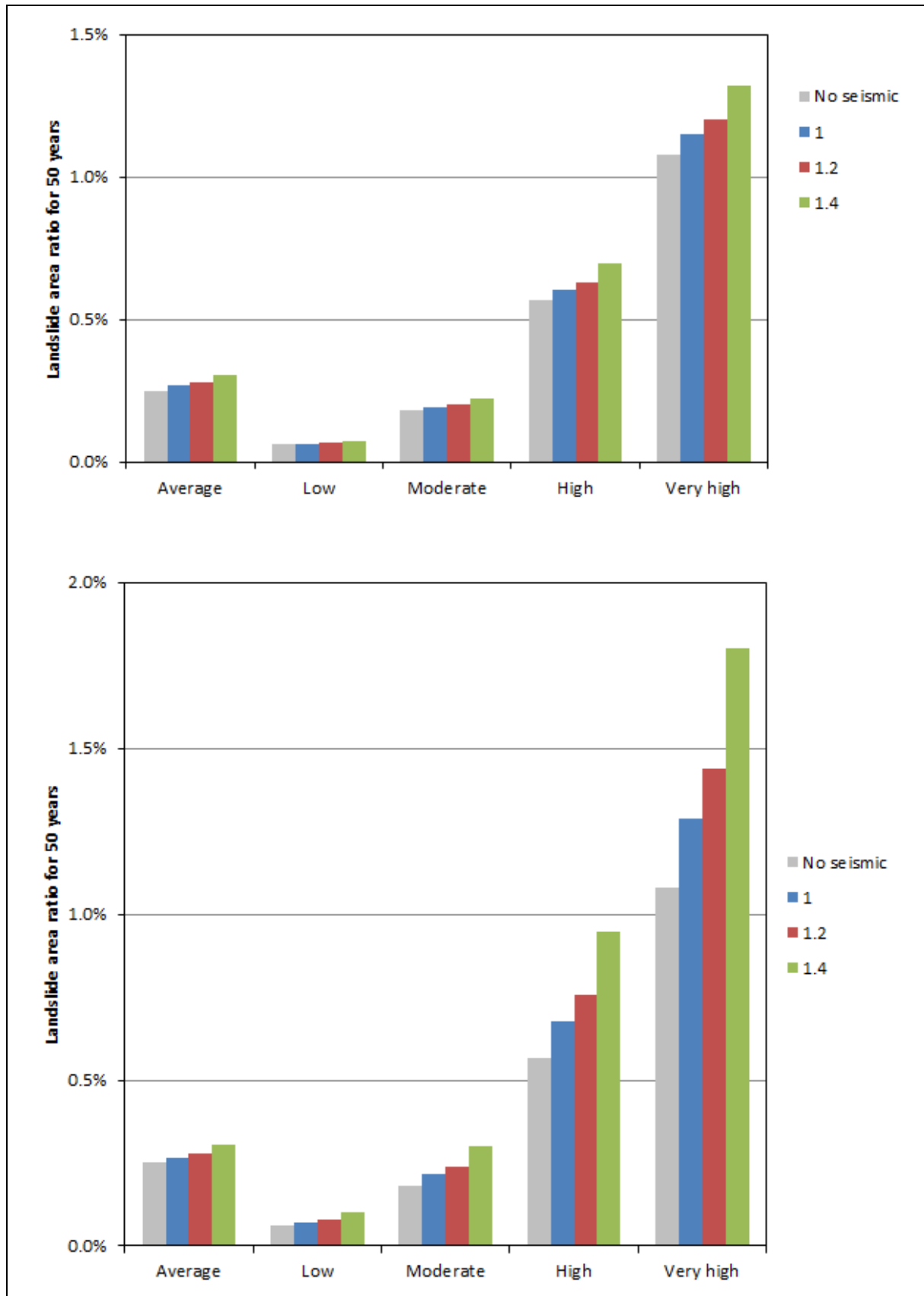
**Figure 6.8   Landslide Area Ratio in 50 Years for the Maximum Credible Seismic Effects
Compared with the Best Estimate**
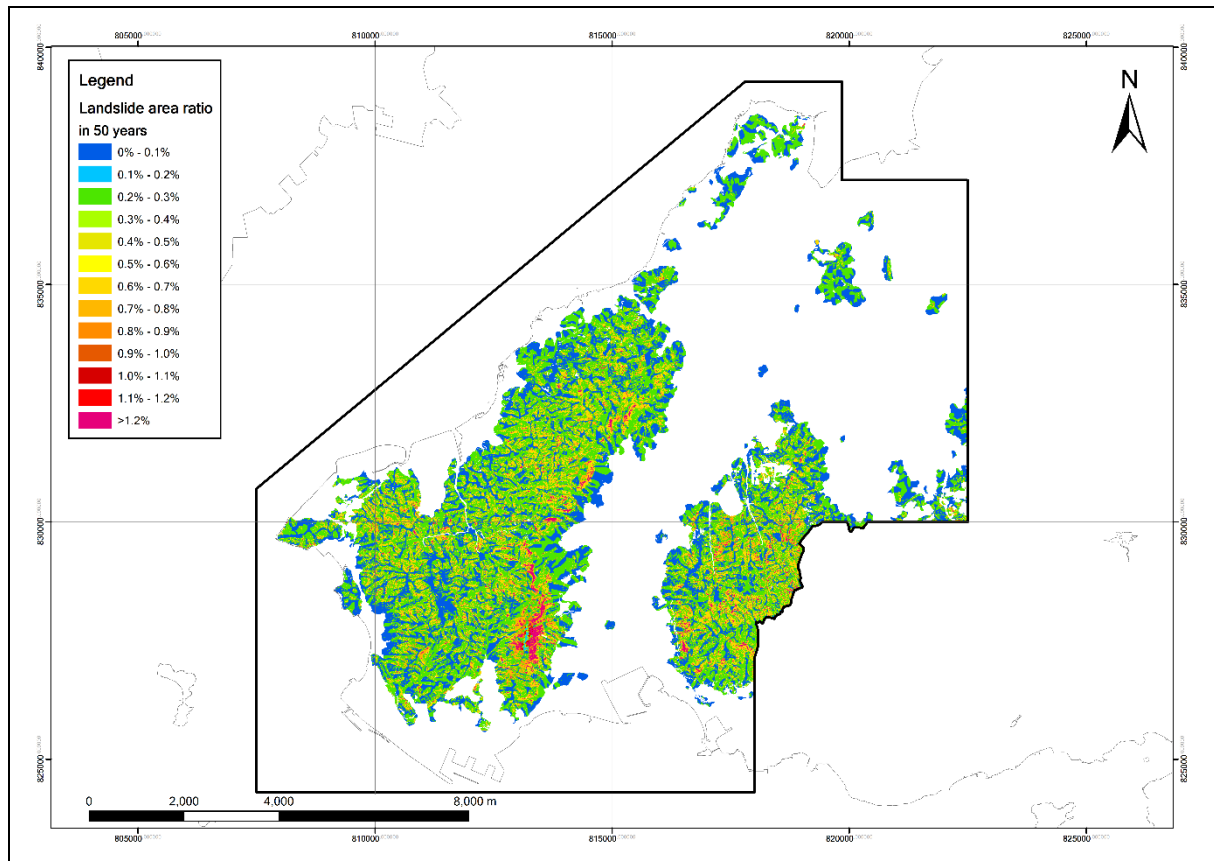
Figure 6.9   Susceptibility Map Considering the Maximum Credible Effect from Seismic Ground Motion

6.1.2   Comparison with Earthquake-induced Landslides in Major Events

A large number of landslides occurred in steeply sloping terrain in Taiwan due to the 1999 Chi-Chi earthquake, which led to very large ground motions in the vicinity of the fault rupture.   This was also observed in the 2008 Sichuan earthquake and in the 1990 Philippines fault event.   Nevertheless, these levels of ground motion are too extreme to realistically represent the situation in Hong Kong.   Also, according to Arup (2015), the bedrock PGA cross the Study Area ranged from about 0.89 m/s² to 0.92 m/s² and 1.94 m/s² to 2 m/s² for 10% and 2% probabilities of being exceeded in the next 50 years.   This means that the variation of the ground motion across the territory is small.   Hence, both the ground motion and the distance to the fault rupture, which have been observed to be major factors affecting earthquake-induced landslides in past major events, are not a concern in the present study.

In this study, the 2% in 50 years ground motion is considered to be the most extreme ground motion for Hong Kong.   This ground motion corresponds to a magnitude 5.5 earthquake with its epicentre within the Study Area (Arup, 2015).   Such an event is not likely to cause a fault rupture at the surface.   At the same time, there is no clear evidence of any active faults that exist in Hong Kong (Sewell & Tang, 2012).   Hence, even for such case, it is considered that widespread landslides similar to those observed in the three afore-mentioned major events will still not occur.   The focus of this study should be remained on hillsides that are already close to failure.

The present study addresses the direct effect of earthquake on the natural hillside stability. Its effect on the post-earthquake susceptibility of rainfall-induced natural terrains landslides due to degradation and distress of hillsides brought about by the earthquake has not been examined.   In addition, any debris resulted from earthquake-induced landslides that may be deposited on natural hillsides is liable to re-mobilisation by subsequent rainstorms.   As such, the potential increase of landslide hazard after earthquake should not be neglected.   Yin (2008) described the post-earthquake situations on slopes with regard to the 2008 Wenchuan Earthquake in China.   He studied the number of events in the affected area before and after the earthquake event and found that there was a large number of slopes considered to be unstable as a consequence of the ground shaking, according to the Chinese Survey.

However, some studies suggested that the effects of earthquake disturbance on slopes would be prolonged but in a diminishing rate.   Ching et al (2012) studied the disturbance effect of the 1999 Chi-Chi Earthquake on slopes by observing the number of landslides during several major rainstorms after the earthquake event.   It was found that although the amount of rainfall in Typhoon Mindulle (July 2004) was much higher than that in Typhoon Toraji (July 2001) and Nari (Sept. 2001), the number of rain-induced landslides in the former event was much less than those in the latter.   This implied that the earthquake disturbance effect could be transient in time and diminish with time.   It was concluded that for the purpose of assessing the landslide susceptibility in the long term, such an effect could be ignored.   Similar findings were proposed by Lin et al (2008), who suggested that the effects of earthquake could be prolonged but in a diminishing rate.   Clearly, continual observations in future earthquake events will enhance the understanding of how long such adverse effects on slopes may persist after major earthquakes.

6.2   Rock and Boulder Fall Susceptibility

In addition to the potential of natural terrain landslides within the Study Area, it is recognised that a number of surface boulders and rock outcrops are present within the natural terrain areas.   A screening of potential rock fall and boulder fall susceptibility has, therefore, been carried out.

This assessment relied primarily on the information contained within the GEO's Boulder Inventory, which records the density of boulder coverage for hillside areas throughout the whole territory of Hong Kong, and the Slope Angle maps developed as part of the landslide susceptibility assessment.   A detailed inventory of boulder fields on natural slopes in Hong Kong was documented by Emery (1998).   This inventory was prepared using aerial photograph interpretation and documented the percentage area covered by boulders as well as the approximate boulder types, typical sizes and shape.

Given that no details of boulder fixity or stability can be inferred from the Boulder Inventory, the potential of boulder fall has been assessed on the basis of the density of boulders present and the gradient of the hillside areas within which they are located.   As for the landslide susceptibility assessment, the combined influence of these two parameters has been assessed following a matrix approach (Table 6.1).

Table 6.1   Combined Influence of Slope Angle and Boulder Density on Boulder Fall Susceptibility

Boulder Density Slope Class	> 50% Coverage	20 to 50% Coverage	< 20% Coverage
Steep (> 40°)	Very High	High	Moderate
Moderately Steep (30°- 40°)	High	Moderate	Low
Gentle (< 30°)	Moderate	Low	Low

The boulder density is presented in Figure 6.10.   The rock fall and boulder fall susceptibility map for the Study Area has been generated in GIS to graphically present those areas falling within different susceptibility classes as shown in Figure 6.11.
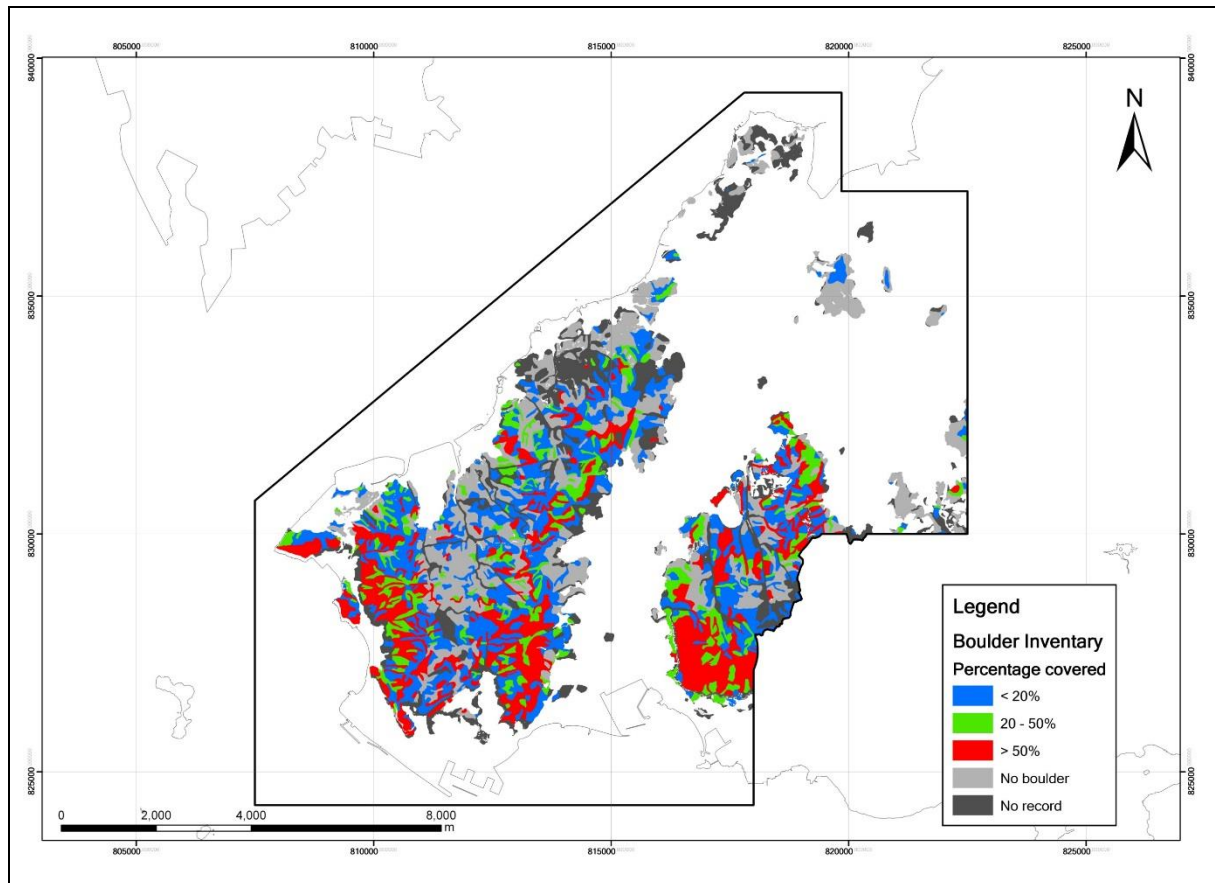
Figure 6.10   Three Classes of Percentage of Boulder Coverage Area
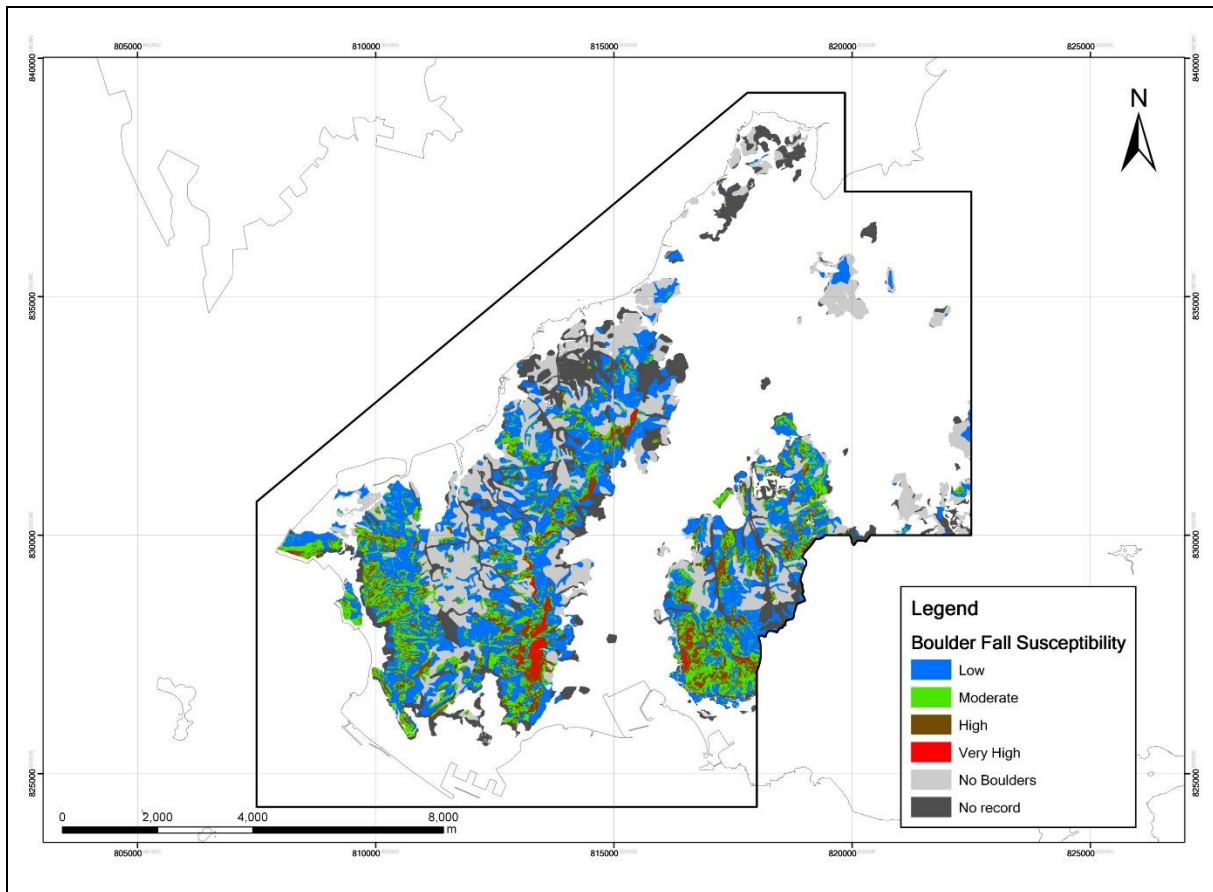
Figure 6.11 Boulder Fall Susceptibility Map

7 Conclusions

The earthquake-induced natural terrain landslide hazard assessment for a Study Area in the North-west New Territories of Hong Kong has been carried out in this study.   The findings of the literature review on local and overseas state-of-the-art papers have been used to consolidate the methodology applied in this study for both natural terrain landslide and boulder fall hazard assessments.

The earthquake-induced landslide displacements have been assessed using both numerical methods (*Oasys* SIREN and Dynamic FLAC) and empirical correlations (Jibson et al, 1998; Hsieh & Lee, 2011) for the 2% and 10% in 50 years seismic ground motions.   It is concluded that the vertical seismic acceleration does not have any significant effect on the generated downslope displacements.   The topographic effects of 30 m, 100 m, and 300 m ridge heights have also been considered.   It is found that the topographic effect due to higher ridges would significantly increase the induced downslope displacements.   The results have been interpreted in terms of the static FoS corresponding to a 100 mm threshold displacement (defined as being likely to trigger earthquake-induced landslides based on the literature review). It is found that the slopes have to be close to failure at the time of earthquake should there be any significant hazard arising from earthquake-induced landslides.

For the seismic stability of boulder fall, a series of simplified one-dimensional dynamic

time stepping analyses have been carried out to determine how close to tipping a boulder (of various sizes) needs to be to trigger instability under the 2%, 10% and 63% in 50 years ground motions. The topographic effects of 30 m, 100 m, and 300 m ridge heights have also been considered for the 2% and 10% in 50 years seismic ground motions. The analyses also cover the combined effect of horizontal and vertical accelerations (without topographic effect) for 2% in 50 years ground motions.   It is found that the boulders have to be close to failure at the time of earthquake should there be any significant earthquake-induced boulder fall hazard.

A seismic microzonation map has been prepared for natural terrain landslide susceptibility to reflect the combined effects of rainfall and seismic ground motions. This relies on a detailed landslide susceptibility mapping derived from past landslides based on the ENTLI database. The observed effects from rainfall have been combined with the calculated seismic ground motion effects by considering how much of the time the natural terrain is close to failure as a result of rainstorms when the seismic ground motion occurs. The assessment is based on the assumptions made by Wong & Ho (2000), who studied the effects of earthquakes on man-made slopes. Overall, the effect of earthquakes on the triggering of landslides in natural terrain is small.   The increase in failure probability is found be to less than one tenth of that expected from rainstorms alone. Apparently, there is uncertainty in some of those assumptions made. Thus, a sensitivity study has been conducted to illustrate the maximum credible effect of seismic ground motions on the natural terrain landslide hazard.   On the basis that the slopes must be very close to failure at the time of earthquake, it is found that the number and size of landslides would probably be similar to those induced solely by rainfall.   In the worst scenario, the hazard would only be marginally larger.

A microzonation map has also been produced in qualitative terms for boulder fall and rock fall susceptibility based on the boulder density and the overall slope angle. It is found that this map is not changed even if seismic ground motions are considered.

The scope of the present study does not include the examination of the degradation of slopes or hillsides, which do not collapse or detach.   In addition, the debris of earthquake-induced landslides that may be deposited on natural hillsides is liable to be re-mobilised by subsequent rainfall.   Therefore, the increase in the likelihood of rain-induced landslides after an earthquake should not be neglected.   It is believed that a 'reactive approach' including inspection and mapping of potential slope distress and major debris deposits close to developments could be a pragmatic approach to deal with the post-earthquake landslide hazard.

8 References

Abrahamson, N.A. & Silva, W.J. (1996). *Empirical Ground Motion Models*.   Report prepared for brookhaven national laboratory, New York, May, 144 p.

AGS (2007).   Guideline for landslide susceptibility, hazard and risk zoning for land use management.   Australian geomechanics society landslide taskforce landslide zoning working group. *Australian Geomechanics*, 42 (1), pp 13-36.

Arup (2015). *Seismic Hazard Analysis of the Hong Kong Region (GEO Report No. 311)*.   Geotechnical Engineering Office, Hong Kong, 327 p.

Arup (2018). *Report on the Seismic Microzonation Assessment of the North-west New Territories (GEO Report No. 338)*. Geotechnical Engineering Office, Hong Kong, 583 p.

Ashford, S.A., Sitar, N., Lysmer, J. & Deng, N. (1997). Topographic effects on the seismic response of steep slopes. *Bulletin of the Seismological Society of America*, vol. 87, no. 3, pp 701-709.

Au-Yeung, Y.S. & Ho, K.K.S. (1995). *Gravity Retaining Walls Subject to Seismic Loading (GEO Report No. 45)*. Geotechnical Engineering Office, Hong Kong, 63 p.

Blake, T.F., Hollingsworth, R.A. & Stewart, J.P. (2002). *Recommended Procedures for Implementation of DGM Special Publication 117 Guidelines for Analyzing and Mitigating Landslide Hazards in California*. ASCE and Southern California Earthquake Center publication.

Celebi, M. (1987). Topographical and geological amplifications determined from strong motion and aftershock records of the 3 march 1985 Chile earthquake. *Bulletin of the Seismological Society of America*, vol. 77, No. 4, pp 1147-1167.

Ching, J., Liao, H.J. & Lee, J.K. (2012). Prediction rainfall-induced landslide potential along a mountain road in Taiwan. *Geotechnique*, vol. 62, issue 6, pp 555-561.

Chung, C.F. & Fabbri, A.G. (2003). Validation of spatial prediction models for landslide hazard mapping. *Natural Hazards*, vol. 30, pp 451-472.

Cole, W.F., Marcum, D.R., Shires, P.O. & Clark, B.R. (1998). *Analysis of Earthquake-reactivated Landslides in the Epicentral Region, Central Santa Cruz Mountains, California*. U.S. Geological Survey Professional Paper 1551-c, pp C165-C185.

Dalrymple, J.B., Blong, R.J. & Conacher, A.J. (1968). A hypothetical nine unit land surface model. *Zeitschrift fur Geomorphologie*, vol. 12, pp 60-76.

Darragh, B., Silva, W. & Gregor, N. (2004). Strong motion record processing for the PEER Center. *Proceedings of COSMOS Invited Workshop on Strong-Motion Record Processing*, Richmond, California, USA, pp 26-27.

Davis, J.C. (2002). *Statistics and Data Analysis in Geology*. 3rd ed. John Wiley & Sons, 638 p.

Ding, Y.Z. (2008). *Risk of Earthquake-induced Landslides in Hong Kong*. Technical report. (in Chinese)

Dobry, R., Idriss, I.M. & Ng, E. (1978). Duration characteristics of horizontal components of strong motion earthquake records. *Bulletin of the Seismological Society of America*, vol. 68, no. 5, pp 1487-1520.

Emery, K.A. (1998). *Boulder Study of Hong Kong - Final Report*. Maunsell Geotechnical Services Ltd. Geotechnical Engineering Office, Hong Kong, 12 p.

Gaudio, V.D. & Wasowski, J. (2011). Advances and problems in understanding the seismic response of potentially unstable slopes. *Special Edition of Journal of Engineering Geology, Toward the Next Generation of Research on Earthquake-induced Landslides: Current Issues and Future Challenges*, vol. 122, pp 73-83.

GCO (1987a). *Geotechnical Area Studies Programme (GASP) Report III, West New Territories*. Geotechnical Control Office, Hong Kong, 155 p. plus 4 maps.

GCO (1987b). *Geotechnical Area Studies Programme (GASP) Report IV, North West New Territories*. Geotechnical Control Office, Hong Kong, 120 p. plus 3 maps.

Geli, L., Bard, P.-Y. & Jullien, B. (1988). The effect of topography on earthquake ground motion: a review and new results. *Bulletin of the Seismological Society of America*, vol. 78, no. 1, pp 42-63.

GEO (2000). *Geological Map of Hong Kong - Millennium Edition, January*. Geotechnical Engineering Office, Hong Kong.

Goovaerts, P. (1997). *Geostatistics for Natural Resources Evaluation*. Oxford University Press, Oxford, 483 p.

Halcrow (2009). *Scoping Study of Natural Terrain Landslide Risk in Hong Kong from a Maximum Credible Earthquake*. Prepared by Halcrow China Limited for Geotechnical Engineering Office, Hong Kong, 110 p.

Hancox, G.T., Perrin, N.D., Dellow, G.D. (1997). *Earthquake-induced Landsliding in New Zealand and Implications for MM Intensity and Seismic Hazard Assessment*. GNS Client Report 43601B.

Hancox, G.T., Perrin, N.D. & Dellow, G.D. (2002). Recent studies of historical earthquake-induced landsliding, ground damage, and MM intensity in New Zealand. *Bulletin of the New Zealand Society for Earthquake Engineering*, vol. 35, no. 2, pp 59-94.

Hancock, J., Watson-Lamprey, J., Abrahamson, N.A., Bommer, J.J., Markatis, A., McCoyh, E. & Mendis, R. (2006) *An Improved Method of Matching Response Spectra of Recorded Earthquake Ground Motion Using Wavelets*. Vol 10, Issue sup001, 67-89.

Haneberg, W.C. (2009). Simplified dynamic analysis of vibration-induced rock toppling. *The Geological Society of America, Technical Note, Environmental & Engineering Geoscience*, vol. xv, no. 1, pp 41-45.

Heckerman, D. (1986). The Certainty-Factor model. S. Shapiro, editor, *Encyclopaedia of Artificial Intelligence*, 2nd Edition, Wiley, New York.

Hsieh, S.Y. & Lee, C.T. (2011).   Empirical estimation of the Newmark displacement from the arias intensity and critical acceleration. *Special Edition of Journal of Engineering Geology, Toward the Next Generation of Research on Earthquake-induced Landslides: Current Issues and Future Challenges*, vol. 122, pp 34-42.

ISSMFE (1993). *Manual for Zonation on Seismic Geotechnical Hazards*.   The Japanese Society of Soil Mechanics and Foundation Engineering.

Jibson, R.W. (1987). *Summary of Research on the Effects of Topographic Amplification of Earthquake Shaking on Slope Stability*.   U.S. Geological Survey Open-File Report 87-268, 166 p.

Jibson, R.W. (1993).   Predicting earthquake-induced landslide displacements using Newmark's sliding block analysis. *Transportation Research Record 1411*, pp 9-17.

Jibson, R.W. (2011).   Methods for assessing the stability of slopes during earthquakes - a retrospective. *Special Edition of Journal of Engineering Geology, Toward the Next Generation of Research on Earthquake-induced Landslides: Current Issues and Future Challenges*, vol. 122, pp 43-50.

Jibson, R.W., Harp, E.L. & Michael, J.M. (1998). *A Method for Producing Digital Probabilistic Seismic Landslide Hazard Maps: An Example from the Los Angeles, California Area*.   U.S. Geological Survey Open-File Report 98-113, 17 p.

Jibson, R.W. & Keefer, D.K. (1993).   Analysis of the seismic origin of landslides: examples from the New Madrid seismic zone. *Geological Society of America Bulletin*, vol. 105, pp 521-536.

Kanagawa Prefectural Government (1986). *Prediction of Seismic Damage in Kanagawa Prefecture*, pp 13-63.   (in Japanese)

Kao, H. & Chen, W.P. (2000).   The Chi-Chi earthquake sequence: active out-of-sequence thrust faulting in Taiwan. *Science*, vol. 288, pp 2346-2349.

Keefer, D.K. (1984).   Landslides caused by earthquakes. *Geological Society of America Bulletin*, vol. 95, pp 406-421.

Keefer, D.K. (1999).   Earthquake-induced landslides and their effects on alluvial fans. *Journal of Sedimentary Research*, vol. 69, pp 84-104.

Keefer, D.K. (2002). *Investigating Landslides Caused by Earthquakes - A Historical Review*. Surveys in Geophysics, Luwer Academic Publishers (Netherlands), vol. 23, pp 473-510.

Keefer, D.K. (2007).   Landslides caused by recent earthquakes: anomalies and relations to general trends. *North American Conference on Landslides*, Vail, Colorado, June 3-8, pp 876-885.

Keefer, D.K. & Wilson, R.C. (1989). *Predicting Earthquake-induced Landslides, with Emphasis on Arid and Semi-arid Environments*. Landslides in a semi-arid environment, Inland Geological Survey Society 2, pp 118-149.

Kirkby, M.J. (1975). *Hydrograph Modelling Strategies*. In: Peel, R., Chisholm, M. & Haggett, P. (Eds.), Process in Physical and Human Geography, Heinemann, London, pp 69-90.

Lee, C.T., Huang, C.C., Lee, J.F., Pan, K.L., Lin, M.L. & Dong, J.J. (2008). Statistical approach to earthquake-induced landslide susceptibility. *Engineering Geology*, vol. 100, pp 43-58.

Liao, H.W. & Lee, C.T. (2000). Landsides triggered by the Chi-Chi earthquake. *Proc. 21st Asian Conference on Remote Sensing*, vols. 1 & 2, pp 383-388.

Lin, M.L., Wang, K.L. & Kao, T.C. (2008). The effects of earthquake on landslides - a case study of Chi-Chi earthquake, 1999. *Special Lecture 6, 10th International Symposium on Landslides and Engineered Slopes*.

Lin, P.S. & Lee, C.T. (2003). Arias intensity in landslide susceptibility analysis. *Proc. 2003 Annual Meeting of Chinese Geophysical Society* (*Taiwan*), pp 91-96 (in Chinese with English abstract) of Geotechnical Engineering, vol. 112, No. 1, pp 44-59.

Lin, Y.H. (2003). *Application of Neural Networks to Landslide Susceptibility Analysis*. M.S. thesis of institute of applied geology, National Central University, 81 p. (in Chinese with English abstract)

Ma, K.F., Lee, C.T. & Tsai, Y.B. (1999). *The Chi-Chi, Taiwan Earthquake: Large Surface Displacements on An Inland Fault*. EOS Transactions, American Geophysical Union, vol. 80 (50), pp 605-611.

MFJV (2003). Landslide susceptibility analysis. Agreement No. 47/2000. *Natural Terrain Hazard Study for Tsing Shan Foothill Area*. Prepared by Maunsell-Fugro Joint Venture. Geotechnical Engineering Office, Hong Kong.

Mora, S. & Vahrson, W-G. (1994). Macrozonation methodology for landslide hazard determination. *Bulletin of the Association of Engineering Geologists*, vol. 31, no. 1, pp 49-58.

Murphy, W. (2006). The role of topographic amplification on the initiation of rock slopes failures during earthquakes. *In: Evans, et al (Ed.), Landslides from Massive Rock Slope Failure*, pp 139-154.

Newmark, N.M. (1965). Effects of earthquakes on dams and embankments. *Geotechnique*, vol. 15, pp 139-159.

Parker, R.N., Densmore, A.L., Rosser, N.J., Michele, M.D., Li, Y., Huang, R., Whadcoat, S. & Petley, D.N. (2011). Mass wasting triggered by the 2008 Wenchuan earthquake is greater than orogenic growth. *Nature Geoscience*, vol. 4, pp 449-452.

Paruelo, J.M., Garbulsky, M.F., Guerschman, J.P. & Jobbagy, E.G. (2004). Two decades of normalized difference vegetation index changes in South America: identifying the imprint of global change. *International Journal of Remote Sensing*, vol. 25, no. 14, pp 2793-2806.

Rathje, E.M., Abrahamson, N.A. & Bray, J.D. (1998). Simplified Frequency Content Estimates of Earthquake Ground Motions. *Journal of Geotechnical Engineering, ASCE*, vol. 124, no. 2, pp 150-159.

Rathje, E.M. & Antonakos, G. (2011). A unified model for predicting earthquake-induced sliding displacement of rigid and flexible slopes. *Special Edition of Journal of Engineering Geology, Toward the Next Generation of Research on Earthquake-induced Landslides: Current Issues and Future Challenges*, vol. 122, pp 51-60.

Rodriguez, C.E., Bommer, J.J. & Chandler, R.J. (1999). Earthquake-induced landslides: 1980-1997. *Soil Dynamics and Earthquake Engineering*, vol. 18, pp 122-127.

Sewell, R.J. & Tang, D.L.K. (2012). *The Potential Evidence for Neotectonic Fault Movement and Correlation with Natural Terrain Landslides in Hong Kong.* (*Geological Report No. GR 4/2012*). Geotechnical Engineering Office, Hong Kong, 33 p.

Tamura, T. (1978). An analysis of the relationship between the areal distribution of earthquake-induced landslides and the earthquake magnitude. *Geographical Review of Japan*, vol. 51, no. 8, pp 662-672. (in Japanese)

Tang, D.L.K., Ding, Y.Z., Lee, C.W., Wong, J.C.F. & Sewell, R.J. (2009). *Study of the Potential Evidence for Neotectonic Movement and Correlation with Natural Terrain Landslides in Hong Kong, Part 1: Ho Lek Pui Area*. (*Geological Report No. GR 1/2009*). Geotechnical Engineering Office, Hong Kong, 44 p.

Tang, D.L.K., Sewell, R.J., Wong, J.C.F. & Ding, Y.Z. (2010). *Study of the Potential Evidence for Neotectonic Movement and Correlation with Natural Terrain Landslides in Hong Kong, Part 3: Tung Chung East.* (*Geological Report No. GR 3/2010*). Geotechnical Engineering Office, Hong Kong, 31 p.

Travasarou, T., Bray, J.D. & Abrahamson, N.A. (2003). Empirical attenuation relationship for arias intensity. *Earthquake Engineering and Structural Dynamics*, vol. 32, pp 1133-1155.

Varnes, D.J. (1984). *Landslide Hazard Zonation: A Review of Principals and Practice*. UNESCO Press, Paris, 63 p.

Wang, K-L. & Lin, M-L. (2010). Development of shallow seismic landslide potential map based on Newmark's displacement: the case of Chi-Chi earthquake, Taiwan. *Environment Earth Sciences*, vol. 60, pp 775-785.

Wasowski, J., Keefer, D.K. & Lee, C.T. (2011). Toward the next generation of research on earthquake-induced landslides: Current issues and future challenges. *Engineering Geology*, vol. 122, pp 1-8.

Wieczorek, G.F., Wilson, R.C. & Harp, E.L. (1985). *Map Showing Slope Stability During Earthquakes in San Mateo County California*. U.S. Geological Survey Miscellaneous Investigations Map I-1257-E, scale 1:62,500.

Wilson, J.P. & Gallant, J.C. (2000). *Terrain Analysis*. John Wiley & Sons, Inc., 479 p.

Wilson, R.C. (1993). *Relation of Arias Intensity to Magnitude and Distance in California*. U.S. Geological Survey Open-File Report 93-556.

Wilson, R.C. & Keefer, D.K. (1983). Dynamic analysis of a slope failure from the 6 August 1979 Coyote Lake, California, earthquake. *Bulletin of the Seismological Society of America*, vol. 73, pp 863-877.

Wilson, R.C. & Keefer, D.K. (1985). Predicting areal limits of earthquake-induced landsliding. *In: Ziony, J.I. (Ed.), Evaluating Earthquake Hazards in the Los Angeles Region An Earth-science Perspective: U.S. Geological Survey Professional Paper 1360*, pp 316-345.

Wong, H.N. & Ho, K.K.S. (2000). *Preliminary Quantitative Risk Assessment of Earthquake-induced Landslides at Man-made Slopes in Hong Kong*. (GEO Report No. 98), Geotechnical Engineering Office, Hong Kong, 69 p.

Wong, H.N. & Pang, P.L.R. (1991). *Assessment of Stability of Slopes Subjected to Blasting Vibration*. (GEO Report No. 15). Geotechnical Engineering Office, Hong Kong, 112 p.

Wong, J.C.F. & Ding, Y.Z. (2010). *Study of the Potential Evidence for Neotectonic Movement and Correlation with Natural Terrain Landslides in Hong Kong, Part 2: Wong Chuk Yeung Area*. (*Geological Report No. GR 1/2010*). Geotechnical Engineering Office, Hong Kong, 40 p.

Wong, J.C.F., Tang, D.L.K., Sewell, R.J. & Lee, C.W. (2010). *Study of the Potential Evidence for Neotectonic Movement and Correlation with Natural Terrain Landslides in Hong Kong, Part 4: Nam Shan and Pui O Areas*. (*Geological Report No. GR 4/2010*). Geotechnical Engineering Office, Hong Kong, 24 p.

Yang, J. (2007). On seismic landslide hazard assessment. *Geotechnique*, vol. 57, no. 8, pp 707-713.

Yasuda, S. & Sugitani, T. (1988). Case histories of slope failure during past earthquakes in Japan. *Proc. 23rd ISSMFE*, pp 891-892. (in Japanese)

Yin, Y. (2008). Researches on the geo-hazards triggered by the Wenchuan earthquake, Sichuan. *Chinese J. Engineering Geology*, vol. 16, pp 433-449. (in Chinese)

GEO PUBLICATIONS AND ORDERING INFORMATION
土力工程處刊物及訂購資料

An up-to-date full list of GEO publications can be found at the CEDD Website http://www.cedd.gov.hk on the Internet under "Publications". The following GEO publications can also be downloaded from the CEDD Website:
- i. Manuals, Guides and Specifications
- ii. GEO technical guidance notes
- iii. GEO reports
- iv. Geotechnical area studies programme
- v. Geological survey memoirs
- vi. Geological survey sheet reports

Copies of some GEO publications (except geological maps and other publications which are free of charge) can be purchased either by:

Writing to
Publications Sales Unit,
Information Services Department,
Room 626, 6th Floor,
North Point Government Offices,
333 Java Road, North Point, Hong Kong.

or
- Calling the Publications Sales Section of Information Services Department (ISD) at (852) 2537 1910
- Visiting the online Government Bookstore at http:// www.bookstore.gov.hk
- Downloading the order form from the ISD website at http://www.isd.gov.hk and submitting the order online or by fax to (852) 2523 7195
- Placing order with ISD by e-mail at puborder@isd.gov.hk

1:100 000, 1:20 000 and 1:5 000 geological maps can be purchased from:

Map Publications Centre/HK,
Survey & Mapping Office, Lands Department,
23th Floor, North Point Government Offices,
333 Java Road, North Point, Hong Kong.
Tel: (852) 2231 3187
Fax: (852) 2116 0774

Any enquires on GEO publications should be directed to:

Chief Geotechnical Engineer/Standards and Testing,
Geotechnical Engineering Office,
Civil Engineering and Development Department,
Civil Engineering and Development Building,
101 Princess Margaret Road,
Homantin, Kowloon, Hong Kong.
Tel: (852) 2762 5346
Fax: (852) 2714 0275
E-mail: frankielclo@cedd.gov.hk

詳盡及最新的土力工程處刊物目錄，已登載於土木工程拓展署的互聯網網頁http://www.cedd.gov.hk 的"刊物"版面之內。以下的土力工程處刊物亦可於該網頁下載：
- i. 指南、指引及規格
- ii. 土力工程處技術指引
- iii. 土力工程處報告
- iv. 岩土工程地區研究計劃
- v. 地質研究報告
- vi. 地質調查圖表報告

讀者可採用以下方法購買部分土力工程處刊物(地質圖及免費刊物除外):

書面訂購
香港北角渣華道333號
北角政府合署6樓626室
政府新聞處
刊物銷售組

或
- 致電政府新聞處刊物銷售小組訂購 (電話：(852) 2537 1910)
- 進入網上「政府書店」選購，網址為 http://www.bookstore.gov.hk
- 透過政府新聞處的網站 (http://www.isd.gov.hk) 於網上遞交訂購表格，或將表格傳真至刊物銷售小組 (傳真：(852) 2523 7195)
- 以電郵方式訂購 (電郵地址：puborder@isd.gov.hk)

讀者可於下列地點購買1:100 000、1:20 000及1:5 000地質圖：

香港北角渣華道333號
北角政府合署23樓
地政總署測繪處
電話: (852) 2231 3187
傳真: (852) 2116 0774

如對本處刊物有任何查詢，請致函：

香港九龍何文田公主道101號
土木工程拓展署大樓
土木工程拓展署
土力工程處
標準及測試部總土力工程師
電話: (852) 2762 5346
傳真: (852) 2714 0275
電子郵件: frankielclo@cedd.gov.hk